Stationary Eddies and Zonal Variations of the Global Hydrological Cycle in a Changing Climate

Thesis by

Robert Christopher Wills

In Partial Fulfillment of the Requirements

for the Degree of

Doctor of Philosophy

California Institute of Technology

Pasadena, California

2016

(Defended December 9, 2015)

For the Earth

Acknowledgements

Throughout my studies and work towards this thesis at Caltech and ETH Zürich, I have had support and inspiration from a number of people whom I would like to thank.

First, I would like to thank my parents, Chris and Teri, for giving me the support and resources to succeed in my studies and in life. And especially for instilling in me a love for nature through countless trips to the mountains. This is a big part of who I am today. Thanks to my brother Daniel for providing your own perspective and making family trips more enjoyable. I am grateful also to all of my grandparents and extended family, but especially my grandpa Jack Wills, who provided an academic perspective in my life and showed me what it is like to be a professor.

To all of my friends at ETH and Caltech, you have made the last 4 1/2 years some of the best of my life so far. I am very grateful to all of you – you know who you are. Without all the fun times we've had, it would not be as easy to work so hard towards this thesis. A special shout out to my housemates at 'The Mansion' in San Gabriel and at 'Schloss Vogelsang' in Zurich. It is so valuable to have friends at home to talk to about life's everyday happenings. My cat Luna has also been a great companion throughout my Ph.D.

I am thankful to my research group for helping me find my bearings in a new research field. Tobias Bischoff was especially helpful early in my studies, patiently showing me some basics about atmospheric energy balances and providing lots of good discussion on research directions. Ori Adam was also a key source of support with regards to figuring out how to acquire and manage large amounts of climate data. His data portal, GOAT, has been a key tool in my thesis. My research benefited from several collaborative projects, with James Rae, Ian Eisenman, Michael Byrne, and Xavier Levine, which made it into this thesis in one form or another. I have had many fruitful discussions also with Momme Hell, Farid Ait Chaalal, Cheikh Mbengue, Zhihong Tan, Sally Zhang, Bettina Meyer, and all the other members of the group over the years. You have all played a role in this thesis. Administrative support has been invaluable to my graduate studies, especially during my adjustment to Switzerland and ETH. For this I am very grateful for all the guidance from Patricia Meile and also for support from Nora Oshima and Liz Boyd at Caltech.

The members of my thesis committee have all given me great support and guidance, especially during my time at Caltech. For that I am thankful to Andy Thompson, Simona Bordoni, Mike Lamb, and Jess Adkins. And finally, I would like to thank the person who has had by far the biggest impact on this thesis, my advisor Tapio Schneider. Your willingness to listen to questions while also letting me wander off on my own tangents has provided me with a wonderful work environment. I am also very thankful for the opportunity to move to Zurich and for all the support through that process. I have learned so much from working in the climate dynamics group at Caltech and ETH.

Abstract

This thesis advances our physical understanding of the sensitivity of the hydrological cycle to global warming. Specifically, it focuses on changes in the longitudinal (zonal) variation of precipitation minus evaporation ($P - E$), which is predominantly controlled by planetary-scale stationary eddies. By studying idealized general circulation model (GCM) experiments with zonally varying boundary conditions, this thesis examines the mechanisms controlling the strength of stationary-eddy circulations and their role in the hydrological cycle. The overarching goal of this research is to understand the cause of changes in regional $P - E$ with global warming. An understanding of such changes can be useful for impact studies focusing on water availability, ecosystem management, and flood risk.

Based on a moisture-budget analysis of ERA-Interim data, we establish an approximation for zonally anomalous $P - E$ in terms of surface moisture content and stationary-eddy vertical motion in the lower troposphere. Part of the success of this approximation comes from our finding that transient-eddy moisture fluxes partially cancel the effect of stationary-eddy moisture advection, allowing divergent circulations to dominate the moisture budget. The lower-tropospheric vertical motion is related to horizontal motion in stationary eddies by Sverdrup and Ekman balance. These moisture- and vorticity-budget balances also hold in idealized and comprehensive GCM simulations across a range of climates.

By examining climate changes in the idealized and comprehensive GCM simulations, we are able to show the utility of the vertical motion $P - E$ approximation for splitting changes in zonally anomalous $P - E$ into thermodynamic and dynamic components. Shifts in divergent stationary-eddy circulations dominate changes in zonally anomalous $P - E$. This limits the local utility of the *wet gets wetter, dry gets drier* idea, where existing $P - E$ patterns are amplified with warming by the increase in atmospheric moisture content, with atmospheric circulations held fixed. The increase in atmospheric moisture content manifests instead in an increase in the amplitude of the zonally anomalous hydrological cycle as measured by the zonal variance of $P-E$. However, dynamic changes, particularly the slowdown of divergent stationary-eddy circulations, limit the strengthening of the zonally anomalous hydrological cycle. In certain idealized cases, dynamic changes are even strong enough to reverse the tendency towards *wet gets wetter, dry gets drier* with warming.

Motivated by the importance of stationary-eddy vertical velocities in the moisture budget analysis, we examine controls on the amplitude of stationary eddies across a wide range of climates in an idealized GCM with simple topographic and ocean-heating zonal asymmetries. An analysis of the thermodynamic equation in the vicinity of topographic forcing reveals the importance of on-slope surface winds, the midlatitude isentropic slope, and latent heating in setting the amplitude of stationary waves. The response of stationary eddies to climate change is determined primarily by the strength of zonal surface winds hitting the mountain. The sensitivity of stationary-eddies to this surface forcing increases with climate change as the slope of midlatitude isentropes decreases. However, latent heating also plays an important role in damping the stationary-eddy response, and this damping becomes stronger with warming as the atmospheric moisture content increases. We find that the response of tropical overturning circulations forced by ocean heat-flux convergence is described by changes in the vertical structure of moist static energy and deep convection. This is used to derive simple scalings for the Walker circulation strength that capture the monotonic decrease with warming found in our idealized simulations.

Through the work of this thesis, the advances made in understanding the amplitude of stationary-waves in a changing climate can be directly applied to better understand and predict changes in the zonally anomalous hydrological cycle.

Contents

II Mechanisms of stationary-eddy change 91

5 Orographic forcing of stationary Rossby waves in a wide range of climates 92

Chapter 1

Introduction

1.1 Motivation

The atmosphere transports water vapor from dry regions to wet regions, setting the global distribution of net precipitation (precipitation minus evaporation, $P - E$). Regions of high $P - E$ have high surface-water availability and can thus support more productive ecosystems and agriculture and better provide for societies' water needs. Changes in $P - E$ in the future can thus have large impacts on people and ecosystems around the world. Regional variations in $P - E$ also extend over ocean, where they determine the regional variations in sea-surface salinity, an important control on the structure of the ocean meridional overturning circulation (Broecker et al., 1985).

In most regions of the tropics, precipitation exceeds evaporation as the low-level winds transport moisture and converge in the Intertropical Convergence Zone (ITCZ). Surrounding this moist region, there are dry zones that extend up to about 35° latitude associated with large-scale subsidence that makes up the descending branch of the Hadley circulation. Beyond 35° latitude, precipitation again exceeds evaporation as synoptic eddies converge moisture that originated in the subtropics. As the climate warms, there is a general tendency for the amplitude of this latitudinal pattern to increase due to an increase in moisture carrying capacity of the atmosphere (Mitchell et al., 1987; Chou and Neelin, 2004; Held and Soden, 2006). Superimposed on this change are shifts in circulation, such as the equatorward shift of the ITCZ (Chou et al., 2009; Seager et al., 2010; Sobel and Camargo, 2011), the expansion of the Hadley cell (Lu et al., 2007), or the poleward shift and intensification of the storm track (Kushner et al., 2001; Yin, 2005) that are indicated as robust responses to warming by some climate models (Collins et al., 2013).

Precipitation minus evaporation also varies strongly with longitude, especially in the Northern Hemisphere and the tropics, due to the influence of stationary eddies forced by topography and longitudinal variations in diabatic heating. This longitudinal, or zonal, variability in $P-E$ makes up 60% of the total global spatial variability of $P-E$ in the modern climate (see Chapter 2). Most land areas have $P-E$ that is 0.25–1 m yr^{-1} different from the zonal mean. Zonally anomalous $P-E$ thus constitutes a large influence on the livelihoods of people globally. Examples of these zonally anomalous $P-E$ patterns are the South Asian and East Asian summer monsoons, the Northern Hemisphere storm tracks, the dryness of the continental midlatitudes, the oceanic subtropical lows, the high precipitation Pacific warm pool, the South Pacific Convergence Zone, and the zonal structure of the ITCZ.

Stationary eddy circulations can have larger responses to climate changes than zonal-mean circulations because they are not subject to angular momentum constraints. Zonally anomalous $P-E$ can thus account for some of the largest climate changes. Interannual and decadal variations in $P-E$, for example on the west coast of North America (Deser et al., 2014) or in the South Asian Monsoon region (Walker et al., 2015), are primarily attributed to variations in the stationary-eddy circulations. Observed precipitation changes in the Southwest US and the Meditteranean over the last decades have been attributed to changes in stationary waves (Seager et al., 2007, 2014). It is an important question to understand how stationary waves and zonally anomalous $P-E$ patterns change across a wide range of climates. This can help us understand what will happen to $P-E$ around the globe as the climate warms in the next century and to understand what $P-E$ looked like in the cold glacial climates of the past and the very warm climates of the more distant past.

The goal of this thesis is to make a make a precise quantitative link between stationary-eddy amplitude and the amplitude of zonal variation of $P-E$ and to understand how stationary-wave amplitude responds to warming. The response to warming will be examined across a wide range of climates for stationary waves forced by simple topography and equatorial heating in an idealized general circulation model (GCM) and for future climate change in state-of-the-art coupled models prepared for the Intergovernmental Panel on Climate Change's (IPCC) 5th Assessment Report (AR5). In this way we seek to both gain insight into the physical mechanisms determining stationary wave change and understand some of the ways that these changes can influence the global hydrological cycle in the future.

1.2 What is a stationary eddy?

As most of this thesis will be about stationary eddies, it is useful to start with a precise definition. For the purposes of this thesis, a stationary eddy is any climatological deviation from the zonal mean, either of winds or of other variables. Climatological can refer to anything from averages over a season to averages over 40 years. This definition includes stationary Rossby waves, which dominate the planetary scale circulation in the midlatitudes, monsoon circulations which develop seasonally, and tropical overturning circulations such as the Walker circulation.

The modern zonal-mean wind climatology contains westerly jets in each hemisphere, sometimes split into separate subtropical and midlatitude jets (Fig. 1.1a). The surface winds in the midlatitudes are westerly and switch to easterly winds at the border of the tropics, about 30° latitude. Meridional winds are ageostrophic and generally much weaker than the zonal winds. Together with the vertical winds they can be represented by an overturning streamfunction (the circulation is clockwise about positive streamfunction contours), which shows two overturning cells in each hemisphere, a Hadley cell and a Ferrel cell (Fig. 1.1b). These circulations are described extensively elsewhere (e.g., Schneider, 2006; Vallis, 2006). Stationary eddies, departures from this zonal-mean climatology, can take the form of rotational horizontal circulations or divergent overturning circulations. Rotational circulations can be represented by a horizontal streamfunction (Fig. 1.1c). These circulations are primarily Rossby waves and include areas where the westerly jet is strengthened (i.e. Pacific and Atlantic storm tracks) or weakened (i.e. Northern hemisphere continents). Divergent circulations include both zonal and meridional overturning circulations. Together they can be represented by a stationary-eddy vertical velocity (Fig. 1.1d). This includes zonal overturning circulations such as the

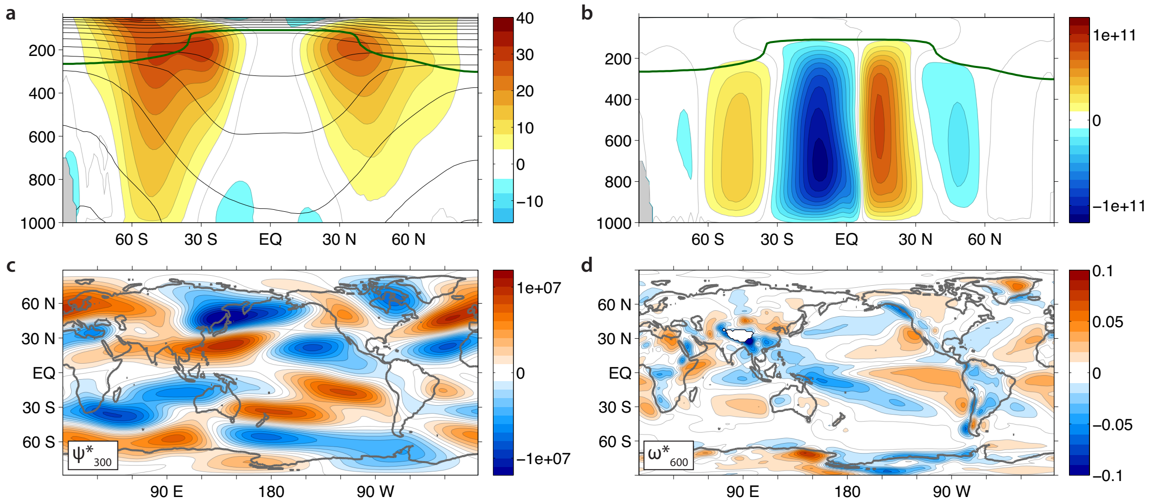

Figure 1.1: The general circulation in ERA-Interim reanalysis (1979-2012). a) Zonal-mean zonal wind (colors), potential temperature (contours, interval = 20 K), and tropopause height determined from the 2 K km^{-1} lapse rate criterion (dark green line). b) Zonal-mean meridional overturning streamfunction showing the Hadley and Ferrel cells. c) The stationary-eddy streamfunction, showing the rotational flow at 300 hPa. d) The stationary-eddy pressure veloctity, $\omega = \frac{Dp}{Dt}$, at 600 hPa, showing the divergent stationary-eddy flow. The vertical velocity has been filtered with a 200 km Gaussian filter.

Walker circulation as well as local enhancements or reductions of Hadley-cell meridional overturning.

Stationary eddies only exist due to zonal variations of the earth surface boundary conditions such as topography and surface heat exchange (Held et al., 2002). The flow around topographic obstacles can set up a stationary Rossby wave if the mountain range is large enough such that the flow around feels the influence of the Earth's rotation. Zonally anomalous surface heating tends to create regions of deep convection, especially in the tropics. This overturning can also force stationary Rossby waves through its interaction with the existing rotational flow. Once stationary eddies have formed in response to zonally varying boundary conditions, they create zonal anomalies in atmospheric latent heating, water vapor and cloud radiative effects, and the fluxes of heat by transient eddies. These zonally anomalous heat sources can further amplify or damp stationary eddies and can be thought of as a feedback on stationary-eddy amplitude.

Most large-scale stationary-eddy circulations outside the deep tropics take the form of stationary Rossby waves. Rossby waves are perturbations of the zonal-mean atmospheric circulation with a scale of several thousand kilometers. They are governed by geostrophic balance, where pressure gradients are balanced by the Coreolis force,

$$\begin{aligned} fu &= -\frac{1}{\rho}\frac{\partial p}{\partial y}, \\ -fv &= -\frac{1}{\rho}\frac{\partial p}{\partial x}. \end{aligned} \tag{1.1}$$

Here f is the Coriolis frequency, u and v are the eastward and northward components of the horizontal wind, and p is the pressure at constant height. By linearizing about a time- and zonal-mean wind, U, a linear dispersion relation for Rossby waves in a single atmospheric layer can be derived, where the zonal phase velocity is given by

$$c_x = U - \frac{\beta}{K}. \tag{1.2}$$

Here $\beta = df/dy$ and $K = \sqrt{k^2 + l^2}$, where k and l are the zonal and meridional wavenumbers respectively. For sufficiently large spatial scales (small K), the phase velocity can go to zero, whereby the Rossby waves become stationary. The scale of stationary Rossby waves is thus given by the stationary wavenumber,

$$K_s = \sqrt{\frac{\beta}{U}} \tag{1.3}$$

For this reason, stationary eddies generally have a scale of 8,000 km or greater. Many other properties of stationary Rossby waves can be derived from a linearization of the momentum equation and are reviewed elsewhere (Hoskins and Karoly, 1981; Held, 1983; Vallis, 2006). Relevant properties of stationary Rossby waves will be presented as they are needed.

Stationary eddies induce zonal anomalies in many other quantities, such as $P - E$, temperature, and specific humidity. Zonal anomalies will be denoted by

$$(\cdot)^* = (\cdot) - [\cdot], \tag{1.4}$$

where $[\cdot]$ denotes a zonal average and $(\cdot)$ denotes the full field. Throughout this thesis, zonally anomalous fields such as the time-mean zonally anomalous specific humidity $\overline{q}^*$ will be considered as part of the stationary eddy. Stationary eddies are thus defined as all zonal variations of time-mean climatic variables about zonal-mean values.

1.3 The problem at hand

There are two overarching themes upon which this thesis makes progress: 1. The link between stationary eddies and the zonal variation of $P-E$ and 2. controls on the amplitude of stationary eddies in a changing climate. We outline the state of the field and some of the specific questions we hope to answer for each of these themes.

1.3.1 Linking zonal asymmetry of the hydrological cycle to stationary eddies

The direct link between water vapor transport by atmospheric circulations and the global distribution of precipitation was established observationally by Benton and Estoque (1954) and Starr and Peixoto (1958), with more detailed studies made possible by the International Geophysical Year (e.g., Peixoto, 1970). This paved the way for studies that were able to attribute the latitudinal pattern of $P-E$ to specific types of circulations such as the Hadley circulation, transient, and stationary eddies (Peixoto and Oort, 1983, 1992). In this way we understand that wet regions of the tropics occur associated with the ascending branch of the Hadley cell and zonal overturning circulations such as the Walker circulation. Similarly the dry subtropical latitudes are associated with the descending branch of the Hadley cell. Transient eddies transport moisture into the midlatitudes, setting the distribution of $P-E$ beyond about 30° latitude.

This link is useful in understanding how $P-E$ responds to climate change. O'Gorman and Schneider (2008b) show how the moisture budget can be used to explain changes in zonal-mean $P-E$ in terms of changes in water vapor, Hadley circulation strength, and transient-eddy kinetic energy across a wide range of climates in an idealized GCM. There has been much focus on the change in $P-E$ that results from the increase in atmospheric water vapor content with warming (Mitchell et al., 1987; Chou and Neelin, 2004; Held and Soden, 2006), because this is a large and robust change that leads to wet zones getting wetter and dry zones getting drier. However, changes in atmospheric circulations can not be ignored (e.g., Held and Soden, 2006; Vecchi and Soden, 2007; Chou et al., 2009; Seager et al., 2010). Increasingly, there is a consensus that we need to focus on understanding changes in atmospheric circulations in order to properly assess changes in the hydrological cycle in the future climate.

All studies of the moisture budget to date have focused either on the zonal-mean hydrological cycle, the full global hydrological cycle, or on specific regions. We hope to provide a new perspective by focusing exclusively on anomalies from the zonal mean, with the expectation that the relative importance of different types of atmospheric circulations will shift with this shift of perspective. The questions we hope to answer are:

1. Can changes in zonally anomalous $P-E$ be tied to the strength of stationary-eddy circulations in a way that is useful in understanding the response to climate change as a product of moisture changes and stationary-eddy changes?
2. What measure of stationary-eddy circulations is most relevant for $P-E$?
3. To what extent are transient eddies important in the zonal variation of $P-E$?
4. Are zonal variations of moisture important for the zonal variation of $P-E$?

1.3.2 Stationary-eddy circulations and climate change

Many properties of stationary waves in midlatitudes are well described by linear quasi-geostrophic theory (Hoskins and Karoly, 1981; Held, 1983). For this reason, linear stationary wave models, general circulation models with the nonlinearities strongly damped (Ting and Yu, 1998; Held et al., 2002) or which explicitly solve the linearized primitive equations (Egger, 1976; Hoskins and Karoly, 1981; Nigam et al., 1986, 1988; Valdes and Hoskins, 1989; Ting, 1994), are often used to study the response of stationary waves to zonally asymmetric forcing. Held et al. (2002), for example, show how the stationary wave climatology in Northern hemisphere winter compares to that simulated by a linear model. While the pattern is well simulated, it relies on specifying zonally anomalous transient-

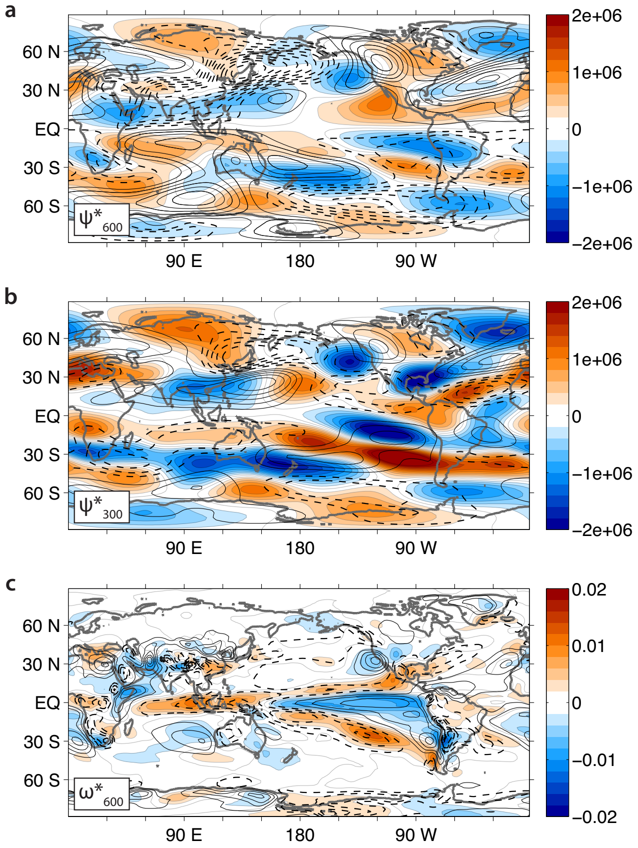

Figure 1.2: Change of stationary-eddy circulations in CMIP5, from the past (1976-2005, historical simulation) to the future (2070-2099, RCP8.5 scenario). a) Change of the stationary-eddy streamfunction at 600 hPa (shading), shown with the past climatology (contours, contour interval 1e6). b) Change of the stationary-eddy streamfunction at 300 hPa (shading), shown with the past climatology (contours, contour interval 2e6). c) Change of the stationary-eddy vertical velocity at 600 hPa (shading), shown with the past climatology (contours, contour interval 0.01). The vertical velocity has been filtered with a 200 km Gaussian filter.

eddy heat and momentum fluxes, which are themselves dependent on the stationary-wave solution. In this way, linear stationary-wave models are a useful tool for attributing aspects of the stationary-wave climatology to different forcings, but they do not give a closed model for stationary waves in terms of the zonal-mean circulation and zonally anomalous boundary conditions. In a study of the stationary-wave response to climate change, Stephenson and Held (1993) find that the linear model response is dominated by changes in latent heating and transient-eddy heat and momentum fluxes, rather than changes in the zonal-mean basic state. This emphasizes the importance of understanding these nonlinearities as they change with the stationary wave.

Several studies have diagnosed the stationary-eddy response to climate change in coupled climate models (Brandefelt and Körnich, 2008; Simpson et al., 2014, 2015). These provide quantitative predictions of what stationary-waves will look like in the future climate. Following these studies, we show in Fig. 1.2 the stationary-eddy changes from 1979-2005 to 2070-2099 diagnosed from 23 models from the Coupled Model Intercomparison Project phase 5 (CMIP5, see Chapter 4 for models used). The future climate (2070-2099) is diagnosed in the Representative Concentration Pathways RCP8.5 scenario, a "business as usual" scenario. The stationary-eddy streamfunction changes, shown for the lower and upper troposphere in Fig. 1.2 a and b, primarily show phase shifts of stationary-eddy circulations. A closer look reveals that changes tend to be out of phase with the climatology, showing a weakening of stationary-eddy circulations. This weakening is much more obvious in the divergent circulations (Fig. 1.2c), where the main mode of change is to reduce stationary-eddy vertical velocities. Part of the reason for this is that the total overturning of the atmosphere must decrease in a warmer climate in order to satisfy energetic constraints on global-mean precipitation (Betts, 1998; Held and Soden, 2006; Vecchi and Soden, 2007; Schneider et al., 2010). However, this decrease in global overturning can be distributed between the Hadley circulation, the Walker circulation, and other stationary-eddy overturning circulations, so this constraint does not provide precise information on how any individual circulation will change. Further, it does not constrain changes in the strength of rotational stationary-eddy circulations.

While this type of analysis gives quantitative predictions of stationary-wave changes over the next century, it gives little insight into the mechanisms behind these changes. For most of this thesis we turn instead to idealized GCM experiments, where we can probe the physical balances maintaining the stationary-eddy circulations over a wide range of parameter space. The key question we seek to answer about stationary waves in a changing climate is: How does the strength of stationary-eddy circulations, both rotational and divergent, respond to climate change? This is complementary to studies that provide dynamical mechanisms for changes in the phase structure of stationary eddies (e.g., Simpson et al., 2015) based on increases in the speed of the subtropical jet and the consequent decrease in stationary-eddy length scale. The change in strength should depend on the type of zonally anomalous forcing, so we will investigate separately stationary eddies forced by orography and by equatorial heating in an idealized GCM. There is an expectation based on the literature that the amplitude of orographic stationary waves should depend on the low-level wind (Hoskins and Karoly, 1981; Held and Ting, 1990), but no study has addressed this together with other factors such as latent heating and transient-eddy changes. Merlis and Schneider (2011) provide a scaling for the Walker circulation strength resulting from equatorial heating, but this depends on an assumption of fixed precipitation, and is thus not a closed theory.

An understanding of the stationary-wave response in the full climate system will require a synthesis of what is learned about stationary waves forced by orography and equatorial heating and what is known about stationary waves resulting from other types of forcing such as subtropical heating (Rodwell and Hoskins, 1996, 2001; Shaw, 2014; Levine and Boos, 2016).

1.4 A guide to this thesis

In this thesis, we examine controls on the global hydrological cycle as it responds to climate change. We focus in particular on variations about the zonal-mean hydrological cycle, where much previous work has focussed exclusively on the zonal-mean. The zonally anomalous hydrological cycle results from stationary-eddy circulations, so we focus also on questions of how stationary eddies respond to climate change. The thesis is split accordingly into two parts. Part I (chapter 2-4) is about changes in the zonally anomalous hydrological cycle with climate change. Part II is about the changes in stationary-eddy circulations that govern these zonal variations.

In chapter 2, we present the zonally anomalous hydrological cycle in the modern climate using ERA-Interim reanalysis. Through an analysis of the zonally anomalous moisture and vorticity budgets we derive an approximate expression for zonally anomalous net precipitation in terms of stationary-eddy vertical motion. We also find that the importance of transient-eddy moisture fluxes and stationary-eddy advection is diminished when the internal cancellation between them is considered. We examine also the implications of this analysis for the Pacific–Atlantic difference in sea-surface salinity. This work is previously published in the Journal of Climate Wills and Schneider

(2015), but has been updated to provide a clearer explanation of the role of near-surface flow over topography.

In chapter 3, we start with a review of the moisture budget decomposition of chapter 2 for the case of idealized GCM simulations forced by two different zonal asymmetries: a Gaussian mountain in the midlatitudes and equatorial heating by ocean heat-flux convergence. These simulations are performed for a wide range of climates, from 280 K to 320 K global-mean surface temperature. We proceed to analyze how the zonally anomalous hydrological cycle responds to climate change in these simulations. The approximate expression of chapter 2 is used to split changes into a thermodynamic component, due to changes in atmospheric moisture content, and a dynamic component, due to changes in stationary-eddy overturning circulations. We show that dynamic changes, due to shifts in stationary-eddy circulations, limit the local utility of the thermodynamic *wet gets wetter, dry gets drier* idea, that has been used extensively in the literature. We present the idea that thermodynamic changes might be more apparent in the amplitude of zonal variations in the hydrological cycle, which we diagnose using the zonal variance of precipitation minus evaporation ($P - E$). We find that the increase in zonal hydrological cycle amplitude does show the effect of increasing atmospheric moisture content, but the slowdown of stationary-eddy circulations also plays a significant role, even reversing the tendency towards *wet gets wetter, dry gets drier* in some latitude bands. This sets up chapter 4, which examines the zonal variance of $P - E$ in the modern climate, and chapters 5 and 6, which examine the mechanisms behind the changes in stationary-eddy circulations in these two experiments.

In chapter 4, we test the ideas of chapter 3 for climate change over the next century, as seen by 23 state-of-the-art coupled climate models. In particular, we focus on the amplitude of the zonally anomalous hydrological cycle, which increase in all models. As in the idealized GCM, dynamic limitations of this amplitude increase are important. Transient-eddy moisture flux changes are more important than in the idealized GCM experiments, so we derive a means of splitting the changes into thermodynamic, dynamic, and transient eddy components based on analysis of a $P-E$ variance budget. Stationary-eddies reduce the amplitude increase with warming. Surprisingly, so do transient eddies, which have traditionally been scaled up with atmospheric moisture content leading to an amplitude increase.

In chapters 5 and 6, we diagnose the change in amplitude of stationary-eddies in the idealized GCM simulations of chapter 3, motivated by their importance for the hydrological cycle. An analysis of the thermodynamic equation sheds light on the role of surface winds in forcing vertical motion in the vicinity of topography (chapter 5). The sensitivity of stationary waves to this surface forcing is set by the midlatitude isentropic slope. Latent heating is found to play an important role in damping the stationary wave response to topography in warm climates. An analysis of the vorticity budget shows that the strength of the stationary-eddy overturning (the Walker circulation) in the equatorial heating experiment is independent of details of the vorticity balance, suggesting that the vorticity budget responds passively to imposed vertical motion (chapter 6). We examine instead the moist static energy budget, through which we come to the conclusion that the strength of the Walker circulation is set by the zonally anomalous net energy input, with a sensitivity that depends on the energy released per unit mass of deep convection. We also address numerous other aspects of the dynamics in these simulations, such as changes in stationary-eddy lengthscale (or lack thereof) and changes in the meridional propagation of wave energy.

In chapter 7, we present the conclusions of this thesis.

Part I

Stationary-eddy controls on the zonal variation of the hydrological cycle

Chapter 2

Zonally anomalous moisture budget in the modern climate

This chapter is modified from work published in the *Journal of Climate* (Wills and Schneider, 2015), The reason for modification is the development of a simpler theoretic framework in (Wills and Schneider, 2016; Chapter 3), which allows for a clearer explanation. The results and conclusions of the paper remain qualitatively unchanged.

Abstract

Transport of water vapor in the atmosphere generates substantial spatial variability of net precipitation (precipitation minus evaporation). Over half of the total spatial variability in annual-mean net precipitation is accounted for by deviations from the zonal mean. Over land, these regional differences determine differences in surface water availability. Over oceans, they account, for example, for the Pacific–Atlantic difference in sea surface salinity, with implications for the deep overturning circulation. This study analyzes the atmospheric water budget in ERA-Interim and MERRA reanalyses, to investigate which physical balances lead to zonal variation in net precipitation. It is found that the leading-order contribution is zonal variation in stationary-eddy vertical motion. Transient eddies modify the pattern of zonally anomalous net precipitation by moving moisture from the subtropical and tropical oceans onto land and poleward across the Northern Hemisphere storm tracks. Zonal variation in specific humidity and stationary-eddy horizontal advection play a

secondary role. The dynamics leading to net precipitation via vertical motion in stationary eddies can be understood from a lower-tropospheric vorticity budget. The large-scale variations of vertical motion are primarily described by Sverdrup balance and Ekman pumping, with some modification by transient eddies. These results suggest that it is important to understand changes in stationary eddies and their influence on the zonal variation of transient eddy fluxes, in order to understand regional changes in net precipitation. They highlight the relative importance of different atmospheric mechanisms for the freshwater forcing of the North Pacific and North Atlantic.

2.1 Introduction

The hydrological cycle is linked to the general circulation of the atmosphere by the transport of water vapor. Precipitation in the tropics occurs as easterly winds converge in the Intertropical Convergence Zone (ITCZ), leading to the vertical motion and moisture transport that make up the ascending branch of the Haldey cell. In the subtropics, strong subsidence associated with the descending branch of the Hadley cell leads to a minimum in precipitation and a region of net evaporation. Beyond this dry zone, transient eddies transport water vapor into midlatitudes, where precipitation associated with transient storm track eddies is high, leading to positive net precipitation (precipitation minus evaporation, $P - E$). These are the basic mechanisms that govern the spatial variation of zonal-mean net precipitation. But the zonal mean accounts for only 40% of the total spatial variance of annual-mean net precipitation.

Accounting for the rest of this spatial variability, variations about the zonal-mean hydrological cycle take the form of extratropical stationary Rossby waves, dry subtropical lows, monsoons, storm tracks, and Walker ciculations. Extratropical stationary Rossby waves are forced by interactions of the jet stream with topography or by the atmospheric response to ocean heat release or dynamical heating by transient eddies (Webster, 1981; Hoskins and Karoly, 1981; Held et al., 2002). They are important for the maintenance of wet and dry zones over North America and Asia (Broccoli and Manabe, 1992), especially in Northern Hemisphere winter. Dry subtropical lows over oceans are associated with upstream Rossby wave propagation from topographic sources (Takahashi and

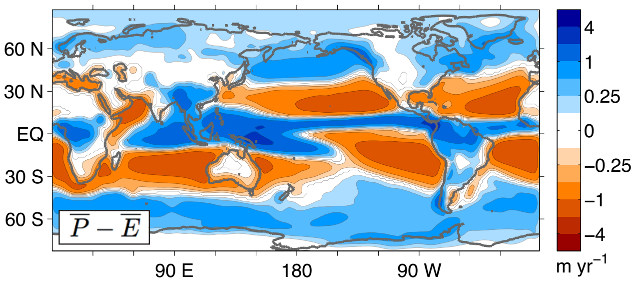

Figure 2.1: Annual-mean net precipitation ($P - E$) from ERA-Interim reanalysis. Here and in all subsequent figures, the fields are smoothed with a 1.5° real-space Gaussian filter to remove small-scale noise. The colorbar is logarithmic, with factors of two between contour levels. All absolute values less than 0.125 m yr^{-1} are white, with a grey contour separating positive and negative values.

Battisti, 2007) or monsoon heating (Rodwell and Hoskins, 1996, 2001) and play a role in steering weather patterns that travel across ocean basins. Monsoons are highly seasonal wet zones associated with low-level wind reversals that are part of a seasonal restructuring of the subtropical meridional overturning circulation (Webster et al., 1998; Bordoni and Schneider, 2008) which can be amplified locally by topographic blocking of moisture and energy fluxes (Boos and Kuang, 2010). Zonal variation in storm track precipitation governs the climates of midlatitude coastal regions and forces ocean basin asymmetry in salinity and deep overturning (Warren, 1983; Emile-Geay et al., 2003; Ferreira et al., 2010). Walker circulations are associated with zonally asymmetric ocean heat flux convergence in the tropics, leading to a region of high evaporation and strong deep convection, e.g., in the Pacific Warm Pool (Gill, 1980; Neelin, 1988; Philander, 1990).

Circulation patterns are tightly coupled to precipitation. Betts (1998) and Held and Soden (2006) suggest that global-mean precipitation can be thought of as a product of the global upward mass transport by all atmospheric circulations and a representative boundary layer moisture content. Similarly, the magnitude of variation in net precipitation with latitude can be directly tied to the strength of the zonal-mean general circulation. O'Gorman and Schneider (2008b) show that subtropical net evaporation due to mean-flow moisture divergence scales with the strength of the Hadley cell and a measure of tropical moisture content. They also relate net precipitation in midlatitudes due to transient-eddy moisture flux convergence to the energy of transient eddies. Can zonally anomalous net precipitation similarly be tied to the strength of zonally anomalous circulations?

Broccoli and Manabe (1992) show in a GCM that the presence of orography is important for maintaining midlatitude dry zones, which occur west of the troughs of orographically forced stationary Rossby waves. Similarly, dry zones can form associated with troughs of Rossby waves propagating upstream from regions of monsoon heating, which may partially account for the aridity of subtropical deserts (Rodwell and Hoskins, 1996, 2001).

While dry zones are associated with regions of low-level mass divergence in stationary Rossby waves, wet zones are often associated with regions of convergence. Several studies point to the role of lower-tropospheric flow convergence downstream of Tibet in setting the strength and spatial extent of the strong East Asian Monsoon precipitation in early summer (Molnar et al., 2010; Chen and Bordoni, 2014). Here we show using reanalyses that the same mechanisms apply to both wet and dry zones and that the lower-tropospheric stationary-eddy mass flux convergence can be used to gain quantitative insight into the magnitude of wet and dry zones globally.

Lower-tropospheric stationary-eddy mass flux convergence leads to vertical motion and vortex stretching, which must be compensated in a steady state by a sink of absolute vorticity. We analyze the zonally anomalous vorticity budget in reanalysis to gain insight into the balances that can sustain this vertical motion. We find that meridional advection of planetary vorticity and surface drag are the primary contributors. This relates the hydrologically relevant stationary-eddy vertical motion to the large-scale horizontal flow of the stationary eddies. Tools for understanding the response of stationary Rossby waves to large-scale forcing by heating and orography (e.g., Hoskins and Karoly, 1981; reviews by Held, 1983 and Held et al., 2002) can thus be applied directly to understanding the zonal variation of net precipitation.

We use ERA-Interim and MERRA reanalyses for this study as detailed in Section 2.2. In section 2.3, we discuss a decomposition of the zonally anomalous moisture budget, leading to the conclusion that vertical motion in stationary eddies sets the predominant pattern of net precipitation, while transient eddies and horizontal advection partially cancel, with the net effect of bringing moisture onto land and poleward across the storm tracks. In section 2.4, we discuss the dynamics leading to vertical motion in stationary eddies using an analysis of the lower-tropospheric zonally anomalous vorticity budget. In section 2.5, we discuss the role of these mechanisms in shaping the asymmetry of sea surface salinity between the North Atlantic and North Pacific, expanding on several other studies that have looked at atmospheric control of northern high-latitude salinity asymmetries (e.g., Warren, 1983; Emile-Geay et al., 2003; Ferreira et al., 2010; Nilsson et al., 2013). In section 2.6 we discuss the extent to which the ideas developed apply to the full moisture budget, including the zonal-mean component. In section 2.7, we provide an overview of the mechanistic picture these physical balances leave us with.

It is worth emphasizing from the outset that in simplifying the zonally anomalous moisture and vorticity budgets to their essential components, we seek not to obtain a complete quantitative picture, but to provide insight into dominant mechanisms.

2.2 Data and methods

Moisture and vorticity budgets are analyzed using the European Center for Medium-Range Weather Forecasts ERA-Interim (1.5°) reanalysis products (Dee et al., 2011). Surface fields are averaged from four-times daily 6 and 12 hour forecast fields produced from forecasts beginning at 0000 and 1200 UTC. Data on pressure levels are averaged from four-times daily analyzed fields produced at 0000, 0600, 1200, and 1800 UTC on 37 unevenly spaced pressure levels. All analyses are done on 1979–2012 climatologies; we checked subsets of this time period for robustness of the results.

Comparisons of the water cycle between multiple reanalysis projects (Trenberth et al., 2007, 2011) show that they all tend to have unphysical regions of net evaporation over land, trends associated with changes of observing system, and an overestimated magnitude of water cycling over oceans (affecting precipitation P and evaporation E but not $P - E$). We are interested in the large-scale balance of terms, which are generally reasonable in reanalyses and should be unaffected by these quantitative issues. All analyses shown here for ERA-Interim were repeated for the NASA Global Modeling and Assimilation Office MERRA (1.5°) reanalysis (Rienecker et al., 2011) using surface data and data assimilated on 42 pressure levels.

Trenberth et al. (2002) point out issues that can arise when analyzing vertically-integrated budgets in reanalyses on pressure levels, where information from pressure levels that are not always present is incorporated via vertical interpolation. Both ERA-Interim and MERRA publish vertically integrated moisture fluxes, which we use to calculate the total moisture flux convergence. However, decomposition of the total flux into stationary and transient components requires additional vertical integrations of different flux components. We checked the robustness of our results between ERA-Interim's interpolated pressure coordinate product, ERA-Interim's hybrid model coordinate product, and MERRA's pressure coordinate product. The large-scale balances are the same irrespective of vertical coordinate system or dataset used, but significant differences exist between pressure and hybrid-coordinate fields directly over topography. These differences cannot be disentangled from the different definitions of stationary and transient eddies in different vertical coordinate systems. All figures show fields from ERA-Interim pressure coordinate and surface fields. Tables show values for both ERA-Interim and MERRA.

To study the influence of zonal variation in net precipitation on ocean freshwater input, a river network dataset must be used to route net precipitation from the continents into the appropriate ocean drainages. We use the STN-30P 0.5° river topology dataset (Fekete et al., 2001; Vörösmarty et al., 2000). This river network model gives the river outlet location for each land point. We make no attempt to account for water storage in the drainage system. This is a justifiable assumption for the annual mean but not for seasonal variations in freshwater forcing.

2.3 Moisture budget

We examine the moisture budget in the present climate using ERA-Interim and MERRA reanalyses. The total net precipitation, $P - E$, is shown in Fig. 2.1 for ERA-Interim. We focus in particular on understanding the mechanisms for zonally anomalous net precipitation (Fig. 2.2e), which accounts for 60% of the spatial variance in the total $P - E$. By definition, the zonal mean $P - E$ (Fig. 2.2f) accounts for the remaining 40%.

The zonal variation of $P - E$ primarily shows zonal variation of precipitation (Fig. 2.2a), especially over oceans. Zonal variation of evaporation (Fig. 2.2c) shows moisture limitation in dry land

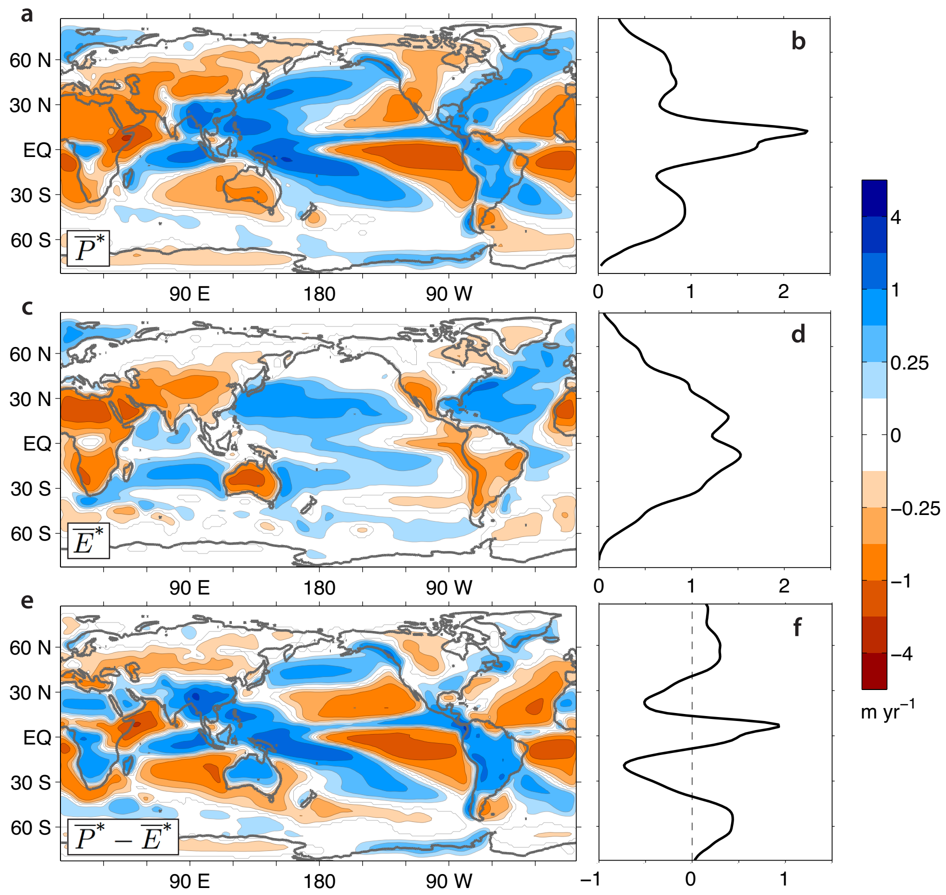

Figure 2.2: Annual-mean hydrological cycle from ERA-Interim reanalysis. (a, b) Precipitation $\overline{P}$ (c, d) evaporation $\overline{E}$ and (e, f) $\overline{P} - \overline{E}$. The full fields are decomposed into zonal-mean components (b, d, f) and zonally anomalous components (a, c, e).

areas and evaporative cooling of warm ocean waters in the western boundary currents.

The moisture budget provides a tool to analyze the flow patterns associated with spatial variation in $P - E$, avoiding complexities associated with studying precipitation or evaporation independently. As net precipitation is the only substantial source/sink of atmospheric water vapor, in steady state it must be equal to the time mean convergence of water vapor flux,

$$\overline{P} - \overline{E} = -\nabla \cdot \langle \overline{\mathbf{u}q} \rangle \, . \tag{2.1}$$

Here ∇ is the nabla operator on a sphere, $\mathbf{u} = (u, v)$ is the horizontal wind, q is the specific humidity, and $\langle\cdot\rangle$ denotes a density weighted vertical integral over the atmospheric column,

$$\langle\cdot\rangle = \int_0^{\overline{p}_s} (\cdot)\,\frac{dp}{g}. \tag{2.2}$$

Any vertical integral between limits a and b other than between 0 hPa and the full time-mean surface pressure, $\overline{p}_s$, will be denoted by $\langle\cdot\rangle_a^b$. This framework for studying moisture flux convergence as a measure of $P-E$ has been used in numerous studies of the hydrological cycle (Peixoto and Oort, 1983, 1992; Held and Soden, 2006; Trenberth et al., 2007, 2011; Seager et al., 2007, 2010, 2014; Newman et al., 2012).

By Reynolds' decomposition of the time-mean moisture flux, the climatology of $P-E$ on monthly or longer timescales can be understood as the sum of the effects of moisture convergence by the time mean flow and transient eddies. We use $(\cdot)'$ to denote deviations from the time mean, $\overline{(\cdot)}$, such that $(\cdot) = \overline{(\cdot)} + (\cdot)'$ and

$$\overline{P} - \overline{E} = -\nabla\cdot\left\langle \overline{\mathbf{u}}\,\overline{q} + \overline{\mathbf{u}'q'}\right\rangle. \tag{2.3}$$

The transient eddy term $(\overline{\mathbf{u}'q'})$ includes all correlations between $\mathbf{u}$ and q that are not represented in their annual-mean climatologies (i.e., including seasonal correlations). Newman et al. (2012) contains a discussion of how this transient-eddy moisture flux is split into synoptic variability (with frequency less than 10 days) and low-frequency variability.

At this point, it is useful to split the moisture budget into zonal-mean and zonally anomalous components, to analyze these portions separately. We use $(\cdot)^*$ to denote deviations from the zonal mean, $[\cdot]$, such that $(\cdot) = [\cdot] + (\cdot)^*$. The zonal-mean moisture budget can be written as[1]

$$\overline{[P]} - \overline{[E]} = -\nabla_y\cdot\left\langle \left[\,\overline{\mathbf{u}'q'}\,\right] + [\overline{\mathbf{u}}]\,[\overline{q}] + [\overline{\mathbf{u}}^*\overline{q}^*]\right\rangle_0^{[\overline{p}_s]}, \tag{2.4}$$

where ∇_y is shorthand for the meridional component of ∇. The zonally anomalous moisture budget

---

[1] By taking the vertical integral with the zonal-mean surface pressure, we are ignoring terms due to the zonal correlation of moisture fluxes and surface pressure, which are small ($\sim 10^{-6}$ m yr^{-1}). Further references to this equation drop the limits of integration for clarity.

can be written as

$$\overline{P}^* - \overline{E}^* = -\nabla \cdot \left\langle \overline{\mathbf{u}'q'} + [\overline{\mathbf{u}}]\,[\overline{q}] + \overline{\mathbf{u}}^\dagger \overline{q}^\dagger \right\rangle^* \tag{2.5}$$

where

$$\overline{\mathbf{u}}^\dagger \overline{q}^\dagger \equiv \overline{\mathbf{u}}^*\,[\overline{q}] + [\overline{\mathbf{u}}]\,\overline{q}^* + \overline{\mathbf{u}}^* \overline{q}^* \tag{2.6}$$

is the sum of all terms involving stationary eddies, including the interactions of stationary eddies $(\cdot)^*$ with the zonal mean $[\cdot]$ (cf. Kaspi and Schneider, 2013). Only the last of the three terms in Eq. (2.6), representing the traditional stationary eddy flux, contributes to the zonal mean. In this framework, stationary eddy contributions include both zonally anomalous flow patterns ($\overline{\mathbf{u}}^*$) and the zonal variations in moisture ($\overline{q}^*$) that result from these circulations. The zonal-mean moisture flux also shows up in the zonally anomalous moisture budget due to zonal variations in surface pressure, which influence the vertical integration. The relative contributions of the terms of Eqs. (2.4) and (2.5) to the total spatial variance in $\overline{P} - \overline{E}$ are tabulated in Table 2.1.

The zonal-mean moisture budget is analyzed in terms of Eq. (2.4) in Peixoto and Oort (1992). In low latitudes it is dominated by the Hadley Cell, which has an equatorward surface branch, resulting in the removal of moisture from the subtropics and convergence in the ITCZ. This is represented by $-\nabla_y \cdot \langle [\overline{\mathbf{u}}]\,[\overline{q}] \rangle$ and is plotted in Fig. 2.3f. Beyond the zero of the mean-flow moisture flux at approximately 30°, the moisture flux convergence is dominated by transient eddies, which transport moisture from the subtropics and tropics to the midlatitude storm tracks, leading to rainfall associated with synoptic variability. Figure 2.3d shows the contribution of transient eddies to $\overline{[P]} - \overline{[E]}$. Stationary eddies also contribute to the zonal-mean hydrological cycle via the correlation of zonal variations in circulation and moisture, $-\nabla_y \cdot \langle [\overline{\mathbf{u}}^* \overline{q}^*] \rangle$, which is shown in Fig. 2.3b.

Table 2.1: Correlation of 1.5° Gaussian filtered moisture flux convergence terms with $\overline{P} - \overline{E}$ (ρ_{P-E}) and global-mean spatial standard deviation, σ, for each field. ERA-Interim and MERRA (in parenthesis) are both shown.

	$\overline{P} - \overline{E}$	$\overline{[P]} - \overline{[E]}$	$\overline{P}^* - \overline{E}^*$	$-\nabla \cdot \langle [\overline{\mathbf{u}}]\,[\overline{q}] \rangle$	$-\nabla \cdot \left\langle \overline{\mathbf{u}'q'} \right\rangle$	$-\nabla \cdot \left\langle \overline{\mathbf{u}}^\dagger \overline{q}^\dagger \right\rangle$
ρ_{P-E}	n/a	0.65 (0.60)	0.76 (0.80)	0.57 (0.57)	0.21 (0.17)	0.62 (0.54)
σ (m yr^{-1})	0.72 (0.62)	0.47 (0.37)	0.54 (0.50)	0.39 (0.38)	0.35 (0.50)	0.60 (0.68)

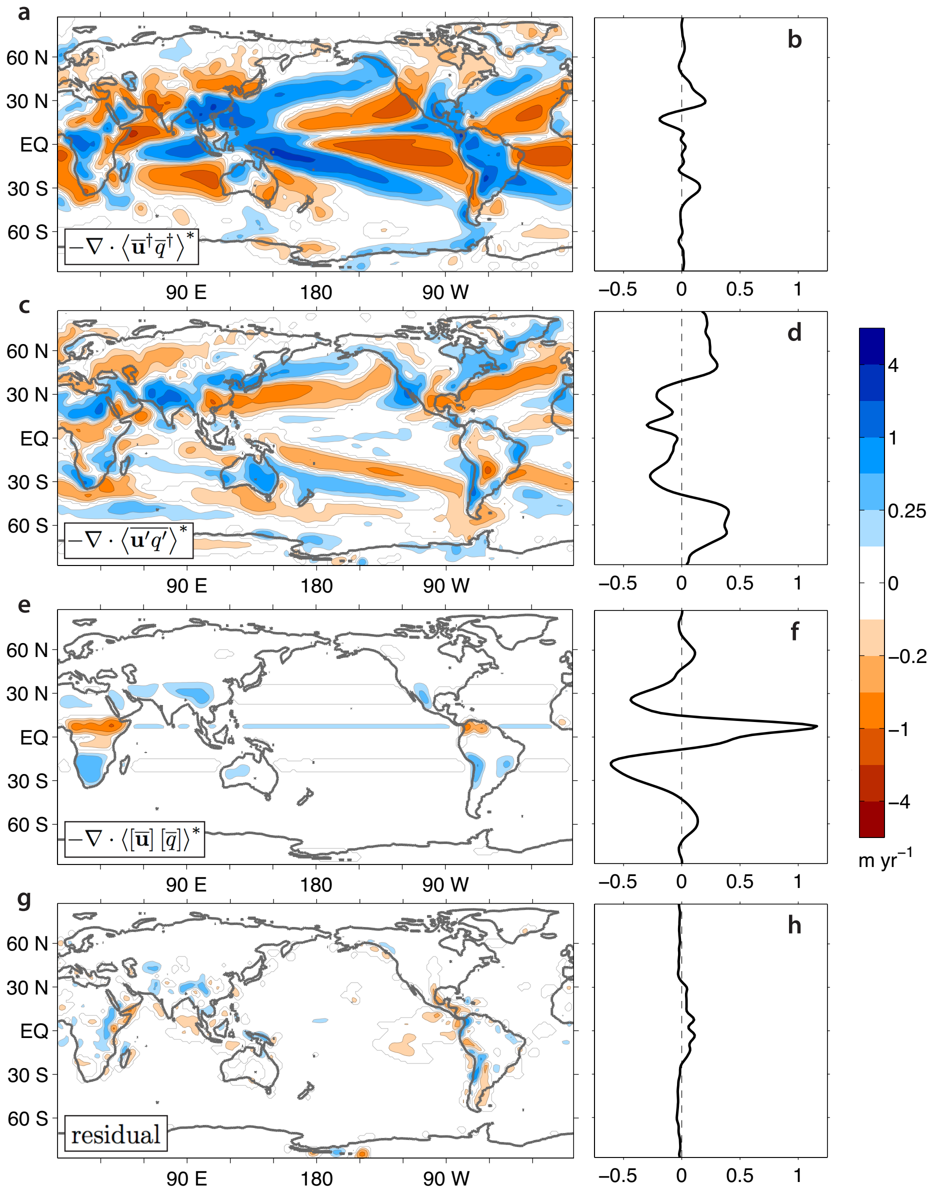

Figure 2.3: Contributions to the column-integrated moisture flux convergence from (a, b) stationary eddies, (c, d) transient eddies, (e, f) the zonal-mean circulation, and (g, h) the residual of this decomposition. The full fields are decomposed into zonal-mean components (b, d, f, h) and zonally anomalous components (a, c, e, g).

Scaling relations for changes in zonal-mean precipitation with climate change (O'Gorman and Schneider, 2008b) start with an understanding of which terms of Eq. (2.4) are dominant in the climate system. By decomposing the zonally anomalous moisture budget into the terms of Eqs. (2.5) and (2.6), we hope to provide similar insight into which components of the circulation need to be understood in order to understand $\overline{P}^* - \overline{E}^*$ across different climates. This is relevant in light of recent studies (e.g., Seager et al., 2007, 2010, 2014), which show that changes in circulation can be as important as changes in atmospheric water vapor content for regional hydroclimate change.

The total zonally anomalous moisture flux can first be separated into that due to stationary eddies ($\overline{\mathbf{u}}^\dagger \overline{q}^\dagger$, Fig. 2.3a), that due to transient eddies ($\overline{\mathbf{u}'q'}$, Fig. 2.3c), and that due to correlations of the zonal-mean flow ($[\overline{\mathbf{u}}]\,[\overline{q}]$). The residual of this decomposition, resulting from discreetization errors, is small (Fig. 2.3e). We find that the stationary-eddy moisture flux convergence (Fig. 2.3a) is leading order in setting the pattern of $\overline{P}^* - \overline{E}^*$, as can be seen, for example, in its strong correlation with $\overline{P}^* - \overline{E}^*$ (Table 2.2). In many regions of the globe, especially over oceans, transient eddies provide a negative feedback by transporting water vapor down moisture gradients set up by the stationary eddies, to reduce zonal variation in moisture. This is an expected result as transient eddies have been observed to cause down-gradient moisture fluxes in a wide range of climates (Caballero and Langen, 2005; O'Gorman and Schneider, 2008b).

The transient-eddy moisture flux convergence (Fig. 2.3c) is large in several coastal land areas that are dried by the stationary eddy fluxes, such as California, Chile, and Northern China. This

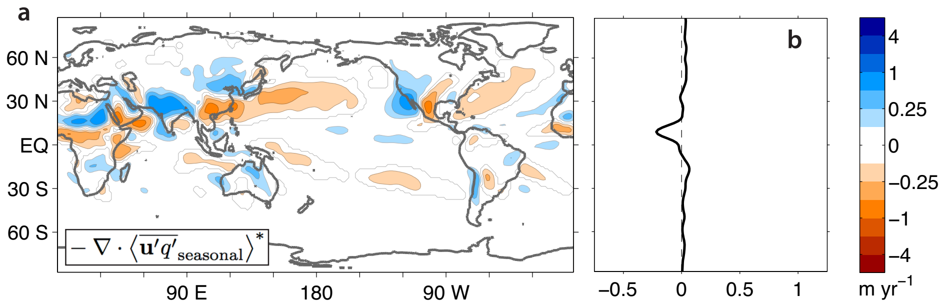

Figure 2.4: Contributions to the column-integrated moisture flux convergence from the seasonal cycle, determined from deviations of monthly means from annual means. The full field is decomposed into a zonal-mean component (b) and a zonally anomalous component (a).

is consistent with what is found in other studies (e.g., Newman et al., 2012) where synoptic and low-frequency variability is seen to be a major influence on moisture transport from ocean to land. Some of the transient eddy transport, especially in monsoonal areas, is accomplished by seasonal correlations, which are not always considered as transient eddies and are therefore shown separately in Fig. 2.4. This term is calculated using a Reynolds' decomposition on monthly means. Transient eddy fluxes also provide a large contribution to $\overline{P}^* - \overline{E}^*$ in the Northern Hemisphere storm tracks through strong local meridional moisture fluxes, as is well established (see, for example, Peixoto and Oort, 1992). Overall, transient-eddy moisture flux convergence has a weak positive correlation with $\overline{P}^* - \overline{E}^*$ (Table 2.2).

The contribution of the convergence of the zonal-mean moisture flux ($[\overline{\mathbf{u}}]\,[\overline{q}]$) to $\overline{P}^* - \overline{E}^*$ (Fig. 2.3e), through the variation of surface pressure (and thus the total mass of the atmospheric column) is small, except in a few regions of low surface pressure (high surface elevation). In these regions, the moistening of the ITCZ and the drying of the Hadley cell subsidence zone are not felt as strongly because some of the (higher) pressure levels used in calculating the zonal mean, and important for the moisture budget, lie below the topography. This effect contributes to the relative dryness of equatorial Africa and South America and the relative wetness of northern and southern Africa in our analysis on pressure levels. We will consider this a stationary-eddy term for the rest of the text.

We seek to understand which portion of Eq. (2.6) explains the large contribution of stationary-eddy moisture fluxes to $\overline{P}^* - \overline{E}^*$. Specifically, we would like to understand:

1. Is the zonal variation of specific humidity, $\overline{q}^*$, an important influence on regional hydroclimate?
2. Does $\overline{P}^* - \overline{E}^*$ arise from stationary-eddy horizontal advection or vertical motion (horizontal divergence)?

For this purpose, we write the time-mean moisture flux convergence as

$$\begin{aligned} &-\nabla\cdot\left\langle \overline{\mathbf{u}}^{\dagger}\overline{q}^{\dagger} + [\overline{\mathbf{u}}]\,[\overline{q}]\right\rangle^* \\ &\qquad = -\left\langle [\overline{q}]\,\nabla_\rho\cdot\overline{\mathbf{u}} + \overline{\mathbf{u}}\cdot\nabla_y\,[\overline{q}] + \overline{q}^*\nabla_\rho\cdot\overline{\mathbf{u}} + \overline{\mathbf{u}}\cdot\nabla\overline{q}^*\right\rangle^*, \end{aligned} \tag{2.7}$$

where ∇_ρ differs from ∇ in that the derivative is density weighted [see Appendix 2A (Section 2.8)].

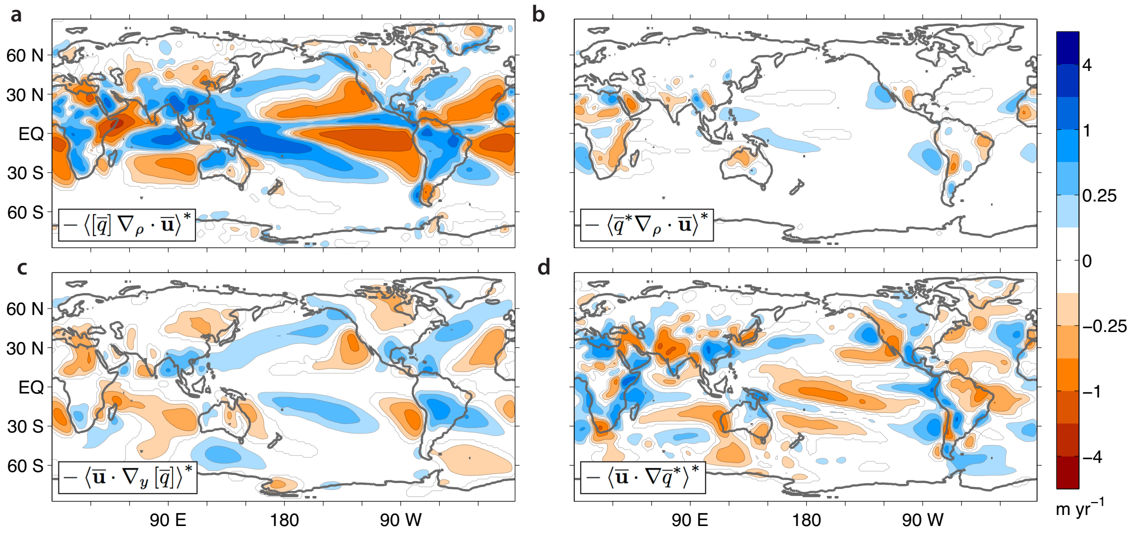

Figure 2.5: Contributions to column integrated moisture flux convergence by stationary eddies from (a) vertical advection of zonal mean specific humidity, (b) vertical advection of zonally anomalous specific humidity, (c) horizontal advection of zonal mean specific humidity, and (d) horizontal advection of zonally anomalous specific humidity. The small moisture flux convergence due to correlations of the zonal-mean moisture flux with zonal variations of surface pressure is included in (a) and (c).

In pressure coordinates, the density used is proportional to the probability that a pressure level is above the surface at a given point in time (Boer, 1982). This differs slightly from the methodology of Newman et al. (2012), who put ∇_ρ in the advective term. While this is an equally valid choice, density weighting the divergence is preferable in this case because $\langle \nabla_\rho \cdot \overline{\mathbf{u}} \rangle_p^{\overline{p}_s} = \overline{\omega}(p)$, where ω is the vertical pressure velocity, a property we will use later in the text. In this decomposition (Eq. 2.7), the first and second terms on the right hand side are the portion of the stationary-eddy moisture flux convergence that does not include $\overline{q}^*$, addressing question 1. The first and third terms are the vertical motion contribution of the stationary eddies to the moisture flux convergence, addressing question 2. Fig. 2.5 shows this decomposition of the stationary-eddy moisture flux convergence.

The stationary-eddy vertical advection of zonal-mean moisture, $-\langle [\overline{q}]\, \nabla_\rho \cdot \overline{\mathbf{u}} \rangle^*$ (Fig. 2.5a), is seen to be the dominant term. Vertical advection of zonally anomalous moisture, $-\langle \overline{q}^* \nabla_\rho \cdot \overline{\mathbf{u}} \rangle^*$ (Fig. 2.5b), is seen to enhance this vertical advection-based pattern of $\overline{P}^* - \overline{E}^*$ over oceans due to relatively high moisture content and reduce it over land due to moisture limitation. This term can be neglected, except over Africa where moisture limitation apparently plays an important role. The horizontal

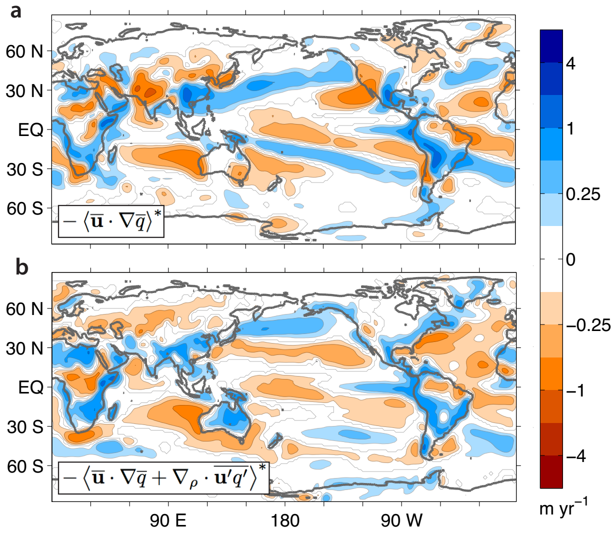

Figure 2.6: (a) Total contribution of horizontal advection to the stationary-eddy moisture flux convergence. This is the sum of the terms in Figs. 2.5c and d. (b) Sum of the horizontal advection and transient eddy contributions to the zonally anomalous moisture flux convergence. This is the sum of the terms in Fig. 2.6a and 2.3c.

moisture advection terms shown in Figs. 2.5c and d, while smaller than the vertical moisture flux, are clearly not negligible. However, the sum of these, $-\langle \overline{\mathbf{u}} \cdot \nabla \overline{q} \rangle^* = -\langle \overline{\mathbf{u}} \cdot \nabla_y [\overline{q}] + (\overline{\mathbf{u}} \cdot \nabla \overline{q}^*) \rangle^*$, the total horizontal moisture advection by stationary eddies (Fig. 2.6a), is seen to be nearly out of phase with the transient-eddy moisture flux convergence (Fig. 2.3c). This suggests that transient eddies transport moisture down moisture gradients set up by time-mean horizontal advection (cf. Couhert et al., 2010), leading to a partial cancellation of these terms. The sum of the horizontal and transient terms (Fig. 2.6b) can be thought of as the net effect of horizontal advection and transient eddies on $\overline{P}^* - \overline{E}^*$, after accounting for their internal cancellation. The primary net influence is to bring moisture from the subtropical and tropical oceans into coastal regions, the equatorial Pacific Cold Tongue, and the across the Northern Hemisphere storm tracks.

Table 2.2: Correlation of 1.5° Gaussian filtered zonally anomalous moisture flux convergence terms with $\overline{P}^* - \overline{E}^*$ ($\rho_{P^*-E^*}$) and global-mean spatial standard deviation, σ, for each field. Compare σ with that for $\overline{P}^* - \overline{E}^*$ in Table 2.1. ERA-Interim and MERRA (in parenthesis) are both shown.

	$-\nabla \cdot \langle \overline{\mathbf{u}}^\dagger\, \overline{q}^\dagger \rangle^*$	$-\nabla \cdot \langle \overline{\mathbf{u}'q'} \rangle^*$	$-\langle [\overline{q}] \nabla_\rho \cdot \overline{\mathbf{u}} \rangle^*$	$-\langle \overline{\mathbf{u}} \cdot \nabla \overline{q} \rangle^*$	$-\langle \overline{\mathbf{u}} \cdot \nabla \overline{q} + \nabla_\rho \cdot \overline{\mathbf{u}'q'} \rangle^*$
$\rho_{P^*-E^*}$	0.84 (0.70)	0.04 (0.05)	0.88 (0.75)	0.33 (0.30)	0.42 (0.37)
σ (m yr^{-1})	0.59 (0.68)	0.28 (0.45)	0.49 (0.51)	0.28 (0.39)	0.25 (0.38)

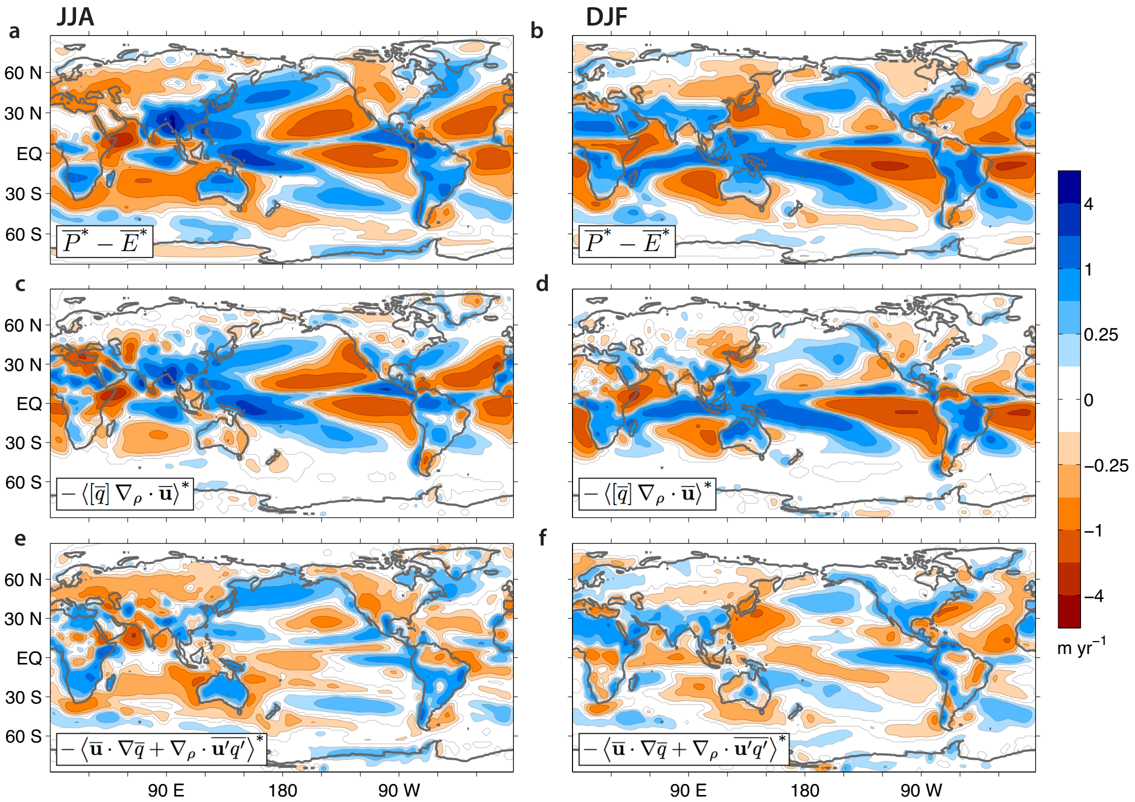

Figure 2.7: (a,c,e) Moisture budget terms for JJA. (b,d,f) Moisture budget terms for DJF.

To summarize, zonal variation in $P-E$ comes about primarily from vertical motion in stationary eddies. Zonal variation of specific humidity has only a small influence on the vertical moisture flux, but it plays a role in the zonal variation of horizontal moisture fluxes and the zonal variation of transient-eddy moisture flux convergence. Together, horizontal advection and transient eddies primarily act to increase moisture convergence and $P-E$ on land, in the equatorial Pacific Cold Tongue, and in the North Pacific storm track. The corresponding moisture flux divergence is spread over most of the subtropical and tropical oceans where the reduction of $P-E$ due to horizontal and transient fluxes is less than 0.5 m yr^{-1} in most areas. Computing a global-mean correlation (Table 2.2), the dominant term involving vertical advection of zonal-mean specific humidity accounts for half (MERRA) to three-quarters (ERA-Interim) of the total spatial variance in $\overline{P}^* - \overline{E}^*$. The low correlation coefficient for the combined transient eddy and horizontal advection term is consistent with its lesser and more regional importance.

The relative importance of stationary-eddy vertical velocities versus transient-eddy moisture flux convergence remains season-by-season, as shown in Fig. 2.7. The seasonal moisture budget balance shown here is also described in Seager et al. (2014), for the particular case of the Mediterranean region, with drying by stationary-wave subsidence in the summer and a balance of transient-eddy moisture flux convergence and stationary-eddy advection in the winter. They then use these results to explain the predicted drying in both seasons over the next 20 years in CMIP5 simulations, illustrating the practicality of this approach. The results in Fig. 2.7 can also be used to confirm, for example, the well known relation between Indian and East Asian Monsoon rainfall and strong summer vertical motion.

2.4 Dynamics of stationary-eddy vertical motion

The moisture budget analysis indicates zonal patterns in net precipitation result primarily from zonal variations in lower-tropospheric vertical velocities associated with stationary eddies. As such, it is important to understand which physical mechanisms lead to these zonal variations in vertical velocity. While condensation of water vapor during convection can play a role in amplifying or damping vertical motion (Emanuel et al., 1994), the physics of lower-tropospheric vertical motion can mostly be thought of as external to this convective heating. We seek insight into the dynamics of vertical motion in stationary eddies via the lower-tropospheric vorticity budget.

To this end, we must understand which portion of the lower troposphere is important for determining the vertical motion that contributes to $\overline{P}^* - \overline{E}^*$. Using the integral form of the mean value theorem, the flow divergence term of the zonally anomalous moisture budget can be approximated as

$$\langle [\overline{q}] \, \nabla_\rho \cdot \overline{\mathbf{u}} \rangle^* = [\overline{q}_{\mathrm{sfc}}] \left(\langle \nabla_\rho \cdot \overline{\mathbf{u}} \rangle_{p_i}^{\overline{p}_s} \right)^* , \tag{2.8}$$

where $\overline{q}_{\mathrm{sfc}}$ is the surface specific humidity and p_i is some pressure level in the vertical domain. By continuity, $\langle \nabla_\rho \cdot \overline{\mathbf{u}} \rangle_{p_i}^{p_s}$ corresponds to a vertical velocity at p_i.

Equation (2.8) is exact for some value of p_i, but is approximate when using one value of p_i

globally. Since specific humidity falls off rapidly with height, this is a good approximation for p_i between about 950 hPa and 400 hPa. We obtain a global mean best fit p_i of 850 hPa by solving for p_i at each grid point and then taking an area-weighted global mean. It corresponds to an altitude of about 1.5 km, thus lying below the water vapor scale height of about 2.3 km, as one would expect. This value matches well with the level of maximum vertical moisture flux of 850 hPa found in observations (Peixoto and Oort, 1992) and the height of maximum vertical mass flux and condensation of 825 hPa found in an idealized model (Schneider et al., 2010). The main spatial variability in the best fit p_i comes from the difference between land and ocean. The global mean best fit p_i's for land and ocean are 875 hPa and 775 hPa respectively. This difference is not large enough to necessitate using different values for land and ocean.

Thus, in the modern climate, $\overline{P}^* - \overline{E}^*$ can be thought of as a product of boundary layer specific humidity and zonally anomalous vertical motion at 850 hPa, $\overline{\omega}^*_{850} = g(\langle \boldsymbol{\nabla}_\rho \cdot \overline{\mathbf{u}}^* \rangle_{850}^{\overline{p}_s})^*$:

$$\overline{P}^* - \overline{E}^* \approx -\frac{1}{g}\left[\overline{q}_{\mathrm{sfc}}\right]\overline{\omega}^*_{850}. \tag{2.9}$$

This approximation is qualitative due to the neglect of transient eddies and horizontal advection, which also contribute to $\overline{P}^* - \overline{E}^*$. The level at which vertical motion contributes most to $P - E$ is likely to change with climate as the center of mass of moisture and condensation moves up in the atmosphere (O'Gorman and Schneider, 2008b; Singh and O'Gorman, 2012). This will be the subject of future study.

To study the physical balances leading to vertical motion at 850 hPa, we will analyze the steady-state vorticity equation integrated from the surface upward. The zonally anomalous component below a level p_i can be written as

$$\left(\left\langle f \nabla \cdot \overline{\mathbf{u}} + \beta \overline{v} + \overline{N} + \overline{T} \right\rangle_{p_i}^{\overline{p}_s}\right)^* = -\nabla \times \overline{\tau}^*, \tag{2.10}$$

where f is the Coriolis frequency, $\beta = df/dy$, τ is the surface stress due to turbulent momentum fluxes, N represents all non-linear interactions within the time mean flow (e.g., relative vorticity

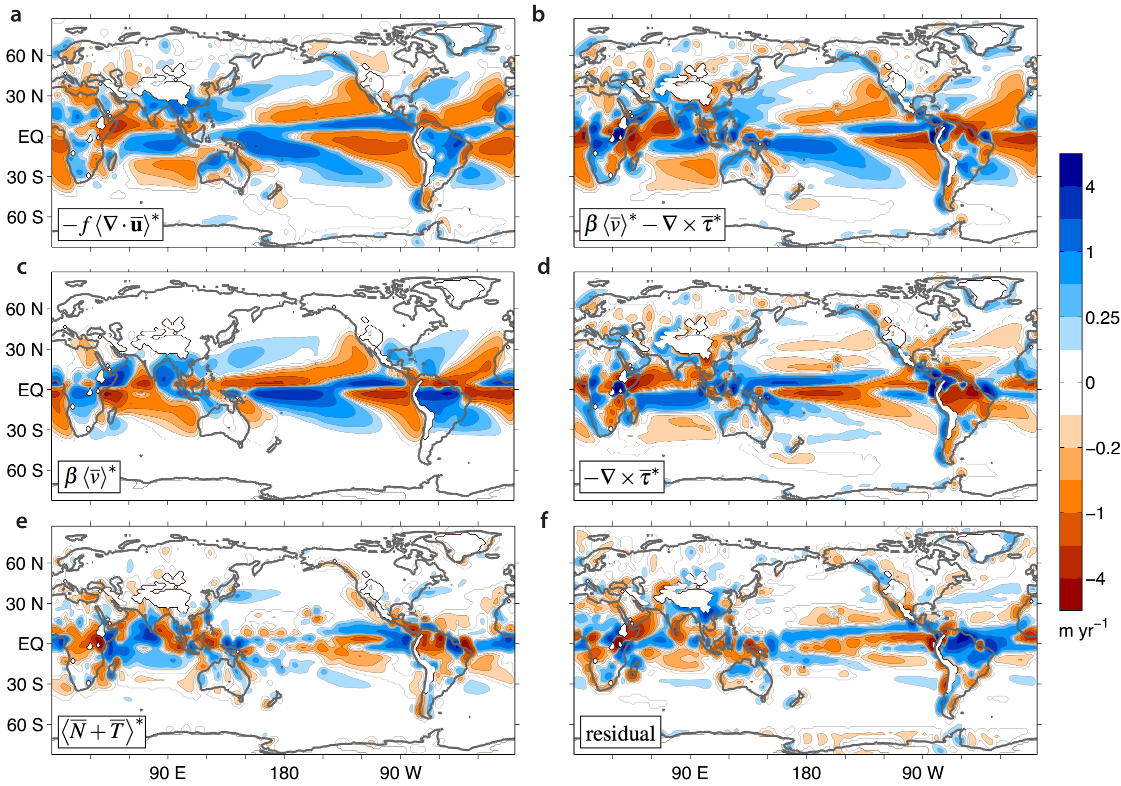

Figure 2.8: Dominant terms in the ERA-Interim zonally anomalous vertically-integrated vorticity budget (from surface to 850 mbar) multiplied by $[\overline{q}_{\mathrm{sfc}}]/f$ such that the stretching term gives the stationary-eddy divergence contribution to $\overline{P}^* - \overline{E}^*$. (a) Absolute vorticity component of stretching term. (b) Sum of beta term and surface drag. (c) Beta term. (d) Surface drag. (e) All nonlinear terms involving transient and stationary eddies. (f) Residual of all calculated vorticity tendencies, $-\left\langle f\nabla\cdot\overline{\mathbf{u}} + \beta\overline{v} + \overline{N} + \overline{T}\right\rangle^* + \nabla\times\overline{\tau}^*$, which can be interpreted as an artificial forcing by the reanalysis. As $f \to 0$ at the equator, the equatorial grid points are omitted for all fields, and contouring interpolates between the next-nearest grid points across the equator. The limits of integration, 850 hPa to $\overline{p}_s$, are omitted from the figure labels.

fluxes), given by

$$\overline{N} = \overline{\mathbf{v}} \cdot \nabla\overline{\zeta} + \overline{\zeta}\nabla\cdot\overline{\mathbf{u}} + \left(\nabla_x\overline{\omega}\right)\partial_p\overline{v} - \left(\nabla_y\overline{\omega}\right)\partial_p\overline{u}, \tag{2.11}$$

and T represents the total transient-eddy vorticity tendency, given by

$$\overline{T} = \overline{\mathbf{v}'\cdot\nabla\zeta'} + \overline{\zeta'\nabla\cdot\mathbf{u}'} + \overline{\left(\nabla_x\omega'\right)\partial_p v'} - \overline{\left(\nabla_y\omega'\right)\partial_p u'}. \tag{2.12}$$

Here ζ is the relative vorticity and $\mathbf{v} = (u, v, \omega)$ is the full 3D velocity. Figure 2.8 shows the terms in the stationary-eddy vorticity equation in ERA-Interim. Each field is multiplied by $[\overline{q}_{\mathrm{sfc}}]/f$ such

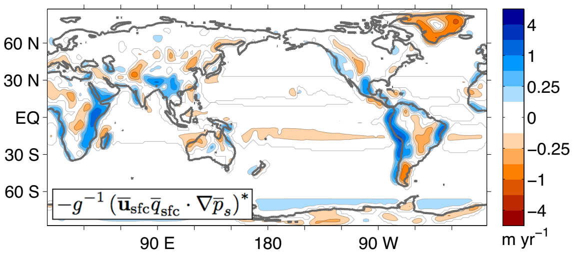

Figure 2.9: Orographic contribution to $\overline{\omega}^*_{850}$ and $\overline{P}^* - \overline{E}^*$, which is not captured by the vorticity budget analysis.

that it shows the contribution of the corresponding vorticity budget term to $\overline{P}^* - \overline{E}^*$ via time-mean vertical motion, as for example,

$$\frac{[\overline{q}_{\rm sfc}]}{f}\left(\langle f\nabla\cdot\overline{\mathbf{u}}\rangle_{p_i}^{\overline{p}_s}\right)^* \approx \langle[\overline{q}]\,\nabla\cdot\overline{\mathbf{u}}\rangle^*\,. \tag{2.13}$$

Note that the contribution of the vorticity equation gives an estimate of $\langle[\overline{q}]\,\nabla\cdot\overline{\mathbf{u}}\rangle^*$ rather than $\langle[\overline{q}]\,\nabla_\rho\cdot\overline{\mathbf{u}}\rangle^*$, because the divergence in the vorticity budget does not arise from use of the continuity equation. These differ by the convergence of surface moisture fluxes onto topography[2],

$$-\langle[\overline{q}]\,\nabla_\rho\cdot\overline{\mathbf{u}}\rangle^* + \langle[\overline{q}]\,\nabla\cdot\overline{\mathbf{u}}\rangle^* \approx -g^{-1}\left(\overline{\mathbf{u}}_{\rm sfc}\overline{q}_{\rm sfc}\cdot\nabla\overline{p}_s\right)^*\,. \tag{2.14}$$

The contribution of this orographic vertical motion to $\overline{P}^* - \overline{E}^*$ is shown in Fig. 2.9. It is the primary reason for differences between $\langle[\overline{q}]\,\nabla\cdot\overline{\mathbf{u}}\rangle^*$ (Fig. 2.5a) and it's estimate based on the vorticity equation (Fig. 2.8a). More details on this surface term can be found in Appendix 2A (Section 2.8).

Stationary eddies have two dominant influences on zonal variation in 850 hPa vertical motion. The first is Sverdrup balance,

$$-\left(\langle f\nabla\cdot\overline{\mathbf{u}}\rangle_{p_i}^{\overline{p}_s}\right)^* \sim \left(\langle\beta\overline{v}\rangle_{p_i}^{\overline{p}_s}\right)^*, \tag{2.15}$$

where stretching of absolute vorticity ($-f\nabla\cdot\overline{\mathbf{u}}^*$) is balanced by planetary vorticity advection ($\beta\overline{v}^*$), such that regions of poleward motion are wetter than the zonal mean (Fig. 2.8c). The second is

---

[2] Note that while the zonal-mean specific humidity is used on the left hand side, the full-field surface specific humidity is used on the right hand side. The reason for this is that the surface specific humidity has large spatial gradients simply due to gradients in surface height.

Ekman pumping,

$$-\left(\langle f\nabla\cdot\overline{\mathbf{u}}\rangle_{p_i}^{\overline{p}_s}\right)^* \sim \nabla\times\overline{\tau}^*, \tag{2.16}$$

here taken to mean the balance of absolute vorticity stretching by surface drag (in a slight deviation from common terminology), such that regions with stationary-eddy cyclones are wetter than the zonal mean (Fig. 2.8d). Figure 2.8b shows the sum of the effects of Sverdrup balance and Ekman pumping. Together, they show the primary large-scale patterns of stationary-eddy vertical motion, and, through the moisture budget balances discussed in section 2.3, $\overline{P}^* - \overline{E}^*$. This can be represented by the qualitative scaling

$$\overline{P}^* - \overline{E}^* \approx \frac{[\overline{q}_{\mathrm{sfc}}]}{fg}\left(\langle\beta\overline{v}\rangle_{850}^{\overline{p}_s} + \nabla\times\overline{\tau}\right)^*. \tag{2.17}$$

The net moisture-weighted vorticity tendency due to all nonlinear terms (Fig. 2.8e) acts mostly on smaller length scales in the the tropics. This is the sum of vorticity advection, nonlinear vorticity stretching, vortex tilting, and baroclinicity. Baroclinicity enters the vorticity equation in pressure coordinates through fluctuations in surface pressure, and is thus classified as a transient eddy in our framework. The only large-scale cancelation internal to these terms is the ~ 1 m yr^{-1} moisture-weighted export of vorticity from the Walker circulation upwelling regions to the Walker circulation subsidence regions by $\overline{N}^*$ (not shown), and the cancellation of this tendency by horizontal transient-eddy vorticity advection.

The reanalysis framework does not guarantee a closed vorticity budget. The net effect of the vorticity budget residual is shown in Fig. 2.8f. While significant, especially over the Pacific and over South America, it does not qualitatively change the balances on large scales that we have described. Overall, a significant portion of large-scale $\overline{P}^* - \overline{E}^*$ variability in the modern climate is seen to occur through lower-tropospheric stationary-eddy vertical motion associated with a combination of Sverdrup balance and Ekman pumping.

2.5 Implications for sea surface salinity

Spatial variability of $P - E$ is a major control on the spatial variability of the surface salinity of the oceans (Warren, 1983; Broecker et al., 1985; Zaucker et al., 1994; Delcroix et al., 1996; Emile-Geay et al., 2003; De Boer et al., 2008; Czaja, 2009; Ferreira et al., 2010; Nilsson et al., 2013). Transport of water by the ocean, sea ice, and rivers are the remaining mechanisms which can lead to spatial variability in freshwater forcing and sea surface salinity (SSS). The zonal variation of $\overline{P} - \overline{E}$ is thus an important control on the SSS difference between the Pacific and Atlantic oceans. Warren (1983, hereafter W83) and Emile-Geay et al. (2003, hereafter EG03) have focused, in particular, on the moisture budget influence on the freshwater forcing of the North Pacific (NP) and North Atlantic (NA) subpolar gyres, where the NA surface water is saltier over a range of latitudes (Fig. 2.10b,c) due in part to the lower $P - E$ freshwater forcing in the NA in these latitudes (Fig. 2.10d,e). This is motivated by the suggestion that the high-latitude surface–deep salinity difference controls the strength of deep ocean overturning (W83; Broecker et al. 1985).

Simulations with coupled atmosphere-ocean models (Ferreira et al., 2010; Nilsson et al., 2013) have shown that a difference in $\overline{P} - \overline{E}$ between two idealized ocean basins, due to, in their case, differing ocean basin width, is enough to restrict deep ocean overturning to the drier ocean basin. In addition to the influence of $\overline{P} - \overline{E}$, the Pacific–Atlantic salinity difference is also thought to be influenced by inter-basin Sverdrup salt transport due to the differing extents of South America and Africa (Reid Jr, 1961; Nilsson et al., 2013), regional details of the ocean basins (e.g., the Mediterranean Sea, the Arctic troughflow, and the farther northward extent of the Atlantic) (Reid, 1979; Weaver et al., 1999; De Boer et al., 2008), and differences in the zero wind-stress curl line which sets the boundary and mixing between the between the subtropical and sub polar gyres (W83, EG03, Czaja 2009). We will focus on the $\overline{P} - \overline{E}$ freshwater forcing aspect of the problem as it is well established to play a large role, and the moisture budget decomposition of Section 2.3 has the potential to elucidate mechanisms for ocean basin $\overline{P} - \overline{E}$ differences.

EG03 gives an overview of contributions to the modern NP salinity budget in comparison with the modern NA, using observational estimates of $P - E$, runoff, salt fluxes, and ocean currents,

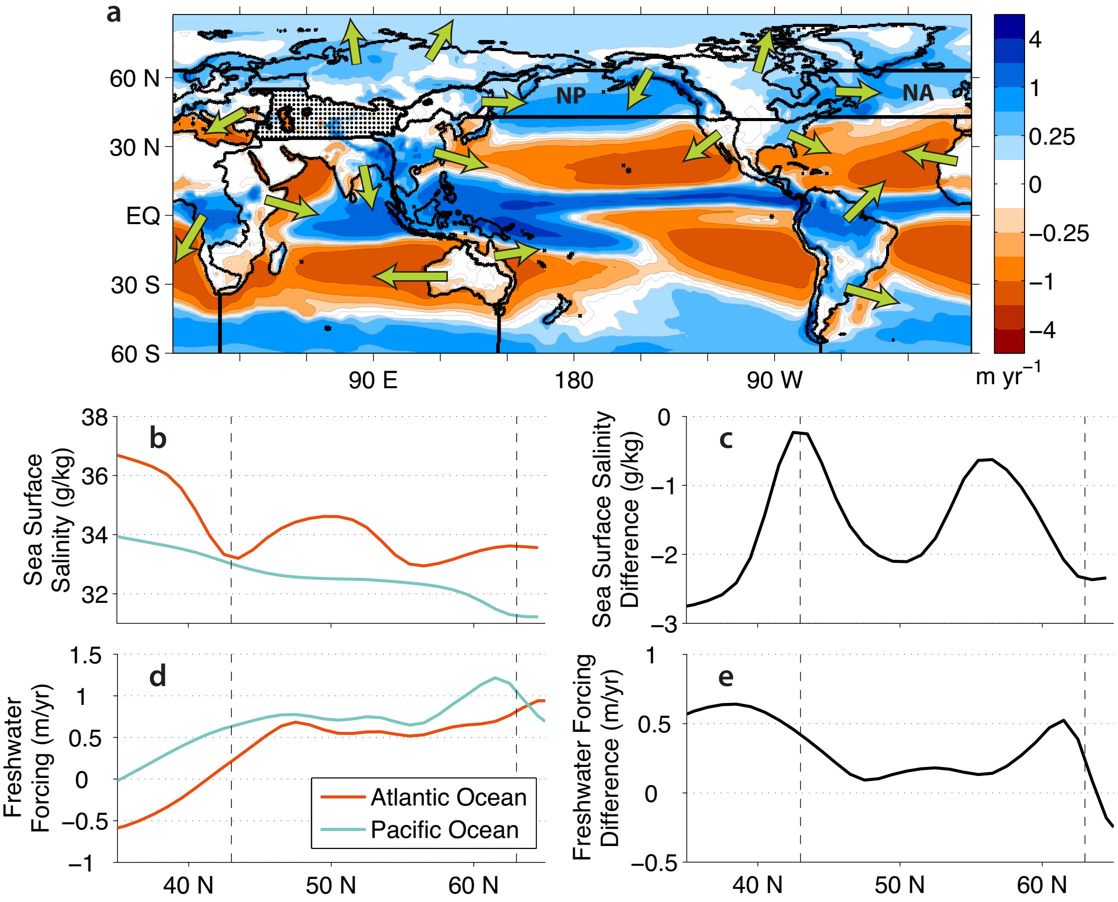

Figure 2.10: (a) Total $\overline{P} - \overline{E}$ and outline of ocean boxes and their catchment basins computed from the STN-30p river topology dataset. The ocean is split into Pacific, Atlantic, and Indian oceans as shown, as well as a North Pacific (NP) and North Atlantic (NA) box as used in Tables 2.3 and 2.4. Endoheric basins are stippled. (b) Ocean basin zonal-mean sea-surface salinity from the World Ocean Atlas (Zweng et al., 2013) in the North Pacific and North Atlantic basins and (c) Pacific–Atlantic difference. (d) Ocean basin zonal-mean freshwater forcing into the North Pacific and North Atlantic and (e) Pacific–Atlantic diference.

an update of previous work by W83. We provide updated $P - E$ fluxes from ERA-Interim and MERRA, decomposing the total freshwater flux into components due to stationary-eddy vertical motion, transient eddies, other stationary-eddy moisture flux terms, and differences in river runoff topology. We approximate the NP and NA sub-polar gyres by a box between 43° and 63° N as shown in Fig. 2.10a. This follows EG03 except for an expansion of the northern boundary from 60° N to 63° N, consistent with the inclusion of the Yukon river (as in EG03). The freshwater flux contributions from the different components of the moisture budget as in Eqs. (2.5) and (2.7) are tabulated in Table 2.3 (in mSv = 10^3 m^{3}s^{-1}).

Table 2.3: Freshwater forcing (mSv) to the oceans between 43° and 63° N. ERA-Interim and MERRA (in parenthesis) are both shown. Values in brackets are from EG03.

	Pacific $P - E$	Pacific Runoff	Atlantic $P - E$	Atlantic Runoff
$\overline{P} - \overline{E}$	213 (210)	70 (54)	103 (110)	64 (40)
	[290 ± 150]	[30 ± 3]	[170]	
$\overline{P}$	417 (394)	140 (139)	340 (326)	148 (142)
	[450 ± 150]		[350]	
$\overline{E}$	204 (185)	70 (86)	237 (216)	85 (102)
	[180 ± 36]		[180 ± 36]	
$\overline{[P]} - \overline{[E]}$	115 (99)	56 (46)	93 (78)	52 (45)
$\overline{P}^* - \overline{E}^*$	98 (113)	14 (6.3)	10 (30)	11 (-3.7)
$-\left\langle \nabla \cdot \left(\overline{\mathbf{u}}^\dagger \overline{q}^\dagger \right) \right\rangle^*$	69 (70)	-13 (-11)	36 (34)	-24 (-27)
$-\langle \nabla_y \cdot ([\overline{\mathbf{u}}]\,[\overline{q}]) \rangle^*$	2.5 (3.9)	-2.9 (-3.7)	3.0 (4.1)	0.9 (0.1)
$-\left\langle \nabla \cdot \overline{\mathbf{u}' q'} \right\rangle^*$	45 (47)	23 (19)	-24 (-23)	29 (29)
$-\langle [\overline{q}]\, \nabla \cdot \overline{\mathbf{u}} \rangle^*$	52 (43)	-0.3 (3.6)	20 (16)	-13 (-15)
$-\langle \overline{q}^* \nabla \cdot \overline{\mathbf{u}} \rangle^*$	-4.5 (-4.4)	1.9 (3.1)	0.2 (-0.7)	-1.0 (-1.5)
$-\langle \overline{\mathbf{u}} \cdot \nabla \overline{q} \rangle^*$	23 (35)	-18 (-22)	19 (23)	-9.9 (-10)
$-g^{-1} \left(\overline{\mathbf{u}}_{\mathrm{sfc}}\, \overline{q}_{\mathrm{sfc}} \cdot \nabla \overline{p}_s \right)^*$	13 (-2.8)	-5.0 (-18)	12 (0.7)	-5.1 (-10)

We use the STN-30p river topology dataset (Fekete et al., 2001; Vörösmarty et al., 2000) to route net precipitation that falls over land into the appropriate ocean basin. The boundaries of the catchments for each ocean basin are shown in Fig. 2.10a. These boundaries compare well to higher-resolution estimates (e.g., Lehner et al., 2008), except for the lack of several major endoheric basins (basins with no outflow to the oceans) such as the Artesian Basin, Australia, the Great Basin, USA,

Table 2.4: Average freshwater forcing (cm yr^{-1}) to the oceans between 43° and 63° N. ERA-Interim and MERRA (in parenthesis) are both shown.

	Pacific $P-E$	Pacific Runoff	Atlantic $P-E$	Atlantic Runoff
$\overline{P}-\overline{E}$	55 (54)	18 (14)	32 (34)	19 (12)
$\overline{P}$	108 (102)	36 (36)	104 (100)	45 (44)
$\overline{E}$	53 (48)	18 (22)	75 (66)	27 (31)
$\overline{[P]}-\overline{[E]}$	30 (26)	14 (12)	28 (24)	16 (14)
$\overline{P}^{*}-\overline{E}^{*}$	25 (29)	3.6 (1.9)	3.2 (9.7)	3.4 (-1.6)
$-\nabla\cdot\left\langle\overline{\mathbf{u}}^{\dagger}\overline{q}^{\dagger}\right\rangle^{*}$	18 (18)	-3.4 (-3.0)	11 (10)	-7.4 (-8.2)
$-\nabla\cdot\left\langle[\overline{\mathbf{u}}]\,[\overline{q}]\right\rangle^{*}$	0.6 (1.0)	-0.8 (-1.0)	0.9 (1.3)	0.0 (0.0)
$-\nabla\cdot\left\langle\overline{\mathbf{u}'q'}\right\rangle^{*}$	12 (12)	6.0 (4.8)	-7.5 (-7.1)	8.8 (9.0)
$-\left\langle[\overline{q}]\,\nabla_{\rho}\cdot\overline{\mathbf{u}}\right\rangle^{*}$	14 (11)	-0.1 (0.9)	6.2 (4.9)	-4.1 (-4.6)
$-\left\langle\overline{q}^{*}\nabla_{\rho}\cdot\overline{\mathbf{u}}\right\rangle^{*}$	-1.2 (-1.1)	0.5 (0.8)	0.1 (-0.2)	-0.3 (-0.5)
$-\left\langle\overline{\mathbf{u}}\cdot\nabla\overline{q}\right\rangle^{*}$	6.0 (9.2)	-4.5 (-5.7)	5.8 (7.0)	-3.0 (-3.1)
$-g^{-1}\left(\overline{\mathbf{u}}_{\mathrm{sfc}}\,\overline{q}_{\mathrm{sfc}}\cdot\nabla\overline{p}_{s}\right)^{*}$	3.4 (-0.7)	-1.3 (-4.7)	3.8 (0.2)	-1.6 (-3.1)

and the large endoheric region of the Sahara desert. Since these are all regions where $P-E\approx 0$, far from the sub polar gyres, this should not affect our analysis. Dai and Trenberth (2002) use the same river runoff routing dataset with ERA-40 reanalysis $P-E$ forcing and find it to be comparable to estimates derived from datasets of river runoff, as used in EG03. The influence of runoff to the total freshwater forcing of the NP and NA is included in Table 2.3.

Since we use approximately the same NP and NA boxes as EG03, the values in Table 2.3 for total $\overline{P}-\overline{E}$ and for $\overline{P}$ and $\overline{E}$ are directly comparable with the values in EG03. For $\overline{P}-\overline{E}$, the ERA-Interim and MERRA values agree well with each other and are well within EG03's published uncertainty range (Table 2.3). The runoff estimates, corresponding to on-land $P-E$, are more spread within the datasets and do not lie within EG03's uncertainty range for the NP. However, EG03 only included the 11 biggest rivers contributing to this box and made no attempt to extrapolate downstream from the farthest downstream gauging station. Dai and Trenberth (2002) show that this extrapolation increases runoff globally by 19%. In particular, for the Columbia river, a key contributor to the NP box, they find that ignoring this downstream extrapolation underestimates the discharge to the ocean by approximately 3 mSv. Therefore, the values in Table 2.3 are within reason and can likely be trusted for the following primarily qualitative arguments.

The net freshwater flux into the Pacific is increased relative to the Atlantic simply because of the larger area of the Pacific. For this reason, it is convenient in many contexts to look instead at the net freshwater flux per area, tabulated in Table 2.4 (in cm yr^{-1}), which differs from Table 2.3 only by a factor of ocean area. The average runoff, shown in Table 2.4 for each ocean basin, is equivalent to spreading the runoff over the full area of the ocean basin. The NP and NA freshwater forcing terms in Table 2.4 are thus area independent, and provide the best comparison between the ocean basins for each term.

As in W83 and EG03, we find that the difference in $\overline{P} - \overline{E}$ between the high-latitude oceans takes the form of a difference in $\overline{E}$ as opposed to a difference in $\overline{P}$. This is at least partially due to the ocean-atmosphere feedback discussed by W83 and Broecker et al. (1985), where deep convection in the NA causes more northward transport of warm ocean waters, which increases evaporation over the NA, reinforcing oceanic deep convection and the overturning circulation. Czaja (2009) argues that looking at the freshwater budget is thus circular because the evaporation reflects the state of the overturning circulation in the ocean basin. But without a difference in atmospheric circulation, a higher $\overline{E}$ would lead to a higher $\overline{P}$ and thus to no difference in freshwater forcing. So, since the relevant quantity for SSS is $\overline{P} - \overline{E}$, the question becomes, how is $\overline{P}$ as large over the NP despite the lower $\overline{E}$? This is a question of moisture transport which motivates studying the moisture budget decomposition that makes up the rest of Tables 2.3 and 2.4.

The stationary-eddy vertical motion term, $-\left\langle [\overline{q}]\, \nabla_\rho \cdot \overline{\mathbf{u}} \right\rangle^*$, is a dominant term, freshening the NP with respect to the NA by 12 cm yr^{-1} (ERA-Interim) on average (including its influence on runoff), consistent with its dominant role in the moisture budget as shown in Section 2.3. The vertical motion over the NP results primarily from poleward motion (Sverdrup balance) and surface stress (Ekman pumping) associated with the Aleutian Low and Pacific subtropical high. Transient-eddy moisture fluxes also act to freshen the NP with respect to the NA by 17 cm yr^{-1} on average, consistent with the mechanism discussed by Ferreira et al. (2010), according to which the North Atlantic storm track has less fetch in which to develop and is weaker as a result, with some moisture transported out of the Atlantic and into continental Asia. Note from Fig. 2.3 that the these high-latitude ocean boxes are among the only ocean areas where transient-eddy moisture flux convergence dominates the contribution of stationary-eddy vertical motion. Other stationary eddy terms, such as the time-mean horizontal moisture advection, $-\left\langle \overline{\mathbf{u}} \cdot \nabla \overline{q} \right\rangle^*$, also play significant roles in the freshwater forcing of the Northern Hemisphere sub-polar gyres, but are not significantly different between the NP and NA. Both ocean basins benefit from orographic precipitation in the eastern side of the basins, which is partially cancelled out by drying downslope winds on the western side of the basins such that the orographic term $\left(-g^{-1}\left(\overline{\mathbf{u}}_{\mathrm{sfc}}\, \overline{q}_{\mathrm{sfc}} \cdot \nabla \overline{p}_s\right)^*\right)$ is not a large contribution. The combination of all of these terms makes the total contribution of $\overline{P}^* - \overline{E}^*$ to the NP–NA freshwater forcing difference a net freshening of the NP by 22 cm yr^{-1}.

Somewhat counterintuitively, the zonal mean, $\overline{[P]} - \overline{[E]}$ can also influence the difference in freshwater forcing simply through the different latitudinal distribution of area of the NP and NA and through ocean basin differences in river routing. The NP has a larger percentage of its area in wetter latitude bands than the NA, leading to a larger direct contribution from $\overline{[P]} - \overline{[E]}$, while the NA has a larger catchment area to surface area ratio, $D_{\mathrm{NA}}/A_{\mathrm{NA}} = 0.57$, than the NP, $D_{\mathrm{NP}}/A_{\mathrm{NP}} = 0.48$, leading to a larger runoff contribution from $\overline{[P]} - \overline{[E]}$. These effects cancel such that the total $\overline{P} - \overline{E}$ freshwater forcing difference between the NP and NA is just due to $\overline{P}^* - \overline{E}^*$.

We can get a rough sense of the contribution of these effects to the NP salinity ($\mathcal{S}_{\mathrm{NP}}$) using the simple box model for NP salinity from EG03:

$$\overline{\mathcal{S}}_{\mathrm{NP}} = \frac{\overline{F}_s}{\overline{V} + \overline{P} - \overline{E} + \overline{R}}. \tag{2.18}$$

Here $\overline{F}_s$ is the total salt flux convergence, $\overline{V}$ is oceanic volume throughflow, and $\overline{R}$ is river runoff. W83 and EG03 have explored the dependencies of this box model, finding that a combination of the high local $\overline{P} - \overline{E}$ and the low through-flow current $\overline{V}$, which increases the sensitivity to changes in the other terms, reduces the salinity of the NP, with a contribution from the low salt flux convergence $\overline{F}_s$ owing to the freshness of the Pacific equatorward of the subpolar gyre.

Using the values $\overline{F_s} = 200 \times 10^6$ kg s^{-1} and $\overline{V} = 5.76 \times 10^9$ kg s^{-1}, from EG03, and $\overline{P} - \overline{E} = 213$ mSv and $\overline{R} = 70$ mSv, according to Table 2.3, we obtain $\overline{\mathrm{S}}_{\mathrm{NP}} = 33.1‰$. This is comparable to the similar calculation in EG03, which obtained 32.9‰, and to an observational average of the upper 200 m of the NP box, obtaining 32.9‰. Substituting the Atlantic values of $\overline{P} - \overline{E}$ (103 mSv) and $\overline{R}$ (64 mSv) from Table 2.3, $\overline{\mathrm{S}}_{\mathrm{NP}}$ increases to 33.7‰. Combined with an increased $\overline{F_s} = 204 \times 10^6$ kg s^{-1} corresponding to a 2‰ increase in the western boundary current salinity as in EG03, we obtain an Atlantic-like $\overline{\mathrm{S}}_{\mathrm{NP}} = 34.4‰$, exceeding the observational average salinity below 200 m of 34.3‰ and thus potentially allowing intermediate to deep convection. For comparison, the average salinity of the NA over the upper 200 m is 34.1‰. All observational salinity data are averaged from the World Ocean Atlas (Zweng et al., 2013).

This analysis suggests that the NP–NA salinity difference comes from a combination of local differences in $\overline{P}-\overline{E}$ and river input and the difference in the salinity of the western boundary currents, which can be attributed to $\overline{P} - \overline{E}$ differences in the subtropics or ocean circulation mechanisms such as the inter-basin Sverdrup salt balance proposed by Reid Jr (1961) and illustrated by the experiments of Nilsson et al. (2013). The local $\overline{P} - \overline{E}$ differences arise from differences in vertical motion associated with the Aleutian Low and subtropical highs as well as differences in transient eddy activity between the ocean basins. The subtropical Pacific–Atlantic $\overline{P} - \overline{E}$ differences are almost entirely due to differences in vertical motion between the ocean basins. However, this is not inconsistent with the importance of zonal moisture transport across Central America as discussed by W83, Zaucker et al. (1994), EG03, and others, as the convergence of this easterly moisture flux would lead to a contribution to the vertical moisture flux term.

2.6 Application to the full moisture budget

Here we apply what we have learned from the zonally anomalous moisture budget to the full moisture budget including zonally anomalous and zonal mean components. As in the zonally anomalous moisture budget, mass convergence and vertical transport (Fig. 2.11a) set the predominant patterns of $\overline{P} - \overline{E}$ (Fig. 2.1) such as the ITCZ, Walker circulation, and subtropical dry zones. Here, the

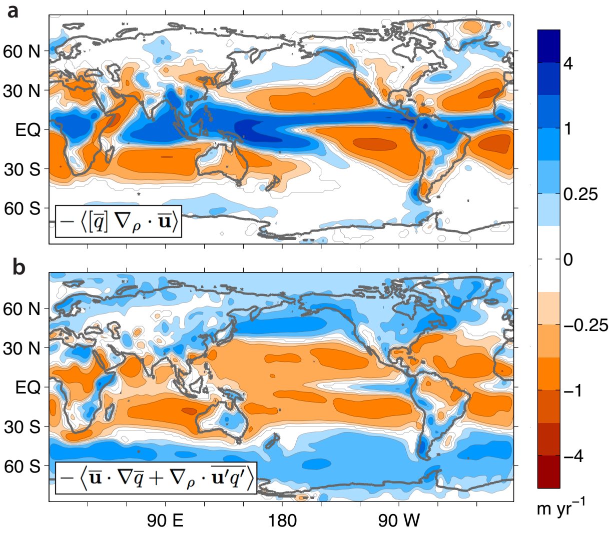

Figure 2.11: Full (zonal-mean + zonally anomalous) moisture budget terms. (a) Time-mean mass divergence component of moisture budget, and (b) time-mean horizontal moisture advection combined with transient-eddy moisture flux convergence.

combined transient-eddy and time-mean horizontal advection term (Fig. 2.11b) plays a significant role. The transient eddies and horizontal transport provide a fairly uniform drying equatorward of 35°, and a fairly uniform moistening poleward of 35°, where this term is the dominant contribution to storm track precipitation.

The vorticity balance beneath 850 hPa (Fig. 2.12) is still predominately Sverdrup balance and Ekman pumping. The descent leading to the subtropical dry zones is balanced by surface drag. The vorticity balance of the ITCZ is a more complex mixture of Sverdrup balance and Ekman pumping, with large cancelations between the beta term and surface drag and a large residual in the reanalysis. The nonlinear terms play a more important role here than in the zonally anomalous budget, maintaining the vertical motion along much of the equator. This vertical motion is maintained through $\overline{T}$ in the Warm Pool and through $\overline{N}$ in the Walker Cell subsidence region.

The mechanisms discussed in the main text apply particularly well for the zonal variation of the moisture budget, but also give insight into the full moisture budget.

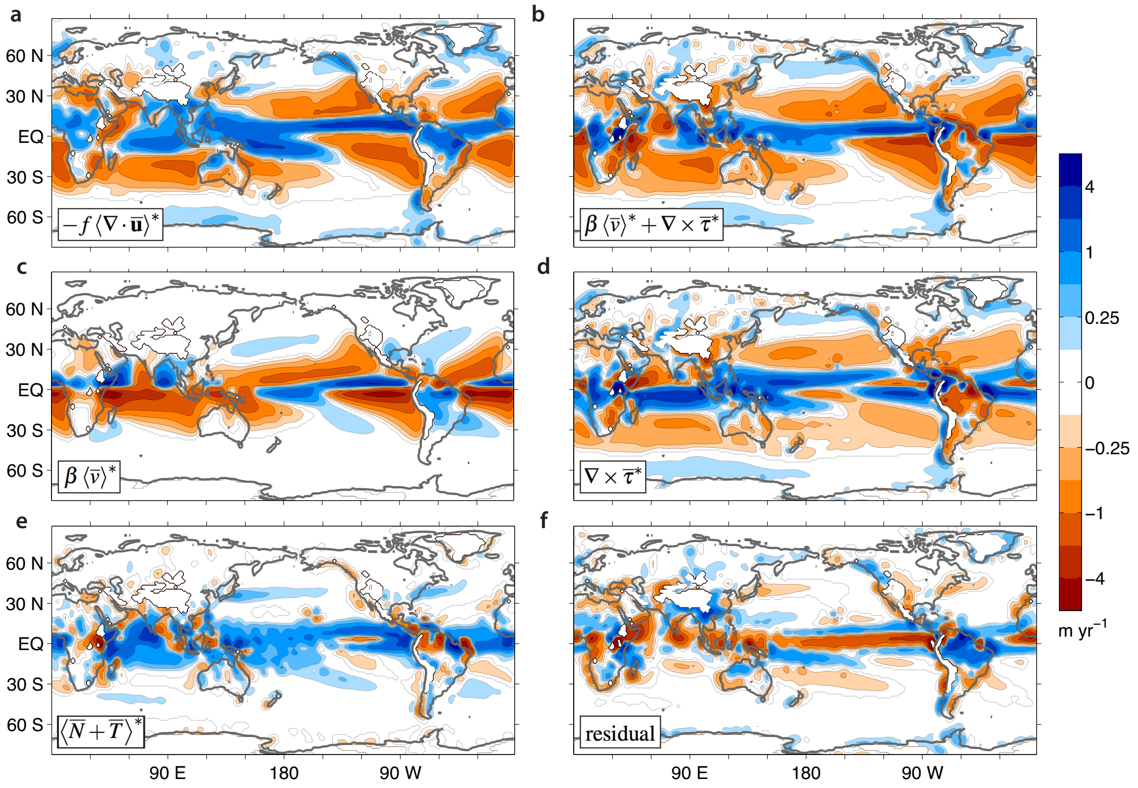

Figure 2.12: Dominant terms in the ERA-Interim total (zonal-mean and zonally anomalous) vertically-integrated vorticity budget (from surface to 850 mbar) multiplied by $[\overline{q}_{\mathrm{sfc}}]/f$ such that the stretching term gives the stationary-eddy divergence contribution to $\overline{P}-\overline{E}$. (a) Absolute vorticity component of stretching term. (b) Sum of beta term and surface drag. (c) Beta term. (d) Surface drag. (e) All nonlinear terms involving transient and stationary eddies. (f) Residual of all calculated vorticity tendencies, $-\left\langle f\nabla\cdot\overline{\mathbf{u}}+\beta\overline{v}+\overline{N}+\overline{T}\right\rangle+\nabla\times\overline{\tau}$, which can be interpreted as an artificial forcing by the reanalysis. Treatment of equatorial grid points and limits of integration as in Fig. 2.8.

2.7 Discussion and conclusions

We have shown that much zonal variation in $P-E$ is linked to lower-tropospheric vertical motion in stationary eddies. This stationary-eddy vertical motion explains planetary-scale patterns such as the Pacific warm pool, the zonal variability of the ITCZ, subtropical dry zones in the eastern ocean basins, and $\overline{P}-\overline{E}$ patterns in some land areas such as inland South America, western Africa, western Australia, and Canada. Transient eddies are also an important component of the zonally anomalous hydrological cycle, primarily acting to bring moisture onto land and across the Northern Hemisphere storm tracks. This is particularly important in coastal land areas that would otherwise be dried by stationary wave subsidence (e.g., western North America, northern China, and Chile). Horizontal advection of moisture by the time-mean flow largely cancels with transient eddy fluxes and does not play a dominant role. These conclusions can mostly be extended to the full moisture budget including zonal mean components.

Overall, the majority of spatial variability in $\overline{P}^* - \overline{E}^*$ is explained by regional differences in vertical motion, not moisture content. This highlights the need to study the response of zonally anomalous circulations to climate change, to understand the potential for regional changes in hydroclimate. In midlatitudes, this would primarily entail the study of stationary Rossby waves, and their interaction with transient Rossby waves. In models, stationary Rossby waves are sensitive to the latitudinal structure of the zonal wind, and to the relative location of the zonal wind to topography and heating (Hoskins and Karoly, 1981). It is thus essential to know the exact response of the zonal wind to climate change in order to know how regional hydroclimate will respond to climate change. In the tropics and subtropics, zonally anomalous circulations take the form of zonal variation of the ITCZ position and the monsoon response to topography and heating, and it is thus essential to understand how these systems respond to climate change.

In some regions, zonally anomalous vertical motion is a direct response to high sea surface temperatures (SSTs) and the resulting evaporation and deep convection (e.g., the Warm Pool) or to subsidence downstream from topography (e.g., directly off the west coast of South America). In others, the vertical motion is forced remotely by stationary Rossby waves and other stationary-eddy circulations (e.g., the dry zone off the coast of California, the wet zone extending across the North Pacific, and the extension of the dry zone off the west of South America into the Central Pacific). Other studies have gone into more detail on the mechanisms in these particular regions (Rodwell and Hoskins, 1996, 2001; Takahashi and Battisti, 2007). In still other regions, such as the South Pacific Convergence Zone and the Gulf of Mexico, there is likely a more complex interaction between remotely forced vertical motion and that forced by local high SSTs.

To address the large-scale balances relating vertical motion to horizontal flow, we have performed a vorticity budget analysis for anomalies from the zonal mean in the lower troposphere (below 850 hPa). Within stationary-eddy circulations, lower-level vertical motion is associated with Sverdrup balance and Ekman pumping on large scales. Through these balances, vertical motion can arise from meridional motion and surface stress curls such that poleward (equatorward) motion or cyclonic (anticyclonic) circulations are linked to upward (downward) motion and wet (dry) regions.

Because SSS reflects the long-term $\overline{P} - \overline{E}$ freshwater forcing of a region, the moisture budget decomposition discussed here can be applied to understand regional differences in SSS. The subpolar oceans in the Northern Hemispere are an interesting example because the ocean basin asymmetry in ocean freshwater forcing and SSS contribute to the asymmetry in deep overturning of the ocean, which is localized to the North Atlantic. Our analysis suggests that changes in SSS and ocean overturning in past climates likely can be understood in terms of changes in the water vapor content at high latitudes (i.e., $[\overline{q}]$), the large scale vertical motion patterns (ω^*), and transient-eddy moisture fluxes. The water vapor content $[\overline{q}]$ is primarily governed by thermodynamics. Stationary-eddy vertical motion ω^* would respond to changes in topography (ice sheets), changes in ocean heat release, and shifts in the jet stream. Transient-eddy moisture fluxes are influenced by the meridional temperature gradient, atmospheric stability, and atmospheric moisture content (Caballero and Langen, 2005; O'Gorman and Schneider, 2008b; Caballero and Hanley, 2012).

Overall, the main conclusion of this study is that zonal variation in $P-E$ is strongly linked to the strength of zonally anomalous circulations, with less dependence on the zonal variation of moisture content. This can be applied to link the understanding of circulation dynamics to an understanding of the hydrological cycle.

2.8 Appendix 2A: Methods for surface intersections

To satisfy conservation equations, it is important to density weight derivatives to ensure conservation of mass. This arises from using the continuity equation,

$$\partial_t \rho_\eta + \nabla_\eta \cdot (\rho_\eta \mathbf{v}) = 0, \tag{2.19}$$

to convert a general conservation law for a field ϕ with a source Φ from advective form to flux form:

$$\begin{aligned} &\partial_t \phi + \mathbf{v} \cdot \nabla \phi = \Phi \\ \rightarrow\ &\frac{1}{\rho_\eta} \partial_t (\rho_\eta \phi) + \frac{1}{\rho_\eta} \nabla_\eta \cdot (\rho_\eta \mathbf{v} \phi) = \Phi, \end{aligned} \tag{2.20}$$

where ∇_η is the derivative on η-coordinate surfaces and $\rho_\eta = \rho \left(\partial_z \eta\right)^{-1}$ is the coordinate system density that satisfies

$$\rho\, dx\, dy\, dz = \rho_\eta\, dx\, dy\, d\eta. \tag{2.21}$$

As such, derivatives must take account of the covariance of density ρ_η and flux $\mathbf{v}\phi$. The shorthand used in the text is

$$\nabla_\rho \cdot (\cdot) \equiv \frac{1}{\rho_\eta} \nabla_\eta \cdot (\rho_\eta \cdot)\,. \tag{2.22}$$

However, in pressure coordinates, ρ_p is simply $\mathrm{H}_\beta(p - p_s)/g$, where $\mathrm{H}_\beta(p - p_s)$ is the Boer beta function (Boer, 1982), a heavyside function that sets the density to zero beneath the surface. This comes into play when computing derivatives as pressure levels cross the surface.

Writing out the density-weighting explicitly for the vertically integrated divergence,

$$\langle \nabla_\rho \cdot \overline{\mathbf{u}} \rangle = \left\langle \nabla \cdot \overline{\mathbf{u}\mathrm{H}_\beta} \right\rangle_0^{p_0}, \tag{2.23}$$

where p_0 is the maximum pressure level. Since time averages are density weighted according to

$$\overline{(\cdot)} = \int \rho_\eta\, (\cdot)\, dt \bigg/ \int \rho_\eta\, dt\ , \tag{2.24}$$

the time-average H_β can be separated from the time-average mass flux such that

$$\langle \nabla_\rho \cdot \overline{\mathbf{u}} \rangle = \left\langle \nabla \cdot \overline{\mathbf{u}} \overline{\mathrm{H}}_\beta \right\rangle_0^{p_0} , \tag{2.25}$$

In this way, we can separate off a surface term due to the gradient of $\overline{\mathrm{H}}_\beta$,

$$\begin{aligned} \langle \nabla_\rho \cdot \overline{\mathbf{u}} \rangle &= \left\langle \overline{\mathrm{H}}_\beta \nabla \cdot \overline{\mathbf{u}} \right\rangle_0^{p_0} + \left\langle \overline{\mathbf{u}} \cdot \nabla \overline{\mathrm{H}}_\beta \right\rangle_0^{p_0} \\ &= \langle \nabla \cdot \overline{\mathbf{u}} \rangle + \overline{\mathbf{u}}_{\mathrm{sfc}} \cdot \nabla \overline{p}_s . \end{aligned} \tag{2.26}$$

We thus recover an expression for the orographic vertical velocity in terms of the difference in divergences:

$$\overline{\omega}_{\mathrm{sfc}} \equiv \overline{\mathbf{u}}_{\mathrm{sfc}} \cdot \nabla \overline{p}_s = \langle \nabla_\rho \cdot \overline{\mathbf{u}} \rangle - \langle \nabla \cdot \overline{\mathbf{u}} \rangle . \tag{2.27}$$

As with time averages, zonal averages are density weighted according to

$$[\cdot] = \int \rho_\eta \, (\cdot) \; dx \Bigg/ \int \rho_\eta \, dx \; , \tag{2.28}$$

such that $\left[\overline{\beta \mathbf{u} q}\right] = \overline{[\beta]} \, [\overline{\mathbf{u} q}]$ as needed for Eq. (2.4).

Chapter 3

Idealized GCM experiments with zonally asymmetric forcing: Zonally anomalous moisture budget

This chapter is submitted to the *Journal of Climate* (Wills and Schneider, 2016).

Abstract

Stationary or low-frequency Rossby waves are the primary drivers of extratropical weather variations on monthly and longer timescales. They take the form of persistent highs and lows, which, for example, shape subtropical dry zones and guide extratropical storms. This paper investigates the stationary Rossby wave response to global warming in an idealized GCM, simulating a wide range of climates by varying longwave absorption. The stationary waves are forced by two idealized zonal asymmetries: a midlatitude Gaussian mountain and equatorial ocean heating. Associated with changes in stationary Rossby waves are changes in the zonal variation of the hydrological cycle. Particularly in the subtropics, the experiments show a nearly constant or decreasing amplitude of the zonally anomalous hydrological cycle in climates warmer than modern despite the *wet gets wetter, dry gets drier* effect associated with increasing atmospheric moisture content. A scaling for zonally anomalous $P-E$, based on zonal-mean surface specific humidity and stationary-eddy vertical motion, disentangles the roles of thermodynamic and dynamic changes. It shows that changes in

lower-tropospheric vertical motion in stationary eddies control changes in the zonally asymmetric hydrological cycle.

3.1 Introduction

The tendency for wet latitude bands to get wetter and for dry latitude bands to get drier has been highlighted as a robust response of the zonal-mean hydrological cycle to global warming (Mitchell et al., 1987; Chou and Neelin, 2004; Held and Soden, 2006). As Held and Soden (2006) point out, this *wet gets wetter, dry gets drier* response relies on the assumption of fixed relative humidity and circulation. It is expected to break down for variations about the zonal mean due to land–sea differences in relative humidity and moisture gradient changes (Byrne and O'Gorman, 2013, 2015; Greve et al., 2014) and due to changes in stationary-eddy circulations, which we will explore in this paper.

Stationary Rossby waves contribute to the maintenance of midlatitude and subtropical dry zones (Broccoli and Manabe, 1992; Rodwell and Hoskins, 1996, 2001; Takahashi and Battisti, 2007) and monsoonal wet zones (Molnar et al., 2010; Chen and Bordoni, 2014). Changes in stationary Rossby waves with climate change could thus have large regional impacts on the hydrological cycle. Such changes have already been implicated in the inceasing aridification of southwest North America and the Mediterranean region (Seager et al., 2007, 2014).

Several studies have analyzed the change in barotropic stationary-eddy streamfunction in climate change scenarios (Stephenson and Held, 1993; Brandefelt and Körnich, 2008; Simpson et al., 2014, 2015). While these studies yield insight into how stationary Rossby waves may change as the climate warms, multiple stationary eddy sources make it difficult to ascertain the mechanisms for the simulated changes. With this in mind, we design two idealized GCM experiments in which simple zonal asymmetries are added to an aquaplanet. We analyze the changes in Rossby waves and the resulting changes in the hydrological cycle in these experiments.

In Section 3.2, we describe two sets of idealized model experiments with zonally asymmetric boundary conditions. In Section 3.3, we analyze the zonally anomalous moisture and vorticity budgets to gain insight into mechanisms governing the spatial distribution of zonally anomalous net precipitation (precipitation minus evaporation, $P - E$) in these experiments. In Section 3.4, we analyze changes in zonally anomalous $P - E$ using the approximations developed in Section 3.3. The result is that changes in zonally anomalous $P - E$ can be understood in terms of changes in the lower-tropospheric manifestation of stationary eddies, which we discuss in Chapter 4. Section 3.5 presents some conclusions and an outlook for applying these findings to more realistic climate models and observations.

3.2 Zonally asymmetric aquaplanet experiments

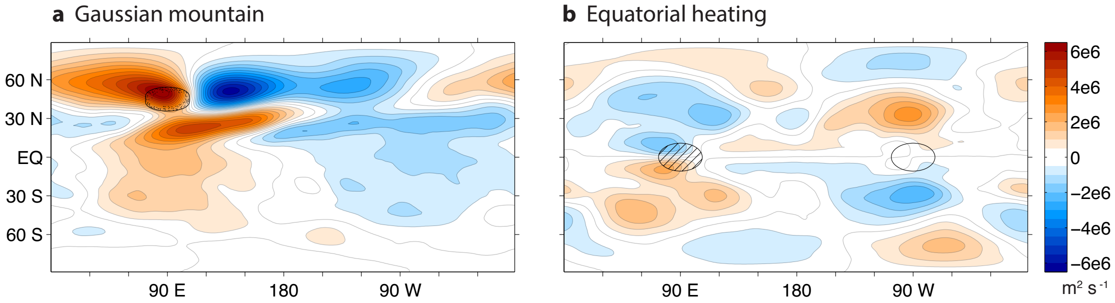

Figure 3.1: Experimental setup and stationary eddy streamfunction at $p = 600$ hPa in the reference climate ($\alpha = 1$) of (a) the Gaussian mountain experiment and (b) the equatorial heating experiment. The black contour in (a) is the 1000 m contour of surface height. In (b), the black circles are the ± 20 W m^2 contours of ocean heat-flux convergence. The hashed circle is the location of the heating (ocean heat flux convergence). The same reference contours are shown in all subsequent map plots.

Stationary eddies are primarily forced by divergence in the vicinity of topography and zonally anomalous surface heating (Hoskins and Karoly, 1981; Held et al., 2002). We set up two sets of aquaplanet experiments to study these forcings separately in an idealized setting. The forcing of stationary eddies by zonal anomalies of transient-eddy heat fluxes and diabatic heating are often considered seperately (e.g., Held et al., 2002). Here the model computes all zonally anomalous heating internal to the atmosphere explicitly so that it is allowed to evolve with climate change. In this way we consider the total stationary wave response to zonally anomalous external forcing.

3.2.1 Model

We use an idealized GCM based on the GFDL Flexible Modeling System (http://www.gfdl.noaa.gov/fms). The convection scheme is essentially that of Frierson et al. (2006) and Frierson (2007), with the modifications described in O'Gorman and Schneider (2008b). The model has a horizontal spectral resolution of T85. Our model setup is similar to O'Gorman and Schneider (2008b) except that we have extended the vertical domain up to $\sigma = p/p_s = 4 \times 10^{-4}$ (pressure p and surface pressure p_s) with 38 vertical levels and included linear damping in an 8-level sponge layer at the top of the domain. The linear damping coefficient increases linearly by level from $(14400\ \mathrm{s})^{-1}$ at the lowest sponge level to $(1800\ \mathrm{s})^{-1}$ at the top model level and is applied only to anomalies from the zonal mean. This helps minimize reflections of stationary waves from the top of the domain[1].

All experiments are run in a perpetual equinox setup, avoiding complexity associated with the seasonal cycle. Radiative transfer is represented by a two-stream scheme for a semi-grey atmosphere, meaning that there are no water vapor or cloud radiative feedbacks. Water-vapor and cloud-radiative feedbacks have been shown to influence the circulation response to global warming in climate models (e.g., Voigt and Shaw, 2015). But we focus on understanding the simple case presented here without these feedbacks, as it is an important prerequisite to a complete understanding. In the grey atmosphere, climate change can be simulated by varying the longwave optical depth, $\tau = \alpha\tau_{\mathrm{ref}}$, where τ_{ref} is a reference optical depth that varies as a function of latitude ϕ and normalized pressure σ

$$\tau_{\mathrm{ref}}\left(\phi, \sigma\right) = \left[f_l\sigma + (1 - f_l)\sigma^4\right]\left[\tau_e + (\tau_p - \tau_e)\sin^2\phi\right], \tag{3.1}$$

and α is a multiplicative factor. Here $f_l = 0.2$, $\tau_e = 7.2$, and $\tau_p = 1.8$. To simulate climates with global-mean surface temperatures ranging from 280 to 316 K, we use $\alpha = [0.6,\ 0.7,\ 0.8,\ 0.9,\ 1.0,\ 1.2,\ 1.4,\ 1.6,\ 1.8,\ 2.0,\ 2.5,\ 3.0,\ 4.0,\ 6.0]$. We refer to $\alpha = 1.0$ as the reference climate, which has a global-mean surface temperature of 289 K. Each simulation is spun up for at least 4 years. All fields shown are averages over the subsequent 8 years.

---

[1] One simulation, the coldest equatorial heating simulation, is run with double these sponge-layer damping coefficients to avoid numerical instabilities in the stratosphere.

The surface boundary condition is a slab ocean with its own surface energy balance such that surface energy fluxes are freely evolving. To simulate a more realistic zonal-mean climate in the tropics, we add a zonal-mean ocean heat-flux convergence,

$$\nabla \cdot F_0 \left(\phi\right) = Q_0 \left(\frac{1-2\phi^2}{\phi_0^2}\right) \exp\left(-\frac{\phi^2}{\phi_0^2}\right). \tag{3.2}$$

As in Bordoni (2007), Bordoni and Schneider (2008), and Merlis and Schneider (2011), we choose values that give an ocean heat-flux convergence similar to the hemispherically and zonally symmetric component in observations: $Q_0 = 50$ W m^{-2} and $\phi_0 = 16°$.

3.2.2 Gaussian mountain range

To study the response of orographically forced stationary waves and wet and dry zones to warming in this idealized configuration, we add a single Gaussian mountain ridge in midlatitudes. The surface height as a function of longitude λ and latitude ϕ is given by

$$z_{\mathrm{sfc}}\left(\lambda, \phi\right) = h_0 \exp\left[-\frac{\left(\lambda - \lambda_0\right)^2}{2\sigma_\lambda^2} - \frac{\max\left(0, \left|\phi - \phi_0\right| - R_\phi\right)^2}{2\sigma_\phi^2}\right]. \tag{3.3}$$

We use $h_0 = 2500$ m, $\phi_0 = 45°$N, $R_\phi = 2.5°$, $\sigma_\phi = 5°$, and $\sigma_\lambda = 12.5°$. As there are no other zonal asymmetries, λ_0 is arbitrary. It will be denoted 90° on plots. The latitudinal position and size of this mountain range are such that it is comparable to the Rocky Mountains. The amplitude of Rossby waves forced is sensitive to the choice of σ_λ and h_0. We choose these values to maximize the Rossby wave response while keeping the mountain size realistic.

No modifications are made to the surface properties; thus this mountain is an aquamountain. Modified simulations with a bucket surface hydrology model and/or a modified surface heat capacity in the vicinity of the mountain did not have a large influence on the large-scale balances described here.

Figure 3.1a shows the 600 hPa Rossby wave response to the mountain. There is both poleward and equatorward deflection of the flow around the mountain. This leads to Rossby wave trains propagating poleward and equatorward. The equatorward Rossby wave train has a large influence on the moisture budget all the way to the equator (Fig. 3.2). In Fig. 3.1a and all subsequent figures, the 1000 m contour of surface height is shown with a black contour, with speckling on the upslope side.

3.2.3 Tropical ocean heat transport

To study the response of stationary eddies forced by tropical heating to warming in this idealized configuration, we add ocean heating and cooling along the equator. The experimental setup is similar to that of Merlis and Schneider (2011), where the zonal symmetry is broken by adding an ocean heat-flux convergence

$$\begin{aligned}\nabla \cdot F_1(\phi) &= Q_1 \exp\left[-\frac{(\lambda-\lambda_E)^2}{2\sigma_\lambda^2} - \frac{\phi^2}{2\sigma_\phi^2}\right] \\ &- Q_1 \exp\left[-\frac{(\lambda-\lambda_W)^2}{2\sigma_\lambda^2} - \frac{\phi^2}{2\sigma_\phi^2}\right].\end{aligned} \tag{3.4}$$

We use $Q_1 = 50$ W m^{-2}, $\lambda_W = 90^\circ$, $\lambda_E = 270^\circ$, $\sigma_\lambda = 12.5^\circ$, and $\sigma_\phi = 8^\circ$.

This setup drives a Walker circulation with ascending branch at 90° and descending branch at 270°. The stationary-eddy streamfunction at 600 hPa is shown in Fig. 3.1b, as well as the locations of the heating (hatched circle) and cooling (open circle). The region of equatorial heating gives rise to lower-tropospheric cyclonic circulations in both hemispheres and anticyclones aloft. The region of equatorial cooling gives rise to the opposite directionality of circulations. The large-scale divergence/convergence generates rotational flow and hence Rossby waves, which propagate into the extratropics (Sardeshmukh and Hoskins, 1988).

3.3 Physical balances

Idealized model experiments have been used to understand the physical balances of the zonal-mean hydrological cycle (e.g., O'Gorman and Schneider, 2008b). The zonally asymmetric experiments allow us to analyze the physical mechanisms of the departures from the zonal-mean hydrological

a Gaussian mountain

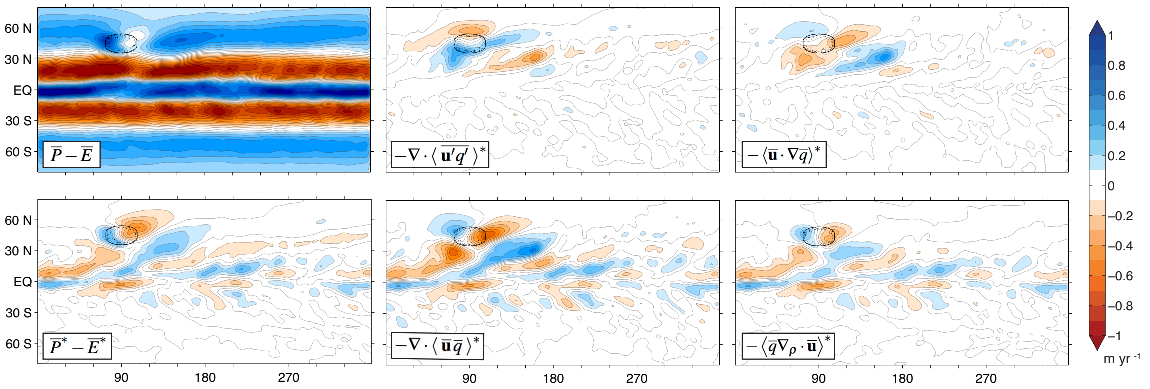

b Equatorial heating

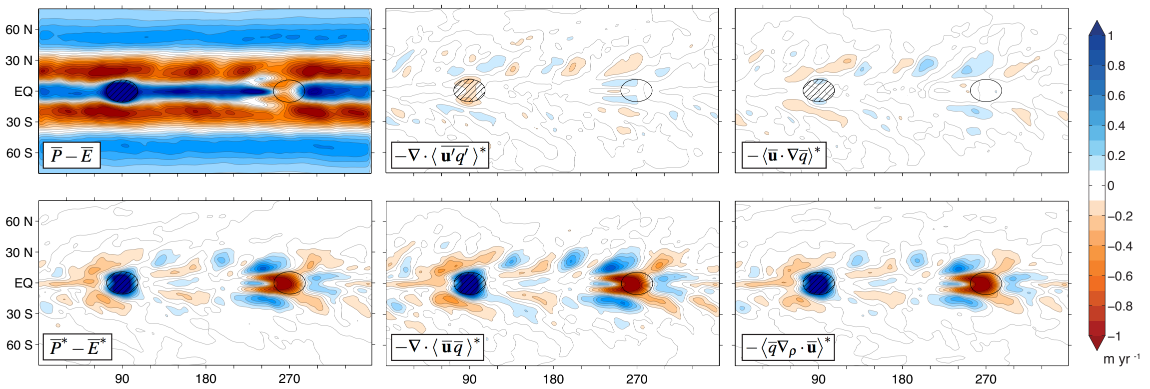

Figure 3.2: Moisture budget terms in the reference climate ($\alpha = 1$) of (a) the Gaussian mountain experiment and (b) the equatorial heating experiment: total $\overline{P} - \overline{E}$, its zonal anomalous component ($\overline{P}^* - \overline{E}^*$), the total zonally-anomalous moisture flux convergence by stationary eddies ($-\langle \nabla \cdot \overline{\mathbf{u}}\,\overline{q} \rangle^*$), the zonally anomalous moisture flux convergence by transient eddies ($-\langle \nabla \cdot \overline{\mathbf{u}'q'} \rangle^*$), the advective component of the stationary-eddy moisture flux convergence ($-\langle \overline{\mathbf{u}} \cdot \nabla \overline{q} \rangle$), and the divergent component of the stationary-eddy moisture flux convergence ($-\langle \overline{q} \nabla_\rho \cdot \overline{\mathbf{u}} \rangle$). Here and in all subsequent latitude–longitude figures, the fields are smoothed with a 1.5° real-space Gaussian filter to focus on large scales. Note that values of $\overline{P} - \overline{E}$ ($\overline{P}^* - \overline{E}^*$) are up to 2.5 (1.6) m yr^{-1} over the equatorial heating, where we allow the colormap to saturate to focus also on subtropical $\overline{P} - \overline{E}$ patterns

cycle. We focus in particular on understanding the mechanisms behind zonal anomalies in net precipitation, $\overline{P}^* - \overline{E}^*$. Here $\overline{(\cdot)}$ represents a long-term time mean and $(\cdot)^*$ represents a departure from a zonal mean $[\cdot]$, such that the full field can be written $(\cdot) = [\cdot] + (\cdot)^*$. Figure 3.2 shows the full net precipitation $\overline{P} - \overline{E}$ as well as stationary-eddy component $\overline{P}^* - \overline{E}^*$ for each experiment. The stationary-eddy component is dominated by the zonal variation of precipitation, $\overline{P}^*$. The zonal variation of evaporation is only important directly on the topography or ocean heat-flux convergence.

The Gaussian mountain leads to a wet zone of orographic precipitation upstream of the mountain range, a large dry zone extending poleward and more than 30° downstream, and an alternating pattern of wet and dry zones in the subtropics and tropics associated with the equatorward Rossby wavetrain (Fig. 3.2a). Some influence of this Rossby wavetrain is also seen in the southern hemisphere subtropics. This equatorward wavetrain does not show up in experiments with a narrower mountain range (cf. Shi and Durran, 2014, where the zonal scale is $\sim 2.5°$).

The equatorial heating/cooling leads to an area of localized high $\overline{P} - \overline{E}$ over the ocean heat flux convergence, a large region of dryness immediately to the west, an extended area of low $\overline{P} - \overline{E}$ around the ocean heat flux divergence, and large wet zones immediately west and poleward (Fig. 3.2b). We would like to understand the physics maintaining these regional $\overline{P} - \overline{E}$ differences and look at how the patterns respond to climate change.

3.3.1 Moisture budget decomposition

Wills and Schneider (2015, Chapter 2, hereafter WS15) outline a decomposition of the zonally anomalous moisture budget to understand $\overline{P}^* - \overline{E}^*$ in ERA-Interim reanalysis. Here, we proceed in a similar fashion to understand which types of circulations are important for maintaining zonal variation in $\overline{P} - \overline{E}$ in these idealized experiments. The zonally anomalous moisture budget can be written as

$$\overline{P}^* - \overline{E}^* = -\nabla \cdot \langle \overline{\mathbf{u}q} \rangle^*, \tag{3.5}$$

where $\mathbf{u} = (u, v)$ is the horizontal wind, q is the specific humidity, ∇ is the nabla operator on a sphere, and $\langle \cdot \rangle$ is a mass weighted vertical integral. While the native coordinates of the idealized GCM are sigma coordinates, we interpolate output to pressure coordinates to evaluate Eq. (3.5) and decompose fluxes into mean-flow and eddy components[2]. This facilitates comparison with WS15, where the same analysis is performed with reanalysis data in pressure coordinates.

The total moisture flux convergence can first be split into a component due to the time-mean flow (stationary eddies) and a component due to transient eddies. We define departures from the

---

[2] The mass-weighted vertical integral of each field is linearly interpolated from sigma to pressure coordinates at each time step such that the interpolation conserves mass.

time mean as $(\cdot)' = (\cdot) - \overline{(\cdot)}$, such that

$$\overline{P}^* - \overline{E}^* = -\nabla \cdot \left\langle \overline{\mathbf{u}}\,\overline{q} + \overline{\mathbf{u}'q'} \right\rangle^* . \tag{3.6}$$

The stationary-eddy moisture flux convergence, $-\nabla \cdot \langle \overline{\mathbf{u}}\,\overline{q} \rangle^*$, can be further split into an advective and divergent component

$$-\nabla \cdot \langle \overline{\mathbf{u}}\,\overline{q} \rangle^* = - \langle \overline{\mathbf{u}} \cdot \nabla \overline{q} + \overline{q} \nabla_\rho \cdot \overline{\mathbf{u}} \rangle^* . \tag{3.7}$$

Here ∇_ρ differs from ∇ in that it is weighted by an effective density, which vanishes on "underground" isobars. That is

$$\nabla_\rho \cdot (\cdot) = \frac{1}{\overline{\rho}_\beta} \nabla \cdot \left(\overline{\rho}_\beta \cdot \right) , \tag{3.8}$$

where

$$\rho_\beta = \begin{cases} 1 & p < p_s \\ & \\ 0 & p > p_s \end{cases} \tag{3.9}$$

is the dimensionless density in pressure coordinates (cf. Boer, 1982).

The transient-eddy term, $-\nabla \cdot \left\langle \overline{\mathbf{u}'q'} \right\rangle^*$, the full stationary-eddy term, $-\nabla \cdot \langle \overline{\mathbf{u}}\,\overline{q} \rangle^*$, the divergent stationary-eddy term, $- \langle \overline{q} \nabla_\rho \cdot \overline{\mathbf{u}} \rangle^*$, and the advective stationary-eddy term, $- \langle \overline{\mathbf{u}} \cdot \nabla \overline{q} \rangle^*$, are shown in Fig. 3.2 for both experiments. As in reanalysis (WS15), the divergent stationary-eddy term accounts for nearly all variance in $\overline{P}^* - \overline{E}^*$ between the equator and 30° or 40° latitude in both experiments. The reason this balance is possible despite large moisture tendencies associated with the transient-eddy and advective stationary-eddy terms is that the combined transient-eddy and advective term (Fig. 3.3) is small. This is consistent with the mechanism discussed by WS15, where transient eddies relax moisture gradients set up by horizontal stationary-eddy moisture fluxes.

Also as in reanalysis, the divergent stationary-eddy term is almost entirely due to zonal anomalies in stationary-eddy mass convergence, $- \langle [\overline{q}]\, \nabla_\rho \cdot \overline{\mathbf{u}} \rangle^*$ (Fig. 3.4), rather than zonal anomalies in specific humidity, $- \langle \overline{q}^* \nabla_\rho \cdot \overline{\mathbf{u}} \rangle^*$. This is partially a result of weak temperature gradients and, consequently, weak moisture gradients in the tropical free troposphere (Charney, 1963; Sobel et al.,

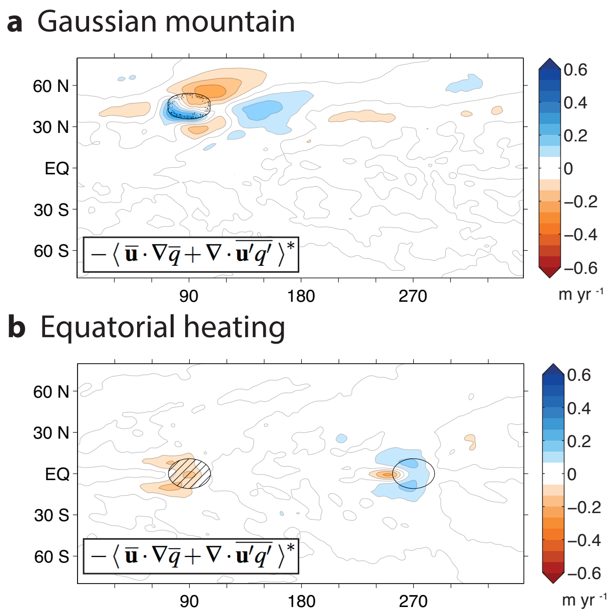

Figure 3.3: The sum of horizontal moisture advection by stationary eddies and transient-eddy moisture flux convergence in the reference climate ($\alpha = 1$) of (a) the Gaussian mountain experiment and (b) the equatorial heating experiment.

2001). Figure 3.4 shows successive approximations to the resulting moisture budget, which should be compared with Fig. 3.3, showing the majority of terms constituting the residual of these approximations. This is primarily a tropical and subtropical dominant moisture balance; the approximations are good up to 30° or 40° latitude.

The moisture budget decomposition shown here differs slightly from those of Newman et al. (2012) and WS15. Newman et al. (2012) puts the ∇_ρ in the advective term instead of the divergent term. WS15 does not use ∇_ρ in either term and instead defines an additional surface term which captures all effects of surface pressure gradients. The decomposition shown here has the advantage that $\nabla_\rho \cdot \overline{\mathbf{u}} = -\frac{1}{\rho_\beta}\partial_p\left(\rho_\beta \overline{\omega}\right)$, by continuity. This leads to the property that an integral of the divergence up to level p_i gives the pressure velocity at p_i,

$$\left\langle \nabla_\rho \cdot \overline{\mathbf{u}} \right\rangle_{p_i} = \frac{1}{g}\,\overline{\omega}\big|_{p_i}\,. \tag{3.10}$$

The density-weighted divergence effectively combines the surface term and the stationary-eddy divergence term of WS15.

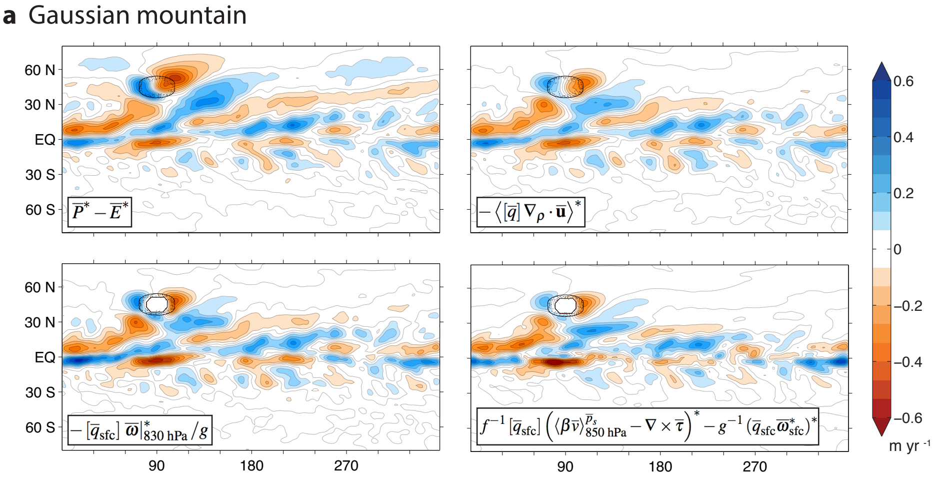

a Gaussian mountain

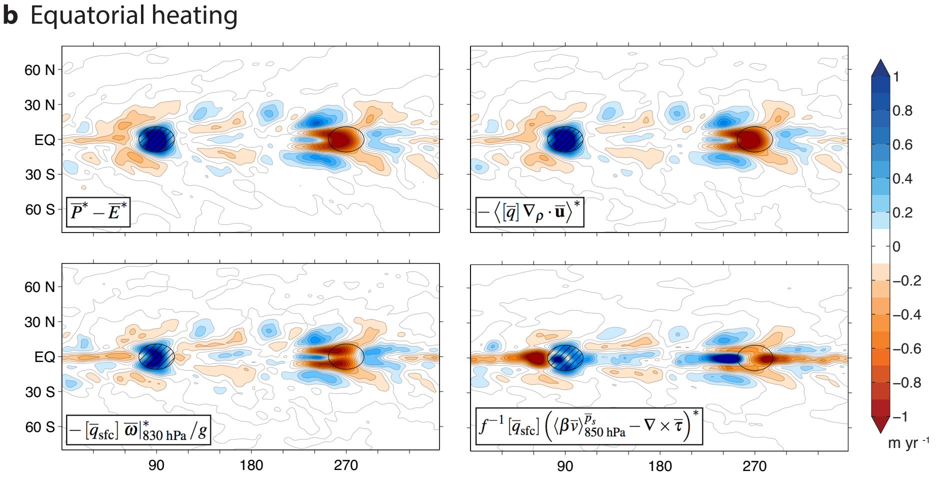

b Equatorial heating

Figure 3.4: Moisture budget terms in the reference climate ($\alpha = 1$) of (a) the Gaussian mountain experiment and (b) the equatorial heating experiment: $\overline{P}^* - \overline{E}^*$ and approximations to $-\langle [\overline{q}]\,\nabla_p \cdot \overline{\mathbf{u}} \rangle^*$, the dominant term determining $\overline{P}^* - \overline{E}^*$.

We can take advantage of the relationship between horizontal divergence and vertical velocity (3.10) to derive a simple approximation for $\overline{P}^* - \overline{E}^*$ if we take $[\overline{q}]$ out of the vertical integral. This can be done with the integral mean value theorem, whereby

$$-\langle [\overline{q}]\,\nabla_p \cdot \overline{\mathbf{u}} \rangle = [\overline{q}_{\mathrm{sfc}}]\,\langle \nabla_p \cdot \overline{\mathbf{u}} \rangle_{p_i} \tag{3.11}$$

for some level p_i in the vertical domain. We calculate p_i for every grid point and every simulation. The global mean p_i in the reference simulations are 860 hPa (orographic forcing) and 840 hPa (equatorial heating). We then approximate this relation by using one value $p_i = 850$ hPa globally

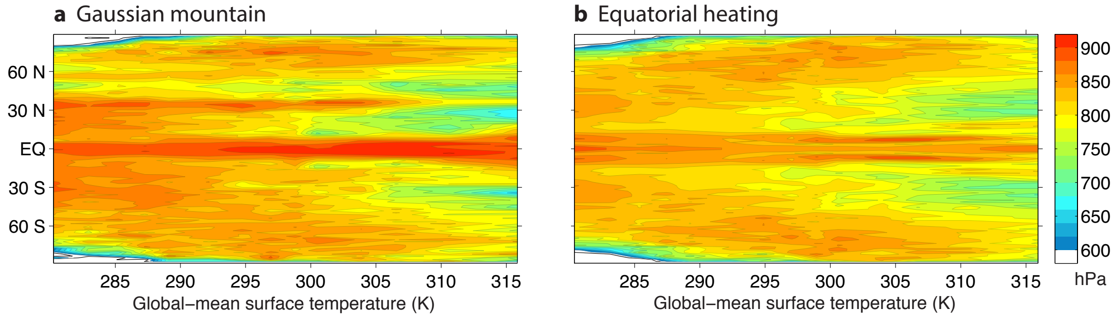

Figure 3.5: Zonal mean of best fit p_i from Eq. 3.11 for (a) the Gaussian mountain experiment and (b) the equatorial heating experiment. Note that values have been symmetrized about the equator for the equatorial heating experiment.

in both experiments. The best-fit value of p_i is shown versus latitude for all simulations in Fig. 3.5. The best-fit value of p_i in the subtropics and midlatitudes is seen to decrease as the climate warms and the depth of the troposphere and the water vapor scale height increase.

Equation (3.11) implies that zonal variation in $\overline{P} - \overline{E}$ is determined by a product of the zonal-mean surface specific humidity and the zonally anomalous vertical motion at 850 hPa,

$$\overline{P}^* - \overline{E}^* \approx -\frac{1}{g} \left[\overline{q}_{\mathrm{sfc}} \right] \overline{\omega}\big|^*_{850\ \mathrm{hPa}} . \tag{3.12}$$

This is shown for the reference simulations in Fig. 3.4. The approximation captures all features of $\overline{P}^* - \overline{E}^*$ in the tropics and subtropics, up to 30°. It starts to break down at higher latitudes, but still generally captures the sign of $\overline{P}^* - \overline{E}^*$. This approximation should not be taken too literally directly over the mountain, where the local $\overline{q}_{\mathrm{sfc}}$ is drastically different from the zonal mean. It is undefined for a small region around the peak of the mountain where the surface extends above 850 hPa. This approximation is identical to that used in WS15 for reanalysis, despite slight differences in the moisture budget decomposition.

3.3.2 Vorticity constraints on vertical motion

Stationary Rossby wave theory (e.g, Hoskins and Karoly, 1981) usually solves for the Rossby wave response to zonally asymmetric topography or heating in terms of a horizontal streamfunction. In

a Gaussian mountain

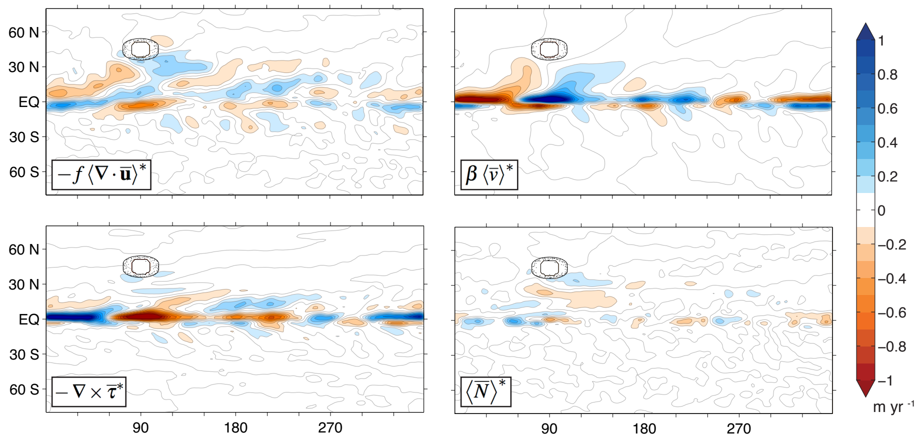

b Equatorial heating

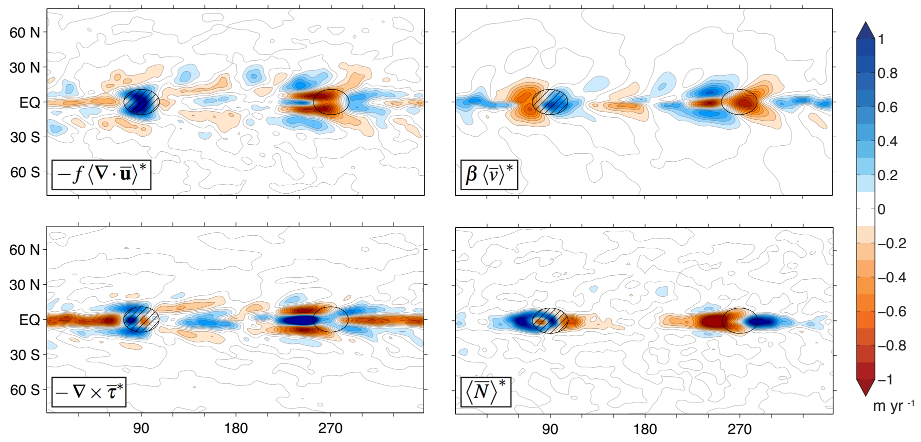

Figure 3.6: Moisture-weighted lower-tropospheric vorticity budget terms in the reference climate ($\alpha = 1$) of (a) the Gaussian mountain experiment and (b) the equatorial heating experiment. All terms are multiplied by $[\overline{q}_{\mathrm{sfc}}]/f$ such that they show a contribution to $\overline{P}^* - \overline{E}^*$. The limits of integration, 850 hPa to $\overline{p}_s$, are dropped from figure labels. Note that $\langle\overline{N}\rangle^*$ is computed as a residual of the other terms.

order to understand how this horizontal flow is related to the stationary-eddy vertical motion that determines $\overline{P}^* - \overline{E}^*$, it is useful to analyze the zonally anomalous vorticity equation. We focus on the zonally anomalous vorticity budget below 850 hPa, which can be written

$$\left(\left\langle f\nabla\cdot\overline{\mathbf{u}} + \beta\overline{v} + \overline{N}\right\rangle_{850\text{ hPa}}^{\overline{p}_s}\right)^* = \nabla\times\overline{\tau}^*, \tag{3.13}$$

where f is the Coriolis frequency, $\beta = df/dy$, τ is the turbulent surface stress, and

$$N = \mathbf{v} \cdot \nabla\zeta + \zeta\nabla \cdot \mathbf{u} + (\nabla_x \cdot \omega)\, \partial_p v - (\nabla_y \cdot \omega)\, \partial_p u \tag{3.14}$$

is the sum of all nonlinear (relative vorticity) terms. This uses the fact that 850 hPa is above the Ekman layer throughout the range of climates.

The terms of the vorticity equation (3.13), weighted by $[\overline{q}_{\mathrm{sfc}}]/f$, are shown in Fig. 3.6, such that the plotted fields are in units of m yr^{-1}. In this way, each term is a contribution to $\overline{P}^* - \overline{E}^*$, as, for example,

$$-\left\langle [\overline{q}]\, \nabla \cdot \overline{\mathbf{u}} \right\rangle^* \approx -\frac{[\overline{q}_{\mathrm{sfc}}]}{f} \left(\langle f\nabla \cdot \overline{\mathbf{u}} \rangle_{850\text{ hPa}}^{\overline{p}_s} \right)^* . \tag{3.15}$$

Note that this differs from $-\left\langle \overline{q}\nabla_\rho \cdot \overline{\mathbf{u}} \right\rangle^*$ by an additional term

$$\begin{aligned} \left(\overline{P}^* - \overline{E}^*\right)_{\text{orographic}} &\equiv -\left\langle \overline{q}\nabla_\rho \cdot \overline{\mathbf{u}} \right\rangle^* + \left\langle \overline{q}\nabla \cdot \overline{\mathbf{u}} \right\rangle^* \\ &\approx -\left\langle [\overline{q}]\, \nabla_\rho \cdot \overline{\mathbf{u}} \right\rangle^* + \left\langle [\overline{q}]\, \nabla \cdot \overline{\mathbf{u}} \right\rangle^* , \end{aligned} \tag{3.16}$$

arising from the difference in density weighting between the moisture and vorticity budgets. It is equivalent to the surface term defined in WS15. It means that, in addition to the stationary-eddy vertical velocities based on the vorticity budget, there is a vertical velocity $\overline{\omega}^*_{\mathrm{sfc}} = (\overline{\mathbf{u}}_{\mathrm{sfc}} \cdot \nabla\overline{p}_s)^*$, which contributes to $\overline{P}^* - \overline{E}^*$ as surface moisture fluxes converge onto sloped surfaces[3];

$$\left(\overline{P}^* - \overline{E}^*\right)_{\text{orographic}} \approx -\frac{1}{g} \left(\overline{q}_{\mathrm{sfc}} \overline{\omega}^*_{\mathrm{sfc}}\right)^* . \tag{3.17}$$

This term is shown in Fig. 3.7 for the Gaussian mountain experiment.

The dominant vorticity balance determining vertical motion at 850 hPa is though the linear (planetary vorticity) terms and surface drag, a combination of Sverdrup balance and Ekman pumping;

$$-\left\langle f\nabla \cdot \overline{\mathbf{u}} \right\rangle^*_{850\text{ hPa}} \approx \langle \beta\overline{v} \rangle^*_{850\text{ hPa}} - \nabla \times \overline{\tau}^* . \tag{3.18}$$

---

[3] While it is a good approximation to use $[\overline{q}]$ in Eq. 3.16, $[\overline{q}_{\mathrm{sfc}}]$ should not be used in Eq. 3.17, because $\overline{q}_{\mathrm{sfc}}$ has large spatial gradients over topography due to the altitude of the mountain.

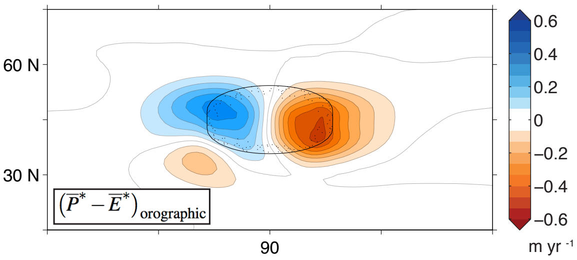

Figure 3.7: Orographic contribution to $\overline{P}^* - \overline{E}^*$ in the Gaussian mountain experiment, calculated here from $-\langle [\overline{q}]\, \nabla_\rho \cdot \overline{\mathbf{u}} \rangle^* + \langle [\overline{q}]\, \nabla \cdot \overline{\mathbf{u}} \rangle^*$. This term is already accounted for in the moisture budget approximation (3.12), but must be added to an approximation based on the vorticity budget (3.19).

The nonlinear terms do not play a large role in the orographic forcing experiments. The nonlinear terms are more important in the tropical heating experiments where they redistribute vorticity along the equator. This agrees well with an analysis of reanalysis data in WS15, where the nonlinear vorticity terms are seen to be mainly important for redistributing vorticity within the tropical Pacific.

The linear vorticity balance can be used to develop an approximation for $\overline{P}^* - \overline{E}^*$ that emphasizes the role of the horizontal flow in stationary eddies:

$$\overline{P}^* - \overline{E}^* = \frac{[\overline{q}_{\mathrm{sfc}}]}{f} \left(\langle \beta \overline{v} \rangle_{850 \text{ hPa}} - \nabla \times \overline{\tau} \right)^* - \frac{1}{g} \left(\overline{q}_{\mathrm{sfc}} \overline{\omega}^*_{\mathrm{sfc}} \right)^* . \qquad (3.19)$$

This is shown for the reference simulations in Fig. 3.4. This approximation results in the interpretation that regions of low-level poleward or cyclonic flow are wetter than the zonal mean, while regions of low-level equatorward or anti-cyclonic flow are drier than the zonal mean. The individual components of this approximation, shown in Fig. 3.6, can be thought of separately as the contributions of meridional motion and surface drag to $\overline{P}^* - \overline{E}^*$. The orographic $\overline{\omega}_{\mathrm{sfc}}$ term (Fig. 3.7) is only important over large gradients of surface pressure, as exist immediately over topography.

3.4 Moisture budget changes

The approximations for $\overline{P}^* - \overline{E}^*$ developed in Section 3 and shown in Fig. 3.4 can be used to understand the response of $\overline{P}^* - \overline{E}^*$ to climate change.

a Gaussian mountain

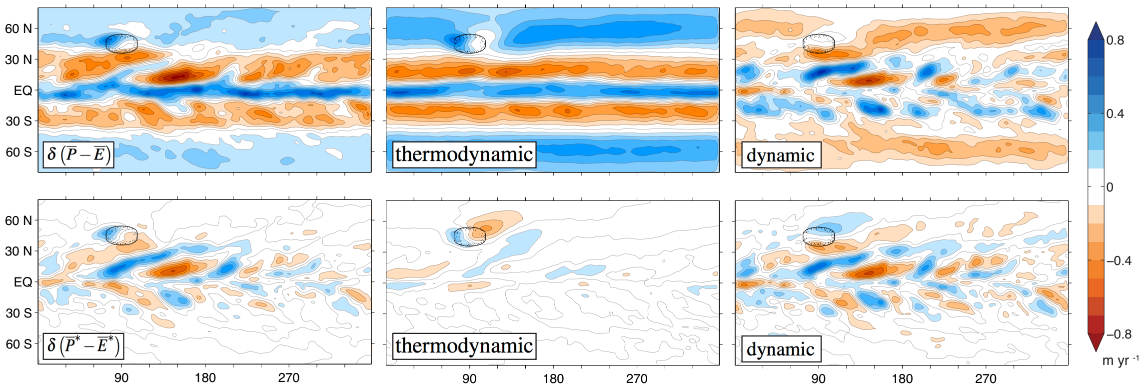

b Equatorial heating

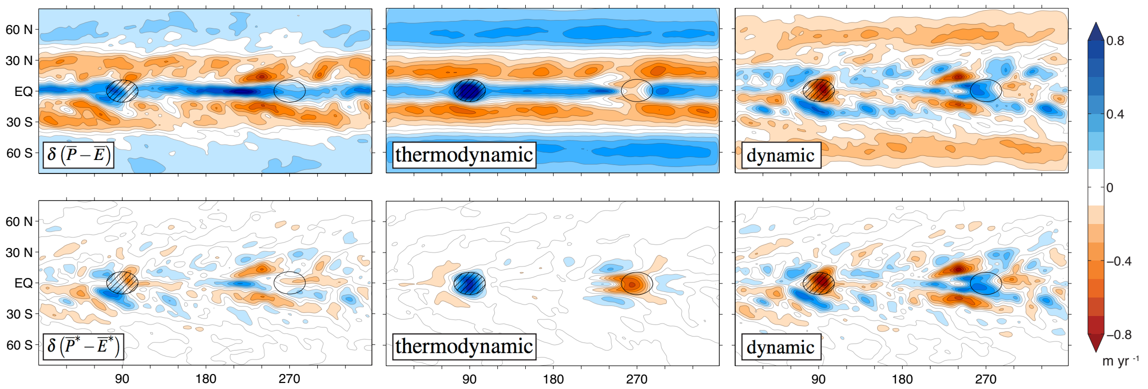

Figure 3.8: Change in total $\overline{P}-\overline{E}$, $\delta\left(\overline{P}-\overline{E}\right)$, and in $\overline{P}^*-\overline{E}^*$, $\delta\left(\overline{P}^*-\overline{E}^*\right)$, from the reference climate ($\alpha = 1$) to the climate with 1.4 times the optical depth ($\alpha = 1.4$), corresponding to a 4.7 K increase in global-mean surface temperature. (a) Gaussian mountain experiment. (b) Equatorial heating experiment. The changes are split into a thermodynamic component, based on the fractional change of surface specific humidity, and a residual, showing all other types of change.

3.4.1 Thermodynamic and dynamic changes

First, we would like to discuss some basic expectations of how $\overline{P}-\overline{E}$ and, in particular, its stationary-eddy component $\overline{P}^*-\overline{E}^*$ would respond to climate change. In the absence of changes in atmospheric circulations or the spatial structure of specific humidity, $\overline{P}-\overline{E}$ would change thermodynamically (cf. Held and Soden, 2006),

$$\delta\left(\overline{P}-\overline{E}\right)_{\text{thermo}} \approx \frac{\delta\overline{q}_{\text{sfc}}}{(\overline{q}_{\text{sfc}})_0}\left(\overline{P}_0-\overline{E}_0\right), \tag{3.20}$$

a Gaussian mountain

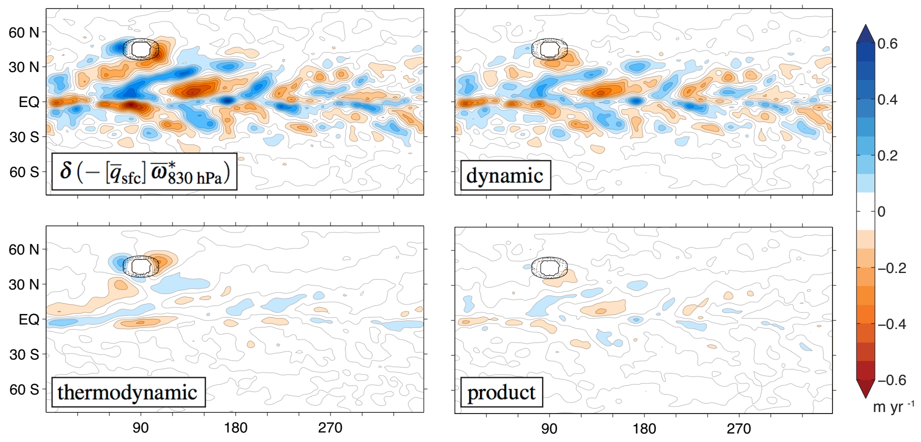

b Equatorial heating

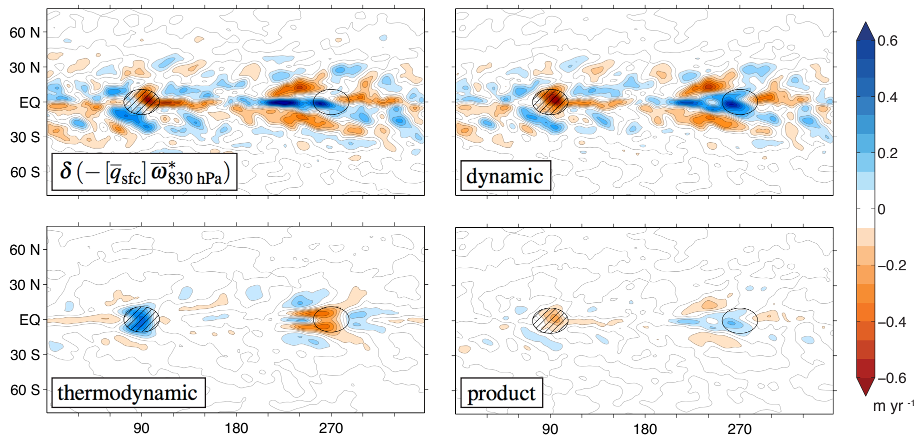

Figure 3.9: Change in the scaling for $\overline{P}^* - \overline{E}^*$, $\delta\,(-[\overline{q}_{\rm sfc}]\,\omega^*_{850})$, from the reference climate ($\alpha = 1$) to the climate with 1.4 times the optical depth ($\alpha = 1.4$). (a) Gaussian mountain experiment. (b) Equatorial heating experiment. The changes are split into a thermodynamic component, based on changes in $[\overline{q}_{\rm sfc}]$, a dynamic component, based on changes in $\overline{\omega}^*_{850}$, and a product of these changes.

where δ is the change of a quantity from one simulation to another, $\delta\phi = \phi_1 - \phi_0$. This would mean that wet zones get wetter and dry zones get drier, with a rate determined by the Clausius-Clapeyron (C-C) relation, up to possible changes in near-surface relative humidity, which are generally small (Held and Soden, 2000, 2006; Schneider et al., 2010). This is qualitatively a good approximation for $\delta\left(\overline{P} - \overline{E}\right)$ in the zonal mean and ocean-basin zonal mean (Held and Soden, 2006; Byrne and O'Gorman, 2015). Byrne and O'Gorman (2015) show how moisture gradient changes can affect $\delta\left(\overline{P} - \overline{E}\right)$ in a purely thermodynamic way, especially over land. We will show how changes in atmospheric circulations affect $\delta\left(\overline{P} - \overline{E}\right)$ and limit the utility of this simple thermodynamic relationship.

While this *wet gets wetter, dry gets drier* scaling is often quoted in reference to regional $\overline{P} - \overline{E}$ changes, there has been little analysis of the extent to which this actually applies. Several studies have even shown that, because of the lack of angular momentum constraints on zonal circulations, any weakening of the hydrological cycle required by energetic contraints may preferentially be taken up by zonal anomalies (Held and Soden, 2006; Vecchi et al., 2006; Vecchi and Soden, 2007; Schneider et al., 2010; Merlis and Schneider, 2011). We might therefore expect that the *wet gets wetter, dry gets drier* scaling does not apply well for anomalies from the zonal mean due to changes in stationary-eddy circulations.

A comparison of $\delta\left(\overline{P} - \overline{E}\right)$ and $\delta\left(\overline{P} - \overline{E}\right)_{\text{thermo}}$ is shown in Fig. 3.8 for changes between the reference simulation ($\alpha = 1$) and a 40% increase in optical depth ($\alpha = 1.4$). The simple thermodynamic scaling captures the sign of changes in most places but generally overestimates those changes. The residual "dynamic" change, $\delta\left(\overline{P} - \overline{E}\right)_{\text{dyn}} = \delta\left(\overline{P} - \overline{E}\right) - \delta\left(\overline{P} - \overline{E}\right)_{\text{thermo}}$, shows a slowdown of the hydrological cycle, especially in the storm tracks. The conclusions are qualitatively similar for 10% and 20% increases in optical depth or for a 10% decrease in optical depth.

The stationary-eddy components of these changes are shown below the full fields in Fig. 3.8. The thermodynamic component of the stationary-eddy change,

$$\delta\left(\overline{P}^{*} - \overline{E}^{*}\right)_{\text{thermo}} \approx \frac{\delta\left[\overline{q}_{\text{sfc}}\right]}{\left[\overline{q}_{\text{sfc}}\right]_0}\left(\overline{P}_0^{*} - \overline{E}_0^{*}\right), \tag{3.21}$$

is much smaller than the simulated changes and does not generally capture the sign of changes[4]. This suggests that because stationary-eddy circulations are freer to change in magnitude and location in response to climate change than zonal-mean circulations, the *wet gets wetter, dry gets drier* paradigm is not useful for anomalies from the zonal mean. While there are several other ways in which one can split up $P - E$ changes into thermodynamic and dynamic components (Wu et al., 2011; Seager et al., 2010; Bony et al., 2013; Byrne and O'Gorman, 2015), none of them change this conclusion:

---

[4] An alternative definition, which includes changes in zonally anomalous moisture, $\delta\left(\overline{P}^{*} - \overline{E}^{*}\right)_{\text{thermo}} \approx \left(\frac{\delta\overline{q}_{\text{sfc}}}{\overline{q}_{\text{sfc}\,0}}\left(\overline{P}_0 - \overline{E}_0\right)\right)^{*}$, differs by less than 0.1 m yr^{-1} in all regions. We maintain the $\left[\overline{q}_{\text{sfc}}\right]$ definition for the simplicity of its interpretation.

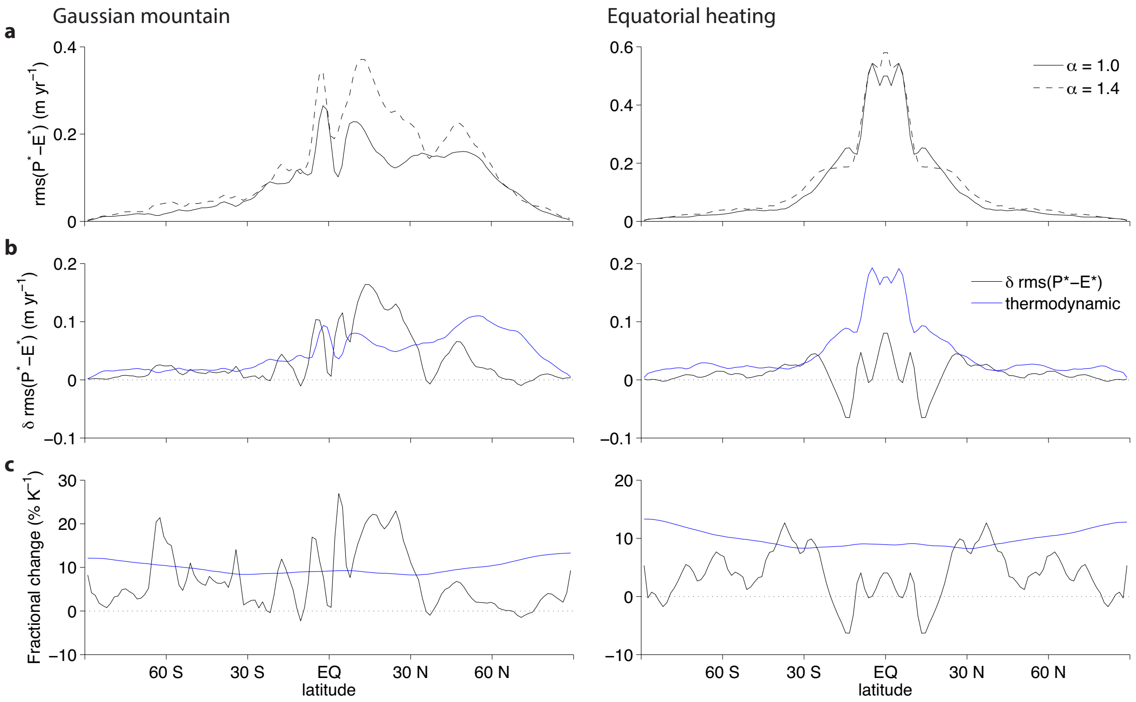

Figure 3.10: (a) Climatology of $\mathrm{rms}\left(\overline{P}^{*}-\overline{E}^{*}\right)$ in the simulations with $\alpha = 1.0$ (solid) and $\alpha = 1.4$ (dashed). (b) Change in $\mathrm{rms}\left(\overline{P}^{*}-\overline{E}^{*}\right)$ with global warming between $\alpha = 1.0$ and $\alpha = 1.4$ and its thermodynamic component (rms applied to Eq. 3.21, blue line). (c) Fractional change in $\mathrm{rms}\left(\overline{P}^{*}-\overline{E}^{*}\right)$ per degree of zonal-mean warming and its thermodynamic component ($\delta\,[\overline{q}_{\mathrm{sfc}}]\,/\,[\overline{q}_{\mathrm{sfc}}]$, blue line). Each plot is shown for (left) the Gaussian mountain experiment and (right) the equatorial heating experiment. Note that values have been symmetrized about the equator for the equatorial heating experiment.

changes in stationary-eddy circulations are of first order importance for $\delta\left(\overline{P}^{*}-\overline{E}^{*}\right)$.

Stationary-eddy changes in the Gaussian mountain experiment take the form of a phase shift of the equatorward Rossby wave train, as can be seen from the different phasing of subtropical wet and dry zones between $\delta\left(\overline{P}^{*}-\overline{E}^{*}\right)_{\mathrm{thermo}}$ and $\delta\left(\overline{P}^{*}-\overline{E}^{*}\right)$ in Fig. 3.8. This results from differences in the meridional group propagation of stationary Rossby waves in a climate with a different zonal-mean circulation. In the equatorial heating experiment, it can be seen from Fig. 3.8 that $\delta\left(\overline{P}^{*}-\overline{E}^{*}\right)_{\mathrm{thermo}}$ is opposite in sign to $\delta\left(\overline{P}^{*}-\overline{E}^{*}\right)$ in most locations. The dynamic change gives evidence of shifting locations of ascent and descent, as well as a general weakening of the tropical overturning. The change in strength of overturning will become clearer as we examine the zonal variance of $\overline{P}^{*}-\overline{E}^{*}$ in Section 3.4.2.

The conclusion about the importance of changes in circulation is further strengthened by looking at the change in the stationary-eddy vertical velocity and its effect on $\overline{P}^* - \overline{E}^*$ according to the approximation (3.12) (Fig. 3.9). The change in vertical velocity $\overline{\omega}^*$ explains most of the change in $\overline{P}^* - \overline{E}^*$ (compare Figs. 3.8 and 3.9). The $\overline{P}^* - \overline{E}^*$ approximation can be exactly split into thermodynamic and dynamic components as

$$\begin{aligned} \delta\left(\overline{P}^* - \overline{E}^*\right) \approx & - [\overline{q}_{\mathrm{sfc}}]_0 \, \delta\overline{\omega}^*_{850\ \mathrm{hPa}} && \text{(dynamic)} \\ & - \delta\, [\overline{q}_{\mathrm{sfc}}] \, (\overline{\omega}^*_{850\ \mathrm{hPa}})_0 && \text{(thermodynamic)} \\ & - \delta\, [\overline{q}_{\mathrm{sfc}}] \, \delta\overline{\omega}^*_{850\ \mathrm{hPa}} && \text{(product),} \end{aligned} \tag{3.22}$$

which are shown in Fig. 3.9. In most regions, the dynamic change leads to a larger change in $\overline{P}^* - \overline{E}^*$ than the thermodynamic change. This is surprising since the dynamic change is not directly related to the increase in atmospheric moisture content, which is large due to the C-C relation (~35% in the tropics for the increase in global-mean surface temperature of 5.7 K shown in Fig. 3.9). Not only is the thermodynamic change smaller, but it is mostly out of phase with the full change. The product of changes in moisture and vertical motion ($-\delta\, [\overline{q}_{\mathrm{sfc}}] \, \delta\overline{\omega}^*_{850\ \mathrm{hPa}}$) looks like the dynamic change, but is approximately 3 times smaller. It is accounting for the interactions of the ~35% change in specific humidity with the modified stationary-eddy circulations.

3.4.2 Changes in zonal variance of net precipitation

Since the geometry of these experiments is idealized and no region in the model corresponds exactly to a region in the real world, it is helpful to analyze the variance of $\overline{P}^* - \overline{E}^*$ averaged over a larger region, such as a latitude band. In other words, while the particular change of stationary-wave phase structure in these experiments would be difficult to generalize to the real world, the change in strength of stationary-eddy circulations may be more general. Therefore, we analyze the root zonal-mean square $\overline{P}^* - \overline{E}^*$, which we denote by $\mathrm{rms}\left(\overline{P}^* - \overline{E}^*\right)$ based on the definition

$$\mathrm{rms}\,(\cdot) \equiv \sqrt{\left[(\cdot)^2\right]}. \tag{3.23}$$

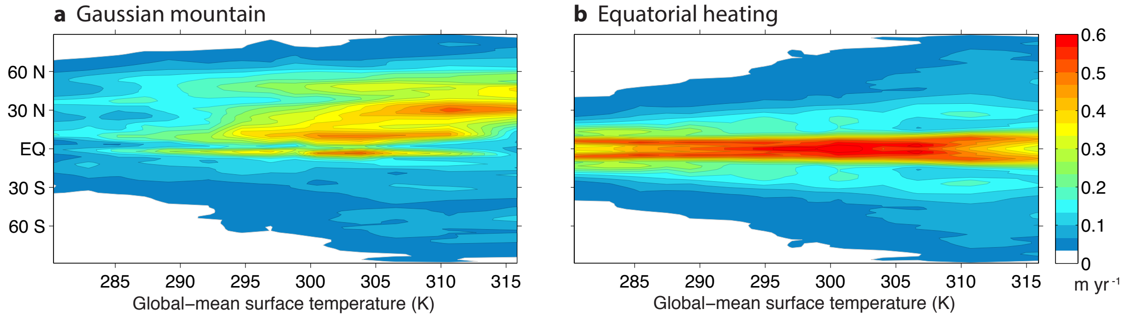

Figure 3.11: Spatial standard deviation $\mathrm{rms}\left(\overline{P}^{*}-\overline{E}^{*}\right)$ versus latitude and global-mean surface temperature across the range of climates for (a) the Gaussian mountain experiment and (b) the equatorial heating experiment. Note that values have been symmetrized about the equator for the equatorial heating experiment.

Figure 3.10 shows the climatology of $\mathrm{rms}\left(\overline{P}^{*}-\overline{E}^{*}\right)$ in the reference climate of both simulations as well as the change in response to a 40% increase in optical depth.

Again, if these changes were purely thermodynamic, we would expect a fairly uniform percentage increase for all latitude bands following the percentage increase in surface specific humidity, $\delta\left[\overline{q}_{\mathrm{sfc}}\right]/\left[\overline{q}_{\mathrm{sfc}}\right]$, which is shown as a blue line in Fig. 3.10c. Note that $\delta\left[\overline{q}_{\mathrm{sfc}}\right]/\left[\overline{q}_{\mathrm{sfc}}\right]$ is larger than 7%/K because the temperature difference between these climates is large enough such that the linear approximation to C-C does not hold. Relative humidity changes are small, consistent with the arguments of Held and Soden (2000). Latitudinal variations of $\delta\left[\overline{q}_{\mathrm{sfc}}\right]/\left[\overline{q}_{\mathrm{sfc}}\right]$ also arise primarily from the nonlinearity of the C-C relation.

The fractional change of $\mathrm{rms}\left(\overline{P}^{*}-\overline{E}^{*}\right)$ is not far from the thermodynamic expectation for the southern hemisphere of the simulations forced by northern-hemisphere orography, though the absolute magnitude of $\mathrm{rms}\left(\overline{P}^{*}-\overline{E}^{*}\right)$ is small because the southern hemisphere's surface is zonally symmetric. Closer to the mountain, where zonal variations are larger, the response is more complex, with some regions near the mountain where the zonal variance of the hydrological cycle increases much less than the thermodynamic expectation (blue line in Fig 3.10b and c) and regions in the northern hemisphere subtropics where it increases much more than the thermodynamic expectation. While the response of $\mathrm{rms}\left(\overline{P}^{*}-\overline{E}^{*}\right)$ far from the mountain is close to thermodynamic, there appear to be large dynamic changes in the entire hemisphere of forcing.

The situation for the equatorial heating experiment is similar: changes in $\mathrm{rms}\left(\overline{P}^{*}-\overline{E}^{*}\right)$ within 30° latitude of the forcing, where $\mathrm{rms}\left(\overline{P}^{*}-\overline{E}^{*}\right)$ is largest, have a complex spatial structure that must be influenced by changes in the strength of stationary-eddy circulations. Beyond 30° latitude, the fractional change is closer to the fractional change in surface specific humidity governed by C-C. The most interesting feature is that $\mathrm{rms}\left(\overline{P}^{*}-\overline{E}^{*}\right)$ actually decreases in the subtropics, meaning that even for a bulk quantity like $\mathrm{rms}\left(\overline{P}^{*}-\overline{E}^{*}\right)$, dynamic changes can be strong enough to reverse the tendency toward *wet gets wetter, dry gets drier.*

The complexity of $\mathrm{rms}\left(\overline{P}^{*}-\overline{E}^{*}\right)$ continues throughout the range of climates as shown in Fig. 3.11, which would change exponentially from left to right if it were not for dynamic changes. This is a useful framework to examine how the zonally anomalous hydrological cycle varies across the full range of climates. Averaging $\mathrm{rms}\left(\overline{P}^{*}-\overline{E}^{*}\right)$ over a few latitude bands is a convenient way to reduce the dimensionality of $\overline{P}^{*}-\overline{E}^{*}$ and examine its response to warming across a wide range of climates, (Fig. 3.12).

The change in $\mathrm{rms}\left(\overline{P}^{*}-\overline{E}^{*}\right)$ in each latitude band can be compared to the change in surface specific humidity (Fig. 3.12, blue lines), which approximately follows the C-C relation. The $\mathrm{rms}\left(\overline{P}^{*}-\overline{E}^{*}\right)$ equatorward of the topographic forcing, between 10°N and 30°N (Fig. 3.12b), exceeds the C-C surface specific humidity line in climates warmer than the reference simulation (289 K global-mean surface temperature), then returns to the C-C line before decreasing in climates warmer than 304 K global-mean surface temperature. The climate becomes more zonal for these very warm climates, leading to the opposite response of zonal variance of $P-E$ from what would be expected under *wet gets wetter, dry gets drier.* The change is similar for $\mathrm{rms}\left(\overline{P}^{*}-\overline{E}^{*}\right)$ in the deep tropics of this experiment ($2^\circ < |\phi| < 10^\circ$): it stays close to the C-C line before decreasing rapidly in very warm climates (Fig. 3.12c). The $\mathrm{rms}\left(\overline{P}^{*}-\overline{E}^{*}\right)$ in the southern hemisphere subtropics (30°S-10°S, Fig. 3.12d), resulting from tunneling of Rossby waves across the equator, and in the midlatitudes in the vicinity of topography (30°-60°N, Fig. 3.12a), are dynamically limited and do not increase as rapidly as predicted from C-C.

The $\mathrm{rms}\left(\overline{P}^{*}-\overline{E}^{*}\right)$ in the deep tropics of the equatorial heating experiment increases much

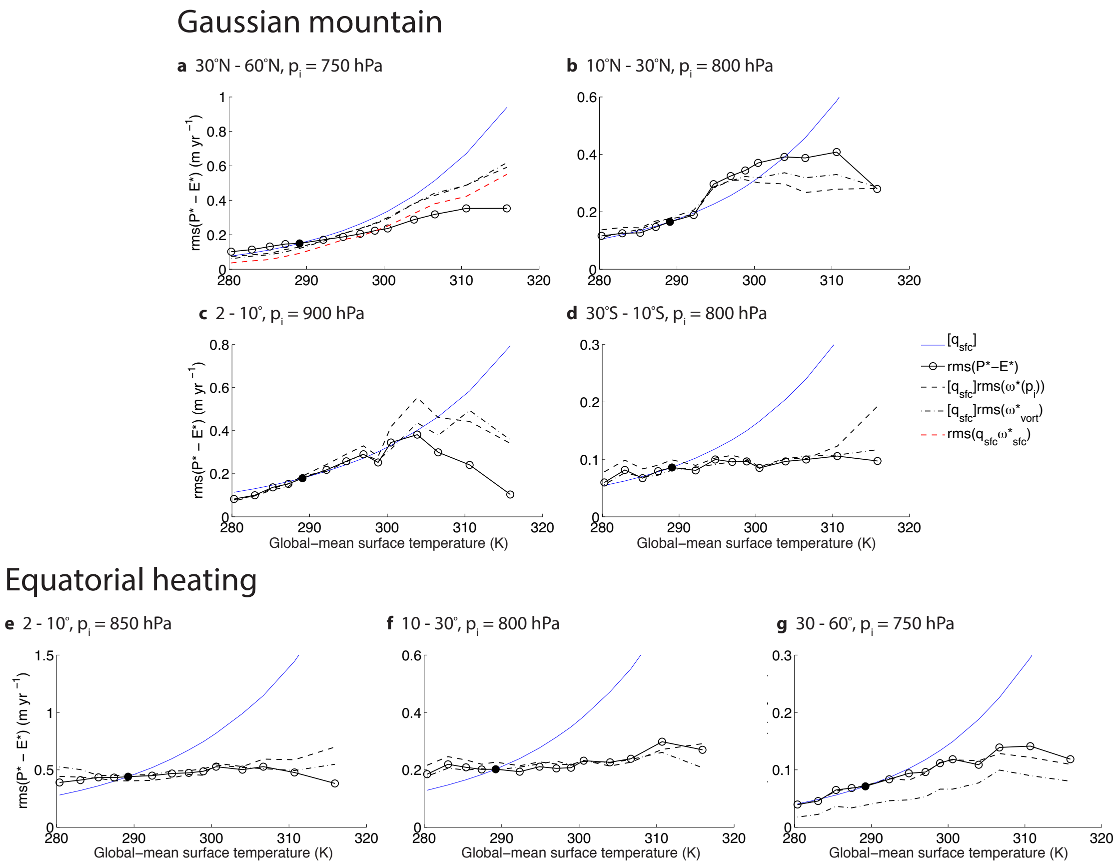

Figure 3.12: Spatial standard deviation $\mathrm{rms}\left(\overline{P}^* - \overline{E}^*\right)$ within a latitude band (solid line with circles) and scalings for the spatial standard deviation based on the flow divergence below p_i (dashed line), on the linear vorticity balance below p_i (dash-dotted line), and on $\overline{\omega}^*_{\mathrm{sfc}}$ over topography (red dashed line). The approximately exponential change in spatial standard deviation of $\overline{P}^* - \overline{E}^*$ expected from a purely thermodynamic change of surface specific humidity is shown as a blue line. (a)-(d) Averages over different latitude bands of the Gaussian mountain experiment. (e)-(g) Averages over different latitude bands of the equatorial heating experiment. The pressure p_i (shown above each subpanel) is chosen for each latitude band separately as described in the text.

more slowly than expected from C-C (Fig. 3.12e). This results from a slowdown of the Walker circulation, which helps to satisfy global energetic constraints on the total upward mass transport of the atmosphere (Betts, 1998; Held and Soden, 2006; Vecchi and Soden, 2007; Schneider et al., 2010). This slowdown of the Walker circulation is reflected in the $\mathrm{rms}\left(\overline{P}^* - \overline{E}^*\right)$ up to at least 30° latitude (Fig. 3.12f). In the extratropics (30°-60°, Fig. 3.12g), $\mathrm{rms}\left(\overline{P}^* - \overline{E}^*\right)$ increases somewhat slower than surface specific humidity, as seen in Fig. 3.10, and stops increasing beyond about 300 K global-mean surface temperature. The dynamic limitation in the midlatitudes of this experiment shows that the slowdown of the Walker circulation can also lead to a slowdown of stationary-eddy

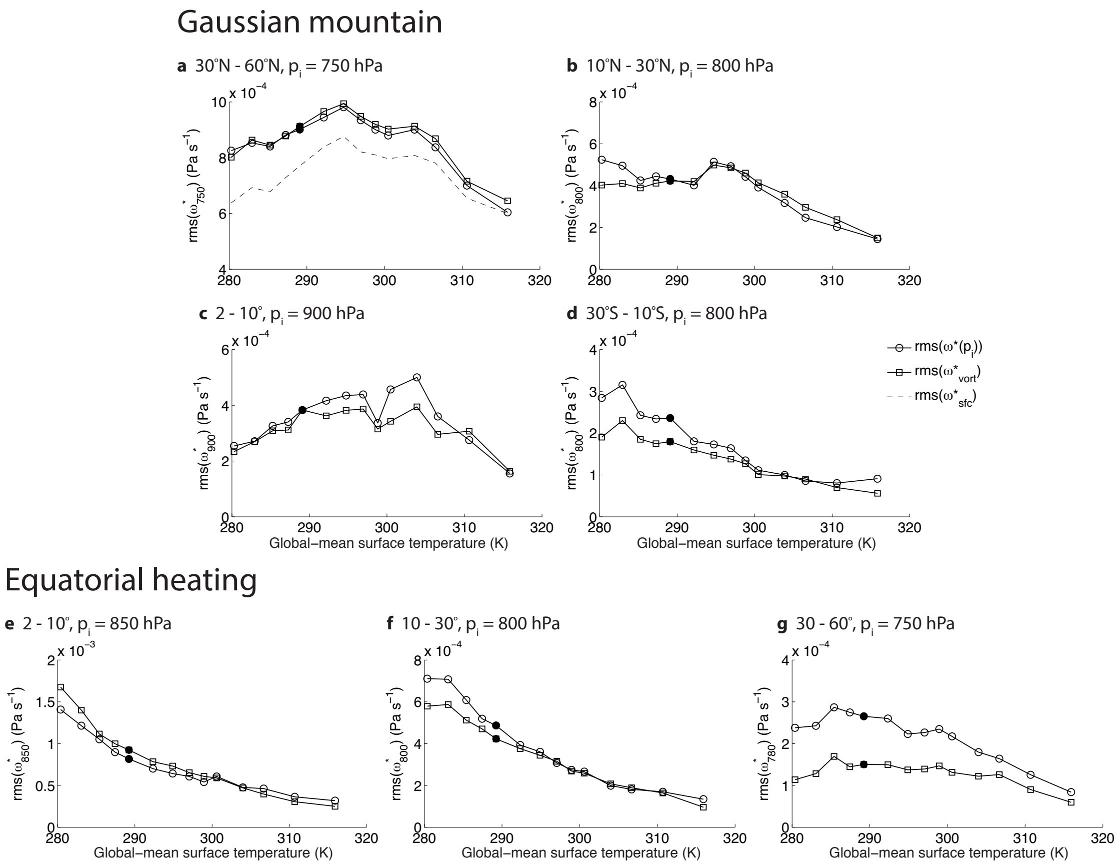

Figure 3.13: Decomposition of the terms that make up the scalings of Fig. 3.12. $[\overline{q}_{\mathrm{sfc}}]$, $\mathrm{rms}\big(\overline{\omega}^*_{p_i}\big)$, and the estimate of $\mathrm{rms}\big(\overline{\omega}^*_{p_i}\big)$ based on $\langle \beta \overline{v}\rangle^* - \nabla \times \tau^* - f\overline{\omega}^*_{\mathrm{sfc}}$ (squares) are shown for (a) 30°N–60°N, (b) 10°N–30°N, (c) ±2–10°, and (d) 30°S–10°S in the Gaussian mountain experiment and (e) ±2–10°, (f) ±10–30°, and (g) ±30–60° in the equatorial heating experiment. Also shown in (a) is $\mathrm{rms}(\overline{\omega}^*_{\mathrm{sfc}})$ (dashed line), which determines the vertical velocity variance over topography. The pressure p_i is the same as in the corresponding experiment and latitude band in Fig. 3.12.

circulations in midlatitudes, through the influence of the Walker circulation on the generation of Rossby waves that propagate into midlatitudes. Some portion of this signal could also be a local response to increased static stability.

Changes in $\mathrm{rms}\Big(\overline{P}^* - \overline{E}^*\Big)$ are well described by changes in rms of the $\overline{P}^* - \overline{E}^*$ approximation (Eq. 3.12):

$$\mathrm{rms}\left(\overline{P}^* - \overline{E}^*\right) \approx \frac{1}{g}\,[\overline{q}_{\mathrm{sfc}}]\,\mathrm{rms}\left(\overline{\omega}^*_{p_i}\right). \tag{3.24}$$

This scaling is shown as dashed lines in Fig. 3.12. We choose p_i seperately for each latitude band to minimize the difference between $g^{-1}\,[\overline{q}_{\mathrm{sfc}}]\mathrm{rms}\big(\overline{\omega}^*_{p_i}\big)$ and $\mathrm{rms}\langle[\overline{q}]\,\nabla\cdot\overline{\mathbf{u}}^*\rangle$, roughly following the zonal-mean p_i shown in Fig. 3.5. It is only marginally more successful to use a p_i that varies with climate, so we keep p_i fixed for simplicity. The main influence of changes in p_i is on the subtropics of the orographic forcing experiment, where almost all differences between the $\overline{P}^* - \overline{E}^*$ variance and the approximation based on $\overline{\omega}^*_{p_i}$ variance are due to the assumption of fixed p_i as p_i, the representative height for condensation in vertical motion, moves upward with warming.

Because the zonal-mean surface specific humidity is not a representative value of specific humidity directly over topography (the height of topography is comparable to the water vapor scale height), this scaling is modified over topography to use the full surface specific humidity;

$$\mathrm{rms}\left(\overline{P}^* - \overline{E}^*\right) \approx \frac{1}{g}\mathrm{rms}\left(\overline{q}_{\mathrm{sfc}}\overline{\omega}^*_{p_i}\right), \tag{3.25}$$

shown as a dashed line in Fig. 3.12a. This modification makes a noticeable difference here, but could probably be avoided for topography which does not extend above 850 hPa or have such a large zonal scale. The difference between $\mathrm{rms}\left(\overline{q}_{\mathrm{sfc}}\overline{\omega}^*_{\mathrm{sfc}}\right)$ and $\mathrm{rms}\left(\overline{P}^* - \overline{E}^*\right)$ in midlatitudes shows that transient eddies increase $\overline{P}^* - \overline{E}^*$ variance in cold climates (i.e. through creation of a storm track) and decrease variance in warm climates (through down-gradient moisture fluxes).

A scaling for $\mathrm{rms}\left(\overline{P}^* - \overline{E}^*\right)$ based on the linear vorticity balance (Eq. 3.19),

$$\mathrm{rms}\left(\overline{P}^* - \overline{E}^*\right) \sim \frac{[\overline{q}_{\mathrm{sfc}}]}{f}\mathrm{rms}\left(\langle\beta\overline{v}\rangle^*_{p_i} + \nabla\times\overline{\tau}^*\right), \tag{3.26}$$

is shown as dash-dotted lines in Fig. 3.12. Again, we must modify the scaling in the vicinity of large topography,

$$\mathrm{rms}\left(\overline{P}^* - \overline{E}^*\right) \sim \frac{1}{f}\mathrm{rms}\left[\overline{q}_{\mathrm{sfc}}\left(\langle\beta\overline{v}\rangle^*_{p_i} + \nabla\times\overline{\tau}^* - \frac{f}{g}\overline{\omega}^*_{\mathrm{sfc}}\right)\right]. \tag{3.27}$$

It is also successful at all latitudes, especially in the subtropics, where nonlinear vorticity tendencies are small[5]. It is surprising that these scalings are successful for the midlatitudes of the orographic forcing experiment, where transient-eddy moisture tendencies are most significant. This success

---

[5] The nearest grid point to the equator in each hemisphere is excluded from this analysis because it causes problems with the vorticity-budget scaling due to strong nonlinear vorticity tendencies (cf. Fig 3.6).

comes from the orographic vertical velocity term [rms $(\overline{q}_{\mathrm{sfc}}\overline{\omega}^*_{\mathrm{sfc}})$, red line in Fig. 3.12a], which explains a large portion of the variance.

The dynamic components of the precipitation variance scalings (3.24) and (3.26, 3.27) are shown in Fig. 3.13. In the orographic forcing experiment, stationary-eddy vertical motion changes non-monotonically, with a slight increase in variance with warming through the colder climates and a strong decrease in variance in the warmest climates (Fig. 3.13a, b, c). This reflects the $\overline{\omega}^*_{\mathrm{sfc}}$ variance (dashed line, Fig. 3.13a), which is responsible for forcing the topographic stationary wave through adiabatic heating and cooling on the topographic slope. The vertical-motion variance in the southern hemisphere subtropics (Fig. 3.13d) behaves differently, decreasing with warming throughout the range of climates. The stationary-eddy vertical-motion changes in the equatorial heating experiment primarily show the weakening of the Walker circulation that has been pointed out as a robust response to global warming (Held and Soden, 2006; Vecchi et al., 2006; Vecchi and Soden, 2007).

The key unanswered questions in understanding how the zonally anomalous hydrological cycle responds to global warming lie in understanding the stationary-eddy vertical-motion response. The response can mostly be understood from the perspective of a combined Sverdrup and Ekman balance (Eq. 3.26; squared lines in Fig. 3.13), relating the vertical motion to the lower-tropospheric meridional motion, surface wind-stress curl, and surface vertical velocity. The question of how rms $\left(\overline{\omega}^*_{p_i}\right)$ responds to climate change is thus also a question of how the lower-level horizontal flow in stationary eddies responds to climate change. We will discuss some of the dynamical questions raised by these experiments in the next chapter.

3.5 Conclusions

Based on moist idealized GCM simulations with zonally varying boundary conditions, we can draw several conclusions about how stationary eddies and zonal variations in the hydrological cycle respond to climate change:

1. Changes in $\overline{P}^* - \overline{E}^*$ are primarily determined by changes in lower-tropospheric stationary-eddy

vertical motion.

2. Shifts in stationary-eddy circulations are large such that *wet gets wetter, dry gets drier* ideas do not apply locally.

3. The zonal-mean spatial variance of $\overline{P}^* - \overline{E}^*$ increases with climate change at a rate near that determined by the Clausius-Clapeyron equation for climates with near-modern surface temperatures when stationary eddies are forced by midlatitude topography.

4. Topographic forcing has a decreased influence on zonal variation of the hydrological cycle for temperatures greater than 305 K in these simulations.

5. The zonal-mean spatial variance of $\overline{P}^* - \overline{E}^*$ hardly changes with climate change when stationary eddies are forced by equatorial heating, implying a strong weakening of the Walker circulation and other stationary-eddy circulations resulting from this forcing.

The zonal-mean spatial variance of $\overline{P}^* - \overline{E}^*$ in the real world will be some combination of changes forced by equatorial heating, topography, as well as other sources such as subtropical heating (Levine and Boos, 2016) and land-sea thermal contrast (Shaw, 2014). It remains an open problem to understand how the zonally asymmetric hydrological cycle in the real world responds to climate change in the presence of all of these different forcings.

3.6 Connection to Part II

The moisture budget decomposition of this chapter allows the change in $\overline{P}^* - \overline{E}^*$ in these two idealized model experiments to be understood in terms of simple thermodynamic changes and changes in lower-tropospheric stationary-eddy vertical motion ($\overline{\omega}^*_{850}$). It is thus important to understand why $\overline{\omega}^*_{850}$ changes as it does with climate change. The lower-level vorticity balance implies that most changes in $\overline{\omega}^*_{850}$ are due to changes in lower-tropospheric stationary-eddy horizontal motion. We thus discuss changes in the lower-tropospheric manifestation of stationary eddies in these experiments in Part II (Chapters 5 and 6).

Several studies have focused on how barotropic stationary eddies respond to climate change using realistic forcing (Stephenson and Held, 1993; Brandefelt and Körnich, 2008; Simpson et al., 2014, 2015). These studies have found robust shifts in stationary-eddy circulations in certain models, but there has been little discussion of the amplitude of stationary waves or the associated vertical velocities. Simulations with linear stationary-wave models or comprehensive climate model simulations with simplified forcing have been used to separate the roles of different forcing mechanisms in the modern stationary wave climatology (Nigam et al., 1986, 1988; Valdes and Hoskins, 1989; Ting, 1994; Held et al., 2002) and in the response of stationary waves to global warming (Stephenson and Held, 1993; Joseph et al., 2004). These studies have given a rough picture of which stationary high- and low-pressure systems result from which forcings and how the stationary wave field changes in response to changes in these forcings or to global climate change. However, stationary-wave models specify zonally anomalous heating and transient-eddy heat and momentum fluxes, all of which are part of the stationary-wave response. The zonally anomalous heating, for example, could respond very differently to climate change when stationary waves are forced by topography or equatorial heating. By using these GCM experiments with simplified geometry, we hope to gain insight into what determines changes in these nonlinear terms as well.

The advantage of the idealized model experiments here is that we can separately analyze the Rossby wave response associated with topographic forcing and equatorial heating. We have already seen how these two types of forcing give different circulation responses to climate change in Fig. 3.13. We would like to understand which changes in the idealized climate with orographic forcing lead to an increase and then decrease with warming of $\mathrm{rms}\left(\overline{\omega}^*_{p_i}\right)$ and which changes in the idealized climate with a Walker circulation lead to a decreasing $\mathrm{rms}\left(\overline{\omega}^*_{p_i}\right)$ throughout the range of climates. Part II will lay out the very different mechanisms governing these changes.

Chapter 4

The amplitude of the zonally anomalous hydrological cycle in CMIP5

This chapter is a draft in preparation with coauthors Michael Byrne and Tapio Schneider.

Abstract

The *wet gets wetter, dry gets drier* paradigm is a useful starting point for understanding zonal-mean changes in precipitation minus evaporation ($P - E$). It can explain the expected moistening of the high latitudes and drying of the subtropics in response to global warming. We examine $P - E$ changes over the next century in comprehensive climate models from the Coupled Model Intercomparison Project Phase 5 (CMIP5). We show that *wet gets wetter, dry gets drier* can not be extended to apply to regional variations about the zonal mean, which account for the majority of the spatial variability of $P - E$ in the modern climate. Wet and dry zones shift substantially in response to shifts in the stationary-eddy circulations that cause them. The largest changes are in the tropical oceans where wet zones get drier and dry zones get wetter in response to a restructuring and decrease in strength of tropical circulations such as the Walker circulation. Further progress can be made by examining changes in the zonal variance of $P - E$. The zonal variance of $P - E$ increases robustly at all latitudes in the Representative Concentration Pathways RCP8.5 scenario, but with a smaller fractional increase than the moisture content of the atmosphere. The variance

change can be split into dynamic and thermodynamic components by relating it to changes in surface specific humidity, stationary-eddy divergent circulations, and transient-eddy fluxes. The modeled sub Clausius-Clapeyron change of zonal $P - E$ variance gives evidence of a decrease in stationary-eddy overturning and in zonally anomalous transient-eddy moisture flux convergence with global warming.

4.1 Introduction

The availability of water will be a crucial issue for society during the next century. This depends on the spatiotemporal variability of net precipitation (precipitation minus evaporation, $P - E$). In the absence of changes in atmospheric circulations, the change of $P - E$ with warming can simply be related to the change in moisture content of the atmosphere (Mitchell et al., 1987; Chou and Neelin, 2004; Held and Soden, 2006). Due to energetic constraints on near-surface relative humidity (Held and Soden, 2000, 2006; Schneider et al., 2010), the moisture content of the atmosphere, which is concentrated near the surface, increases substantially with warming approximately following the Clausius-Clapeyron relation. This provides a simple framework for predicting qualitative changes in $P - E$ with warming; wet regions will get wetter and dry regions will get drier, simply because the same circulations transport more moisture. This framework works best for large spatial averages, because circulations shifts such as the expansion of the Hadley cell lead to local departures from this thermodynamic *wet gets wetter* mechanism (Chou and Neelin, 2004; Held and Soden, 2006; Chou et al., 2009). Weakening of overturning circulations, especially in the tropics, can also offset part of this thermodynamic change (Chou and Neelin, 2004; Held and Soden, 2006; Vecchi and Soden, 2007; Chou et al., 2009; Seager et al., 2010).

Most of the success of the *wet gets wetter* mechanism comes from its applicability to zonal-mean $P - E$, because zonal-mean overturning circulations such as the Hadley circulation are subject to angular-momentum constraints limiting their response to climate change (Held and Hou, 1980; Schneider, 2006; Walker and Schneider, 2006; Schneider et al., 2010). The remaining zonally anomalous $P - E$, obtained by subtracting off the zonal-mean, explains 60% of the total spatial $P - E$

variance in the modern climate (Wills and Schneider, 2015). We will analyze to what extent the *wet gets wetter* mechanism is useful for changes in zonally anomalous $P - E$. The location and strength of regions of stationary-eddy divergence and convergence are only loosely set by zonally anomalies in heating and topography, so we might expect dynamic changes in zonally anomalous $P - E$ to be large. We suggest looking instead at the zonal variance of $P - E$, which provides a bulk measure of the amplitude of zonal hydrological cycle variations. The zonal variance of $P - E$ is unaffected by zonal circulation shifts and should change more thermodynamically. To the extent it does not, it implies a zonal-mean slowdown of stationary-eddy overturning circulations and/or decreased moisture fluxes by transient eddies.

4.2 Changes in the zonally anomalous hydrological cycle

We analyze the change of $P - E$ in the Coupled Model Intercomparison Project phase 5 (CMIP5) from the $PAST$ (1976-2005) to the $FUTURE$ (2070-2099) as seen by the RCP8.5 scenario. All models that have published monthly-mean precipitation (P), evaporation (E), surface temperature (T_{sfc}), surface specific humidity (q_{sfc}), horizontal wind ($\mathbf{u}$), specific humidity (q), and vertical pressure velocity (ω) are considered. These 23 models are listed in Table 4.1 in the Supplementary Information.

The annual-mean climatology of $P - E$ in the $PAST$ is shown in Fig. 4.1a. The zonally anomalous component, $P^* - E^*$, is shown in Fig. 4.1b. Here stationary-eddy components are determined by $(\cdot)^* = (\cdot) - [\cdot]$, where $[\cdot]$ denotes a zonal mean. By studying zonally anomalous $P - E$, we are focussing on wet regions such as the South Asian and East Asian monsoons, the maritime continent, the South Pacific Convergence Zone, and the northern hemisphere storm tracks and dry regions such as the subtropical lows, the Mediterranean, the northern hemisphere boreal forests, and the Horn of Africa.

By the end of the century, there are many $P - E$ changes that are robust across the models (Fig. 4.1c). Some changes, such as the moistening tendency poleward of 45° latitude and the drying tendency in the subtropics are well produced by a simple thermodynamic scaling similar to that in

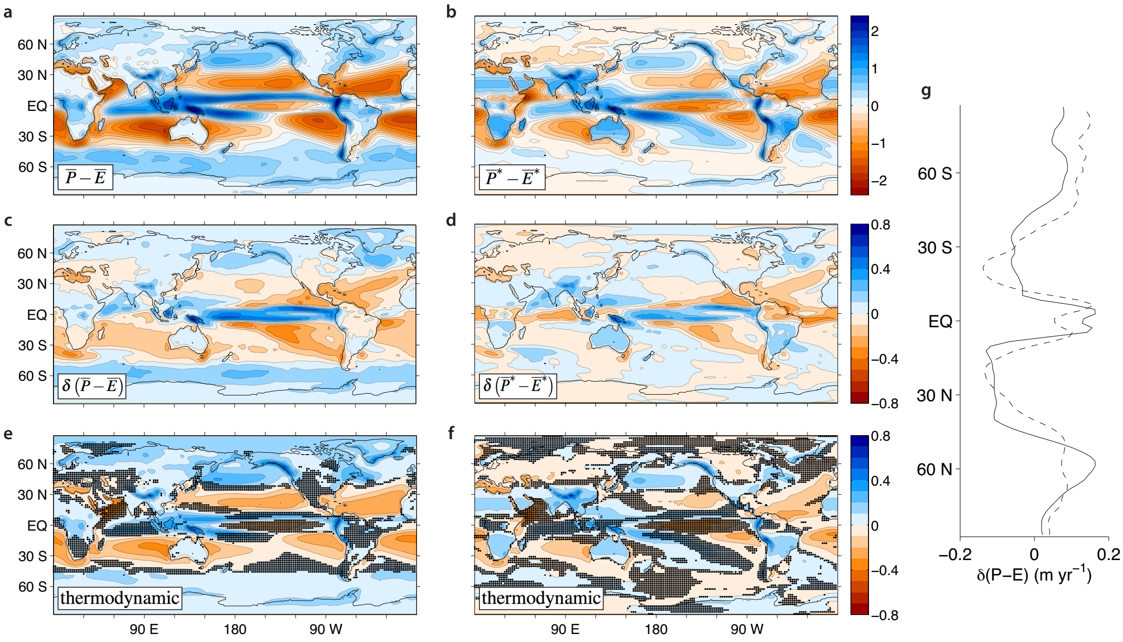

Figure 4.1: Multi-model mean 1976-2005 climatology of a) $P-E$ and b) P^*-E^*. Change of c) $P-E$ and d) P^*-E^* by the end of the century (2070-2099) in the RCP8.5 scenario. e,f) Thermodynamic contribution to (c) and (d) respectively as estimated from the fractional change in surface specific humidity (Eq. 4.1). Stippling indicates where the thermodynamic expectation is opposite in sign to the simulated change. g) Zonal mean of $P-E$ change and simple thermodynamic scaling (Eq. 4.1).

Held and Soden (2006),

$$\delta\left(P-E\right) \sim \frac{\delta q_{\mathrm{sfc}}}{q_{\mathrm{sfc}}}\left(P-E\right). \tag{4.1}$$

We use surface specific humidity instead of surface temperature for simplicity, since it is largely determined by changes in surface temperature due to small changes in surface relative humidity (Held and Soden, 2000, 2006; Schneider et al., 2010). This scaling is particularly good for the zonal mean change (Fig. 4.1g), which was the focus of Held and Soden (2006). The regions where it predicts the wrong sign of change (stippling in Fig. 4.1e) are due to the expansion of the subtropical dry zones (Hu and Fu, 2007; Lu et al., 2007), the drying of land areas due in part to horizontal gradients of changes in specific humidity (Byrne and O'Gorman, 2013, 2015), or due to changes in tropical circulations (Chou and Neelin, 2004; Vecchi et al., 2006; Vecchi and Soden, 2007).

To illustrate the extent to which *wet gets wetter* ideas do not apply to zonal variations of $P-E$, we show the P^*-E^* change (Fig. 4.1d) and an adaptation of the simple thermodynamic scaling

(Fig. 4.1f),

$$\delta\left(P^* - E^*\right) \sim \frac{\delta[q_{\mathrm{sfc}}]}{[q_{\mathrm{sfc}}]}\left(P^* - E^*\right), \tag{4.2}$$

in terms of the zonal-mean surface specific humidity $[q_{\mathrm{sfc}}]$. Again, the regions where the sign is incorrect are indicated with stippling, which covers 35% of the globe. Changes in phase and amplitude of stationary-eddy circulations are large enough such that many zonally anomalous wet regions get drier and dry regions wetter. Most notably, the estimate from the simple scaling disagrees with modelled changes over most of the tropical oceans, where the changes are largest. Tropical circulations are well known to have large changes in amplitude with global warming (Held and Soden, 2006; Vecchi and Soden, 2007), but this analysis suggests that the spatial structure is substantially altered as well. Notably, the zonally anomalous simple scaling gets the sign correct over most land areas. This is because $P - E$ changes over land are generally smaller than the zonal mean, which reflects the smaller magnitude of the $P - E$ climatology over land. These conclusions are unchanged by accounting for changes in the zonally-anomalous surface specific humidity, $\delta q^*_{\mathrm{sfc}}$, in the simple scaling (Eq. 4.2).

4.3 Zonal variance of P - E

The increased moisture content of the atmosphere can still manifest in an increase in the amplitude of zonal variations of the hydrological cycle. This is characterized by the root zonal variance of $P - E$,

$$\mathrm{rms}(P^* - E^*) \equiv \left[\left(P^* - E^*\right)^2\right]^{1/2}, \tag{4.3}$$

where $[\cdot]$ denotes a zonal average. The climatology of $\mathrm{rms}(P^* - E^*)$ in the *PAST*, averaged over the 23 CMIP5 models, is shown in Fig 4.2a. The zonally anomalous hydrological cycle is strongest in the tropics where the moisture content of the atmosphere is greater. It is stronger in the northern hemisphere midlatitudes than the southern hemisphere midlatitudes because the earth surface is more zonally asymmetric in the northern hemisphere. The change and fractional change of $\mathrm{rms}(P^* - E^*)$ are shown in Fig 4.2b and c. The amplitude of zonal variations in $P - E$ increases at all latitudes

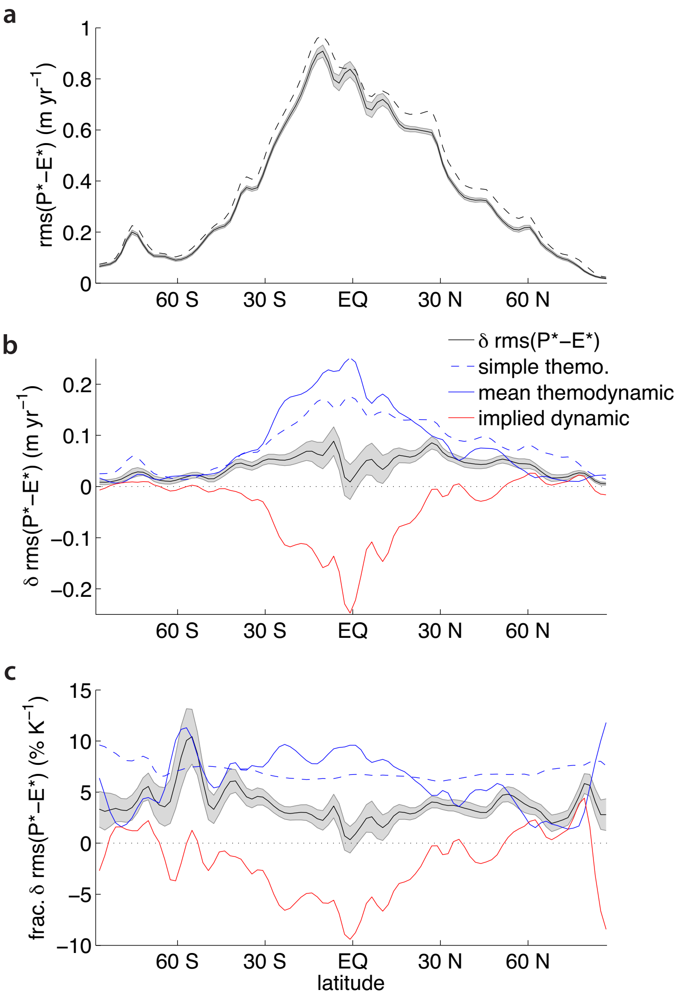

Figure 4.2: a) *PAST* (solid line) and *FUTURE* (dashed-line) climatology of the zonal standard deviation of $P^* - E^*$, $\mathrm{rms}(P^* - E^*)$. Shading shows the range of 95% (2σ) of the expected sampling variability of this 30-year average based on the year-to-year variance during 1976-2005. b) Change in $\mathrm{rms}(P^* - E^*)$ and the simple thermodynamic (Eq. 4.6) and full thermodynamic ($\delta\mathrm{RMS}_{\mathrm{mthermo}}$) estimates of this change. Also shown is an implied dynamic contribution based on the difference between the mean-thermodynamic term and the actual change. Shading as in a). c) Fractional change in $\mathrm{rms}(P^* - E^*)$ over the same time period per degree warming of the zonal-mean surface temperature. Also shown are the fractional changes of the terms shown in b). The shading is rescaled from the shading in a) assuming no sampling variability of the temperature change.

by 2-5 % K^{-1}. This ensemble-mean increase is greater than the expected variability due to inter-annual variability of $P^* - E^*$ in the historical simulation, shown as grey shading in Fig 4.2 (see Methods section). All fields are filtered with a 200-km Gaussian filter before any variance statistics are computed. The motivation for this filtering is the large amount of grid-scale noise present in some models, even for unprocessed fields like the vertical velocity at 850 hPa (see Supplementary Figure 1).

The change in $\mathrm{rms}(P^* - E^*)$ can be split into thermodynamic, dynamic, and transient-eddy components based on the $P^* - E^*$ variance budget using the approximate relation,

$$\delta\,\mathrm{rms}(P^* - E^*) \approx \frac{\delta\left[(P^* - E^*)^2\right]}{2 \cdot \mathrm{rms}(P_1^* - E_1^*)}, \tag{4.4}$$

which is derived in the Methods section. The change in $P^* - E^*$ variance is given by

$$\delta\left[(P^* - E^*)^2\right] = 2\left[(P^* - E^*)\,\delta(P^* - E^*)\right] + \delta(P^* - E^*)^2. \tag{4.5}$$

The second term, which is nonlinear in changes, is included in the analysis, but is generally much smaller than the first term.

A simple thermodynamic scaling is obtained by substituting the simple thermodynamic scaling for $P^* - E^*$ (Eq. 4.2) into the variance budget (neglecting the nonlinear term), obtaining

$$\delta\,\mathrm{rms}(P^* - E^*) \sim \frac{\delta[q_{\mathrm{sfc}}]}{[q_{\mathrm{sfc}}]}\mathrm{rms}(P_1^* - E_1^*). \tag{4.6}$$

This is shown as a dashed blue line in Fig. 4.2b and c. The fractional change is simply given by $\delta[q_{\mathrm{sfc}}]/[q_{\mathrm{sfc}}]$ and is approximately 7% K^{-1} at all latitudes. The change in $\mathrm{rms}(P^* - E^*)$ is robustly less than this simple thermodynamic estimate at all latitudes except for a small band of the Southern Ocean, where the variance is small to begin with. We will explore which dynamic changes make up the difference between the simple thermodynamic scaling and the change in $\mathrm{rms}(P^* - E^*)$. But first, it is beneficial to use a more accurate thermodynamic change term.

We split changes in $P^* - E^*$ according to

$$\delta(P^* - E^*) = \underset{\text{(thermo.)}}{-\nabla\cdot\langle\mathbf{u}_1\delta q\rangle^*} \underset{\text{(dynamic)}}{- \nabla\cdot\langle\delta\mathbf{u}\,q_2\rangle^*} \underset{\text{(transient)}}{- \delta\left(\nabla\cdot\langle\mathbf{u}'q'\rangle\right)^*}, \tag{4.7}$$

where $\mathbf{u}$ is the horizontal wind, q is the specific humidity, and $\langle\cdot\rangle$ denotes a mass-weighted vertical integral over the whole domain. The dynamic term here combines the stationary-eddy components of the dynamic and nonlinear terms of Seager et al. (2010) such that the decomposition is exact. Based on this expression we can split $\delta\,\mathrm{rms}(P^* - E^*)$ into thermodynamic, dynamic, and transient-eddy contributions,

$$\delta\,\mathrm{rms}(P^* - E^*) \approx \delta\mathrm{RMS}_{\mathrm{mthermo}} + \delta\mathrm{RMS}_{\mathrm{mdyn}} + \delta\mathrm{RMS}_{\mathrm{trans}}. \tag{4.8}$$

The expressions for the three terms on the right hand side are given in the Methods section. They are referred to as the mean-thermodynamic, mean-dynamic, and transient terms throughout the rest of the text. They include the nonlinear correlation terms such that Eq. 4.8 is only approximate due to the approximation in Eq. 4.4, relating change in rms to changes in variance.

The mean-thermodynamic term $\delta\mathrm{RMS}_{\mathrm{mthermo}}$ is shown as a solid blue line in Fig. 4.2b and c. It differs from the simple-thermodynamic term primarily because it is derived from the time-mean flow contribution to $P^* - E^*$, as opposed to the full $P^* - E^*$ including the contribution of transient eddies. We will treat transient-eddies separately, eventually coming to the conclusion that defining a thermodynamic change in zonally anomalous transient-eddy moisture flux convergence is not useful. The thermodynamic change is greater than the actual change except at high latitudes. This implies a dynamic change, which is shown as a red line in Fig. 4.2b and c. The implied dynamic change is concentrated in the tropics and subtropics. We will explore the stationary- and transient-eddy contributions in the next section.

4.4 The strength of stationary-eddy circulations

In explaining dynamic causes of changes in amplitude of the zonally anomalous hydrological cycle, we will focus in particular on the stationary-eddy vertical motion at 850 hPa, ω^*_{850}. This is based on the findings of Wills and Schneider (2015, 2016), who show that $P^* - E^*$ can be approximated by

$$P^* - E^* \approx -g^{-1}\,[q_{\mathrm{sfc}}]\,\omega^*_{850}. \tag{4.9}$$

The intuition behind this is that divergent stationary-eddy circulations carry moisture from the boundary layer to a mean condensation height at about 850 hPa. This has also been shown to govern changes in $\mathrm{rms}(P^* - E^*)$ in simple idealized model experiments (Wills and Schneider, 2016),

$$\delta\,\mathrm{rms}(P^* - E^*) \approx g^{-1}\delta\left([q_{\mathrm{sfc}}]\,\mathrm{rms}\left(\omega^*_{850}\right)\right). \tag{4.10}$$

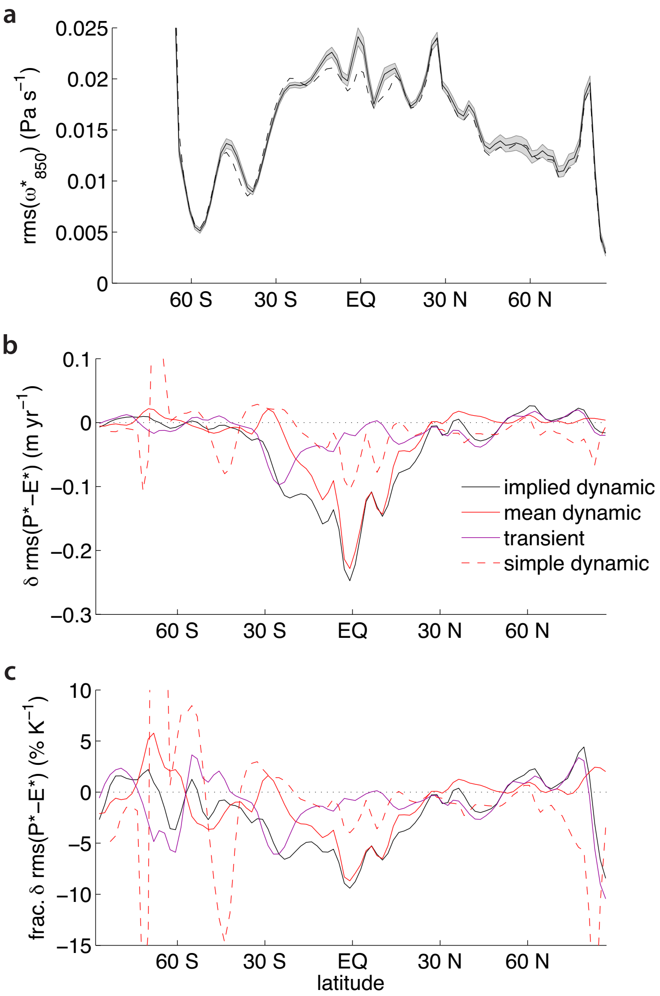

Figure 4.3: a) *PAST* (solid line) and *FUTURE* (dashed-line) climatology of the zonal standard deviation of ω^*_{850}. Shading shows the range of 95% (2σ) of the expected sampling variability of this 30-year average based on the year-to-year variance during 1976-2005. b) Changes in the zonal variance of dynamic and transient-eddy contributions to $P^* - E^*$, $\delta\mathrm{RMS}_{\mathrm{mdyn}}$ and $\delta\mathrm{RMS}_{\mathrm{trans}}$. These add up to the implied dynamic change, which was shown in Fig. 4.2. Also shown is a simple estimate of the dynamic change (Eq. 4.10). c) Fractional change in variance of the moisture budget terms shown in b).

The climatology of $\mathrm{rms}(\omega^*_{850})$, the zonal variance of stationary-eddy vertical motion, is shown in Fig. 4.3. It is highest in the tropics and subtropics. The secondary maxima in the high latitudes come from topographic vertical motions around Greenland and Antarctica.

Figure 4.3b and c show how dynamic changes contribute to the change in $\mathrm{rms}(P^* - E^*)$. The stationary-eddy dynamic component ($\delta\mathrm{RMS}_{\mathrm{mdyn}}$, solid red lines) is the leading contribution, especially within 30° latitude of the equator. One contribution to this stationary-eddy change is what we will refer to as the simple dynamic change (dashed red lines),

$$\delta\,\mathrm{rms}(P^* - E^*) \approx g^{-1}\,[q_{\mathrm{sfc}}]\,\delta\,\mathrm{rms}\left(\omega^*_{850}\right). \tag{4.11}$$

The simple dynamic change shows a slowdown of divergent stationary-eddy circulations. It is a major component of the implied dynamic change (black line) within 15° latitude of the equator. This is consistent with ideas that tropical overturning circulations must decrease with global warming such that energetic constraints on global-mean precipitation are satisfied (Betts, 1998; Held and Soden, 2006; Vecchi and Soden, 2007; Schneider et al., 2010). The reductions of stationary-eddy overturning are robust beyond the range of internal variability for some latitude bands in the tropics and southern hemisphere midlatitudes (Fig. 4.3a). Other components of the stationary-eddy dynamic change include correlations of the dynamic change with the climatological dynamic $P^* - E^*$ contribution and changes in the vertical structure of the atmosphere.

Changes in the zonal variance of transient-eddy moisture flux ($\delta \mathrm{RMS}_{\mathrm{trans}}$, purple lines) are important at higher latitudes. Note, however, that the transient-eddy contribution is predominantly negative. This is an unexpected result, since most studies of zonal-mean $P - E$ changes use in some way a scaling up of transient-eddy moisture fluxes by moisture changes (Held and Soden, 2006; Wu et al., 2011; Byrne and O'Gorman, 2015). Transient-eddy moisture fluxes (at least zonally anomalous ones) do not simply increase linearly with the surface specific humidity. This is perhaps not surprising given the dependence of transient-eddy fluxes on temperature gradients and thus moisture gradients (O'Gorman and Schneider, 2008b; Byrne and O'Gorman, 2015). Together, reductions of stationary-eddy vertical motions and transient-eddy moisture fluxes act to decrease $\mathrm{rms}(P^* - E^*)$ at all latitudes, but especially in the tropics.

So far, all figures and discussion have been of multi-model means. Given the spread in zonal-mean $P - E$ (Voigt and Shaw, 2015), it would be surprising if the models agreed on the climatology of $\mathrm{rms}(P^* - E^*)$. We show the global-mean, tropical-mean, and extratropical-mean $\mathrm{rms}(P^* - E^*)$ for all models on the x-axis of Fig. 4.4. For comparison, we compute the climatology of $\mathrm{rms}(P^* - E^*)$ in ERA-Interim reanalysis for the period 1979–2012. Averages over the same latitude bands are shown as orange stars in Fig. 4.4. The spread in $\mathrm{rms}(P^* - E^*)$ is large. The ERA-Interim value is in the upper end of the range in the tropics and global mean and far beyond the upper end of the range in the extratropics. CMIP5 models are not simulating enough zonal variability in midlatitude $P - E$.

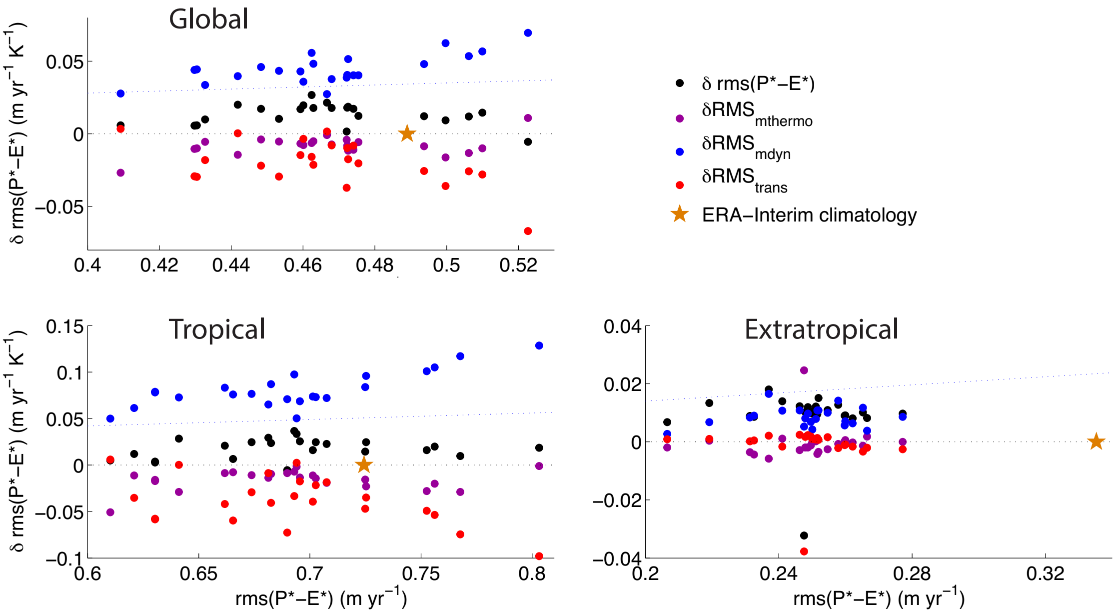

Figure 4.4: Global-mean, tropical-mean (±0–30°), and extratropical-mean (±30–75°) $\delta\,\mathrm{rms}(P^{*}-E^{*})$ plotted versus the *PAST* climatology of $\mathrm{rms}(P^{*}-E^{*})$ for each model. The global average of the mean-thermodynamic, mean-dynamic, and transient contributions to this change are shown separately in blue, red, and purple dots. For comparison, the climatology of $\mathrm{rms}(P^{*}-E^{*})$ in ERA-Interim reanalysis for the period 1979-2012 is shown with an orange star.

The y-axis in Fig. 4.4 shows the change in $\mathrm{rms}(P^{*}-E^{*})$ per degree of warming (computed locally) in these latitude bands, as well as the full thermodynamic, dynamic, and transient-eddy components. Spread in $\mathrm{rms}(P^{*}-E^{*})$ is large, but several aspects of the change are robust. All models except 1 (GFDL-ESM2G) show an increase in global-mean $\mathrm{rms}(P^{*}-E^{*})$ with warming. All models have an increase that is less than the expectation from thermodynamics alone. The majority of models show a larger change coming from stationary-eddy than transient-eddy dynamic changes. Note also that the thermodynamic contribution is generally larger than 7% K^{-1} (shown as a blue dotted line). This arrises from the difference between the simple- and mean-thermodynamic terms as well as the nonlinearity of changes.

4.5 Conclusions

All CMIP5 models studied (except 1) show an increase in strength of the zonally anomalous hydrological cycle with warming in the RCP8.5 scenario. This increase is larger than the uncertainty due to natural variability. This increase comes about primarily from the increasing moisture content of the atmosphere. However, this change is smaller than expected from various estimates of the thermodynamic change based solely on the increased atmospheric moisture content. Dynamic changes work to reduce the increase in zonal variance of the hydrological cycle. Within 15° of the equator, the dynamic change shows a reduction of the strength of stationary-eddy circulations, particularly vertical motion at 850 hPa. Transient-eddies also act to reduce the zonal variance change at higher latitudes. This study emphasizes the importance of understanding stationary-eddy vertical velocities. In the tropics, there are some constraints on stationary-eddy vertical velocity changes from energetic and moist static energy arguments (Betts, 1998; Chou and Neelin, 2004; Held and Soden, 2006), but understanding stationary eddy vertical velocities in the subtropics and midlatitudes remains an open challenge.

4.6 Methods

Uncertainty from inter-annual variability

The inter-annual variance σ^2_{rms} of $\mathrm{rms}(P^* - E^*)$ during 1976-2005 in the historical simulation is averaged over all ensemble members. 95% of 30-year averages of $\mathrm{rms}(P^* - E^*)$ should lie within a spread of $\pm\frac{2}{\sqrt{30}}\sigma_{\mathrm{rms}}$ if there is no trend in $\mathrm{rms}(P^* - E^*)$. We thus use this value for error bars in Fig. 4.2. Error bars are computed in an analagous way for $\mathrm{rms}(\omega^*_{850})$ in Fig. 4.3.

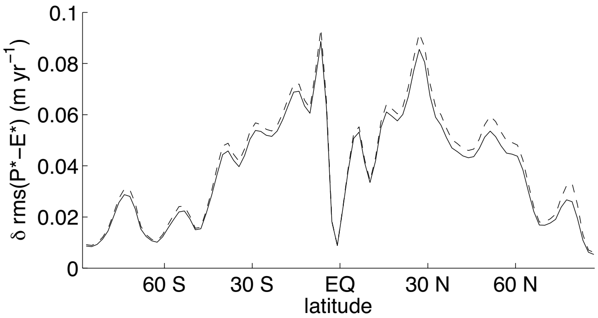

Figure 4.5: $\delta\,\mathrm{rms}(P^* - E^*)$ (solid line) and its approximation by Eq. 4.15 (dashed line).

Spatial variance budget

We analyze changes in $\mathrm{rms}(P^* - E^*)$ by relating it to the change of spatial variance in $P^* - E^*$, which can be expanded as

$$\begin{aligned}\delta\left[(P^* - E^*)^2\right] &= \left[(P_2^* - E_2^*)^2\right] - \left[(P_1^* - E_1^*)^2\right]\\ &= (\mathrm{rms}(P_2^* - E_2^*))^2 - (\mathrm{rms}(P_1^* - E_1^*))^2\\ &= (\delta\,\mathrm{rms}(P^* - E^*) + \mathrm{rms}(P_1^* - E_1^*))^2 - (\mathrm{rms}(P_1^* - E_1^*))^2\\ &= (\delta\,\mathrm{rms}(P^* - E^*))^2 + 2\cdot\delta\,\mathrm{rms}(P^* - E^*)\cdot\mathrm{rms}(P_1^* - E_1^*)^2.\end{aligned} \tag{4.12}$$

The first quadratic term is small and can be neglected. The result is an expression for $\delta\,\mathrm{rms}(P^* - E^*)$ in terms of $\delta\left[(P^* - E^*)^2\right]$,

$$\delta\,\mathrm{rms}(P^* - E^*) \approx \frac{\delta\left[(P^* - E^*)^2\right]}{2\cdot\mathrm{rms}(P_1^* - E_1^*)}, \tag{4.13}$$

where the quadratic nonlinearity has been removed. The quality of this approximation is shown in Fig. 4.5.

We split the change in $\delta\,\mathrm{rms}(P^* - E^*)$ into thermodynamic, dynamic, and transient-eddy components based on

$$
\begin{aligned}
\delta(P^* - E^*) &= -\nabla\cdot\langle \mathbf{u}_1 \delta q\rangle^* - \nabla\cdot\langle \delta\mathbf{u}\, q_2\rangle^* - \delta\left(\nabla\cdot\langle \mathbf{u}' q'\rangle\right)^* \\
&\equiv \quad \Delta_{\mathrm{thermo}} \quad + \quad \Delta_{\mathrm{dyn}} \quad + \quad \Delta_{\mathrm{trans}}.
\end{aligned}
\tag{4.14}
$$

The transient-eddy term Δ_{trans} is diagnosed as a residual. Substituting this decomposition into Eq. 4.15, we obtain

$$
\delta\,\mathrm{rms}(P^* - E^*) \approx \delta\mathrm{RMS}_{\mathrm{mthermo}} + \delta\mathrm{RMS}_{\mathrm{mdyn}} + \delta\mathrm{RMS}_{\mathrm{trans}}, \tag{4.15}
$$

where

$$
\begin{aligned}
\delta\mathrm{RMS}_{\mathrm{mthermo}} &\equiv \frac{1}{2}\frac{1}{\mathrm{rms}(P_1^* - E_1^*)}\left[2(P_1^* - E_1^*)\Delta_{\mathrm{thermo}} + \Delta_{\mathrm{thermo}}^2\right], \\
\delta\mathrm{RMS}_{\mathrm{mdyn}} &\equiv \frac{1}{2}\frac{1}{\mathrm{rms}(P_1^* - E_1^*)}\left[2(P_1^* - E_1^*)\Delta_{\mathrm{dyn}} + \Delta_{\mathrm{dyn}}^2 + 2\Delta_{\mathrm{dyn}}\Delta_{\mathrm{thermo}}\right], \\
&\text{and} \\
\delta\mathrm{RMS}_{\mathrm{trans}} &\equiv \frac{1}{2}\frac{1}{\mathrm{rms}(P_1^* - E_1^*)}\left[2(P_1^* - E_1^*)\Delta_{\mathrm{trans}} + \Delta_{\mathrm{trans}}^2 + 2\Delta_{\mathrm{trans}}\left(\Delta_{\mathrm{thermo}} + \Delta_{\mathrm{dyn}}\right)\right].
\end{aligned}
\tag{4.16}
$$

The quadratic terms in 4.16 are generally small, but significant. As such, the changes in $\delta\,\mathrm{rms}(P^* - E^*)$ can be understood as being proportional to the zonal correlation of Δ_{trans}, Δ_{trans}, and Δ_{trans} with $P_1^* - E_1^*$, but we maintain the quadratic terms for completeness. The philosophy behind the arrangement of quadratic terms is that $\delta\mathrm{RMS}_{\mathrm{mthermo}}$ should be the change expected with no knowledge of what happens to the dynamic terms, that $\delta\mathrm{RMS}_{\mathrm{mdyn}}$ should be the improvement by including stationary-eddy changes with no knowledge of transient-eddy changes, and that $\delta\mathrm{RMS}_{\mathrm{trans}}$ should be everything else.

4.7 Supplementary Information

We include a list of CMIP5 models used (Table 4.1) and an illustration of the grid-scale noise present in unprocessed ω_{850}^* (Fig. 4.6).

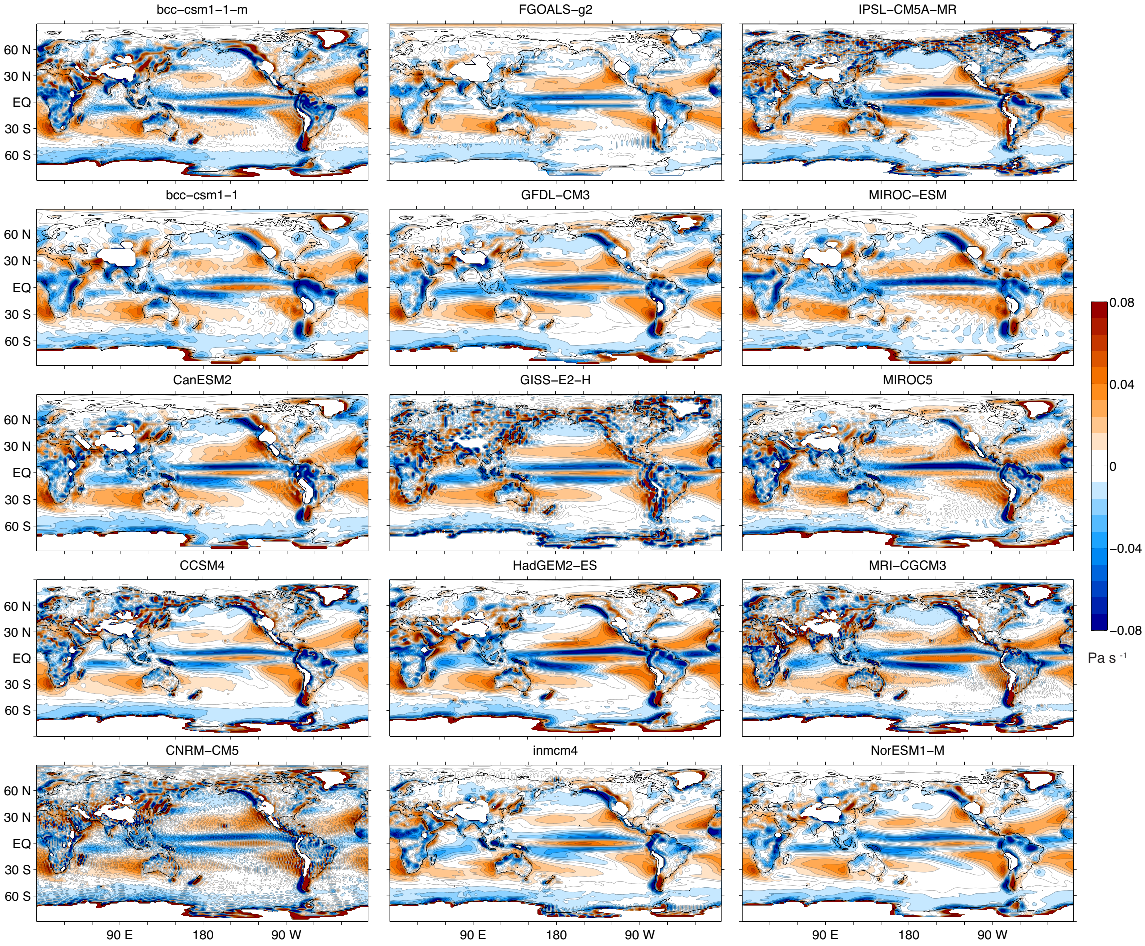

Figure 4.6: Raw unfiltered 30-year average ω_{850} for the *PAST* (1976-2005) climate from selected CMIP5 models. The grid scale noise evident in these fields is the motivation for the filtering used in computing fields throughout this chapter.

Table 4.1: CMIP5 models used for zonally-anomalous moisture budget analysis.

Model	Description
CCSM4	Community Climate System Model, version 4
CESM1-BGC	Community Earth System Model–Biogeochemistry, version 1
CESM1-CAM5	Community Earth System Model, version 1 (Community Atmosphere Model, version 5)
CNRM-CM5	Centre National de Recherches Meteorologiques Coupled Global Climate Model, version 5
CanESM2	Second Generation Canadian Earth System Model
FGOALS-g2	Flexible Global Ocean–Atmosphere–Land System Model grid-point, version 1.0
GFDL-CM3	Geophysical Fluid Dynamics Laboratory Climate Model, version 3
GFDL-ESM2G	Geophysical Fluid Dynamics Laboratory Earth System Model with Generalized Ocean Layer Dynamics (GOLD) component
GFDL-ESM2M	Geophysical Fluid Dynamics Laboratory Earth System Model with Modular Ocean Model 4 (MOM4) component (ESM2M)
GISS-E2-H	Goddard Institute for Space Studies Model E, coupled with the HYCOM ocean model
HadGEM2-ES	Hadley Centre Global Environment Model, version 2 - Earth System
IPSL-CM5A-LR	L'Institut Pierre-Simon Laplace Coupled Model, version 5, coupled with NEMO, low resolution
IPSL-CM5A-MR	L'Institut Pierre-Simon Laplace Coupled Model, version 5, coupled with NEMO, mid resolution
IPSL-CM5B-LR	L'Institut Pierre-Simon Laplace Coupled Model, version 5, coupled with NEMO, low resolution
MIROC-ESM	Model for Interdisciplinary Research on Climate, Earth System Model
MIROC-ESM-CHEM	Model for Interdisciplinary Research on Climate, Earth System Model, Chemistry Coupled
MIROC5	Model for Interdisciplinary Research on Climate, version 5
MRI-CGCM3	Meteorological Research Institute Coupled Atmosphere–Ocean General Circulation Model, version 3
NorESM1-M	Norwegian Earth System Model, version 1 (intermediate resolution)
NorESM1-ME	Norwegian Earth System Model, version 1 (intermediate resolution), with prognostic biogeochemical cycling
bcc-csm1-1	Beijing Climate Center, Climate System Model, version 1.1
bcc-csm1-1-m	Beijing Climate Center, Climate System Model, version 1.1, moderate resolution
inmcm4	Institute of Numerical Mathematics Coupled Model, version 4.0

Part II

Mechanisms of stationary-eddy change

Chapter 5

Orographic forcing of stationary Rossby waves in a wide range of climates

Abstract

Orographic stationary Rossby waves are an important influence on the large-scale stationary-eddy circulation of the atmosphere, especially in Northern Hemisphere winter. The forcing of stationary waves by topography is typically addressed in linear stationary wave models, where any influence of the mountain on diabatic heating is treated separately. This chapter presents an analysis of the forcing of stationary waves by an idealized topographic source in a fully-nonlinear GCM. In this way, all influences of the mountain on the stationary-eddy circulation are diagnosed explicitly. The change in amplitude of the stationary-eddy circulation with warming of the mean climate depends on the latitude of the topography. An analysis of the thermodynamic equation reveals that the latitude dependency results from differences in the zonal-mean zonal surface winds at the latitude of the mountain. The response of the stationary-eddy amplitude to climate change can be qualitatively predicted from the zonal surface winds, the slope of midlatitude isentropes, and the strength of latent heating, which damps the orographic stationary eddy. This chapter also examines changes in meridional and vertical dispersion of stationary-eddy energy and changes in stationary-eddy lengthscale. Changes in lengthscale and dispersion are small and consistent with previous theoretical work.

5.1 Introduction

Orographic stationary Rossby waves play a large role in the stationary-eddy wind field in Northern Hemisphere winter (Broccoli and Manabe, 1992; Held et al., 2002), with consequences for the zonal variation of $P-E$ (Broccoli and Manabe, 1992; Wills and Schneider, 2015, 2016). Previous work has used linear stationary-wave models to diagnose the extent to which topography influences the modern stationary-wave climatology (Nigam et al., 1988; Valdes and Hoskins, 1989; Ting, 1994; Held et al., 2002) and the orographic stationary Rossby wave contribution to the change with climate change (Stephenson and Held, 1993; Joseph et al., 2004). This work is grounded in linear quasi-geostrophic theory, in which Rossby wave theory is generally based (Hoskins and Karoly, 1981; Held, 1983).

A linear quasi-geostrophic analysis of the response of stationary waves to topographic forcing identifies the low-level zonal wind as a key factor controlling the magnitude of response (Hoskins and Karoly, 1981; Held, 1983; Held and Ting, 1990). The interaction of surface winds with a mountain of height h creates a vertical velocity $w_{\mathrm{sfc}} = \mathbf{u}_{\mathrm{sfc}} \cdot \nabla h$. The orographic vertical velocity w_{sfc} is dominated by the zonal-mean zonal wind component, which responds non-monotonically to climate change mirroring changes in transient-eddy momentum flux convergence. The adiabatic heating/cooling induced by this vertical velocity in the presence of stable stratification must be balanced by horizontal heat fluxes and diabatic tendencies. A large portion of this heating/cooling is balanced by meridional advection, inducing a stationary-eddy wind $\overline{v}^*$, and setting up the stationary wave that propagates eastward. The response of the resulting stationary wave to warming will thus depend on w_{sfc} as well as the thermodynamic structure of the atmosphere (i.e., meridional temperature gradients, static stability, and diabatic tendencies).

Linear stationary-wave models generally treat diabatic heating separately from topographic forcing even though there are latent heating tendencies that result directly from the topographic influence (e.g. orographic precipitation). Additionally, it is often challenging to determine the relevant stratification, zonal wind, and meridional temperature gradients for a quasi-geostrophic analysis, especially with large climate changes where the vertical structure of the atmosphere is changing. We turn instead to a direct analysis of the thermodynamic equation. In this way, we can construct a budget for the stationary-eddy meridional wind variance and assess the various influences on stationary-wave amplitude with climate change.

To facilitate this analysis, we set up simulations where mountain latitude and longwave absorption are varied. These simulations are described in Section 5.2. Since an important control on the stationary eddies is the structure of the zonal-mean climate, we analyze zonal-mean climate changes in these experiments in Section 5.3. The stationary-eddy amplitude response is presented in Section 5.4. An analysis of the thermodynamic mechansims controlling the stationary-eddy amplitude response are presented in Section 5.5. The change in stationary-eddy amplitude is just one aspect of the stationary-eddy changes with warming. In Section 5.6 we investigate changes in the meridional and vertical propagation of stationary-eddies from the source region. In Section 5.7 we analyze changes in the zonal length scale of stationary-eddies. These changes in the structure of stationary waves away from the source region influence the surface expression of stationary waves, such as $\overline{P}^* - \overline{E}^*$.

5.2 Additional experiments

In order to isolate the response of orographically forced stationary Rossby waves to global warming, we add a single large-scale mountain ridge to an idealized GCM simulation with otherwise zonally-symmetric aquaplanet boundary conditions. These simulations are described in Chapter 3. To understand the controls on the stationary-wave amplitude, it will be illustrative to use several different mountain configurations. The surface topography is specified by

$$z_{\mathrm{sfc}}\left(\lambda, \phi\right) = h_0 \exp\left[-\frac{\left(\lambda - \lambda_0\right)^2}{2\sigma_\lambda^2} - \frac{\max\left(0, \left|\phi - \phi_0\right| - R_\phi\right)^2}{2\sigma_\phi^2}\right], \tag{5.1}$$

where we use $h_0 = 2500$ m, $R_\phi = 2.5°$, $\sigma_\phi = 5°$, and $\sigma_\lambda = 12.5°$. We analyze experiments with $\phi_0 = 45°$N, 36°N, and 54°N, which we refer to as R45, R54, and R36 respectively. The R45 experiment is set up to be qualitatively similar to the orographic forcing by the Rocky Mountains and is the experiment analyzed in Chapter 3. Additional mountain configurations are examined in

5.3 Zonal-mean climate

In these simulations, the zonal asymmetry of the boundary conditions (i.e. the topography) is fixed across the range of climates. Any changes in the amplitude of stationary waves must thus result from changes in the zonal-mean basic state. For this reason we first present the zonal-mean basic state in these simulations. For the most part, the zonal-mean climate is unchanged by the presence of zonal asymmetries. Zonal-mean quantities are mostly unaffected by the presence of zonally asymmetric boundary conditions. We compare zonal-mean quantities with the zonally-symmetric southern hemisphere or a separate zonally-symmetric experiment where relevant.

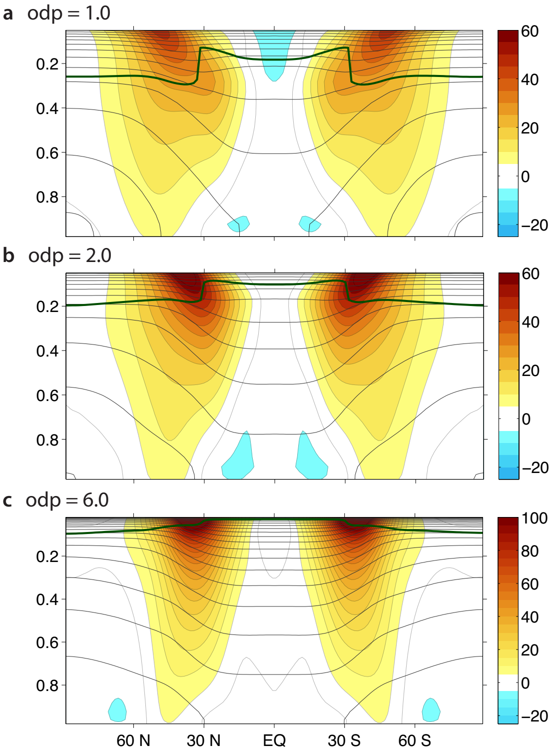

Figure 5.1: Zonal-mean zonal wind $[\overline{u}]$ (shading, contour interval 5 m s^{-1}) and potential temperature $[\overline{\theta}]$ (black contours, contours interval 20 K) for (a) $\alpha = 1.0$, (b) $\alpha = 2.0$, and (c) $\alpha = 6.0$ of a reference experiment with no zonally asymmetric forcing. A dark green line shows the tropopause height as determined by the 2 K km^{-1} lapse-rate criterion. All fields are computed from the R45 experiment. The symmetry of the northern and southern hemispheres shows that these fields are not dependent on the zonally asymmetric forcing.

5.3.1 Jet changes

The jet stream and atmospheric thermal structure are the primary properties of the zonal-mean climate that determine the response of stationary waves to zonally anomalous forcing. We present the zonal-mean zonal wind and potential temperature in Fig. 5.1 for the reference climate and 2 warmer climates. As the climate warms, the atmosphere becomes more stable (as determined by the vertical derivative of potential temperature), meridional temperature gradients get weaker in the lower troposphere but stronger in the upper troposphere, the midlatitude eddy-driven jet disappears in favor of a single subtropical jet, and the height of the tropopause increases. Note that because of the increase in tropopause height, the jet at tropopause level gets stronger with warming despite the decrease in lower-tropospheric meridional temperature gradients. Another notable change is that the atmosphere becomes superrotating, where $[\overline{u}] > 0$ at the equator, for the warmest two climates ($\alpha = 4.0, 6.0$). The superrotation is weak enough such that it does not significantly affect the propagation of Rossby waves across the equator, but it may play a role in the dynamics of the equatorial heating experiment (Chapter 6).

An interesting aspect to the zonal wind change in this model is that the midlatitude surface westerlies shift equatorward and polar easterlies strengthen and expand as the climate warms (Fig. 5.2a). The presence of a mountain tends to weaken the zonal-mean surface westerlies, but does not explain the equatorward shift with warming (Fig. 5.2b). Most evidence in comprehensive models and observations indicate a poleward shift of surface westerlies with warming (Kushner et al., 2001; Yin, 2005; Chen and Held, 2007), though this response has only been probed over a fraction of the range of global-mean surface temperatures explored here. The changes in the idealized model are consistent with the changes in transient-eddy kinetic energy (see 5.3.2). In light of these differences, the orographic forcing results should be interpreted as the response to the particular zonal surface-wind change in this idealized GCM. Generalizing these ideas to climate change in Earth's real climate system requires an understanding of the differences in zonal surface-wind response.

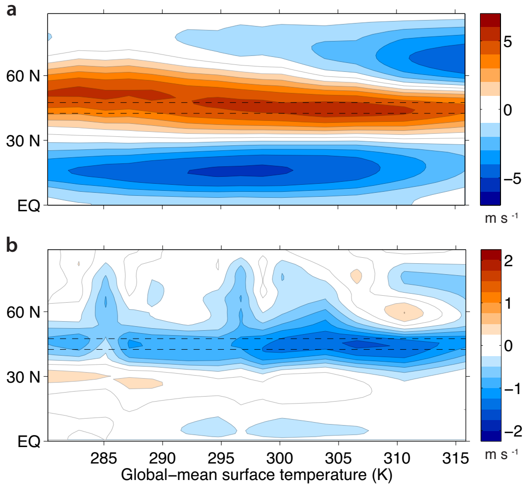

Figure 5.2: Zonal-mean zonal surface wind across a wide range of climates in a) the northern hemisphere of R45 b) the difference between the northern hemisphere and southern hemisphere. Dashed lines show the extent of the maximum topographic relief in the R45 experiment.

5.3.2 Transient eddy changes

Synoptic eddies affect the forcing of stationary eddies in 2 main ways. First, transient-eddy momentum flux convergence sets the strength and position of the surface zonal winds. Second, zonally-anomalous transient-eddy heat and momentum fluxes can either force or damp stationary waves through their influence on the stationary-eddy energy and momentum budgets. If the transient eddies can be thought to act diffusively (cf. Caballero and Langen, 2005), these zonally anomalous fluxes should scale with a bulk measure of the transient-eddy activity and the strength of the stationary-eddy temperature or vorticity gradients they are acting on. As a bulk measure of transient-eddy activity, we choose the transient-eddy kinetic energy (tEKE). This is shown in Fig. 5.3a, integrated over the troposphere. The non-monotonicity of tEKE has been explained previously in the same model as resulting from changes in mean available potential energy (MAPE) (O'Gorman and Schneider, 2008a).

The slight poleward shift of full-tropospheric tEKE does not fit with the equatorward shift of surface winds (Fig. 5.2) or the much stronger poleward shift of lower-troposheric tEKE previously reported for this model (Schneider et al., 2010). To understand the reasons for this we split tEKE into lower-tropospheric (below $\sigma = 0.72$) and upper-tropospheric (tropopause level plus two levels above

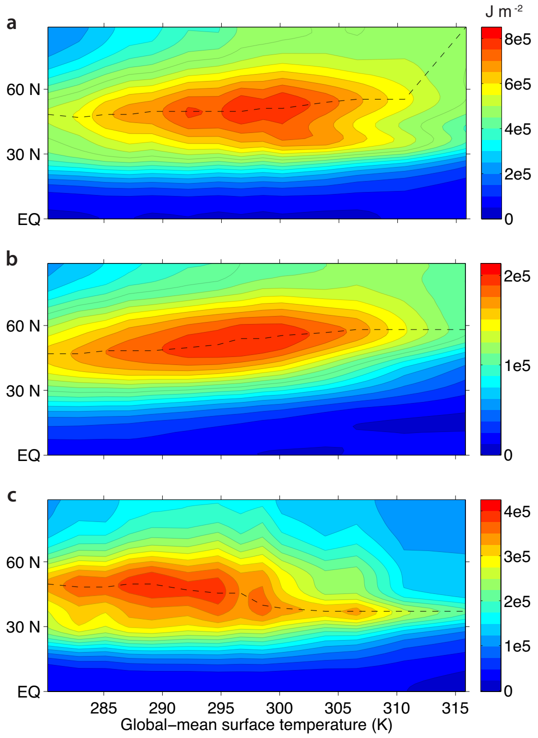

Figure 5.3: Zonal-mean transient-eddy kinetic energy (tEKE) vertically integrated (a) over the full troposphere (b) from the surface to $\sigma = 0.72$, and (c) from 2 levels above the tropopause to 3 levels below the tropopause.

and 3 below) components. The tEKE behaves very differently with climate change for the upper-tropospheric and lower-tropospheric components. While the lower-tropospheric tEKE exhibits the strong poleward shift reported in Schneider et al. (2010) and explained in a dry-model context by Mbengue and Schneider (2013), the upper-tropospheric tEKE shifts equatorward. The poleward shift of lower-tropopsheric tEKE and other measures of storm track activity has been seen in observations and comprehensive models (Fyfe, 2003; Yin, 2005; Bender et al., 2012), but, as far as we are aware, this is the first mention of an equatorward shift of upper-tropospheric tEKE with warming. This result could be unique to this model. The relevance of this is that the surface winds, which follow the upper-tropospheric eddy momentum flux convergence, also shift equatorward (Fig. 5.2). Some aspects of the orographic aspects of the orographic stationary Rossby wave response depend on this equatorward shift with warming, as we will see in the following sections.

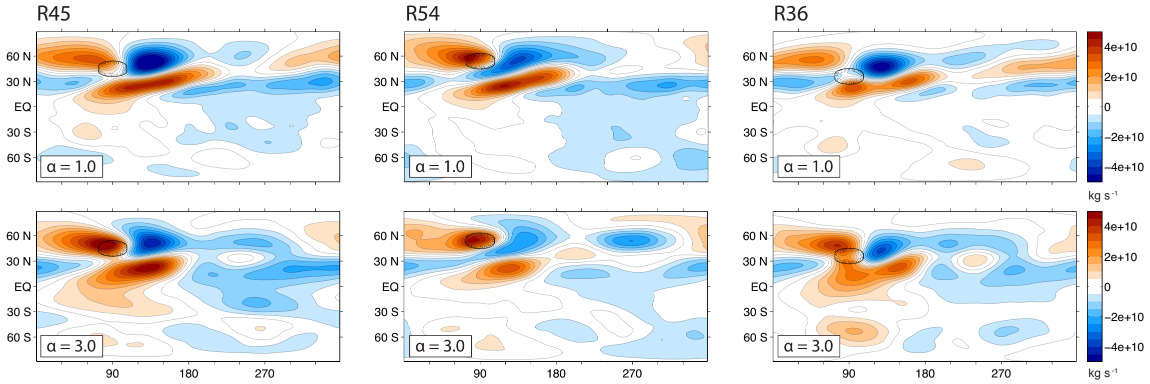

Figure 5.4: Barotropic streamfunction response to orographic forcing in the reference simulation ($\alpha = 1$) and in the 3x optical depth simulation ($\alpha = 3$) for all three mountain configurations (R45, R54, R36). The black contour is the 1000 m contour of surface height.

5.4 Stationary wave response

The barotropic stationary-eddy streamfunction response to orographic forcing at 3 different latitudes is shown in Fig. 5.4 for the reference climate ($\alpha = 1$) and for 3x optical depth ($\alpha = 3$). Here stationary eddies are characterized by the deviation of the time-mean flow from the zonal-mean climatology. Full fields are thus decomposed into a time-mean zonal-mean component $\overline{[\cdot]}$, a stationary-eddy component, $\overline{(\cdot)}^*$, and a transient-eddy component, $(\cdot)'$.

In R45, the stationary-eddy response is characterized by an anticyclone northwest of the mountain and a cyclone extending from south of the mountain to northeast of the mountain. This sets an equatorward wavetrain, which is largely absorbed in the tropical easterlies. The equatorward wavetrain sets up a strong, diagonally oriented, subtropical low 0 - 90° downstream of the mountain. The response in the warmer climate has a smaller zonal and meridional scale and the downstream response more closely resembles separate poleward and equatorward wavetrains. In R54, the high-latitude anticyclone sits closer to the mountain, but the response looks qualitatively similar, expect that there is a more pronounced decrease in stationary-wave amplitude with climate change. In R36, the large stationary-eddy cyclone is split across the mountain, from southwest to northeast, and the zonal and meridional scale of the wave increase with warming.

The phase response over the topography in R45 and R54 fits qualitatively with what was found

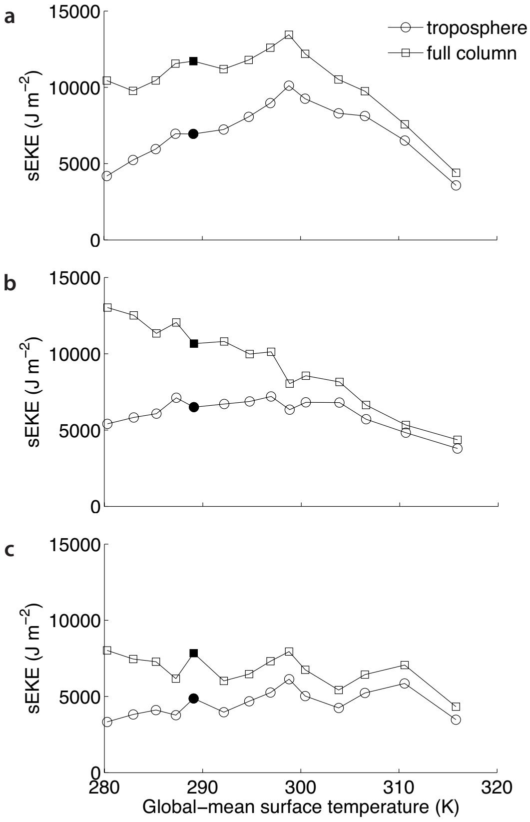

Figure 5.5: Variation of global-mean sEKE with global warming in experiments R45 (a), R54 (b), and R36 (c). Vertical integrals are performed over the full model column (squares) or the troposphere (circles), where the tropopause is determined from the 2 K km^{-1} lapse-rate criterion. Filled circles indicate the reference climate ($\alpha = 1$).

by Hoskins and Karoly (1981) using baroclinic theory on a beta plane. The R36 experiment is somewhat in between the regimes studied by Hoskins and Karoly (1981) and Rodwell and Hoskins (2001), but resembles qualitatively the non-linear regime in Rodwell and Hoskins (2001). While these studies and several others have focused on the phase structure of stationary Rossby waves in response to orographic forcing, they have not examined mechanistically the amplitude of the Rossby wave response. We can see already in Fig. 5.4 that the amplitude of the pattern varies significantly between the experiments, in addition to the phasing. In this study we hope to explain mechanistically how the global amplitude of the orographic stationary Rossby wave response changes across experiments and with climate change. Towards this end, we plot in Fig. 5.5 the change across the range of climates of the vertically integrated stationary-eddy kinetic energy, sEKE $\equiv$

$\frac{1}{2}\langle \overline{u}^{*2} + \overline{v}^{*2} \rangle = -\langle \overline{\psi}^{*} \overline{\zeta}^{*} \rangle$. Note that this simply differs by a length scale from the vertically-integrated enstrophy, $\langle \overline{\zeta}^{*2} \rangle$, or squared streamfunction, $\langle \overline{\psi}^{*2} \rangle$. Here $\langle \cdot \rangle$ represents a mass-weighted total-column vertical integral.

The tendency of change for sEKE in the R45 experiment is an increase with warming in climates below 300 K global-mean surface temperature (more robust for the troposphere than for the full column) and a strong decrease with further warming. In contrast, the R54 experiment has a strong decrease in full-column sEKE with warming throughout the range of climates. The tropospheric sEKE in R54 has little robust change because of the competing effects of the decreasing full-column sEKE and the increasing tropopause height. The R36 experiment has little robust change in sEKE with warming for either the full-column of the troposphere. There is also less sEKE than in the other two experiments. Note that the stratospheric sEKE (difference between the two lines) decreases with warming in all 3 experiments simply due to the expansion of the troposphere. We would like to understand these changes and why they differ between experiments.

5.5 Stationary-eddy thermodynamics

To understand the way in which adiabatic heating/cooling forces stationary waves as air goes over the mountain, we examine an approximate steady-state thermodynamic balance,

$$\overline{u}^{\dagger} \partial_x \overline{\theta}^{\dagger} + \overline{v}^{*} \partial_y \overline{\theta} + \overline{\omega}^{*} \partial_p [\overline{\theta}] \approx \overline{Q}^{*}, \tag{5.2}$$

where θ is the potential temperature and

$$\overline{Q}^{*} = \overline{Q}^{*}_{\text{latent}} + \overline{Q}^{*}_{\text{radiation}} + \overline{Q}^{*}_{\text{sub-grid}} + \overline{Q}^{*}_{\text{trans}} \tag{5.3}$$

is the zonally anomalous heating tendency by latent heating, radiation, sub-grid-scale turbulent mixing, and transient-eddies. The transient-eddy heating term is simply the transient-eddy potential temperature flux convergence, $\overline{Q}^{*}_{\text{trans}} = -\nabla_p \cdot \left(\overline{\mathbf{v}'\theta'}\right)$. The only approximations applied so far in

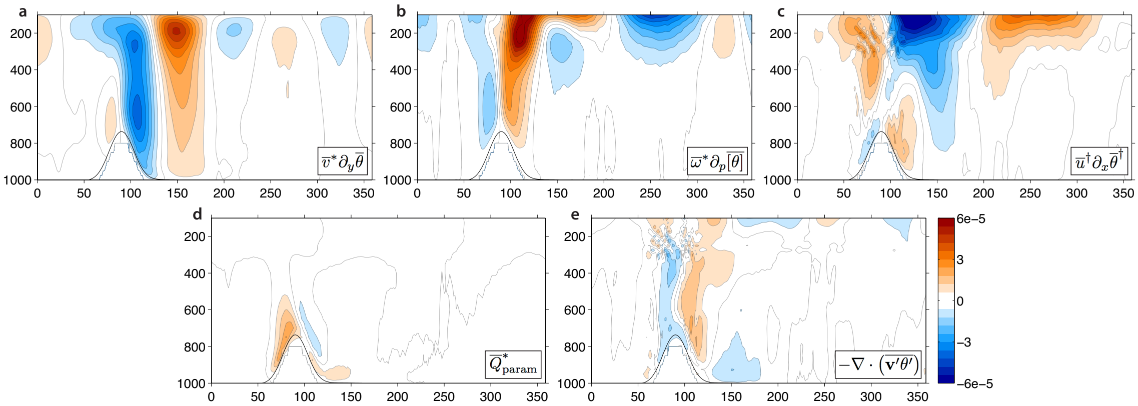

Figure 5.6: Vertical profile of terms in the stationary-eddy thermodynamic equation (Eq. 5.2; units of K s^{-1}) averaged over $\phi \in [42.5\ 47.5]$ in the reference climate ($\alpha = 1.0$) of R45. a) Meridional, b) vertical, and c) zonal advection of potential temperature by stationary eddies ignoring the zonal-mean meridional and vertical wind. d) All diabatic tendencies (latent heating, radiation, parameterized boundary layer mixing). e) Transient-eddy potential temperature flux convergence. Signs are chosen such that heating is red and cooling is blue. The residual is distributed amongst the zonal advection and transient-eddy terms as described in the text. A black-line shows the time-mean surface pressure.

Eq. 5.2 are to assume that the vertical gradient of potential temperature is dominated by its zonal-mean value and to neglect the zonal-mean meridional wind. The vertical profiles of these terms over the mountain in the R45 experiment are shown in Figs. 5.6 and 5.7 for the reference climate and the warmest climate respectively. The parameterized heating, $\overline{Q}^*_{\text{param}} = \overline{Q}^*_{\text{latent}} + \overline{Q}^*_{\text{radiation}} + \overline{Q}^*_{\text{sub-grid}}$, which is dominated by latent heating, is analyzed separately from the transient-eddy heating tendency.

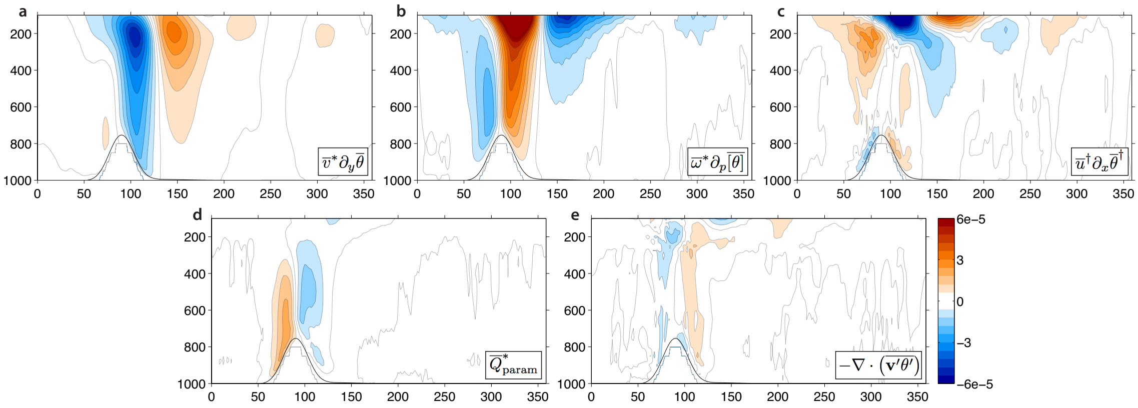

Figure 5.7: Same as Fig. 5.6 for $\alpha = 3.0$ in the R45 experiment.

While the model uses σ coordinates, we interpolate to pressure coordinates to avoid large spatial gradients on σ surfaces as the coordinate surface slopes over the mountain. The interpolation is done at every 6-hour analysis timestep, by linearly interpolating the vertical integral of each quantity. This helps ensure that mass is conserved in the interpolation. However, quantities with large vertical gradients, such as potential temperature, are shifted around in the vertical, creating large-amplitude grid-scale noise, which integrates to zero. The residual of this interpolated budget is shown in Fig. 5.8c. We distribute it to the other terms in a way that minimizes the total variance of all terms (i.e., we put the residual with the term in which it is most correlated at each level). Above 600 hPa, this is the zonal advection term (Fig. 5.8a), which is noisy due to noise in $\overline{\theta}$. Below 600 hPa, this is the transient-eddy term, which is noisy due to the density weighted derivatives across the surface (Fig. 5.8b). The profiles shown in Figs. 5.6 and 5.7 are the result after distributing this residual.

The adiabatic heating/cooling ($\overline{\omega}^*\partial_p\overline{[\theta]}$) is primarily balanced by stationary-eddy meridional advection ($\overline{v}^*\partial_y\overline{\theta}$) in the midlatitudes, where meridional temperature gradients are large. In this way, a stationary-eddy $\overline{v}^*$ is forced by flow over the mountain. If this simple two-term balance applied across the range of climates, $\overline{v}^{*2}$ would scale with the inverse square isentropic slope $(\partial_y\overline{[\theta]}/\partial_p\overline{[\theta]})^{-2}$ and $\overline{\omega}^{*2}$. The vertical velocity $\overline{\omega}^*$ is partially determined by the surface winds and the mountain surface pressure gradient because $\overline{\omega}^*_{\text{sfc}} = (\overline{\mathbf{u}}_{\text{sfc}} \cdot \nabla\overline{p}_s)^*$.

A simple scaling based on this two term balance would look something like

$$\overline{v}^{*2} \sim \left(\frac{\partial_p\overline{[\theta]}}{\partial_y\overline{[\theta]}}\right)^2 \overline{\omega}^{*2}_{\text{sfc}}. \tag{5.4}$$

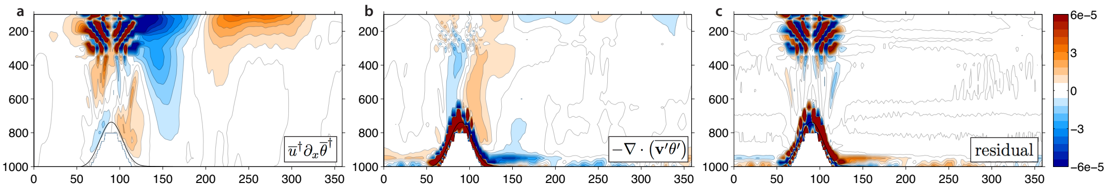

Figure 5.8: Thermodynamic equation terms in the reference climate ($\alpha = 1.0$) of R45 before the residual has been distributed in a way such that the sum of variances of all terms is minimized.

Figure 5.9 shows how the quantities in this scaling change across the range of climates in the 3 orographic forcing experiments at a representative 600 hPa level in the mid-troposphere. All quantities are averaged within 10° latitude of the topography center. To some extent, the change in $\overline{\omega}^{*2}_{\mathrm{sfc}}$ is mirrored in the change of $\overline{v}^{*2}$, with a non-monotonic response in R45, a strong non-monotonic decrease in R54, and little change in R36. But based solely on the strong increase in inverse isentropic slope $(\partial_y\overline{[\theta]}/\partial_p\overline{[\theta]})^{-1}$, one would expect an increase in the stationary-wave amplitude. The dashed line in 5.9a shows the resulting $\overline{v}^{*2}$ estimate. Considering the simplicity, this estimate is quite good for moderate climates, but diverges from the actual $\overline{v}^{*2}$ in warm climates, especially in the R54 experiment. Clearly the truth is more complicated than this simple scaling. Even in these simple idealized experiments, zonal-anomalies of heating, especially latent heating and the transient-eddy heat flux convergence, play an important role in setting the amplitude of stationary eddies. This is apparent in Fig. 5.7, where the latent heating term is large and out of phase with the initial forcing by $\overline{\omega}^{*}_{\mathrm{sfc}}$.

Further progress can be made by rearranging the thermodynamic equation (5.2) into an equation for $\overline{v}^{*}$,

$$\overline{v}^{*} \approx \frac{1}{\partial_y\overline{\theta}}\left(\overline{Q}^{*} - \overline{u}^{\dagger}\partial_x\overline{\theta}^{\dagger} - \overline{\omega}^{*}\partial_p\overline{[\theta]}\right), \tag{5.5}$$

relating the stationary-eddy wind to bulk thermodynamic properties. This equation simply states that, in the presence of a meridional temperature gradient, the net heating of zonal advection, vertical advection, and diabatic terms can be balanced by meridional advection. We make a budget for the meridional component of sEKE by squaring this equation to get

$$\overline{v}^{*2} \approx \frac{1}{\left(\partial_y\overline{\theta}\right)^2}\left(\overline{Q}^{*2} + Z^2 + W^2 - 2\overline{Q}^{*}\left(Z+W\right) + 2ZW\right), \tag{5.6}$$

where $Z \equiv \overline{u}^{\dagger}\partial_x\overline{\theta}^{\dagger}$ and $W \equiv \overline{\omega}^{*}\partial_p\overline{[\theta]}$. We investigate the response of this equation to climate change averaged over a region near the mountain in the R45 experiment (30 to 60°N, 60 to 120° longitude).

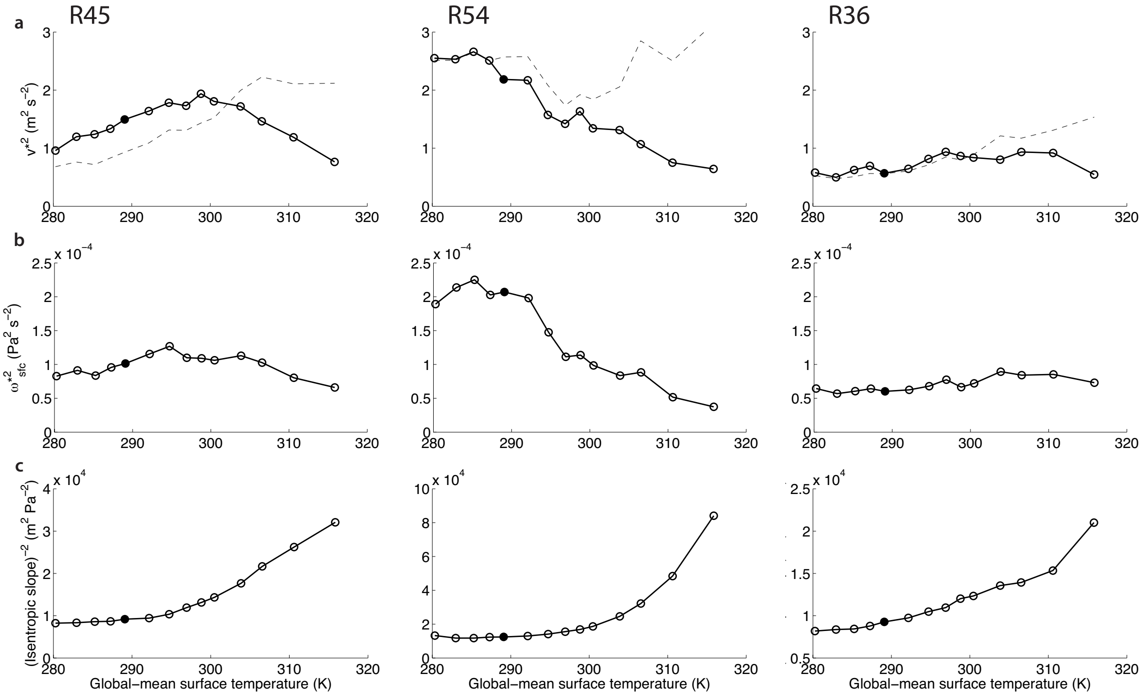

Figure 5.9: Climate change sweeps of a) 600 hPa stationary-eddy meridional wind variance in each experiment and its dominant determining factors: b) surface vertical pressure velocity and c) the squared inverse isentropic slope at 600 hPa, $(\partial_y\overline{[\theta]}/\partial_p\overline{[\theta]})^{-2}$. All quantities are averaged over latitudes within 10° of the mountain center.

To facilitate this calculation we compute an effective meridional temperature gradient,

$$(\partial_y \theta_{\text{eff}})^2(p) = \frac{\{\left(\overline{v}^* \partial_y \overline{\theta}\right)^2\}}{\{\overline{v}^{*2}\}}, \tag{5.7}$$

where $\{\cdot\}$ denotes a latitude–longitude average on a pressure level. This avoids problems of dividing by near-zero local meridional temperature gradients. The tropospheric integral of $\{\overline{v}^{*2}\}$ is shown in Fig. 5.10a. Its non-monotonic change with climate change is well described by the approximation

$$\{\overline{v}^{*2}\} \approx \frac{1}{(\partial_y\theta_{\text{eff}})^2}\left\{\overline{Q}^{*2} + Z^2 + W^2 - 2\overline{Q}^{*}\left(Z+W\right) + 2ZW\right\}, \tag{5.8}$$

the components of which are shown seperately in Fig. 5.10a. This applies equally well to an integral over the lower-troposphere (below 880 hPa), shown in Fig. 5.10b. Effective meridional temperature gradients, shown in Fig. 5.10c, are included in the denominator of each term. The temperature

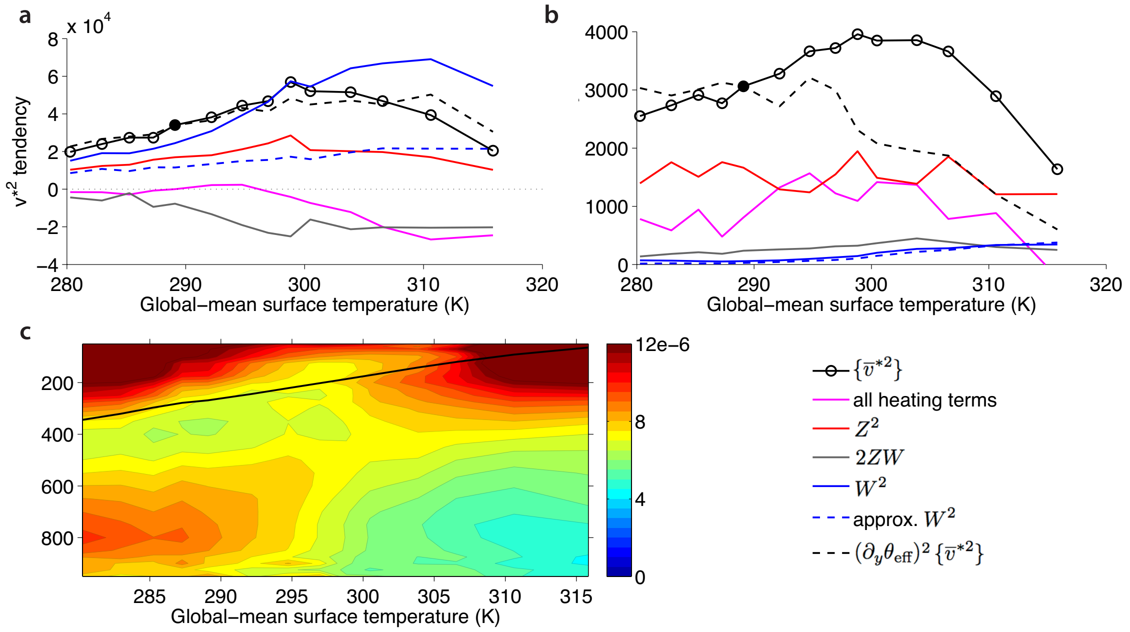

Figure 5.10: Decomposition of the $\overline{v}^{*2}$ budget (Eq. 5.6) for a) the full troposphere and b) the boundary layer (below $p = 850$ hPa) across the range of climates in the R45 experiment. Averages are taken in a box around the mountain ($\lambda \in [60\ 120]$, $\phi \in [30\ 60]$). All terms are scaled by $(\partial_y \theta_{\text{eff}})^{-1}$, which is a function of height. $(\partial_y \theta_{\text{eff}})$ is shown in (c) for the full range of climates in units of K m^{-1}. The black line shows the height of the tropopause.

gradient change can either give an increase of $\{\overline{v}^{*2}\}$ with warming, for terms concentrated in the lower troposphere, or a decrease for terms concentrated in the upper troposphere.

The variance of the vertical advection, W^2 (weighted by $(\partial_y \theta_{\text{eff}})^{-2}$), gives a good leading order approximation to tropospheric $\overline{v}^{*2}$, but several other terms play an important role. Most importantly, the net effect of zonally anomalous heating $[\overline{Q}^{*2} - 2\overline{Q}^{*}(Z+W)]$ is to damp the stationary eddy circulations in warm climates. This is the main reason why the amplitude of stationary eddies decreases in warm climates. The zonal advection term Z^2, due to the bending of isentropes into the mountain, is also important, though it does not change substantially with climate change. It is dominated by the advection by the zonal-mean zonal wind $[\overline{u}]$ and can thus be thought of as a linear term.

Another interesting finding from this analysis is that the W^2 term is larger than expected from the initial $\overline{\omega}^{*}_{\text{sfc}}$ perturbation, which would give a contribution to the W^2 term of $\partial_p[\overline{\theta}]\,(\sigma\overline{\omega}^{*}_{\text{sfc}})^2$, shown as a dashed blue line in Fig. 5.10a and b. The reason for this difference is the formation of a baroclinic vertical wind due to Sverdrup balance, $f\partial_p\overline{\omega}^* \approx \beta\overline{v}^*$, following the generation of a stationary eddy $\overline{v}^*$.

The response of orographic Rossby wave amplitude to climate change is thus determined by the initial $\overline{\omega}^*_{\mathrm{sfc}}$ perturbation, the thermal structure of the atmosphere, the linear amplification of $\overline{\omega}^*$ by Sverdrup balance, and zonally anomalous heating. We examine these factors in more detail in the following sections.

5.5.1 Zonally anomalous heating

To understand the role of zonally anomalous heating, we break up the term $\overline{Q}^*$ into its components due to transient eddies, latent heating, radiation, and sub-grid-scale turbulent mixing (Eq. 5.3). The profiles of $\overline{Q}^*_{\mathrm{param}}$ in Figs. 5.6d and 5.7d already suggest that latent-heating is important. We split the total heating term of the $\overline{v}^{*2}$ budget, $(\partial_y\theta_{\mathrm{eff}})^{-1}\left(\overline{Q}^{*2} - 2\overline{Q}^*\left(Z+W\right)\right)$, into its components in Fig. 5.11. For example, the latent-heating term is given by $(\partial_y\theta_{\mathrm{eff}})^{-1}\left(\overline{Q}^{*2}_{\mathrm{latent}} - 2\overline{Q}^*_{\mathrm{latent}}\left(Z+W\right)\right)$. It is leading order and negative throughout the range of climates. This means that latent heating damps stationary-eddy motions forced by orography as latent heating partially cancels the adiabatic cooling in the ascending motion on the upstream side of the mountain. The transient-eddy heating term is also leading order. It is positive throughout the range of climates. This results as transient-eddies move heat into the coldest region of the stationary eddy, downstream of the mountain, working against the stationary-eddy heat transport. This is analogous to the interaction of transient and stationary eddies in the entrance region of storm tracks forced by surface heating (Kaspi and Schneider, 2013), where stationary eddies act to maintain baroclinicity as transient eddies act to destroy it.

The correlation term dependent on $\overline{Q}^*_{\mathrm{latent}}\overline{Q}^*_{\mathrm{trans}}$ is small. All other terms are included with the radiation and sub-grid scale mixing term (red line in Fig. 5.11). This term is the net effect of all boundary layer processes and it does not have a significant influence on the amplitude of stationary eddies. Our motivation for grouping all these terms together is that there are large cancellations within this term, important for setting the thermodynamic structure of the boundary layer, which

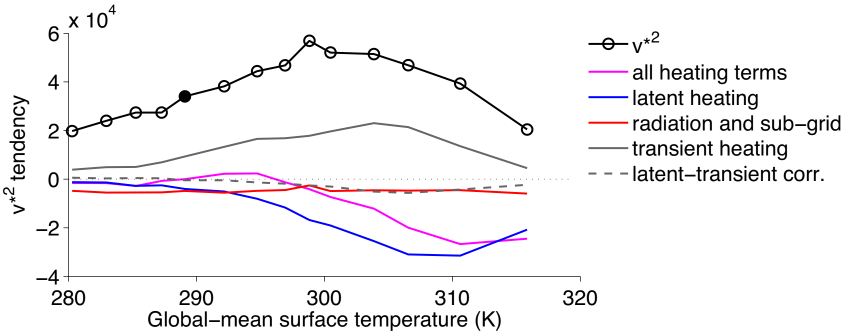

Figure 5.11: Decomposition of the zonally anomalous heating contribution to the $\overline{v}^{*2}$ budget, $(\partial_y\theta_{\mathrm{eff}})^{-1}\left(\overline{Q}^{*2} - 2\overline{Q}^{*}\,(Z+W)\right)$ (pink line), into components due to latent heating, transient-eddy heating, and radiation and sub-grid scale mixing. The correlation term between the latent and transient-eddy heating is shown, but all other correlations terms are included with the radiation and sub-grid scale mixing term, which represents the net effect of all boundary layer processes.

are not important for the stationary-eddy forcing in the free troposphere.

While zonal anomalies in latent and transient-eddy heating modultate the stationary-waves, they are themselves dependent on the stationary-eddy flow. Without zonally anomalous vertical motion, there would be no zonal anomalies in condensation. Without zonal anomalies in temperature (or tEKE), there would be no zonally anomalous transient-eddy heat fluxes. Both of these important processes can be thought of as feedbacks on stationary-wave change, rather than driving mechanisms themselves. So, despite the importance of these nonlinearities, the initial linear perturbation by the surface vertical velocity should still be the focus for stationary-wave amplitude change. The net feedback on this initial perturbation by zonally anomalous heating is negative (damping) and becomes more negative with warming.

5.5.2 Surface vertical velocity

The essential difference between R45, R54, and R36 are the different responses of $\overline{\omega}^{*}_{\mathrm{sfc}}$ to climate change, which we examine here in more detail. The spatial structure of $\overline{\omega}^{*}_{\mathrm{sfc}}$ in R45 is shown in Fig. 5.12a. It can be split up into components due to the zonal-mean and stationary-eddy surface wind according to

$$\overline{\omega}^{*}_{\mathrm{sfc}} = \left([\overline{\mathbf{u}}_{\mathrm{sfc}}] + \overline{\mathbf{u}}^{*}_{\mathrm{sfc}}\right)\cdot\nabla\overline{p}^{*}_{\mathrm{sfc}} + \overline{v}^{*}_{\mathrm{sfc}}\partial_y\left[\overline{p}_{\mathrm{sfc}}\right]. \tag{5.9}$$

The first two terms of this decomposition are shown in Fig. 5.12 b and c respectively. The third term on the right-hand side of Eq. 5.9 is negligible because $|\nabla \overline{p}^*_{\mathrm{sfc}}| \gg |\partial_y\, [\overline{p}_{\mathrm{sfc}}]|$[1]. The larger zonal-mean wind term can be further approximated by its zonal component $[\overline{\mathbf{u}}_{\mathrm{sfc}}] \cdot \nabla \overline{p}^*_{\mathrm{sfc}} \approx [\overline{u}_{\mathrm{sfc}}]\, \partial_x \overline{p}^*_{\mathrm{sfc}}$, shown in Fig. 5.12d. This term by itself gives a rough estimate of the magnitude of orographic forcing by $\overline{\varpi}^*_{\mathrm{sfc}}$ and can be calculated from the zonal-mean zonal surface wind climatology (Fig. 5.13a), which is mostly independent of the existence of the stationary wave (cf. Fig. 5.2).

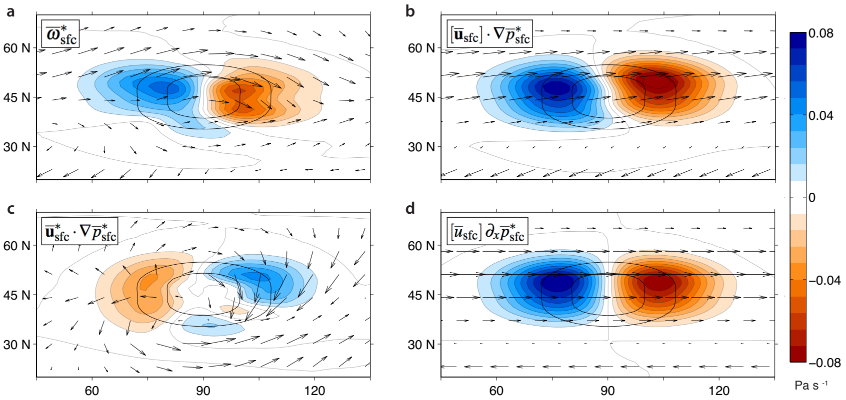

Figure 5.12: a) Map of $\overline{\varpi}^*_{\mathrm{sfc}}$ over topography (shading) in the reference climate of R45 (a). Also shown are the horizontal surface winds ($\overline{\mathbf{u}}_{\mathrm{sfc}}$, arrows) and two contours (900 and 800 hPa) of $\overline{p}_{\mathrm{sfc}}$ (black contours). (b), (c), and (d) show components of $\overline{\varpi}^*_{\mathrm{sfc}}$ based on the decomposition in Eq. 5.9.

We would like to make a scaling for the zonally-averaged spatial variance of $\overline{\varpi}^*_{\mathrm{sfc}}$, which is shown in Fig. 5.13d. Despite the importance of eddy winds in the phase structure of the response to orographic forcing (Chen and Trenberth, 1988), one might expect $[\overline{u}_{\mathrm{sfc}}]\, \partial_x \overline{p}^*_{\mathrm{sfc}}$ (Fig. 5.12d) to give a rough idea of changes in $\left[\overline{\varpi}^{*2}_{\mathrm{sfc}}\right]$ according to

$$\delta \left[\overline{\varpi}^{*2}_{\mathrm{sfc}}\right] \sim \delta \left[[\overline{u}_{\mathrm{sfc}}]^2 \left(\partial_x \overline{p}^*_{\mathrm{sfc}}\right)^2 \right]. \tag{5.10}$$

The rescaled spatial variance of $[\overline{u}_{\mathrm{sfc}}]\, \partial_x \overline{p}^*_{\mathrm{sfc}}$ is shown as a dashed line in Fig. 5.13d. The rescaling parameter is 0.4, so the eddy surface winds clearly play a role in reducing the amplitude of the response, but the goodness of fit for R45 and R54 suggests that the strength of eddy surface winds scale with the strength of the zonal-mean zonal surface wind. Based on this scaling, the two main

---

[1] A component due to the temporal correlations of the surface winds and the surface pressure gradients, $\overline{\mathbf{u}'_{\mathrm{sfc}} \cdot \nabla p'_s}$, is also negligible.

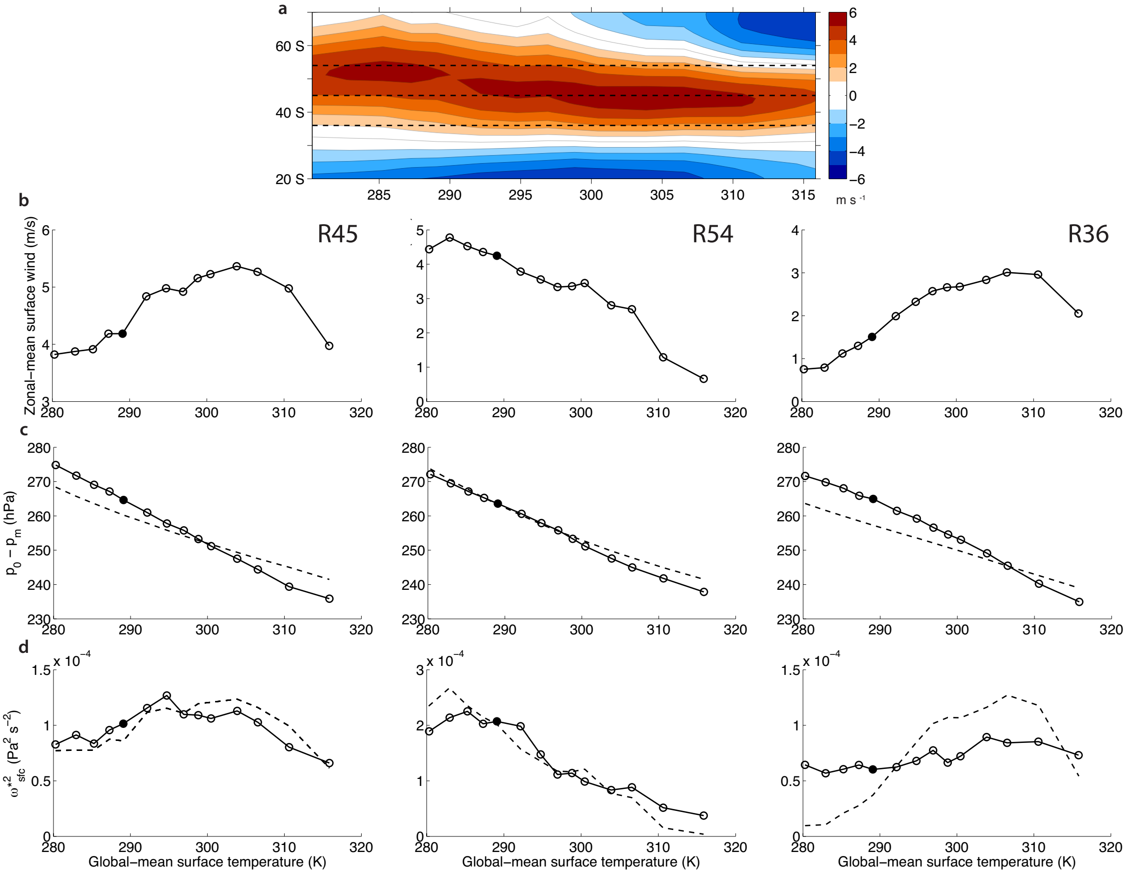

Figure 5.13: Influences on orographic forcing by $\overline{\omega}^*_{\mathrm{sfc}}$. a) Variation of zonal-mean zonal surface wind ($[\overline{u}_{\mathrm{sfc}}]$) with warming across the range of climates. Dashed lines indicate the latitude of the mountain center in each experiment. b) Average of $[\overline{u}_{\mathrm{sfc}}]$ over the range of latitudes where the mountain reaches maximum height in each experiment. c) Difference in surface pressure from the top of the mountain to a reference location and a scaling based on Eq. 5.13. d) Zonal-mean $\overline{\omega}^{*2}_{\mathrm{sfc}}$ averaged within 10° latitude of the mountain center and an estimate based on $[\overline{u}_{\mathrm{sfc}}]$ (Eq. 5.10).

influences on orographic forcing are $[\overline{u}_{\mathrm{sfc}}]$ at the latitude of the mountain and the zonal surface-pressure gradients at these latitudes. The change of the relevant surface zonal winds across the range of climates is shown for all 3 experiments in Fig. 5.13b, where $[\overline{u}_{\mathrm{sfc}}]$ is averaged over the latitudes where the topography reaches maximum height ($\phi \in [42.5, 47.5]$ for R45). The rough sense of change in stationary-wave amplitude is set by the change of $[\overline{u}_{\mathrm{sfc}}]$ over the mountain, with an increase then a decrease in R45 and a strong decrease in R54.

The $[\overline{u}_{\mathrm{sfc}}]$ is relevant to the extent that the surface winds near the mountain are dominated by the zonal-mean zonal component. This is not the case for R36 and the warmest climates of R54,

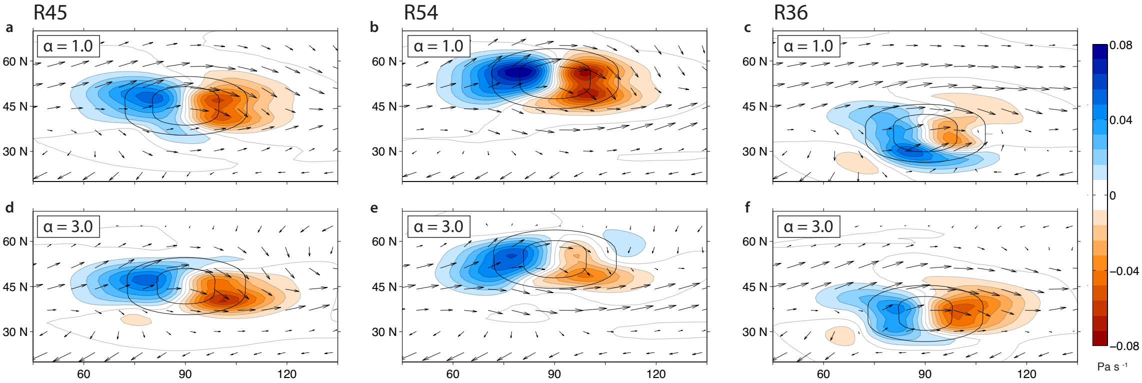

Figure 5.14: Maps of $\overline{\omega}^*_{\mathrm{sfc}}$ over topography (shading) in a,b) R45, c,d) R54, and e,f) R36, in the reference climate (a,c,e) and in the 3x optical depth simulations (b,d,f). Also shown are the horizontal surface winds ($\overline{\mathbf{u}}_{\mathrm{sfc}}$, arrows) and two contours (900 and 800 hPa) of $\overline{p}_{\mathrm{sfc}}$ (black contours).

where $[\overline{u}_{\mathrm{sfc}}]$ at the mountain is small. This can be seen from Fig. 5.14, which shows $\overline{\mathbf{u}}_{\mathrm{sfc}}$ and the resulting $\overline{\omega}^*_{\mathrm{sfc}}$ for $\alpha = 1$ and $\alpha = 3$ for all 3 experiments. Here it can be seen that the main difference between the surface winds and the zonal-mean values is due to the tendency of the wind to be deflected around the mountain following contours of surface pressure. The strength of the wind over the mountain is similar to the zonal-mean zonal wind in R45 and R54. In the R36 experiment, it is not valid to use the zonal-mean zonal surface wind as a scaling for $\left[\overline{\omega}^2_{\mathrm{sfc}}\right]$; the meridional surface wind on the equatorial side of the mountain plays a significant role (Fig. 5.14c,f).

The surface pressure variance part of the scaling is given by the difference in surface pressure between the top of the mountain (p_m) and a reference point at sea level (p_0),

$$\left[\left(\partial_x \overline{p}^*_{\mathrm{sfc}}\right)^2\right] = \left(p_m - p_0\right)^2 / \pi^2 r_e^2 \cos^2\phi. \tag{5.11}$$

The orographic pressure difference, $p_m - p_0$, decreases across the range of climates in all 3 experiments (Fig. 5.13d). This change is dominated by an increase in p_m which gives a tendency towards weaker orographic stationary waves in warmer climates. Since $\nabla\overline{p}^*_{\mathrm{sfc}}$ also shows up in the nonlinear orographic forcing by stationary-eddy surface winds, the influence of p_m on the total orographic forcing should remain, no matter the structure of the surface winds.

Using hydrostatic balance, $\partial_z \ln p = g/r_d T$, we may obtain an expression for the pressure at height z_m (the height of the mountain) over a point where the surface pressure is p_0 by integrating vertically from the surface

$$\ln p(z_m) \approx \ln p_0 - \int_0^{z_m} \frac{g}{r_d T} dz. \tag{5.12}$$

Assuming that horizontal pressure differences at z_m (normally of order 10 hPa) are much less than $p_0 - p_m \sim 250$ hPa, then $p(z_m) \approx p_m$. Substituting an approximate temperature profile $T(z) = T_0 - \Gamma z$, we obtain an expression for the top of mountain pressure in terms of a lapse rate Γ and a reference surface temperature T_0,

$$p_m \approx p_0 \left(1 - \frac{\Gamma z_m}{T_0}\right)^{g/r_d\Gamma}. \tag{5.13}$$

Evaluating T_0 as an average surface temperature at the latitude of the mountain in the eastern hemisphere (away from the mountain) and Γ as an average lapse rate over the bottom 250 hPa of the troposphere in the same region, we obtain the approximate $p_0 - p_m$ shown as a dashed line in Fig. 5.13c. By fixing T_0 and Γ independently, we can see that the increase in top-of-mountain pressure is a direct influence of the increasing surface temperature via the equation of state.

The orographic vertical surface winds, which set the initial orographic perturbation to the atmosphere, are sensitive to changes in the zonal-mean zonal surface winds, the top-of-mountain surface pressure, and the stationary-eddy modification of the surface winds. When topography is fully in the surface westerlies, the orographic stationary Rossby wave amplitude reflects the strength of zonal-mean zonal surface winds. Additionally, there is a tendency towards weaker forcing in warmer climates as the top-of-mountain surface pressure increases, a consequence of the equation of state. It is worth noting that the R54 experiment was designed to get the maximum zonal surface-wind response to climate change at the latitude of the mountain, with the hypothesis that as the zonal winds go to zero at this latitude, the stationary-wave response would also go to zero. The experiment verified this hypothesis. In this sense, this theory leads to semi-quantitative predictions of sEKE in terms of zonal surface-wind changes.

5.5.3 Vertical profile of vertical velocities

The surface vertical velocity must be balanced by a column-integrated divergence in steady state. If this divergence were barotropic (horizontal velocities independent of height), then the vertical velocity profile would be of the form $\sigma\overline{\omega}^*_{\mathrm{sfc}}$, which was already used to compute an approximate W^2 in Fig 5.10. To analyze the actual vertical velocity profiles over the mountain we average $\overline{\omega}(\sigma)$ for each level in a box surrounding the mountain (e.g. $\phi \in [30°\mathrm{N}\ 60°\mathrm{N}]$, $\lambda \in [60°\ 120°]$ for R45). Figure 5.15 shows averages conditional on the sign of $\overline{\omega}^*_{\mathrm{sfc}}$. In this way, we can see that the profiles of vertical velocity on the upwind side of the mountain (5.15a) look very different from the profiles on the downwind side (5.15b). The upwind vertical velocities are close to the barotropic expectation $\sigma\overline{\omega}^*_{\mathrm{sfc}}$, but the downwind vertical velocities extend through the free troposphere. For all but the coldest climates in R45, the vertical velocities even increase with height until they reach the upper troposphere. The profiles are the most baroclinic for the R36 experiment.

This asymmetry arrises because of the asymmetry in $\overline{v}^*$, which is larger (in absolute value) downstream of the mountain. This amplifies the descent through the advection of planetary vorticity $\beta\overline{v}^*$ and other vorticity terms. However, the vorticity budget near the mountain is complex, and the vertical velocity profile cannot be recreated without employing the full nonlinear vorticity equation. Overall, the vertical structure of vertical velocities should be thought of as an amplification of the initial vertical velocity response by the presence of the stationary eddy. The reason this is focused on the downwind side of the mountain is due to the eastward group velocity of stationary eddies and the latent heating, which damps stationary eddy motions on the upwind side.

5.5.4 Summary: thermodynamic controls of stationary-wave amplitude

The mechanisms by which flow over topography forces stationary eddies are shown schematically in Fig. 5.16. As surface winds converge with topography they force adiabatic cooling as they ascend over topography and adiabatic heating as they descend. Stationary-eddy meridional velocities arise to balance this heating/cooling. Differences in the strength of surface winds and in the isentropic slope account for most of the differences in stationary-wave response across different latitudes of

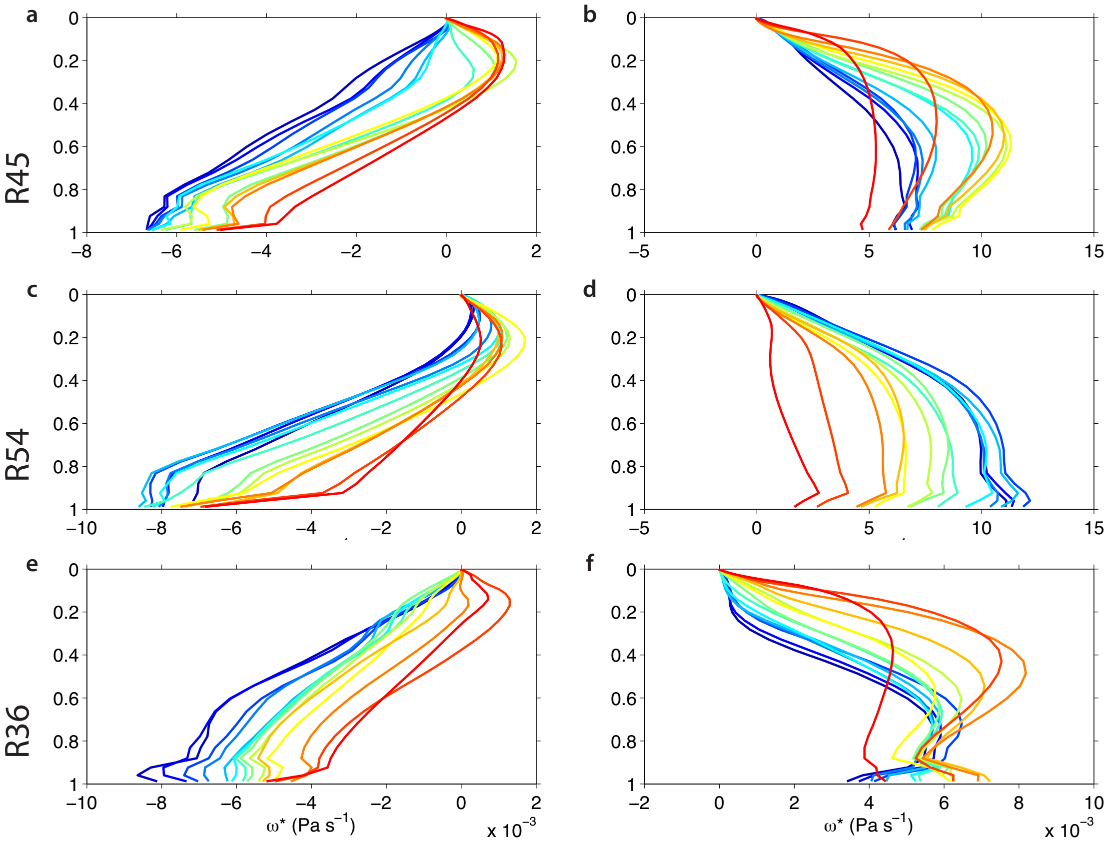

Figure 5.15: Vertical profiles of $\overline{\omega}^*$ averaged over $\phi \in [30°\text{N } 60°\text{N}]$, $\lambda \in [60° \; 120°]$ conditional on a,c,e) upward and b,d,e) downward surface vertical velocities, $\overline{\omega}^*_{\text{sfc}}$. The colors show the full range of climates (coldest = blue, warmest = red) for the a,b) R45, c,d) R54, and e,f) R36 experiments.

forcing and different mean climate states. For smaller isentropic slopes as found in warmer climates, larger meridional velocities are required to balance a given heating/cooling. This picture is complicated by other types of heating, latent heating and transient-eddy heat fluxes. Latent heating and eastward group propagation break the symmetry of the problem, leading to a cold anomaly downstream of the mountain (this is described in Hoskins and Karoly (1981) in the absence of latent heating). Transient eddies act on the resulting temperature gradients, heating this cold anomaly. The latent heating is out of phase with the initial adiabatic heating/cooling and thus damps the resulting stationary eddy. Transient-eddy heat flux convergence is in phase with the initial heating/cooling and thus amplifies the stationary eddy. The adiabatic heating is also amplified in the descent region by stationary-eddy subsidence. All of this leads to a large equatorward velocity downstream of the mountain. This perturbation then propagates downstream according to Rossby wave

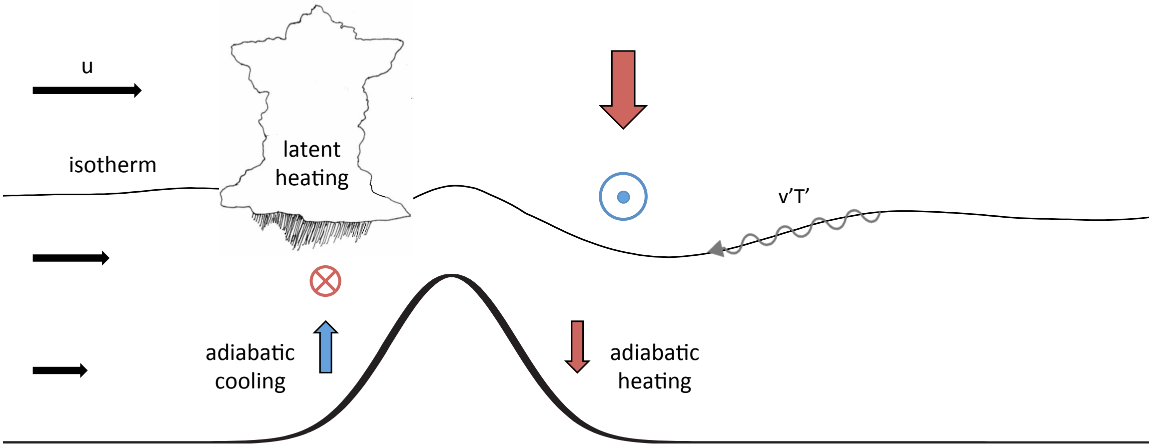

Figure 5.16: Schematic of the effect of topography on stationary-eddy thermodynamics. The response is asymmetric, with larger meridional winds on the downstream side of the mountain associated with a cold anomaly. Nonlinear terms such as the geostrophic vertical wind and the transient-eddy heat fluxes act primarily in this downstream region, while latent heating acts in the upstream region.

dynamics (Hoskins and Karoly, 1981).

5.6 Meridional and vertical dispersion

This chapter has focused on the amplitude of orographically forced Rossby waves directly over the topographic forcing. To the extent that the resulting Rossby wave acts linearly, this will set the global sEKE in this simple setup with a single zonal asymmetry. Through comparison of Figs. 5.5 and 5.9, this is at least qualitatively true. However, changes in the distribution of sEKE within the climate system are interesting in their own right and could influence the amplitude of zonal anomalies in other climate variables such as $P - E$ (see Chapter 3). We discuss these changes qualitatively, as the theory governing the meridional and vertical propagation is well established (Hoskins and Karoly, 1981; Held, 1983; Plumb, 1985)

Figure 5.17 shows the latitude-sigma distribution of sEKE in the three orographic forcing experiments, for the reference climate and a warmer climate ($\alpha = 3.0$). The sEKE is high near the surface at the latitude of forcing, is high following the latitudinal and vertical propagation of stationary eddies, then has a local maximum in the upper troposphere at the latitude of maximum zonal

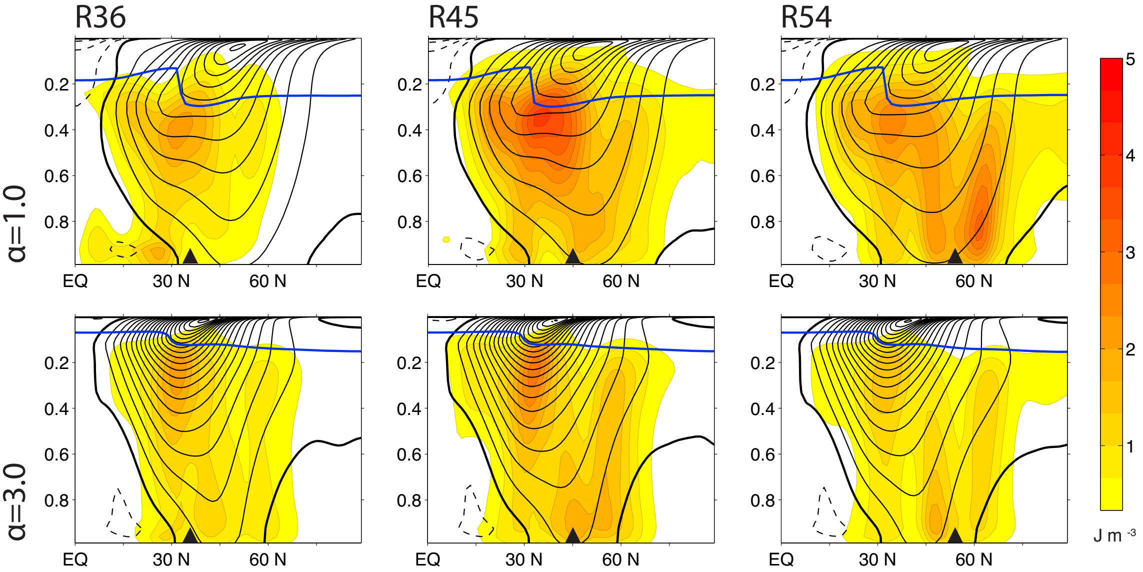

Figure 5.17: Vertical profile of sEKE $= \frac{1}{2}\rho\left(\overline{u}^{*2} + \overline{v}^{*2}\right)$ superimposed on contours of the zonal-mean wind (contour interval 5 m s^{-1}, thick contour is $[u] = 0$ line). The reference climate ($\alpha = 1.0$, top) and a warm climate ($\alpha = 3.0$, bottom) are shown for R36, R45, and R54. Also shown is the tropopause height computed from the 2 K km^{-1} lapse-rate criterion (blue line). The triangle in each plot shows the latitude of topographic forcing.

wind. The upper-tropospheric maximum reflects the refraction of Rossby waves into the jet stream (Hoskins and Karoly, 1981). This upper-tropospheric peak defines the latitude of the maximum of vertically-integrated sEKE throughout the range of climates, as shown in Fig. 5.18. Despite the differences in forcing and the resulting differences in global-mean sEKE, all three orographic forcing experiments have sEKE maxima at about the same latitude. This latitude is approximately that of the maximum jet speed near the tropopause (dashed line in Fig. 5.18 computed from the upper-tropospheric zonal wind, shown in a). As the jet becomes more subtropical with warming, stationary-eddies also move equatorward into the subtropics.

The vertical dispersion of stationary Rossby waves is inhibited in warm climates due to the increased upper tropospheric shear resulting from tropical upper-tropospheric warming. This can be seen using the Charney and Drazin (1961) refractive index and primarily affects the distribution of sEKE in the stratosphere (compare the decay of sEKE beyond the tropopause for $\alpha = 1.0$ and $\alpha = 3.0$ in Fig. 5.17). This effect starts to limit sEKE to the lower-troposphere in the warmest climates resulting in a reduction of upper-tropospheric sEKE, as is already apparent in $\alpha = 3.0$

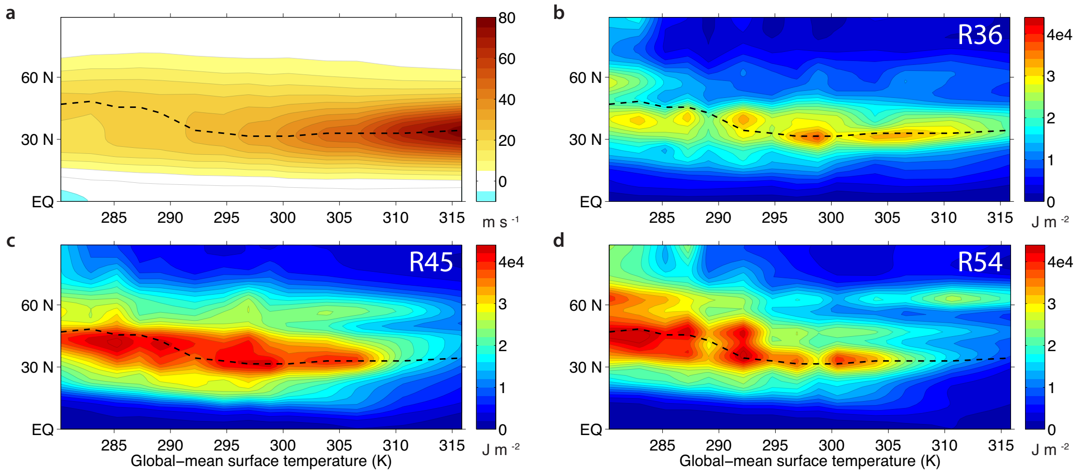

Figure 5.18: a) Upper tropospheric zonal wind, averaged over the 5 levels below the extratropical (35-70° latitude) tropopause. The maximum value for each climate is shown with a dashed line. b-d) Tropospheric vertically-integrated sEKE versus latitude across the range of climates in R36, R45, and R54. Dashed line as in a).

(Fig. 5.17). This trapping of stationary waves in the lower troposphere may contribute to the decrease in sEKE in the warmest climates. However, this is just an alternative perspective on the decrease in amplitude of upper-tropospheric stationary eddies that results from the increase in upper-tropospheric temperature gradient, as already seen in the thermodynamic analysis (Fig. 5.10c).

5.7 Changes in stationary-eddy length scale

Changes in stationary-eddy length scale can be an important aspect of changes in stationary waves with warming. An increase in stationary wave length scale has been implicated in northern hemisphere $\overline{v}^*$ changes over the next century (Simpson et al., 2015). In CMIP5, this change arises simply from the increase in jet speed in the upper troposphere due to tropical upper-tropospheric warming. Other studies have argued for increased persistence of high wavenumber Rossby waves as a result of polar amplification and a decrease in strength of the jet stream (Francis and Vavrus, 2012; see also Barnes, 2013). Polar amplification and tropical upper-tropospheric warming are competing effects on the strength of the jet and it is still uncertain how these changes will play out in the future climate

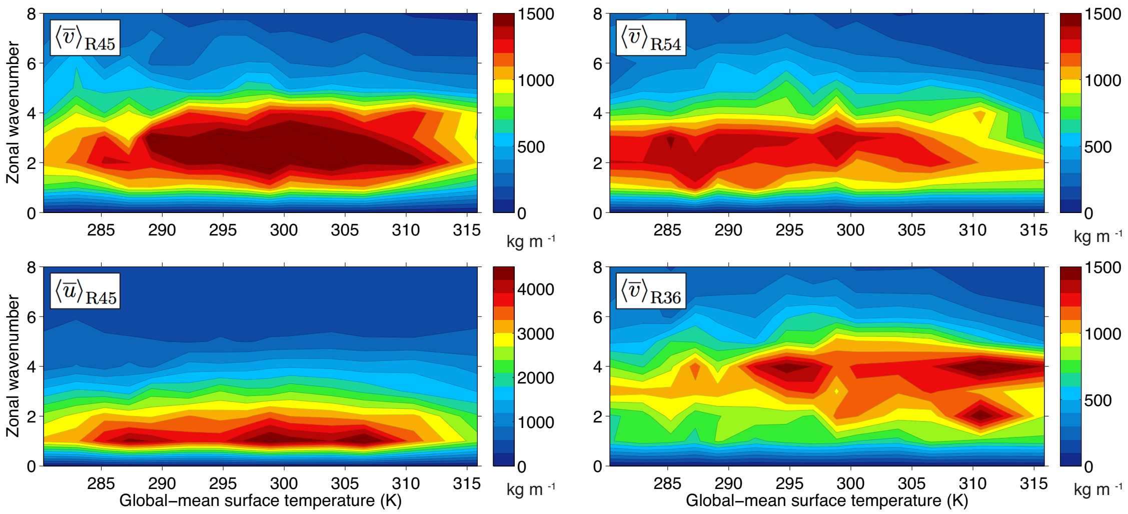

Figure 5.19: Meridional-average zonal wavenumber spectra of the vertically integrated (barotropic) winds, $\langle\overline{v}\rangle$ and $\langle\overline{u}\rangle$, versus global-mean surface temperature. The spectra of $\langle\overline{v}\rangle$ is shown for R45, R54, and R36. The spectra of $\langle\overline{u}\rangle$ is dominated by k = 1 in all three experiments, so it is only shown for R45.

(Barnes and Screen, 2015). Our model has both polar amplification and tropical upper-tropospheric warming, with the net result of a reduction in strength of the eddy driven jet (Fig. 5.1) and a large increase in strength of the subtropical jet and upper-tropospheric zonal wind (Fig. 5.18a). We would like to understand how these changes affect the stationary-eddy length scale. We investigate the latitudinally averaged zonal phase spectra of the vertically-integrated meridional wind $\langle\overline{v}\rangle^*$, shown in Fig. 5.19 (results are qualitatively similar for the 600 hPa meridional wind).

None of the phase spectra show considerable shifts with climate change (note that the change in amplitude of wavenumbers 2-4 simply reflects that change in total sEKE). The phase spectra in R45 and R54 show little spectral density beyond a zonal wavenumber of $k = 4$. In R36, there is little spectral density beyond $k = 5$. The increase in zonal wind in CMIP5 mostly has an effect on wavenumbers $k > 4$, which are not strongly forced in our model given the topography used. This is based on the changes in the stationary-eddy wavenumber,

$$K_s = \sqrt{k^2 + l^2} \approx \sqrt{\frac{\beta}{[\overline{u}]}}, \tag{5.14}$$

which would decrease with warming, allowing eastward advection of high-wavenumber Rossby waves by the zonal wind. Based on the upper-tropospheric zonal wind in Fig. 5.18a, the stationary-eddy wavenumber does not decrease below $K_s = 4$ until the warmest two climates, above 305 K global-mean surface temperature. As such, the low wavenumbers forced by these experiments can be stationary in the jet stream throughout the range of climates. Consequently, the zonal wavenumber spectrum remains mostly unchanged across the range of climates.

The zonal wavenumber spectrum of the vertically-integrated zonal wind $\langle \overline{u} \rangle^*$ is dominated by k = 1 for all climates and all experiments (Fig. 5.19, omitted for R54 and R36). The stationary eddies forced by the topography in these idealized model experiments are planetary scale, such that they are not affected by changes in the stationary-eddy wavenumber K_s.

5.8 Discussion and conclusions

It is clear from the last two sections that changes in meridional/vertical dispersion and changes in stationary-eddy lengthscale are not the dominant changes in stationary-eddies with climate change. The non-monotonic change in global stationary-eddy kinetic energy (or stationary-eddy amplitude) is felt in most regions of the globe. As such, the key findings of this chapter are the mechanisms by which changes in zonal-mean winds, meridional temperature gradients, stratification, and zonally anomalous latent heating influence the amplitude of orographic stationary waves across a wide range of climates.

The zonal-mean winds influence the forcing of orographic stationary waves primarily through their role in the orographic vertical wind, $\overline{\omega}^*_{\mathrm{sfc}}$. This orographic slope wind is also important in determining orographic $P-E$, as was pointed out in Chapter 3. Here, we will discuss the implications of the findings of this chapter for orographic $P-E$ and then present our conclusions.

5.8.1 On orographic P - E

In Chapter 3, we presented an expression for orographic net precipitation:

$$\left(\overline{P}^* - \overline{E}^*\right)_{\text{orographic}} \approx -\frac{1}{g}\left(\overline{q}_{\mathrm{sfc}}\overline{\omega}^*_{\mathrm{sfc}}\right)^*. \tag{5.15}$$

In this chapter, we investigated changes in $\overline{\omega}^*_{\mathrm{sfc}}$ in 3 different orographic forcing experiments (Section 5.5.2). We found that changes in the zonal-mean zonal surface wind $[\overline{u}_{\mathrm{sfc}}]$ roughly determine changes in $\overline{\omega}^*_{\mathrm{sfc}}$ according to,

$$\overline{\omega}^*_{\mathrm{sfc}} \sim [\overline{u}_{\mathrm{sfc}}]\,\partial_x \overline{p}^*_{\mathrm{sfc}}. \tag{5.16}$$

The decrease in surface-pressure gradients due to the warming of the mean climate also plays an important role.

Putting this together, we have everything needed to say how orographic $\overline{P}^* - \overline{E}^*$ responds to climate change in a variety of cases. A scaling of the form

$$\left(\overline{P}^* - \overline{E}^*\right)_{\mathrm{orographic}} \sim -\overline{q}_{\mathrm{sfc}}\,[\overline{u}_{\mathrm{sfc}}]\,\partial_x \overline{p}^*_{\mathrm{sfc}} \tag{5.17}$$

should suffice for a qualitative assessment of changes in orographic $P-E$. Note that this expression applies both for the wet zone on the windward side of the mountain and the rain shadow in the lee of the mountain. Keep in mind however, that this does not include the influence of transient-eddy moisture fluxes, which are also important in some cases.

Based on this expression, we can say that orographic $P-E$ is likely to increase with global warming as the moisture content of the atmosphere increases. This would be partially offset by the decrease in surface pressure gradients with warming. The expected poleward migration of surface winds (Kushner et al., 2001; Yin, 2005) in the Earth climate system would probably also play a role in amplifying orographic $P-E$ at high latitudes while reducing it at lower latitudes. We believe this compliments studies of orographic precipitation (Roe, 2005; Shi and Durran, 2014), because while some applications require knowledge of orographic precipitation, other applications, such as hydrology and geomorphology require knowledge of orographic $P-E$.

5.8.2 Conclusions

In this chapter, we set out to understand why the the zonal variance of stationary-eddy vertical velocity increased with warming until about 300 K global-mean surface temperature, then decreased with further warming. These changes are related to a global change in stationary-eddy kinetic energy (sEKE). This change is sensitive to the latitude of topography. Idealized GCM experiment with topography at different latitudes create qualitatively different sEKE responses. The reason for this sensitivity is that the zonal winds at the latitude of the mountain are a key factor in forcing orographic stationary waves, through their contribution to orographic ascent / descent and adiabatic cooling / heating. The stationary-eddy meridional winds needed to balance this heating / cooling depend on the isentropic slope, which decreases with warming, leading to an increase in stationary-wave amplitude. Latent heating, which damps orographic stationary-eddies throughout the range of climates studied, becomes important in warm climates, leading to a reduction in stationary-wave amplitude. The amplification of subsidence downstream of topography by the stationary-eddy vorticity balance and transient-eddy heat fluxes, both tend to increase the amplitude of orographic stationary waves, but do not have a large response to climate change.

To summarize, we group the most important influences on orographic stationary Rossby waves by whether they increase of decrease the stationary-wave amplitude with warming.

Non-monotonic change with warming:

- Change in zonal surface winds at the latitude of the mountain

Decreased stationary-wave amplitude with warming:

- Decrease in top-of-mountain surface pressure due to increased surface temperature
- Increased damping by latent heating

Increased stationary-wave amplitude with warming:

- Decreased isentropic slope due to increased extratropical static stability and reduced meridional temperature gradients

Amplify changes due to other factors:

- Amplified stationary-wave subsidence downstream of topography
- Transient-eddy heat fluxes into cold region downstream of topography

Chapter 6

Circulation changes in the equatorial heating experiment

Abstract

This chapter considers changes in zonally anomalous tropical circulations with global warming under fixed ocean heat-flux forcing. A decrease in strength of such circulations has been identified as a robust response to climate change, though there are still open questions on the mechanisms behind this response. Variation of the aspect ratio of ocean heating in an idealized GCM reveals that the Walker circulation strength is constant across a wide range of vorticity budget regimes. This suggests that there are independent energetic constraints on the Walker circulation strength. These energetic constraints take the form of an increase in gross moist stability (GMS) with warming across a wide range of climates, which increases the energy expended per unit mass of deep convection. The increase in GMS with warming results primarily from the increasing depth of deep convection and the corresponding increase in tropopause height. These mechanisms are used to derive quantitative scalings for the change in Walker circulation strength with warming. By using baroclinic mode theory, the Walker circulation strength can be estimated solely from the profile of tropical-mean temperature and the strength of zonally anomalous heating. This chapter also examines the consequences of these Walker circulation strength on the extratropical circulation. The extratropical response is determined primarily by the wavenumber spectrum of tropical forcing and the existence of turning latitudes.

6.1 Introduction

The slowdown of the tropical overturning circulations, such as Walker circulations, with global warming is robust across many types of models and observations (Held and Soden, 2006; Vecchi et al., 2006; Vecchi and Soden, 2007; Merlis and Schneider, 2011). Global energetic constraints on evaporation/precipitation lead to a reduction of the strength of overturning circulations globally in response to increases in the surface specific humidity or the lapse rate of specific humidity (Betts, 1998; Held and Soden, 2006; Vecchi and Soden, 2007; Schneider et al., 2010). Zonally anomalous circulations in the tropics make up 40% of the total overturning of the atmosphere in idealized GCM experiments with zonally anomalous ocean heating (experiments presented herein; calculated from the upward portion of $\overline{\omega}_{500}$), so the naive assumption would be that they account for 40% of the decrease in overturning resulting from energetic limitations. As pointed out by Held and Soden (2006) and Vecchi and Soden (2007), it is not unreasonable to think that even more of the decrease in overturning will be concentrated in the zonally anomalous circulations, since zonal-mean circulations (e.g., the Hadley cell) have to obey angular momentum constraints as well as energetic constraints.

However, the global energetic constraints do not provide a quantitative theory for the strength of zonal overturning circulations in particular. We need to look elsewhere to explain the decrease in tropical $\mathrm{rms}\big(\overline{\omega}^{*}_{p_i}\big)$ shown in Fig. 3.13. Merlis and Schneider (2011) observe that if $\overline{P}^{*}$ is constant across a range of climates, the Walker circulation strength is constrained to decrease rapidly with warming according to

$$\overline{\omega^{\uparrow}}^{*} \sim -\frac{\overline{P}^{*}}{\Delta_v q_s}, \tag{6.1}$$

where $\omega^{\uparrow}$ is the upward portion of vertical velocity and $\Delta_v q_s$ is the tropospheric vertical difference of saturation specific humidity. The strength of the upwelling branch of the Walker circulation thus scales with $(\Delta_v q_s)^{-1}$ or approximately inversely with surface specific humidity. We can obtain a similar result using Eq. 3.12 where

$$\overline{\omega}^*_{850\ \mathrm{hPa}} \sim -g\frac{\overline{P}^* - \overline{E}^*}{[\overline{q}_{\mathrm{sfc}}]}. \tag{6.2}$$

Thus the strength of the Walker circulation scales with $[\overline{q}_{\mathrm{sfc}}]^{-1}$ as long as $\overline{P}^* - \overline{E}^*$ is fixed across the range of climates. Neither of these explanations is a closed theory because we have not yet explained why $\overline{P}^* - \overline{E}^*$ is constant across the range of climates; an independent theory of the Walker circulation strength is required.

The vorticity budget provides some additional constraints on vertical motion, as was seen already in Chapters 2 and 3. This analysis can be further modified to focus on mid-tropospheric vertical velocities and the strength of overturning in particular. An alternative perspective comes from integrating over the upper troposphere instead of the lower troposphere, eliminating the importance of surface drag. A number of studies have used the moist static energy (MSE) equation and baroclinic mode theory to further constrain tropical circulations (Neelin and Held, 1987; Neelin and Zeng, 2000; Chou and Neelin, 2004). In particular, Chou and Neelin (2004) propose the *anomalous gross moist stability* mechanism that explains some aspects of the slowdown of tropical overturning circulations with warming based on the increase of gross moist stability (GMS), an effective static stability felt by tropical circulations. The increase is due to an increasing depth of deep convection and is partially cancelled by an increase in lower-tropospheric specific humidity. This increases the atmospheric energy requirements for deep convection. This is closely related to the *warm gets wetter* mechanism, where regions with enhanced SST warming experience locally reduced GMS and enhanced precipitation (Xie et al., 2010; Huang et al., 2013). It has not been examined whether GMS continues to increase with warming beyond next-century or doubled-CO_2 climates. We will examine the MSE equation in idealized GCM simulations with zonally anomalous ocean heating to see how the *anomalous gross moist stability* mechanism plays out across a wide range of climates.

The idealized GCM experiments used are the equatorial heating experiments of Chapter 3, with several additional configurations introduced in Section 6.2. The vorticity budget controls on mid-tropospheric vertical velocities are analyzed in Section 6.3, uncovering a consistent circulation strength across a wide range of vorticity budget regimes. In Section 6.4, we analyze energetic controls on the Walker circulation strength, as diagnosed from the MSE equation and gross moist stability. The influence Walker circulation changes have on extratropical stationary eddies is then considered in Section 6.5. Section 6.6 provides some discussion and conclusions, including a synthesis with other parts of this thesis.

6.2 Additional experiments

Variations of the aspect ratio of the equatorial heating will prove insightful in the mechanisms governing Walker circulation strength. Chapter 3 uses equatorial heating of the form,

$$\begin{aligned}\nabla \cdot F_1(\phi) = Q_1 \exp&\left[-\frac{(\lambda-\lambda_E)^2}{2\sigma_\lambda^2} - \frac{\phi^2}{2\sigma_\phi^2}\right]\\ - Q_1 \exp&\left[-\frac{(\lambda-\lambda_W)^2}{2\sigma_\lambda^2} - \frac{\phi^2}{2\sigma_\phi^2}\right],\end{aligned} \tag{6.3}$$

with $Q_1 = 50$ W m^{-2}, $\lambda_W = 90^\circ$, $\lambda_E = 270^\circ$, $\sigma_\lambda = 12.5^\circ$, and $\sigma_\phi = 8^\circ$. The heating thus has an aspect ratio $a = \sigma_\lambda/\sigma_\phi = 1.56$. We now consider 5 experiments with

$$\begin{pmatrix}\sigma_\phi\\ \sigma_\lambda\\ a\end{pmatrix} = \begin{pmatrix}5^\circ\\ 20^\circ\\ 4\end{pmatrix}, \begin{pmatrix}6^\circ\\ 16.67^\circ\\ 2.78\end{pmatrix}, \begin{pmatrix}7^\circ\\ 14.25^\circ\\ 2.04\end{pmatrix}, \begin{pmatrix}8^\circ\\ 12.5^\circ\\ 1.56\end{pmatrix}, \begin{pmatrix}10^\circ\\ 10^\circ\\ 1\end{pmatrix},$$

which we refer to as Q5, Q6, Q7, Q8, and Q10 respectively. The area-integrated amplitude of forcing is kept fixed by keeping Q_1 and $\sigma_\lambda \cdot \sigma_\phi$ constant.

6.3 Walker circulation vorticity budget

The vorticity budget of the Walker circulation, which was already addressed for the lower troposphere in Section 3.3.2, is a good place to start to understand controls on Walker circulation strength. This is motivated in part by the results of Levine and Boos (2016), where the lower-tropospheric vorticity budget was used to relate stationary-eddy ascending motion forced by subtropical heating to lower-tropospheric zonal temperature gradients. Zonal temperature gradients in the tropics are understood to decrease rapidly with warming based on energetic constraints on evaporation (Merlis and Schneider, 2011). If the Walker circulation strength could be tied to zonal temperature gradients, then the decrease in Walker circulation strength would be a direct result of the energetic constraints on evaporation. This would also fit with the observed correlation between zonal SST gradients and the strength of Walker circulations (Bjerknes, 1969).

The conclusion of Section 3.3.2 was that stationary-eddy vertical motion is well described by a combined Sverdrup-Ekman balance in the lower troposphere, except within 2° latitude of the equator. The budget of Section 3.3.2 was focused on understanding $\overline{P}^* - \overline{E}^*$ and thus focused on a moisture-weighted vorticity budget analysis from the surface to 850 hPa. If our goal is to understand the strength of the Walker circulation, it is beneficial to focus instead on the vorticity budget controls on $\overline{\omega}^*$ in the free troposphere. We examine a budget for $\overline{\omega}^*$ based on the zonally anomalous vorticity equation integrated from the surface or from the top of the domain,

$$\overline{\omega}^*(p) = -\frac{g}{f}\left\langle \beta\overline{v}^* + \overline{T}^* + \overline{N}^* \right\rangle_p^{p_s} - \frac{g}{f}\nabla \times \overline{\tau}^* \tag{6.4a}$$

$$\overline{\omega}^*(p) = \frac{g}{f}\left\langle \beta\overline{v}^* + \overline{T}^* + \overline{N}^* \right\rangle_0^{p}. \tag{6.4b}$$

We focus on applying the $\overline{\omega}^*$ (vorticity) budget (Eq. 6.4) at a representative 600 hPa level.

With two equations for $\overline{\omega}^*_{600}$ and multiple experiments, it is best to first look at average contributions of the different vorticity-budget terms to $\overline{\omega}^*_{600}$, before looking at the spatial distribution of

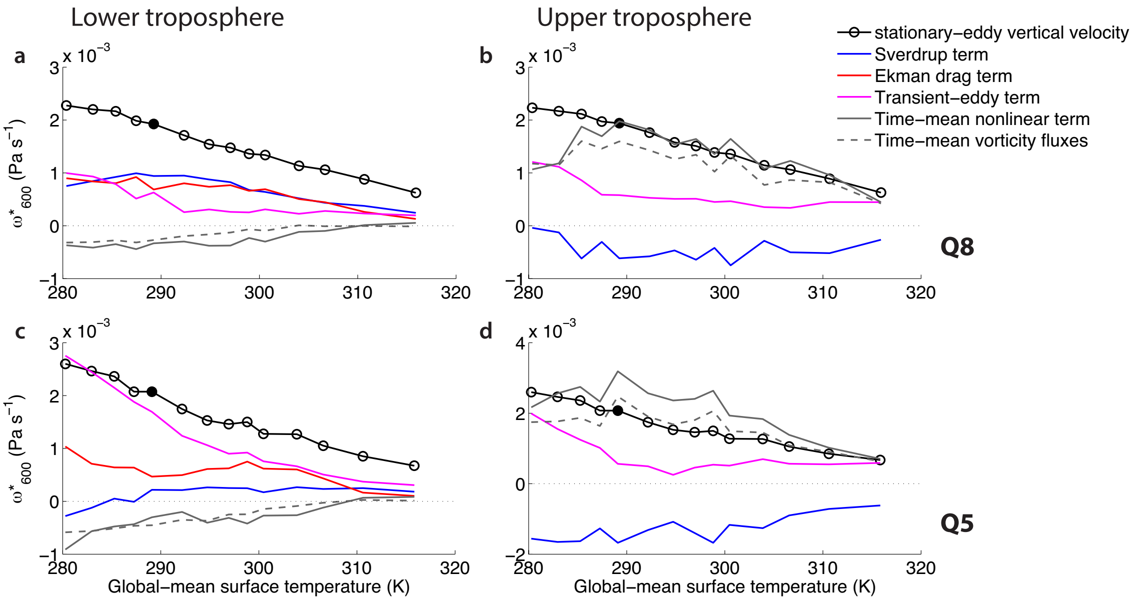

Figure 6.1: Vorticity budget controls on $|\overline{\omega}^*_{600}\rangle = -\langle\overline{\omega}^*_{600}|$ (black line) across the range of climates in a,b) Q8 and c,d) Q5. Vorticity budgets are calculated integrated (left) below 600 hPa or (right) above 600 hPa.

these terms. To this end we look at vorticity budget terms averaged with the operator,

$$|\cdot\rangle \equiv \int (\cdot)\mathrm{H}(\overline{\omega}^*_{600})d\mathcal{A}, \tag{6.5}$$

where the integration area is global. For terms that average to zero (stationary-eddy components), this differs only by a sign from

$$\langle\cdot| \equiv \int (\cdot)\mathrm{H}(-\overline{\omega}^*_{600})d\mathcal{A}. \tag{6.6}$$

The contributions to $\overline{\omega}^*_{600}$ based on the heavyside-averaged upper- and lower- tropospheric vorticity equations are shown in Fig. 6.1 for experiments Q8 and Q5.

The experiments show similar vorticity balances in the upper troposphere, with time-mean nonlinear terms ($\overline{N}^*$, grey line), and particularly horizontal vorticity fluxes by stationary eddies (dashed grey line), governing the changes in $\overline{\omega}^*_{600}$ for all climates except the coldest 2. However, in the lower troposphere, the vorticity budgets are drastically different. In Q8, the declining strength of $\overline{\omega}^*_{600}$ with warming comes primarily from the combined Ekman-Sverdrup balance (red and blue lines),

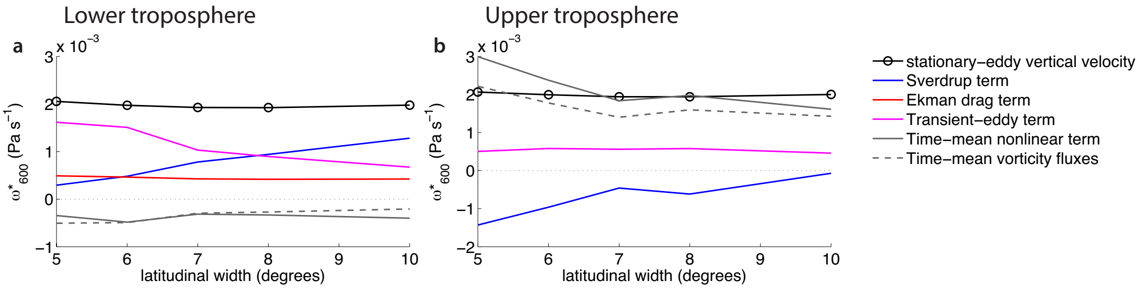

Figure 6.2: Vorticity budget controls on $|\overline{\omega}^*_{600}\rangle = -\langle\overline{\omega}^*_{600}|$ (black line) across the range of latitudinal widths of forcing. Vorticity budgets are calculated integrated a) below 600 hPa or b) above 600 hPa.

with some contribution from transient-eddy vorticity fluxes. On the other hand, in Q5, most of the decrease in $\overline{\omega}^*_{600}$ comes from the decrease in transient-eddy vorticity fluxes (pink line). Despite these differences, there is not much difference between the actual vertical velocities in these experiments.

This is even more apparent when examining the vorticity budget as the aspect ratio is varied with the optical depth at a reference value ($\alpha = 1.0$), as shown in Fig. 6.2. The lower-tropospheric transient eddies become less important for the vertical velocity as the latitudinal width of the heating increases. The Sverdrup balance vertical velocity, $-\frac{g}{f}\,|\langle\beta\overline{v}^*\rangle\rangle$ increases such that the vertical velocity at 600 hPa remains unchanged throughout the range of aspect ratios. In the upper troposphere, there is a decrease in the extent to which the Sverdrup balance vertical velocity is out of phase with the full vertical velocity. There is a corresponding change in the fraction of the vertical velocity that is balanced by stationary-eddy vorticity fluxes.

The fact that the vertical velocity is unchanged despite large changes in the underlying vorticity balance suggests that there must be independent constraints on the vertical velocity and that the vorticity budget is balanced in whatever way is easiest based on the background absolute vorticity. This is our motivation for investigating energetic constraints on Walker circulation vertical motion in the next section. Despite this, we would like to examine some aspects of the linear and transient-eddy regimes of the lower-tropospheric vorticity balance.

The spatial distribution of vorticity terms is shown for the linear regime (represented by Q8) in Fig. 6.3. The spatial distribution of Sverdrup upwelling ($-\frac{g}{f}\,\langle\beta\overline{v}^*\rangle$) is qualitatively similar to distribution of zonal temperature gradients, with poleward motion east of the heating and west

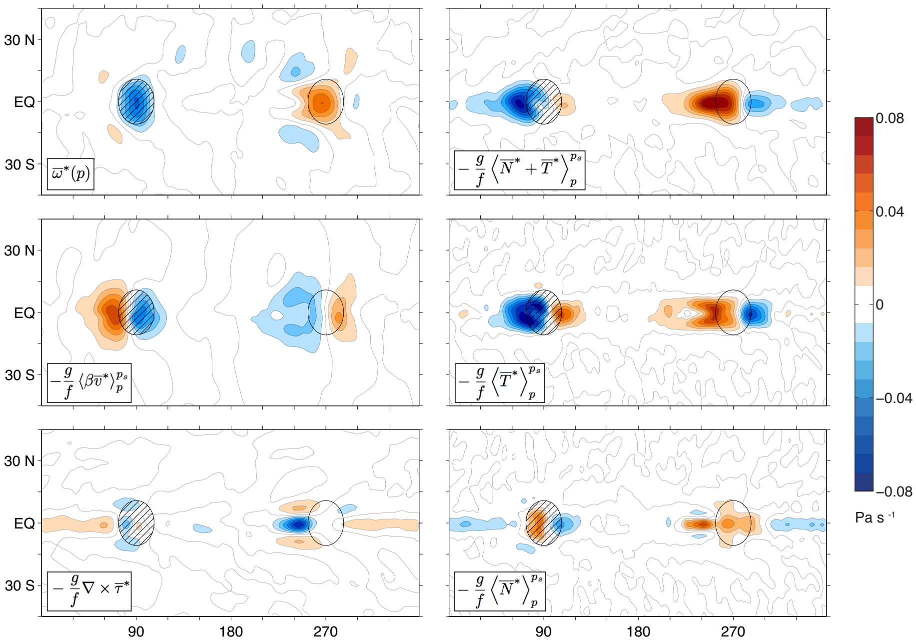

Figure 6.3: Lower tropospheric vorticity budget controls on $\overline{\omega}^*_{600}$ in the reference climate ($\alpha = 1.0$) of Q8. Terms are labelled as defined in the text.

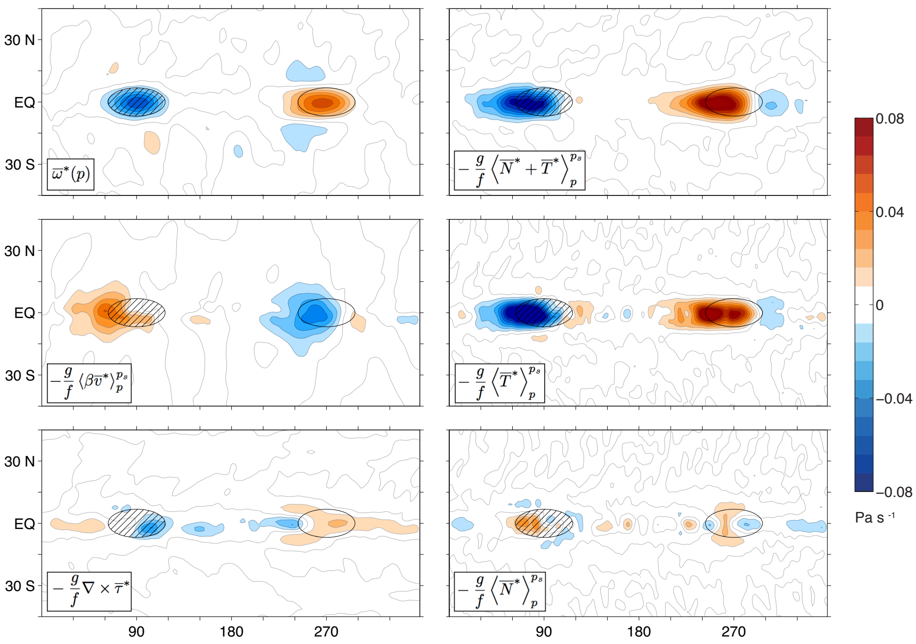

Figure 6.4: Lower tropospheric vorticity budget controls on $\overline{\omega}^*_{600}$ in the reference climate ($\alpha = 1.0$) of Q5. Terms are labelled as defined in the text.

of the cooling and equatorward motion west of the heating and east of the cooling. However, we find that thermal wind balance is not accurate enough this close to the equator to quantitatively link Sverdrup vertical motion and zonal temperature gradients. Additionally, the Sverdrup vertical velocity is mostly phase shifted from the actual vertical velocity where stationary-eddy overturning is strongest. The positive contribution to stationary-eddy overturning mostly comes on the edges of the convecting region, where the Sverdrup term is in phase. In the region of heating, transient-eddies are important for the westward propagation of the zone of convection. This could be accomplished by vorticity tendencies associated with equatorial Rossby waves and Kelvin waves.

The regime where the lower-tropospheric vorticity budget is dominated by transient eddies (represented by experiment Q5) is shown in 6.4. In this case, as in the linear regime, vertical motion is mostly confined to the region directly over the ocean heating/cooling. Here the Sverdrup term ($-\frac{g}{f}\langle\beta\overline{v}^*\rangle$) actually plays a role in reducing the vertical motion associated with transient-eddy vorticity tendencies. This results as ageostrophic meridional motion transports mass into the convergence

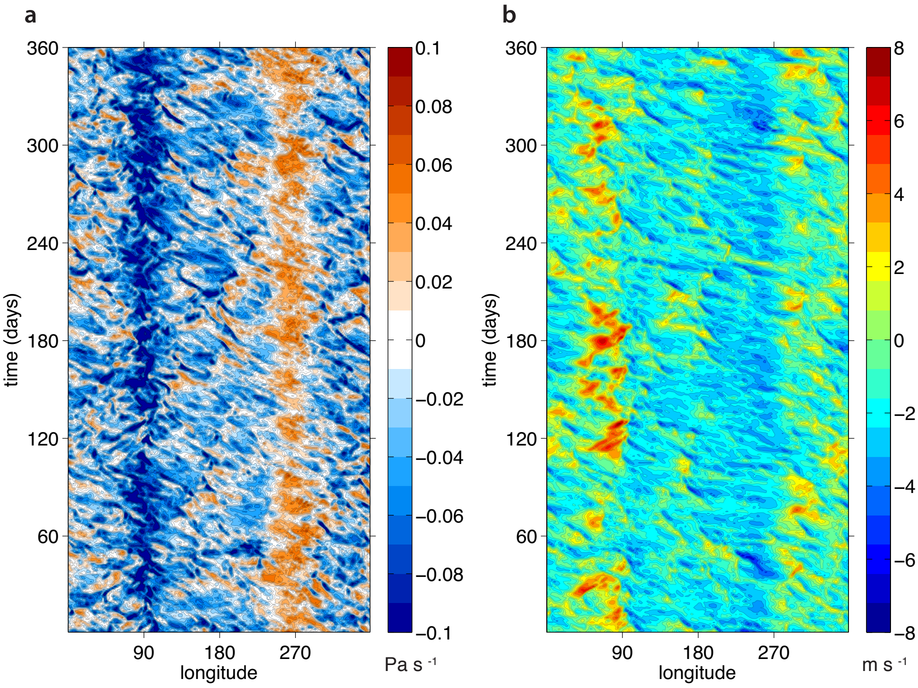

Figure 6.5: Hovmöller diagrams for one year of simulation in the transient-eddy dominated regime (Q5). a) $\overline{\omega}_{600}$ averaged within 5° of the equator and b) $\overline{u}_{\mathrm{sfc}}$ averaged within 2° of the equator.

zone on the equator. Vertical motion can thus only come from nonlinear vorticity fluxes. This is predominantly accomplished by transient eddies ($-\frac{g}{f}\left\langle \overline{T}^{*}\right\rangle_{p}^{p_s}$).

To investigate the source of this transient-eddy vorticity tendency, we present in Fig. 6.5 Hovmöller diagrams for one-year of simulation in the reference climate of the Q5 experiment, where the transient-eddy tendency is strongest. The left panel shows the bursty nature of convection over the heat source (90° longitude) seen in the vertical velocity at 600 hPa. Many of these bursts are fed by westward propagating easterly anomalies in the zonal surface wind (right pannel). This is characteristic of equatorial Rossby waves.

6.4 Gross moist stability and the slowdown of the Walker circulation

The moist static energy (MSE) equation and convective quasi-equilibrium theory (QET) are often used together to model divergent circulations in the tropics (Neelin and Held, 1987; Neelin and Zeng, 2000; Chou and Neelin, 2004; Neelin, 2007; Emanuel, 2007). The MSE equation is a combination of the thermodynamic and moisture equations that accounts for the cancellation of adiabatic cooling and latent heating. It can be expressed as

$$\partial_t \left\langle c_p T + Lq \right\rangle + \left\langle \mathbf{u} \cdot \nabla \left(c_p T + Lq \right) \right\rangle + \left\langle \omega \partial_p h \right\rangle = \mathcal{F}_{\mathrm{net}}, \tag{6.7}$$

where $h = c_p T + gz + Lq$ is the moist static energy, $\mathcal{F}_{\mathrm{net}}$ is the total heating of the atmospheric column by fluxes at the surface and the top of the atmosphere, c_p is the heat capacity of air at constant pressure, L is the latent heat of vaporization, and all other symbols have been introduced previously (see Appendix B for a table of symbols). The net heating can be combined with the surface energy balance such that it can be expressed in terms of the top-of-atmosphere incoming-shortwave and outgoing-longwave radiative tendencies $\mathcal{S}$ and $\mathcal{L}$ and the energy uptake $\mathcal{O}$ by the

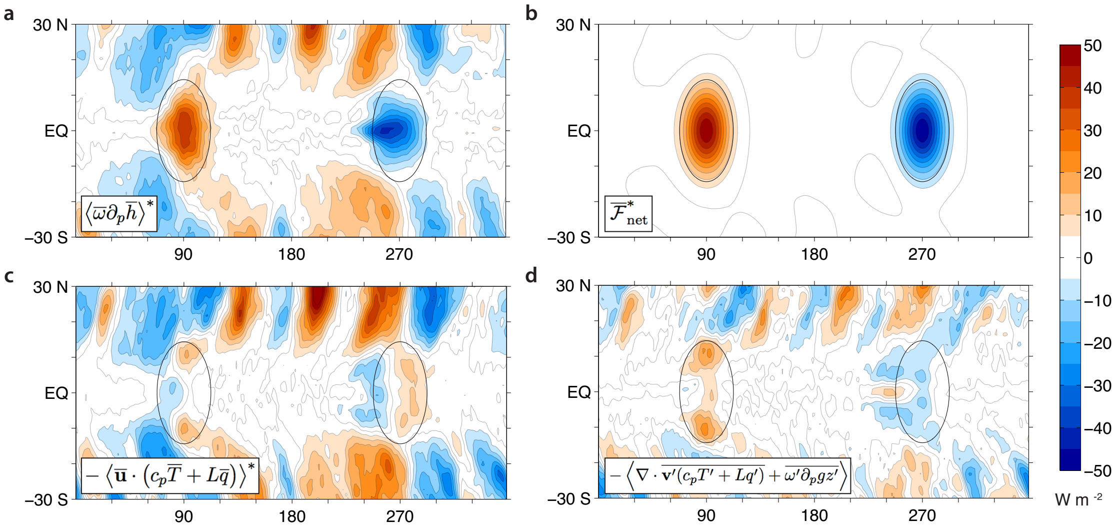

Figure 6.6: Terms of the zonally anomalous moist static energy equation integrated from the surface to the tropopause (plots are indistinguishable if the integration is continued to the top of the domain). Signs are chosen such that all other terms add up to the vertical motion term $\langle\overline{\omega}\partial_p\overline{h}\rangle$. Black contours show where the imposed heating is above 10 W m^{-2} or below -10 W m^{-2}. The transient-eddy term is computed as a residual.

(ocean) surface,

$$\mathcal{F}_{\text{net}} = \mathcal{S} - \mathcal{L} - \mathcal{O}. \tag{6.8}$$

We investigate zonal anomalies in the time-mean MSE equation,

$$\left\langle\overline{\mathbf{u}}\cdot\nabla\left(c_p\overline{T}+L\overline{q}\right)\right\rangle^* + \left\langle\overline{\omega}\partial_p\overline{h}\right\rangle^* + \left\langle\nabla\cdot\overline{\mathbf{v}'(c_pT'+Lq')}+\overline{\omega'\partial_p gz'}\right\rangle = \overline{\mathcal{F}}^*_{\text{net}}. \tag{6.9}$$

The zonally-anomalous column heating is dominated by the ocean heat-flux convergence, which influences the atmosphere primarily through evaporative cooling of the surface,

$$\overline{\mathcal{F}}^*_{\text{net}} \approx -\overline{\mathcal{O}}^* \approx \overline{E}^*, \tag{6.10}$$

as in Merlis and Schneider (2011). Other contributions to $\overline{\mathcal{F}}^*_{\text{net}}$ include zonally anomalous longwave radiative tendencies, but are generally small in the idealized GCM. The terms of the zonally anomalous MSE equation in the reference climate of Q8 are shown in Fig. 6.6. The dominant balance in the convective region is between the zonally anomalous column heating ($-\overline{\mathcal{F}}^*_{\text{net}}$, Fig. 6.6b) and the vertical-motion term ($\left\langle \overline{\omega}\partial_p\overline{h}\right\rangle^*$, Fig. 6.6a), which releases energy through deep convection;

$$\left\langle \overline{\omega}\partial_p\overline{h}\right\rangle^* \approx \overline{\mathcal{F}}^*_{\text{net}}. \tag{6.11}$$

The energy input, $\overline{\mathcal{F}}^*_{\text{net}} \approx -\overline{\mathcal{O}}^*$, is a prescribed Gaussian of amplitude 50 W m^{-2} centered at 90°E on the equator (see Eq 6.3). The stationary- and transient-eddy advection terms (Fig. 6.6c,d) also play a role, especially on the edges of the convective region, as is discussed by Chou and Neelin (2004).

In order to derive constraints on the stationary-eddy vertical velocities, we need to separate the vertical velocity and the MSE stratification in the vertical MSE-advection term. This can be accomplished using a separation of variables,

$$\overline{\omega}(x, y, p) \approx -\Omega_1(p)\nabla \cdot \mathbf{u}_1(x, y), \tag{6.12}$$

where $\Omega_1(p)$ contains all information about the profiles of vertical velocity and $\nabla\cdot\mathbf{u}_1(x, y)$ corresponds to the divergence measured at the lifted condensation level (LCL). The subscript 1 refers to the first baroclinic mode, which dominates the vertical structure of tropical circulations (Neelin and Zeng, 2000). This arrises from a linearization of temperature deviations from a tropical-mean temperature profile, $T_r(p)$:

$$T(\mathbf{x}, p, t) \approx T_r(p) + A_1(p)T_1(\mathbf{x}, t), \tag{6.13}$$

where $T_1(\mathbf{x}, t)$ is the temperature deviation at the LCL and $A_1(p)$ describes the sensitivity of free-tropospheric temperature to perturbations at the LCL based on QET (Emanuel et al., 1994; Neelin and Zeng, 2000). This approach was developed by Neelin and Yu (1994) and Yu and Neelin (1997) (see also review by Neelin, 2007). The derivation of $A_1(p)$ and $\Omega_1(p)$ can be found in Appendix 6A, which follows Levine and Boos (2016).

If the winds can be separated in this way, then the vertical MSE-advection term becomes

$$\left\langle \overline{\omega} \partial_p \overline{h} \right\rangle^* \approx M \nabla \cdot \mathbf{u}_1^*, \tag{6.14}$$

where

$$M \equiv - \left\langle \Omega_1(p) \partial_p \overline{h} \right\rangle, \tag{6.15}$$

is the gross moist stability (GMS). This weighted average of the MSE stratification provides an effective static stability for deep convection, accounting for the effect of latent heating. The GMS has been found to increase with global warming in coupled climate models (Chou and Neelin, 2004; Chou et al., 2013), leading to a decrease in stationary-eddy vertical velocities if $\left\langle \overline{\omega} \partial_p \overline{h} \right\rangle^*$ is held approximately fixed by energetic constraints. It should be noted that the same GMS concept has also been applied to the Hadley circulation, with slightly different notation (Kang et al., 2009). The GMS changes with warming can be different for the Hadley and Walker circulations because the GMS depends on the vertical structure of vertical velocities, which are different for these two types of circulations. We would like to investigate changes in the Walker-circulation GMS across a wide range of climates in the equatorial heating experiment and use these changes to derive scalings for the change in Walker circulation strength with global warming.

6.4.1 Estimating gross moist stability

Moist static energy decreases with height in the boundary layer then increases with height in the free troposphere and stratosphere, as can be seen in Fig. 6.7a for the full range of climates. The value of MSE increases monotonically with warming at all levels, shown explicitly for the surface, LCL, and tropopause in Fig. 6.7b. Because the MSE profile is non-monotonic, the GMS depends sensitively on the $\Omega_1(p)$ that is used. It is only a useful quantity if $\Omega_1(p)$ accurately represents the vertical velocity profiles in these simulations. For comparison, we compute stationary-eddy vertical velocity profiles by averaging over the convecting region ($\overline{\mathcal{O}}^* < -10$ W m^{-2}) at each level. We will denote such averages with a $\hat{(\cdot)}$. The vertical velocity profile $-\hat{\omega}(p)^*$ is shown in Fig. 6.8a.

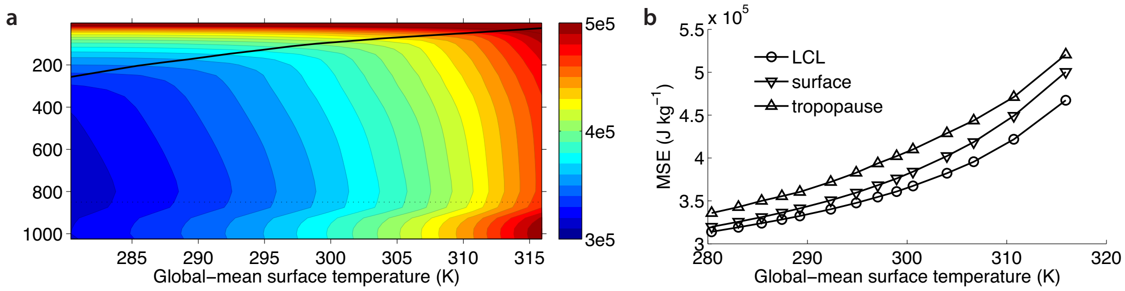

Figure 6.7: a) Vertical profile of zonal-mean moist static energy as a function of mean climate. A black line shows the height of the tropical tropopause. Both quantities are averaged for $\phi \in [-10\ 10]$. b) Value of zonal-mean moist static energy at select vertical levels.

We compute the wind mode $\Omega_1(p)$ following Levine and Boos (2016), who present a generalization of the model found in Neelin and Zeng (2000). The generalization simply relaxes some of the approximations on the relative importance of temperature, moisture, and geopotential for MSE, such that the $\Omega_1(p)$ modes are relevant over the full range of climates in these idealized simulations. The wind mode is related to the temperature mode $A_1(p)$ through the use of thermal wind balance and the continuity equation. The temperature mode relates the amplitude of deviations from the tropical-mean temperature profile to deviations of the sub-cloud MSE. This assumes a state of convective equilibrium, where saturated MSE is constant above the LCL (Emanuel et al., 1994; Emanuel, 2007). We assume a fixed LCL height with warming, which is consistent with small changes in relative humidity (Schneider et al., 2010). The derivation of $\Omega_1(p)$ can be found in Appendix 6A (Section 6.7). The result of this quasi-equilibrium theory (QET) is that $\Omega_1(p)$ can be computed from the tropical-mean temperature profile $T_r(p)$. The resulting $\Omega_1(p)$ are shown in Fig 6.8c for the full range of climates.

We can more easily compare the modeled vertical velocity profiles in the convecting region $-\hat{\omega}(p)^*$ with $\Omega_1(p)$ if we normalize such that the maximum values are the same for each climate. The normalized vertical velocity profile,

$$\Omega_{1e}(p) \equiv -\hat{\omega}(p)^* \frac{\max(\Omega_1(p))}{\max(-\hat{\omega}(p)^*)}, \qquad (6.16)$$

is shown in Fig 6.8b. The resulting empirical vertical wind modes $\Omega_{1e}(p)$ are quite similar to $\Omega_1(p)$

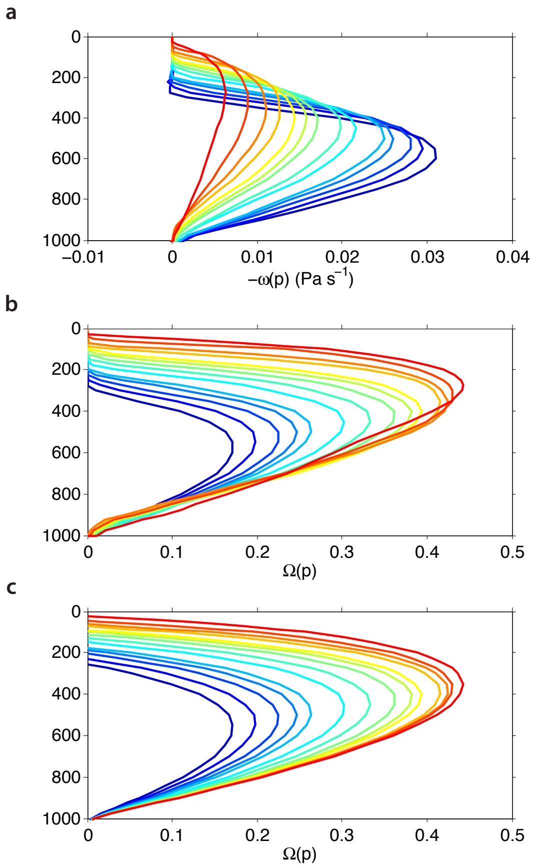

Figure 6.8: a) Stationary-eddy vertical-velocity profiles averaged over the ascent region, diagnosed as the region where the imposed heating is above 10 W m^{-2}. b) Non-dimensional stationary-eddy vertical-vertical velocity profiles that have been normalized such that the maximum value is the same as the QET $\Omega_1(p)$ profile. We call this $\Omega_{1e}(p)$. c) Non-dimensional QET vertical-velocity profile $\Omega_1(p)$. In all figures, profiles are shown for 14 mean climate states color coded from coldest (blue) to warmest (red).

across the range of climates. Differences are largest near the surface, near the tropopause and in the warmest climates.

We compute the GMS from both $\Omega_{1e}(p)$ and $\Omega_1(p)$ using Eq. 6.15,

$$\begin{aligned} M_e &= -\left\langle \Omega_{1e}(p)\partial_p \overline{h} \right\rangle , \\ M &= -\left\langle \Omega_1(p)\partial_p \overline{h} \right\rangle . \end{aligned} \tag{6.17}$$

Both show a pronounced increase with warming through 310 K global-mean surface temperature (Fig. 6.9a). The QET estimate (M, dashed line) shows the same magnitude of increase with climate

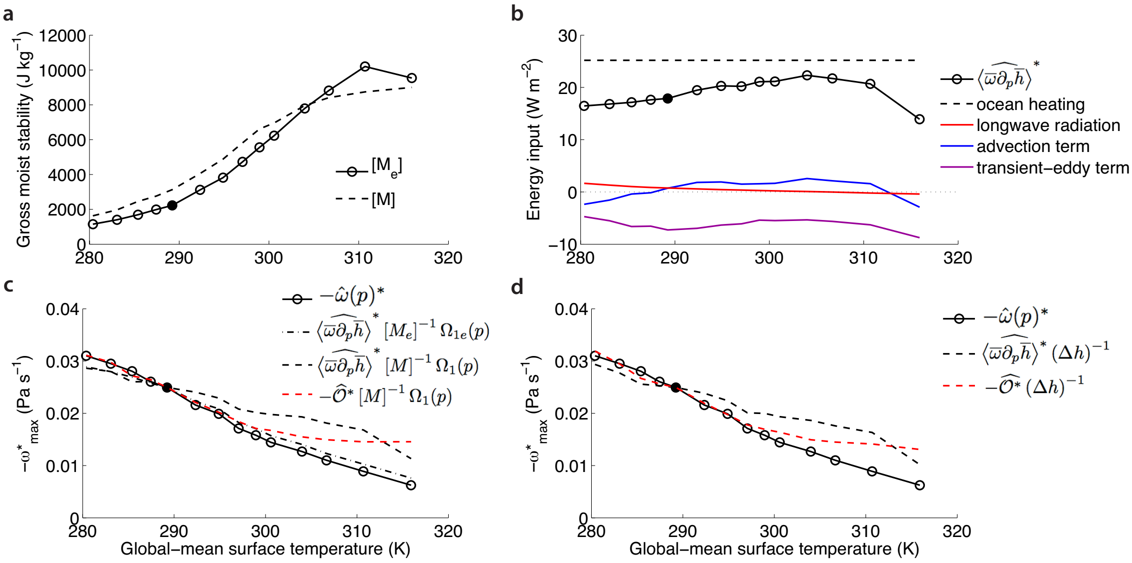

Figure 6.9: Controls on the strength of the Walker circulation. a) Zonal-mean GMS $[M]$ computed using $\Omega_{1e}(p)$ (solid line) and $\Omega_1(p)$ (dashed-line). b) Terms of the zonally anomalous moist static energy equation averaged over the region where the imposed heating is above 10 W m^{-2}. The vertical-motion term $\langle \widehat{\overline{\omega}\partial_p\overline{h}} \rangle^*$ is primarily balanced by the zonally anomalous ocean heat-flux convergence (black dashed line). c,d) Scalings for Walker circulation strength. The maximum of the stationary-eddy vertical velocity profile, averaged over the region where the imposed heating is above 10 W m^{-2} and estimates c) based on the zonal-mean GMS $[M]$ or d) tropopause–LCL moist static energy difference Δh.

change as the more appropriate empirical M_e. Overall, M provides a good approximation to M_e.

Levine and Boos (2016) use the same method for computing $\Omega_1(p)$, but proceed in a different way, for an application to subtropical circulations. Instead of computing the GMS, they combine the linear vorticity balance in the subtropical boundary layer with the baroclinic wind modes to form a theory for stationary-eddy vertical velocities. This theory is successful at describing the strength of subtropical stationary-eddy circulations. This does not work in the tropics, because of the compensation and nonlinearity in the vorticity budget, as discussed in Section 6.3. We proceed to constrain the stationary-eddy vertical velocities instead through the GMS and the dominant balance in the MSE budget (Eq. 6.11). There is nothing to suggest that the GMS constraint wouldn't also work in the subtropics.

6.4.2 Scaling estimates for Walker circulation strength

Combined with an understanding of how zonal anomalies in the other terms of the MSE equation change with climate change, we can make an estimate of changes in $\hat{\omega}(p)^*$ (the strength of the Walker circulation upwelling branch) based on the relation

$$-\hat{\omega}(p)^* \approx \frac{\widehat{\langle \overline{\omega} \partial_p \overline{h} \rangle}^*}{[M]} \Omega_1(p). \tag{6.18}$$

This relationship captures the *anomalous gross moist stability* mechanism of Chou and Neelin (2004). From here we make further simplifications.

We do not a priori know anything about $\widehat{\langle \overline{\omega} \partial_p \overline{h} \rangle}^*$. Luckily, fractional changes are smaller than changes in M. This is shown in Fig. 6.9b, along with averages of other MSE budget terms over the convective region. The leading order balance is $\widehat{\langle \overline{\omega} \partial_p \overline{h} \rangle}^* \approx -\widehat{\mathcal{O}^*}$, which is shown as a dashed line in Fig. 6.9b. This relates the numerator of Eq. 6.18 directly to the strength of zonally anomalous ocean heating. A quantitatively accurate picture would require understanding the advection and transient-eddy terms as well, but we will not delve further into them here.

We present scalings for changes in $-\hat{\omega}(p)^*$ in Fig. 6.9c and d. All scalings are normalized by the value of $-\hat{\omega}(p)^*$ in the reference climate[1], such that we are focusing on changes in $-\hat{\omega}(p)^*$ rather than the absolute value. The first scaling, $\widehat{\langle \overline{\omega} \partial_p \overline{h} \rangle}^* [M_e]^{-1} \Omega_{1e}(p)$ (dash-dotted line), is only approximate due to neglecting zonal variations of M_e and due to deviations of vertical velocities from the empirical profile $\Omega_{1e}(p)$. As such, it gives an accurate expression for $-\hat{\omega}(p)^*$. Substituting M for M_e (dashed line) looses some accuracy but still captures the decrease in Walker circulation strength with warming. Even the simple expression

$$-\hat{\omega}(p)^* \sim -\frac{\widehat{\mathcal{O}^*}}{[M]} \Omega_1(p) \tag{6.19}$$

captures the sense of the Walker circulation decrease with warming (red dashed line), though there may be a cancellation of errors based on M and errors from approximating $\widehat{\langle \overline{\omega} \partial_p \overline{h} \rangle}^*$ with the ocean

---

[1] In Fig. 6.9c the rescaling factors are ~ 1, but the simpler scalings in Fig. 6.9d require larger rescaling factors.

heat-flux convergence. The implication of this scaling is that the Walker circulation strength is linearly proportional to the asymmetry of ocean heat release and inversely proportional to the gross moist stability, which is a strongly increasing function of mean temperature.

The gross moist stability is not the most straightforward quantity to calculate or intuit. See, for example, the decomposition of GMS changes into components due to changes in stratification, changes in moisture lapse rate, and changes in the depth of deep convection and tropopause height in Chou et al. (2013). While the increase in moisture lapse rate gives a decrease in GMS, the increased tropical dry static stability, deep convective depth, and tropopause height all give an increase in GMS. The same cancellations are apparent in the idealized GCM simulations presented here (e.g., in Fig. 6.7). Here we attempt to simplify the scalings of Fig. 6.9c by approximating the GMS in terms of a bulk MSE difference.

If the vertical velocity profile were approximated by a uniform profile between the LCL and the tropopause and zero otherwise, the GMS would simplify to

$$[M_{\text{simple}}] \equiv \Delta h \equiv \left[\overline{h}_{\text{tropopause}}\right] - \left[\overline{h}_{\text{LCL}}\right]. \tag{6.20}$$

The motivation for choosing the LCL instead of the surface is that it represents the fact that vertical velocities are small in the boundary layer where MSE is strongly stratified. We can use this expression to derive scalings for Walker circulation strength,

$$\begin{gathered} -\hat{\omega}(p)^* \sim \frac{\widehat{\langle \overline{\omega} \partial_p \overline{h} \rangle}^*}{\Delta h}, \\ \text{or} \\ -\hat{\omega}(p)^* \sim -\frac{\widehat{\mathcal{O}^*}}{\Delta h}. \end{gathered} \tag{6.21}$$

These scaling estimates are shown in Fig. 6.9d and are virtually indistinguishable from the scalings based on the full GMS. When interpreting Δh, keep in mind Fig. 6.7, which shows $\left[\overline{h}_{\text{tropopause}}\right]$, $\left[\overline{h}_{\text{LCL}}\right]$, as well as $\left[\overline{h}_{\text{sfc}}\right]$.

6.4.3 Summary: Local energetic constraints on Walker circulation strength

The scalings of Eq. 6.18, 6.19, and 6.21, provide a simple picture of how local energetic constraints can lead to the slowdown of the Walker circulation with global warming. The gross moist stability (GMS) provides a measure of how much energy is released through deep convection, per unit mass (note that it has units of J kg^{-1}). Convection takes energy from the net heating of the atmospheric column and converts it into kinetic energy. As the mean climate warms, deep convection releases more energy per unit mass. A large contribution to this is that the height of convective outflows, where convective parcels reach a level of neutral buoyancy, increases. This increases the energetic demands through the increasing change of gravitational potential energy. Convective quasi-equilibrium (QET) theory was used to derive vertical velocity profiles that capture this increase in the energetic requirements of deep convection.

The result is that the strength of the Walker circulation is given by

$$\text{Walker circulation strength} = \frac{\text{total zonally anomalous heating of atmospheric column}}{\text{energetic requirements per unit mass of deep convection}}. \tag{6.22}$$

In the simple idealized model experiments presented here, the total heating of the atmospheric column is simply given by the fixed ocean heat-flux convergence and the response to climate change is simply determined by the increase in energetic requirements for deep convection, diagnosed by the GMS.

6.5 Forcing of extratropical Rossby waves

Walker circulations are important globally because the upper level divergent flow in the tropics can force Rossby waves that propagate into the extratropics (Sardeshmukh and Hoskins, 1988; Seager et al., 2005). Here we will examine how the amplitude of extratropical stationary Rossby waves changes with the strength of the Walker circulation. The naive assumption would be that extratropical stationary Rossby waves decrease in strength at the same rate as the Walker circulation. The generation of rotational flow by tropical divergence has been addressed by Sardeshmukh and

Hoskins (1988) using an analysis of the wave activity equation, derived from the vorticity equation. We adapt this framework for the case of stationary eddies.

We can examine the sources and sinks of stationary-eddy rotational flow by looking at the stationary-eddy vorticity equation, which can be written in terms of a stationary-eddy source $\overline{G}^*$ and sink $\overline{D}^*$:

$$\partial_t \overline{\zeta}^* + \overline{\mathbf{v}}_\psi^\dagger \cdot \nabla \overline{\zeta}_a^\dagger = \overline{G}^* - \overline{D}^*. \tag{6.23}$$

Here ζ is the relative vorticity, ζ_a is the absolute vorticity, $\mathbf{v}_\psi = (-\partial_y \psi, \partial_x \psi, 0)$ is the rotational component of the velocity, and stationary-eddy terms are written using dagger notation,

$$a^\dagger b^\dagger = a^* \left[b\right] + \left[a\right] b^* + a^* b^*, \tag{6.24}$$

such that we include terms that average to zero in the zonal-mean and are thus only important in this zonal varying analysis (cf. Kaspi and Schneider, 2013).

The generation and dissipation terms need to include all terms of the vorticity equation not included on the left hand side. Based on the observation that zonally anomalous transient-eddy vorticity tendencies are primarily dissipative (i.e. they are negatively correlated with $\overline{\zeta}^*$), we categorize them as a sink. We thus write

$$\overline{G}^* = -\nabla_h \cdot \left(\overline{\mathbf{v}}_\chi^\dagger \overline{\zeta}_a^\dagger\right) - \overline{\omega}^\dagger \frac{\partial \overline{\zeta}^\dagger}{\partial p} \tag{6.25}$$

and

$$\overline{D}^* = -\nabla \times \overline{\tau}^* + \nabla_h \cdot \left(\overline{\mathbf{v}'\zeta'}\right)^* + \overline{\omega' \frac{\partial \zeta'}{\partial p}}^* . \tag{6.26}$$

Here $\mathbf{v}_\chi = \mathbf{v} - \mathbf{v}_\psi$ is the divergent component of the velocity. The twisting-tilting of the time-mean (transient-eddy) flow is included with $\overline{G}^*$ ($\overline{D}^*$), but is neglected from the notation.

Eq. 6.23 implies the enstrophy equation

$$\frac{D_\psi}{Dt} \left(\frac{1}{2} \overline{\zeta}^{*2}\right) + \overline{v}_\psi^* \overline{\zeta}^* \partial_y \left[\overline{\zeta}_a\right] = \overline{\zeta}^* \overline{G}^* - \overline{\zeta}^* \overline{D}^*. \tag{6.27}$$

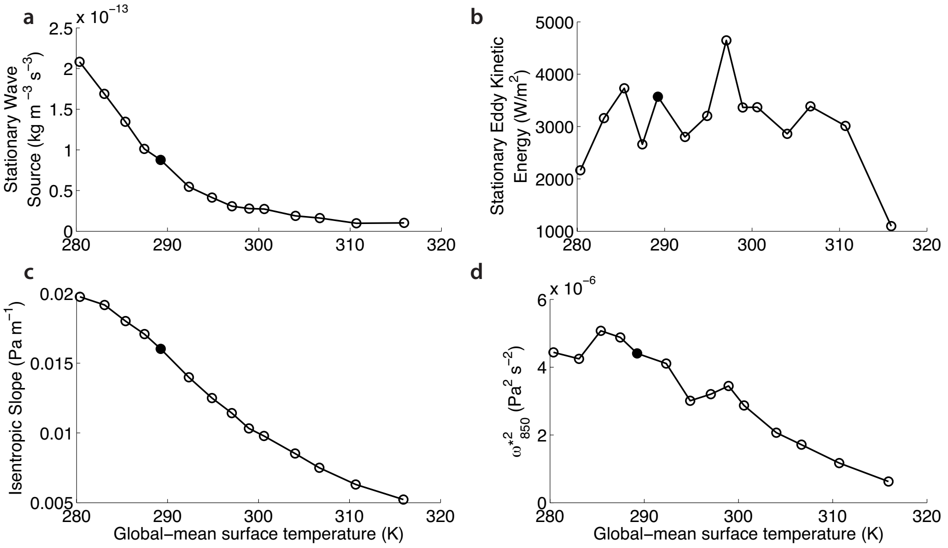

Figure 6.10: a) Tropical entropy source $\overline{\zeta}^*\overline{G}^*$ averaged with 10° latitude of the equator. b) sEKE averaged over $|\phi| > 30°$. c) Isentropic slope $\partial_y[\overline{\theta}]/\partial_p[\overline{\theta}]$ at 850 hPa averaged over $30° < |\phi| < 60°$. d) Variance of $\overline{\omega}^*_{850}$ averaged over $|\phi| > 30°$. All fields are from the Q8 experiment.

The Walker circulation forces extratropical Rossby waves through $\overline{\zeta}^*\overline{G}^*$, so we focus on this term. The integral of $\overline{\zeta}^*\overline{G}^*$ over the deep tropics ($\phi \in [-10\ 10]$) is shown in Fig. 6.10a. It decreases with the strength of the Walker circulation[2]. However, the extratropical sEKE ($\phi \in \pm[30\ 75]$, Fig. 6.10b) does not decrease accordingly. There are several peaks in sEKE as climate is varied. While the enstrophy budget (Eq. 6.27) gives constraints on enstrophy, not sEKE, these only differ by a lengthscale, and the same behaviour is seen for enstrophy.

This suggests that the decrease in variance of extratropical $\overline{\omega}^*_{850}$, seen in Fig. 3.13g and 6.10d may be instead related to the reduction of extratropical static stability. The isentropic slope relates meridional and vertical motion in the extratropics, as was seen in Section 5.5. The extratropical isentropic slope decreases with warming in these experiments as shown in Fig. 6.10c. This reduction in isentropic slope could manifest in a reduction in $\overline{\omega}^*_{850}$, even without much change in horizontal winds, according to a thermodynamic balance between meridional and vertical advection,

$$\overline{\omega}^* \sim \frac{\partial_y[\overline{\theta}]}{\partial_p[\overline{\theta}]}\overline{v}^*. \tag{6.28}$$

---

[2] This term governs the generation of stationary-eddy enstrophy. It is perhaps worth examining also the generation of transient-eddy enstrophy by the Walker circulation, because the transient-eddies may become stationary at higher latitudes.

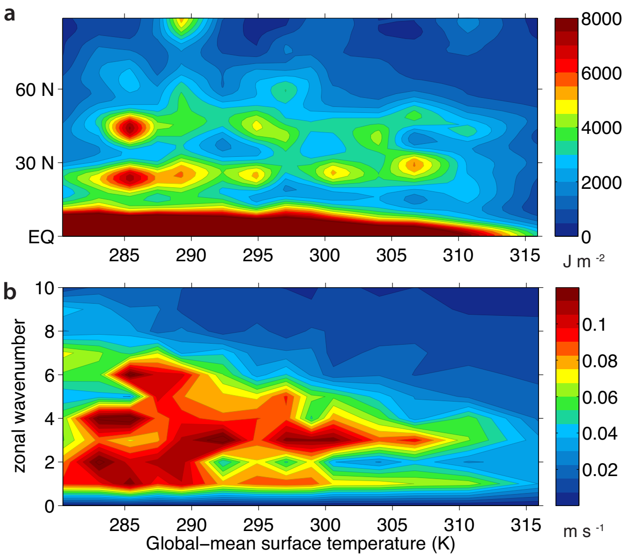

Figure 6.11: a) Extratropical sEKE as a function of latitude and global-mean surface temperature in the Q8 experiment. Values have been averaged over both hemispheres. b) Global-mean zonal wavenumber of $\overline{v}_{600}$ as a function of global-mean surface temperature in the Q8 experiment.

The implication is that the remote influence of stationary waves on extratropical $\overline{\omega}^*_{850}$, regardless of the stationary wave source, is reduced simply by the reduction in midlatitude isentropic slope with warming. This could also be the reason for the decrease in southern hemisphere $\overline{\omega}^*_{850}$ variance in the orographic forcing experiment (Fig. 3.13d).

Even if the extratropical sEKE response in the equatorial heating experiment is not the dominant influence on $\overline{\omega}^*_{850}$ variance, we would still like to understand this response. Plotting the latitudinal distribution of sEKE (Fig. 6.11a) is revealing. The sEKE is peaked at only a few latitudes in each climate. This immediately suggests some kind of resonant behaviour, such as may occur at turning latitudes (Hoskins and Karoly, 1981). To investigate this, we plot the change in globally-integrated zonal wavenumber in Fig. 6.11b. Each climate tends to be dominated by 1 or 2 wavenumbers, and these wavenumbers differ between climates, sometimes even switching from $k = 1$ and 3 dominance, to $k = 2$ and 4 dominance, and back again over the course of a 5 K global-mean surface temperature change. Overall there is a tendency towards larger scales (lower k) with warming, which is consistent with the increase in strength of the subtropical jet, causing high k Rossby waves to be reflected at a turning latitude (Hoskins and Karoly, 1981).

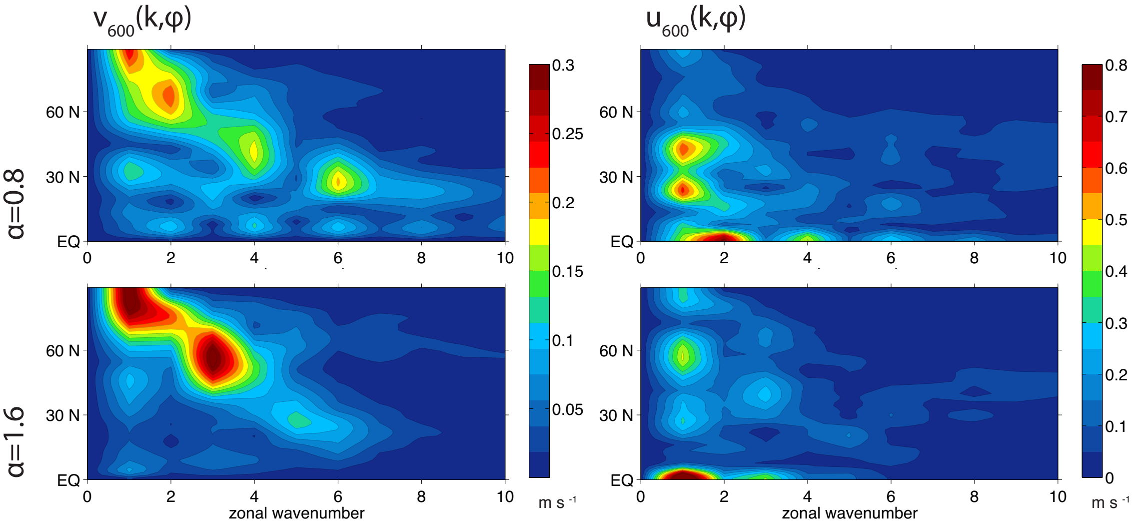

Figure 6.12: Examples of zonal wavenumber spectra from the equatorial heating experiment, showing resonances at turning latitudes. The zonal wavenumber spectra of $\overline{u}_{600}$ and $\overline{v}_{600}$ are shown for $\alpha = 0.8$ and $\alpha = 1.6$ of the Q8 experiment (corresponding to global-mean surface temperatures of 285 K and 297 K). All values have been averaged over both hemispheres.

By examining individual simulations, we can investigate which latitudes the resonances are occurring at. We plot the zonal wavenumber spectra of $\overline{u}_{600}$ and $\overline{v}_{600}$ versus latitude in Fig. 6.12. We choose two climates that appear to have the most resonant behaviour, $\alpha = 0.8$ and $\alpha = 1.6$, which correspond to global-mean surface temperatures of 285 K and 297 K respectively. The diagonal line that is apparent in the $\overline{v}_{600}$ spectra represents the turning latitude as a function of wavenumber. At this latitude, the wavenumber reaches its maximum amplitude. It can be seen that higher wavenumbers reach their turning latitude at a lower latitudes. All of this fits with the theory and modeling work of Hoskins and Karoly (1981). But this still doesn't explain the dominance of only a few wavenumbers (i.e. the dominance of even wavenumbers in $\alpha = 0.8$ and odd wavenumber in $\alpha = 1.6$). This dominance is already apparent in the zonal wind in the tropics. By examining map plots, we can see that this corresponds to a complete restructuring of the divergent winds maintaining the Walker circulation, from a more meridional overturning circulation for even wavenumber cases, to a more zonal overturning for odd wavenumber cases. This is very interesting, but we have already figured out enough interesting things for one chapter, so we will leave this a mystery.

6.6 Discussion and Conclusions

This chapter has presented idealized GCM experiments with zonally anomalous ocean heating, where the aspect ratio of heating and the global longwave optical depth are varied independently. An analysis of the vorticity budget as the heating aspect ratio was varied revealed a near-constant Walker circulation strength despite large changes in the underlying vorticity balance, from a linear regime when the heating is spread over a range of latitudes, to a highly nonlinear regime when the heating is constrained to the equator. This suggests that any theory for Walker circulation strength must be independent of the vorticity budget.

A local theory for the strength of Walker circulation upwelling is derived from the MSE equation, using the concept of a gross moist stability (GMS), which acts as an effective static stability for tropical deep convection. This is related to the GMS that is used to understand Hadley circulation changes with climate change (Kang et al., 2009), but must account for the different nature of vertical velocity profiles in the Walker and Hadley circulations. The vertical structure of zonally anomalous tropical circulations is well described by baroclinic mode theory (Neelin and Zeng, 2000). This can be used to derive a GMS for the Walker circulation based solely on the tropical-mean temperature profile. This analysis reveals that the GMS increases with warming across a wide range of climates in the idealized GCM used here. As a result, the Walker circulation decreases with warming across the range of climates. In this framework, the (inverse of the) GMS acts as a Carnot efficiency, characterizing how much work can be done in lifting air parcels as heat is removed from a warm ocean surface;

$$\text{Walker circulation mass flux} = \frac{\text{zonally anomalous heating}}{\text{GMS efficiency}}. \tag{6.29}$$

The resulting decrease in strength of the Walker circulation with warming does not manifest on the extratropical circulation in a straightforward way due to the complexities of the meridional Rossby wave dispersion. The change in extratropical stationary-wave activity with warming is noisy in these experiments, resulting from resonances at critical latitudes. The amplitude of extratropical stationary waves forced by the Walker circulation thus depends on the zonal wavenumber spectrum of the forcing and the strength and structure of the subtropical jet. The Walker circulation in these experiments seems to exist in two stable states, one dominated by even zonal wavenumbers with predominantly meridional overturning, and one dominated by odd zonal wavenumbers with predominantly zonal overturning. The reasons behind these two different states must be understood to understand the extratropical consequences of the Walker circulation changes presented here.

6.6.1 On Walker circulations and zonal SST gradients

Much of the early work on Walker circulations has focused on the role of tropical SSTs (Bjerknes, 1969, 1972). Sea surface temperature are also more easily measured than the surface and top-of-atmosphere energy fluxes that are used in the theory of this chapter. This is especially true for paleoclimate applications. Luckily, there exists a link between SSTs and evaporation, which is the dominant energetic term that balances ocean heat-flux convergence. Merlis and Schneider (2011) show that east–west differences in evaporation, ΔE, are dominated by east–west differences in saturation specific humidity (q_s), which are a function of east–west differences in SST (ignoring air-sea temperature differences),

$$\Delta E \sim \Delta q_s(\mathrm{SST}). \tag{6.30}$$

This relation can be inverted to give an expression for the east–west SST difference:

$$\Delta \mathrm{SST} \sim \left(\frac{\partial q_s}{\partial T}\right)^{-1} \Delta E. \tag{6.31}$$

The result is that the east-west differences in evaporation and SST are linearly related, though with a coefficient that varies strongly with temperature, the derivative of the Clausius-Clapeyron relation. The implication of this, given the linearity of Walker circulation response to energetic forcing (Eq. 6.22/6.29, see also Appendix A), is that the sensitivity of Walker circulations to SST gradients could depend on mean temperature. However, in these idealized GCM experiments, as the mean climate is warmed, the decreasing sensitivity to SSTs is offset by the increase in gross moist stability such that fractional changes in Walker circulation strength are similar to fractional changes in SST gradient.

Further modeling studies would be required to test if this cancellation always plays out in this way, such that SST gradients and Walker circulation strength are linearly related across a wide range of climates. Where possible, the more physical zonally anomalous heat input should be used in place of zonally anomalous SSTs.

6.6.2 Part II synthesis

We have taken a grand tour of the influences on the amplitude and spatial distribution of stationary-eddy kinetic energy (sEKE) that is forced by midlatitude topography and equatorial heating. We have focused in particular on how these influences change with global warming, by studying a wide range of climates in an idealized GCM. We will now discuss some salient features of these results and present our conclusions.

The main insights into the amplitude of stationary eddies in both topographic and equatorial heating cases came from the analysis of the stationary-wave energetics. In the orographic forcing case, we start from the classical analysis of Hoskins and Karoly (1981) of how the orographic boundary condition influences the free troposphere through the thermodynamic equation. We turn this basic idea into a budget for the meridional component of stationary-eddy kinetic energy. The classical idea, where the orographic vertical velocities force meridional winds with a sensitivity that depends inversely on the isentropic slope, is a valuable starting point. However, we find that latent heating and transient-eddy heat fluxes significantly modify the response. The transient-eddy heat fluxes are anti-correlated with meridional stationary-eddy advection and thus amplify the stationary-wave response. The latent heating reduces the adiabatic cooling of the initial upslope wind perturbation and thus damps the stationary wave in all climates. The latent heating becomes a dominant influence in warm climates, causing a reduction of orographic forcing of stationary waves irregardless of the latitude of topography. The importance of these nonlinearities suggests that orographic stationary waves may be nonlinear in the amplitude of forcing (see Appendix A, where this is tested). This analysis provides knowledge of controls on orographic stationary wave amplitude beyond what is possible with linear models. The local thermodynamics over the topography are found to be important globally due to relatively minor changes in meridional energy propagation and stationary-wave lengthscales in these idealized GCM simulations.

Stationary-eddy overturning and thus $\overline{P}^* - \overline{E}^*$ in the equatorial heating experiment is dominated by a Walker circulation, with an ascending branch over the ocean heating and a descending branch over the ocean cooling. We explain the decrease in Walker circulation strength with warming based on energetic constraints on deep convection. This builds on the *anomalous gross moist stability* mechanism of Chou and Neelin (2004), by showing how convective quasi-equilibrium profiles change over a wide range of climates leading to a robust increase in the energetic requirements per unit mass of deep convection. We provide a qualitative simplification of the this energy requirement in terms of the moist static energy difference between the lifted condensation level and the tropopause. A side product of this analysis is that we can make quantitative predictions of the full 3D structure of stationary-eddy vertical motion in the tropics, simply in terms of the mean tropical temperature and the zonally anomalous energy input. The take-home understanding of the Walker circulation is that the strength of overturning is set by the energy available, divided by the energy required for deep convection, which can be derived in terms of convective quasi-equilibrium theory.

The energetic conclusions on Walker circulations hold throughout a range of vorticity equation regimes, obtained by varying the aspect ratio of the heat source. In equatorially confined Walker circulations, the vertical motion is maintained by transient-eddy vorticity tendencies, while in wider Walker circulations, the vertical motion is partially maintained by Sverdrup balance. This suggests that Walker circulations are energetically controlled and the vorticity equation responds passively to the convective vertical velocities in whatever means possible based on the background absolute vorticity. The vorticity budget is also used to derive the forcing of extratropical Rossby waves by the Walker circulation. However, any signal of the decrease in Walker circulation strength is lost due to amplification of Rossby waves at turning latitudes, which vary substantially with climate change due to changes in the subtropical jet.

The stationary-eddy signal far from the forcing (beyond the subtropical jet in the equatorial heating experiment or beyond the equatorial easterlies in the orographic forcing experiment) becomes obscured by details of the meridional propagation. For this remote forcing, a dominant factor in the strength of lower-tropospheric vertical motions is the isentropic slope, which controls the strength of vertical velocities needed to balance meridional heat transport by stationary eddies. This decrease in isentropic slope tends to reduce lower-tropospheric vertical velocities and $\overline{P}^* - \overline{E}^*$ that result from distant teleconnections as the climate is warmed.

Chapters 5 and 6 made significant progress on understanding controls of sEKE and lower-tropospheric vertical velocities in a changing climate. This motivates future work on other types of stationary-eddy forcing as well as a synthesis of these ideas for applications to the full climate system.

6.6.3 A brief note on other analyses performed

It was a long process in coming to our present state of understanding of why stationary-eddy circulations changes as they do in these zonally asymmetric idealized model experiments. I wanted to briefly mention a few other budgets and analysis that were performed in coming to the current state of understanding. I learned something from each of them, even if they were not crucial to the final story.

In order to understand the stationary-wave response in the Gaussian mountain experiment, I focused for some time on the vertically integrated vorticity budget. This is dominated by the stretching of planetary vorticity, which integrates to the vertical surface wind ω^*_{sfc}, the dominant factor in the energy budget analysis. The problem with the vorticity budget is that the correlation of this forcing with the existing vorticity structure is important in order to amplify or damp the wave (cf. Eq. 6.27). For the case of the planetary vorticity stretching, this correlation is predominantly in the upper troposphere. This upper tropospheric correlation was dependent on the vertical profile of vertical velocities and the existing vorticity distribution, both of which depend on the stationary wave. This analysis did not present a way to relate stationary wave amplitude to zonal-mean quantities, besides to identify the importance of ω^*_{sfc}.

Lorenz (1955) studies the energy cycle of the atmosphere, defining an available potential energy that can be converted into the kinetic energy of atmospheric circulations. This framework has been generalized by Hernández-Deckers and von Storch (2010, 2011) to include stationary-eddy circulations. The result is a budget for sEKE that depends on conversion from stationary-eddy available potential energy (seAPE), conversion to transient-eddy and zonal-mean kinetic energy, and dissipation by surface friction. The dominant source of sEKE was seen to be the conversion of mean available potential energy (MAPE) to sEKE through the intermediary of seAPE. This conversion happened predominantly downstream of the mountain through large stationary-eddy heat fluxes. The sensitivity of sEKE to these heat fluxes depends on the inverse isentropic slope. These ideas fit very well with what was found in the thermodynamic equation analysis (Section 5.5). But there is no clear way to close the budget for the stationary-eddy heat fluxes, without already knowing the amplitude of stationary eddies.

The theromodynamic equation analysis (Section 5.5) combines what was learned from the vorticity and sEKE budget analyses. It has the advantage that the orographic vertical velocities can be clearly tied to meridional velocities through the isentropic slope.

Acknowledgements

This work is collaborative work with Xavier Levine and Tapio Schneider.

6.7 Appendix 6A: Derivation of vertical velocity mode

This derivation of the vertical wind modes $\Omega_1(p)$ follows Levine and Boos (2016).

The basis for an understanding of the vertical structure of perturbations to the tropical atmosphere is that variations in saturation moist static energy (MSE) are invariant with height above the LCL (Emanuel, 2007), a state called convective quasi equilibrium. Temperature variations at a pressure p can be related to the saturation MSE (h^*) by differentiating the expression for saturation MSE with respect to temperature,

$$\left.\frac{dh^*}{dT}\right|_p = 1 + z_T + q_T, \tag{6.32}$$

where

$$q_T = \frac{L}{c_p}\left.\frac{dq^*}{dT}\right|_p = \frac{Lq_r}{c_p r_v T_r^2}\left(1 + \frac{r_v}{r_d}q_r - q_r\right), \tag{6.33}$$

$$z_T = \frac{z}{c_p}\left.\frac{dz}{dT}\right|_p = -\frac{r_d}{c_p}\log\frac{p}{p_s}. \tag{6.34}$$

Hydrostatic balance was used to express the sensitivity of geopotential to temperature as a function of pressure. These expressions depend on the tropical mean temperature T_r and specific humidity q_r at level p, were $(\cdot)_r$ denotes a tropical average at constant p.

Similarly, LCL temperature variations (T_b) can be related to LCL saturation MSE variations (h_b^*),

$$\frac{dh_b^*}{dT_b} = 1 + (z_T)_b + (q_T)_b, \tag{6.35}$$

where the subscript b denotes values at the LCL. This allows us to define what we will call a temperature mode, which relates variations in LCL temperature to variations in temperature in the free troposphere,

$$A_1(p) \equiv \left.\frac{dT}{dT_b}\right|_p = \left.\frac{dh^*}{dT}\right|_p \left(\frac{dh_b^*}{dT_b}\right)^{-1} = \frac{1 + (z_T)_b + (q_T)_b}{1 + z_T + q_T}. \tag{6.36}$$

The Quasi-equilibrium circulation model introduced by Neelin and Zeng (2000) makes further simplifications of this expression as detailed in Levine and Boos (2016). We use the full expression

(6.36) in order to best capture changes in the vertical structure of tropical perturbations across a wide range of climates.

The result is that tropical temperatures are given approximately by,

$$T(\mathbf{x}, p, t) \approx T_r(p) + A_1(p) T_1(\mathbf{x}, t), \tag{6.37}$$

where T_1 is the local temperature anomaly at the LCL. By plugging this modal decomposition into the momentum equation in a hydrostatic atmosphere, we obtain expressions for the horizontal wind $\mathbf{u}(\mathbf{x}, p, t) = \mathbf{u}_r(p) + V_1(p)\mathbf{u}_1(\mathbf{x}, t)$,

$$D_t \mathbf{u}_1 + f\hat{\mathbf{k}} \times \mathbf{u}_1 \approx -r_d \nabla T_1 \tag{6.38}$$

and

$$V_1(p) = A_1^+ - \frac{1}{p_t - p_s} \int_{p_s}^{p_t} A_1^+ dp, \tag{6.39}$$

where

$$A_1^+ = \int_{p_s}^{p} A_1 dp. \tag{6.40}$$

Here p_t is the height of the tropopause. The surface pressure gradient term of the momentum was neglected.

Finally, we get the vertical wind mode by using continuity,

$$\Omega_1(p) = \frac{1}{p_s} \int_{p_s}^{p} V_1 dp. \tag{6.41}$$

The result is that $\Omega_1(p)$ is determined from the temperature mode (Eq. 6.36) through use of the relations (6.39), (6.40), and (6.41). Due to multiple tropospheric averages, the vertical wind mode is quite sensitive to changes in the tropopause height.

Chapter 7

Conclusions

Here I summarize what progress has been made towards understanding how stationary eddies and zonal variations of the global hydrological cycle respond to climate change.

One of the major questions this thesis sought to answer is: What measure of atmospheric circulations determines the zonal pattern of precipitation minus evaporation ($P-E$)? We have successfully answered this question. In reanalysis and in climate models, the stationary-eddy vertical motion at 850 hPa is directly tied to zonal $P-E$ anomalies. This can be understood as a consequence of vertical motion being a quicker path to saturation than horizontal motion and as a result of the average condensation level being around 850 hPa in the modern climate. This understanding is valuable because it allows development of an approximate expression for P^*-E^* (zonally anomalous $P-E$) that depends only on 850 hPa stationary-eddy vertical velocities and zonal-mean surface specific humidity. Part of the success of this approximation comes from a cancellation between stationary-eddy moisture advection and transient-eddy moisture fluxes. Since transient eddies act diffusively on moisture (up to saturation), they tend to reduce moisture gradients set up by the time-mean flow, especially in midlatitudes. Moisture gradients are also weak in the tropics as a consequence of weak temperature gradients. As a result, zonal anomalies in specific humidity do not have a large influence on P^*-E^*.

The benefit of this simple approximation for P^*-E^* is fully realized in the analysis of climate change experiments, where P^*-E^* changes can be split up into thermodynamic changes, due to changes in zonal-mean surface specific humidity, and dynamic changes, due to changes in stationary-eddy vertical motion. Even for relatively small changes in forcing, shifts in stationary-eddy circulations are large, such that *wet gets wetter, dry gets drier* ideas do not apply locally. The *wet gets wetter, dry gets drier* idea, where existing $P - E$ patterns are amplified at a fractional rate of 7% K^{-1} due to an increase in atmospheric moisture content, is used extensively in the literature, often implicitly used to infer local changes. Our analysis shows that shifts in stationary-eddy circulations can be more important in many areas, especially in the tropics.

We investigate the amplitude of the zonally anomalous hydrological cycle using the zonal standard deviation of $P - E$. The zonal hydrological cycle amplitude tends to increase in a warming climate, due to the increase in atmospheric moisture content, but in many cases the increase is much less than that expected from the increase in moisture. The difference between the change in amplitude and the thermodynamic expectation is primarily a consequence of the reduction in strength of stationary-eddy overturning circulations. In idealized model experiments with simple zonal experiments, we even find configurations where these circulation changes are strong enough such that they reverse the tendency towards *wet gets wetter, dry gets drier*, reducing the zonal hydrological cycle amplitude with warming. These conclusions apply also to simulations of the next century, where all models studied show a zonal hydrological cycle amplitude increase less than that which would result purely from an increase in moisture.

The importance of changes in stationary-eddy circulations in determining $P^* - E^*$ led us to investigate controls on stationary-eddy amplitude in idealized model experiments with simple zonal asymmetries. The amplitude of stationary eddies forced by topography in midlatitudes was seen to behave non-monotonically with warming, with a response that depended on the latitude of forcing. The strength of the Walker circulation forced by zonally anomalous ocean heating was seen to decrease monotonically with warming. The Walker circulation response is independent of particulars of forcing geometry.

We investigated the mechanisms governing the orographic stationary wave response using the thermodynamic equation. Orographic slope winds force stationary-eddy meridional wind with a sensitivity that depends on the slope of isentropes. This effect by itself would lead to increased orographic forcing with warming due to decreases in isentropic slope. However, the orographic winds have a strong response to climate change that depends on zonal surface winds at the latitude of the mountain. The non-monotonicity of stationary-wave amplitude thus results from the non-monotonicity in the strength of surface winds. The surface wind response is also the main reason for the latitudinal dependence, as the surface winds shift equatorward with warming in our model. The stationary-eddy response departs from that predicted by the surface winds and isentropic slope in warm climates. The reason for this departure is the increased importance of latent heating, which damps stationary eddies due to its correlation with adiabatic cooling. Transient eddies also play a role in the energy budget downstream of the mountain, slightly amplifying the stationary wave response. The main take away points are that orographic stationary eddies are forced by surface zonal winds, that the sensitivity increase with warming due to a reduced isentropic slope, and that latent heating significantly damps stationary eddies in warm climates. These quantities can be related to zonal-mean quantities, so this can be used as a qualitative, but predictive theory for the response of orographic stationary waves to warming.

The monotonic decrease in Walker circulation strength is attributed to the increased energetic requirement of deep convection, with the zonally anomalous energy input held approximately fixed by the ocean heat-flux convergence. The increased energetic requirement of deep convection can be derived by examining the profile of moist static energy and considering that deep convection is deeper in a warmer climate because convected parcels rise higher before reaching a level of neutral buoyancy. Interestingly, the extratropical Rossby waves forced by the Walker circulation do not show a clear sign of the decrease in strength of the Walker circulation, due in part to the importance of Rossby wave turning latitudes.

We have made significant progress on understanding stationary-eddy controls of $P - E$ in a changing climate. We have also made progress towards a mechanistic understanding of changes in stationary eddies in two idealized cases. This provides a framework for understanding how regional $P - E$ responds to climate change that can be applied to regional impacts studies. An understanding of the full climate system will also require an analysis of other types of zonally asymmetric forcing such as subtropical and extratropical heating.

Appendix A

Forcing sensitivity

In the process of obtaining the idealized model results of Chapters 3, 5, and 6, we performed numerous other idealized GCM experiments with zonally varying boundary conditions. We present some here with the hope that they may provide some insight into the robustness of the results and guide others who wish to set up similar experiments.

A.1 Linearity of response

So far we have ignored changes in the amplitude of zonally asymmetric forcing and focused instead on changes in mean climate state. Ultimately, an application of these ideas requires some knowledge of the linearity of the response as well.

Due to the importance of latent-heating and transient-eddy nonlinearities in the orographic forcing experiment, there is no reason to think that the response would be very linear in mountain height. We investigate two smaller mountains of height $h_0 = 1000$ and 250 m. The $\overline{P}^* - \overline{E}^*$ response in these two cases, as well as the reference case ($h_0 = 2500$ m) are shown in Fig. A.1. We vary the colorbar range such that it is proportional to mountain height. A linear response to mountain height would show up as stationary-eddy patterns that are represented by the same number of contours in each subpanel, though noise will show up more in the lowest amplitude experiment. The response near the mountain appears quite nonlinear. The downstream dry zone is represented by 10 contours in $h_0 = 250$ and only 2 in $h_0 = 2500$. This is a reduction in $\frac{1}{h_0}(\overline{P}^* - \overline{E}^*)$ by a factor of 5. Comparable reductions are seen elsewhere in the topographic $\overline{P}^* - \overline{E}^*$ response.

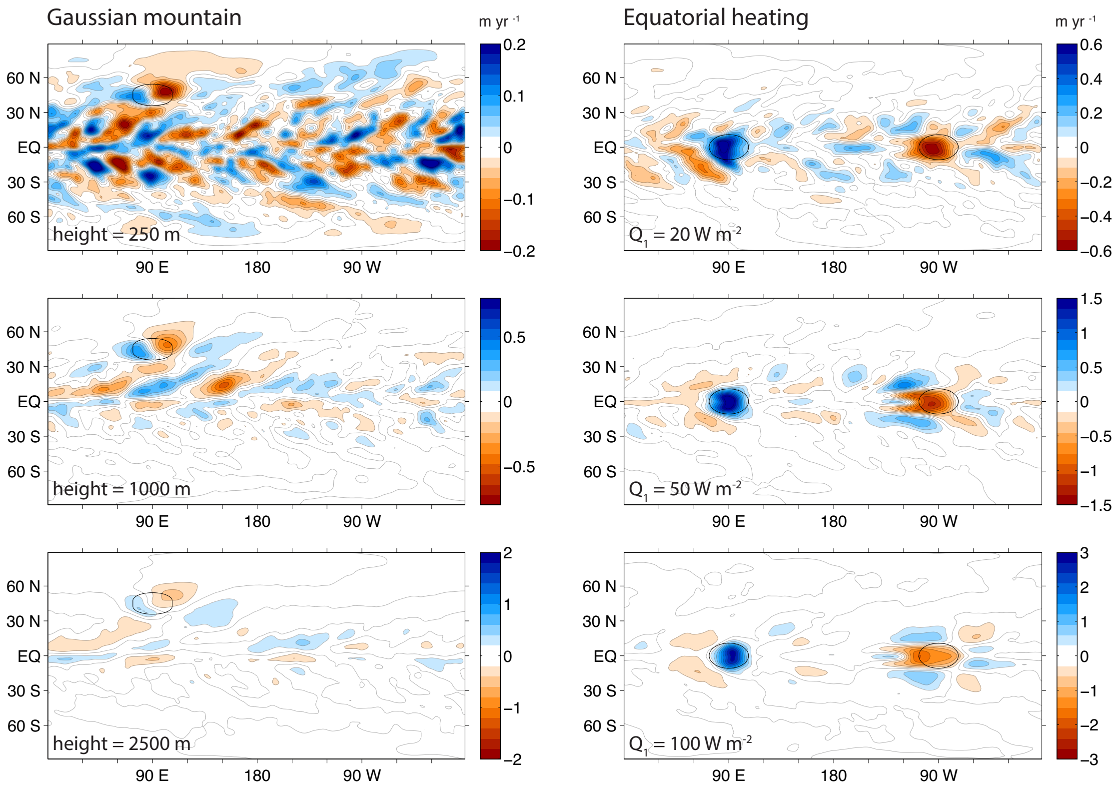

Figure A.1: Linearity (or lack thereof) of the $\overline{P}^* - \overline{E}^*$ response in the Gaussian mountain (left) and equatorial heating (right) experiments. For each experiment, 3 values of the forcing amplitude are shown, with the colorbar scaled by the forcing amplitude (i.e. the colorbar range doubles for a doubling of forcing). All simulations are spun up for 9 years and averaged over the subsequent 6 years. All fields are filtered with a 1.5° Gaussian filter.

On the other hand, the equatorial heating response appears quite linear over a range of zonally asymmetric ocean heat-flux convergence amplitudes Q_1 ranging from 20 W m^{-2} to 100 W m^{-2} (Fig. A.1). This is particularly true in the ascending branch of the Walker circulation, over the heat source. Other regions have a relative reduction of $\overline{P}^* - \overline{E}^*$, though none as strong as the factor of 5 found in the orographic forcing experiment. For example, the descending branch becomes more distributed in the $Q_1 = 100$ W m^{-2} case and is reduced in relative strength by a about a factor of 2 compared to the $Q_1 = 20$ W m^{-2} case. The linearity of the ascending motion response is expected based on our results in Chapter 4, where we found that the Walker circulation strength scales with the zonally anomalous energy input. A lack of linearity would indicate the emerging importance of stationary- and transient- eddy advection terms in the vertically-integrated MSE equation.

The linearity of the equatorial heating response and the strong nonlinearity of the orographic forcing response should be kept in mind when interpreting the results of Chapters 3 and 4.

A.2 The longitudinal width of topography

The modelled stationary-wave response to topography depends on the longitudinal width of topography σ_λ. We make a parameter sweep, $\sigma_\lambda =$[6, 7, 8, 10, 12, 16, 20, 30, 40, 50]. The other parameters of the surface topography,

$$z_{\mathrm{sfc}}\left(\lambda, \phi\right) = h_0 \exp\left[-\frac{\left(\lambda - \lambda_0\right)^2}{2\sigma_\lambda^2} - \frac{\max\left(0, \left|\phi - \phi_0\right| - R_\phi\right)^2}{2\sigma_\phi^2}\right], \tag{A.1}$$

are kept fixed at $h_0 = 4000$ m, $\phi_0 = 40°$N, $\lambda_0 = 90°$, $\sigma_\phi = 7.5°$, and $R_\phi = 2.5°$. We have also tried narrower mountains, $\sigma_\lambda \leq 5°$, but this starts to create lots of grid-scale noise at T85 resolution. Such resolution issues are likely the cause of grid-scale noise in IPCC models (Fig. 4.6).

We would like the topography to force planetary Rossby waves. For narrow mountains, the response will be confined to the local orographic precipitation influence. For example, Shi and Durran (2014) have a similar idealized GCM experiment with $\sigma_\lambda = 1.8°$ in order to focus on the response of orographic precipitation to global warming (in a much higher resolution model). As such, zonal precipitation variations in their simulations are confined to the regions immediately over topography (see Fig. 2 in Shi and Durran 2014).

Across the range of longitudinal widths explored here, there is a significant downstream Rossby wave response. However, Fig. A.2 shows an increase in the meridional component of sEKE as the longitudinal width is increased up to 16°. We interpret this as an increased forcing of stationary Rossby waves due to the increased zonal scale of the mountain. We choose $\sigma_\lambda = 12.5°$ for the simulations of Chapter 3 and 4 in order to strike a balance between taking advantage of this increase in forcing and keeping the size realistic based on real-world topography. The resulting topography corresponds roughly to the combined size and location of the Rocky Mountains, Sierra Nevada, and Pacific Northwest Coast ranges.

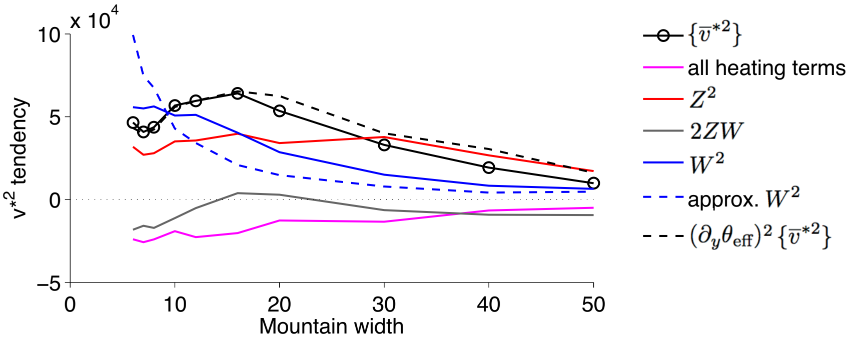

Figure A.2: Sensitivity of the globally averaged $\overline{v}^{*2}$ budget, derived and analyzed in section 5.5, to changes in the longitudinal width of the mountain range, σ_λ. The fifth simulation from the left, $\sigma_\lambda = 12$ is closest to the simulations analyzed elsewhere in this thesis.

Figure A.2 shows the controls on $\overline{v}^{*2}$ as analyzed in Section 5.5 with the thermodynamic equation. As the longitudinal width of the mountain is increased beyond the sEKE maximum at 16°, it is interesting to note that the balance of terms changes. The relative importance of the adiabatic heating/cooling term (W^2) is reduced, while the tilting of isentropes in the vicinity of the mountain (Z^2) remains important. For very large mountain widths, the thermal forcing of the mountain by adiabatic heating/cooling (per area) is small enough that it can be balanced by zonal temperature gradients. This leads to a reduction of the orographic response.

A.3 Realistic topography in an aquaplanet

We present here the $\overline{P}^* - \overline{E}^*$ response to modern topography in our idealized GCM, without any other zonal asymmetries such as land-sea thermal contrast or ocean heat-flux convergences. This simulation gives insight into which portion of the stationary wave field in the modern climate can be accounted for by topography alone. This can be compared with the linear stationary-wave model study of Held et al. (2002), who study the response to heating as well [see also Nigam et al. (1986, 1988); Valdes and Hoskins (1989); Ting (1994); Held et al. (2002)]. The main difference here is that the zonally varying transient-eddy heat fluxes forced by the topography are included, while they are diagnosed separately in the linear model. This is especially interesting in light of the large role of transient-eddy heat fluxes in the response to climate change as presented in section 5.5.

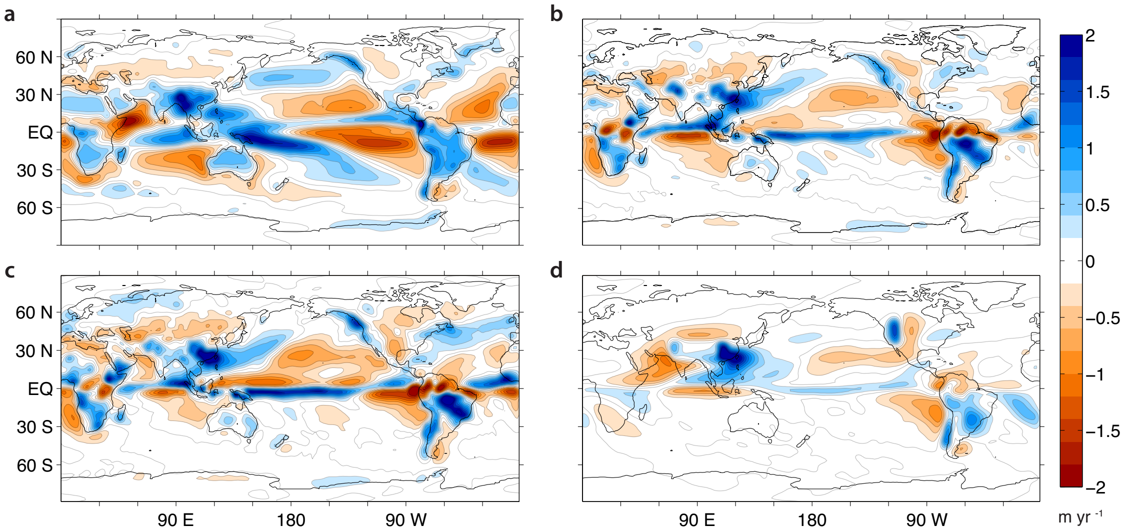

Figure A.3: $\overline{P}^* - \overline{E}^*$ climatology in a) ERA-Interim climatology and in b,c) an idealized GCM experiment with b) full modern topography, c) last glacial maximum (LGM) topography, d) and simple topography with 3 Gaussian mountains corresponding to Tibet, the Rockies, and the Andes. The idealized GCM simulations have no land-sea thermal contrast, seasonal cycle, water-vapor radiative feedback, clouds, or sea ice. All idealized GCM fields are filtered with a 1.5° Gaussian filter.

The model setup is as described in Chapter 3. It should be emphasized that there is no land-sea thermal contrast, seasonal cycle, water-vapor radiative feedback, clouds, or sea ice, so any resemblance to the real-world $\overline{P}^* - \overline{E}^*$ (shown for ERA-Interim, 1979-2012 in Fig. A.3a) is remarkable. Modern topography and last glacial maximum (LGM) topography from the ICE5G reconstruction (Peltier, 2004) are linearly interpolated to T85 resolution and specified in the model. The resulting $\overline{P}^* - \overline{E}^*$ responses are shown in Fig. A.3b (modern) and A.3c (LGM). While many features, especially in the tropics, are far from the reanalysis climatology, the Northern Hemisphere extratropical $\overline{P}^* - \overline{E}^*$ response shares many features with reanalysis. This is the region where topography is thought to have the largest influence on stationary waves (Chen and Trenberth, 1988; Broccoli and Manabe, 1992; Held et al., 2002). The $\overline{P}^* - \overline{E}^*$ patterns over North America, northeastern Asia, North Pacific, and North Atlantic are all qualitatively reproduced. Parts of the South America, southern Africa, southern Indian and Atlantic ocean, and Eastern Pacific $\overline{P}^* - \overline{E}^*$ patterns are also not so far off. This makes a case for the importance of topography for midlatitude $\overline{P}^* - \overline{E}^*$ patterns, which are also known to be strongly influenced by tropical ocean heating / SSTs (e.g., Seager et al.

2005).

We take this experiment a step further by simplifying the modern topography to 3 Gaussian mountains corresponding to the Rockies, the Andes, and Tibet. Based on Eq. A.1, the topography is specified as $h_0 =$ (3000 m, 4000 m, 5000 m), $\phi_0 =$ (45°N, 20°S, 30°N), $\lambda_0 =$ (110°W, 90°W, 90°E), $R_\phi =$ (5°, 20°, 2.5°), $R_\lambda =$ (0°, 0°, 15°), and $\sigma_\phi = \sigma_\lambda = 5°$, corresponding to (Rockies, Andes, Tibet). The $\overline{P}^* - \overline{E}^*$ response in this setup is shown in Fig. A.3d. A few features of the real-world $\overline{P}^* - \overline{E}^*$ are reproduced by this setup. Namely, the wetness of the East Asian monsoons region and South America and the dryness of the subtropical lows in the eastern Pacific, especially off the coast of South America. This setup was also used to test the linearity of the stationary-wave response to the superposition of multiple sources. To leading order, the $\overline{P}^* - \overline{E}^*$ response in Fig. A.3d can be reproduced from a linear superposition of the $\overline{P}^* - \overline{E}^*$ responses to each of the 3 Gaussian mountains seperately.

We also investigate LGM topography, because large northern hemisphere ice sheet changes relative to present day should provide an interesting response. Note that the longwave optical depth, corresponding to greenhouse gas concentrations, is kept fixed. The most striking feature of the resulting $\overline{P}^* - \overline{E}^*$ pattern (A.3c) is an intensification of North Atlantic storm track precipitation, here associated with stationary-eddy as well as transient-eddy moisture fluxes. The close relation of topography changes and $P - E$ changes over the North Atlantic was highlighted in (Eisenman et al., 2009), where these $P - E$ changes exert an inmportant influence on the Atlantic meridional overturning circulation. While the $\overline{P}^* - \overline{E}^*$ responses in these simple setups should not be taken too seriously, they capture an intriguing amount of the real-world extratropical $\overline{P}^* - \overline{E}^*$ variability.

Appendix B

List of symbols

Table B.1: We define here some of the symbols that are used repeatedly throughout this thesis.

symbol	description
$(\cdot)^*$	stationary-eddy component
$(\cdot)'$	transient-eddy component
$a^\dagger b^\dagger$	full stationary-eddy term, $a^*\,[b] + [a]\,b^* + a^* b^*$
$[\cdot]$	zonal average
$\overline{(\cdot)}$	time average
$\langle\cdot\rangle$	vertical integral
rms	zonal standard deviation (when applied to stationary-eddy quantity), $[(\cdot)^2]^{1/2}$
P	precipitation rate
E	evaporation rate
α	optical depth parameter (odp)
δ	change with climate change
λ	longitude
ϕ	latitude
p	pressure
p_s	surface pressure
p_t	tropopause pressure
σ	p/p_s
x	east–west distance, $2\pi\lambda r_e$
y	north–south distance, $2\pi\phi r_e$
r_e	radius of the Earth
z	height coordinate
z_{sfc}	surface height
β	df/dy
f	coreolis parameter
H	heavyside function

symbol	description
F	ocean heat transport
$\mathcal{F}_{\text{net}}$	total energy input to the atmospheric column, $\mathcal{S} - \mathcal{L} - \mathcal{O}$
$\mathcal{S}$	top-of-atmosphere incoming shortwave radiation
$\mathcal{L}$	top-of-atmosphere outgoing longwave radiation
$\mathcal{O}$	heat uptake by the ocean
c_p	heat capacity at constant pressure (fixed at 1004 J kg^{-1} K^{-1} in idealized GCM)
r_d	specific ideal gas constant of dry air (287 J kg^{-1} K^{-1})
r_v	specific ideal gas constant of water vapor (461 J kg^{-1} K^{-1})
g	gravitational constant
L	latent heat of vaporization (fixed at $2.5\text{x}10^6$ in idealized GCM)
h	moist static energy $c_pT + gz + Lq$
K_s	stationary wavenumber, $(\beta/[\overline{u}])^{1/2}$
k	zonal wavenumber
M	gross moist stability (GMS)
N	nonlinear vorticity tendencies
ψ	horizontal streamfunction
q	specific humidity
q_{sfc}	surface specific humidity
Q	heating rate
ρ	density
sEKE	stationary-eddy kinetic energy
tEKE	transient-eddy kinetic energy
T	transient-eddy vorticity tendencies (when used in the vorticity equation)
T	temperature
Γ	lapse rate, dT/dz
θ	potential temperature
τ	surface wind stress
u	zonal wind
$\mathbf{u}$	hotizontal wind, $u\hat{\mathbf{x}} + v\hat{\mathbf{y}}$
v	meridional wind
$\mathbf{v}$	3d wind field, $u\hat{\mathbf{x}} + v\hat{\mathbf{y}} + \omega\hat{\mathbf{z}}$
w	vertical wind
ω	pressure-coordinate vertical wind, $\frac{Dp}{dt}$
ω_{sfc}	$\mathbf{u} \cdot \nabla p_s$
$\Omega_1(p)$	vertical wind mode
ζ	relative vorticity
ζ_a	absolute vorticity

Bibliography

Barnes, E. A., 2013: Revisiting the evidence linking Arctic amplification to extreme weather in midlatitudes. *Geophysical Research Letters*, **40 (17)**, 4734–4739.

Barnes, E. A., and J. A. Screen, 2015: The impact of Arctic warming on the midlatitude jet-stream: Can it? has it? will it? *Wiley Interdisciplinary Reviews: Climate Change*, **6 (3)**, 277–286.

Bender, F. A., V. Ramanathan, and G. Tselioudis, 2012: Changes in extratropical storm track cloudiness 1983–2008: observational support for a poleward shift. *Climate Dynamics*, **38 (9-10)**, 2037–2053.

Benton, G. S., and M. A. Estoque, 1954: Water-vapor transfer over the north american continent. *Journal of Meteorology*, **11 (6)**, 462–477.

Betts, A. K., 1998: Climate-convection feedbacks: Some further issues. *Clim. Change*, **39**, 35–38.

Bjerknes, J., 1969: Atmospheric teleconnections from the equatorial Pacific. *Monthly Weather Review*, **97 (3)**, 163–172.

Bjerknes, J., 1972: Large-scale atmospheric response to the 1964-65 Pacific equatorial warming. *Journal of Physical Oceanography*, **2 (3)**, 212–217.

Boer, G. J., 1982: Diagnostic equations in isobaric coordinates. *Monthly Weather Review*, **110 (12)**, 1801–1820.

Bony, S., G. Bellon, D. Klocke, S. Sherwood, S. Fermepin, and S. Denvil, 2013: Robust direct effect of carbon dioxide on tropical circulation and regional precipitation. *Nature Geoscience*, **6 (6)**, 447–451.

Boos, W. R., and Z. Kuang, 2010: Dominant control of the south asian monsoon by orographic insulation versus plateau heating. *Nature*, **463 (7278)**, 218–222.

Bordoni, S., 2007: On the role of eddies in monsoonal circulations: Observations and theory. Ph.D. thesis, University of California, Los Angeles.

Bordoni, S., and T. Schneider, 2008: Monsoons as eddy-mediated regime transitions of the tropical overturning circulation. *Nat. Geosci.*, **1 (8)**, 515–519.

Brandefelt, J., and H. Körnich, 2008: Northern hemisphere stationary waves in future climate projections. *J. Climate*, **21 (23)**, 6341–6353.

Broccoli, A., and S. Manabe, 1992: The effects of orography on midlatitude northern hemisphere dry climates. *J. Climate*, **5 (11)**, 1181–1201.

Broecker, W. S., D. M. Peteet, and D. Rind, 1985: Does the ocean-atmosphere system have more than one stable mode of operation? *Nature*, **315 (6014)**, 21–26.

Byrne, M. P., and P. A. O'Gorman, 2013: Link between land-ocean warming contrast and surface relative humidities in simulations with coupled climate models. *Geophys. Res. Lett.*, **40 (19)**, 5223–5227.

Byrne, M. P., and P. A. O'Gorman, 2015: The response of precipitation minus evapotranspiration to climate warming: Why the "wet-get-wetter, dry-get-drier" scaling does not hold over land. *J. Climate*, **28 (20)**, 8078–8092.

Caballero, R., and J. Hanley, 2012: Midlatitude eddies, storm-track diffusivity, and poleward moisture transport in warm climates. *J. Atmos. Sci.*, **69 (11)**, 3237–3250.

Caballero, R., and P. L. Langen, 2005: The dynamic range of poleward energy transport in an atmospheric general circulation model. *Geophys. Res. Lett.*, **32 (2)**.

Charney, J. G., 1963: A note on large-scale motions in the tropics. *J. Atmos. Sci.*, **20 (6)**, 607–609.

Charney, J. G., and P. G. Drazin, 1961: Propagation of planetary-scale disturbances from the lower into the upper atmosphere. *J. Geophys. Res.*, **66 (1)**, 83–109.

Chen, G., and I. M. Held, 2007: Phase speed spectra and the recent poleward shift of southern hemisphere surface westerlies. *Geophysical Research Letters*, **34 (21)**.

Chen, J., and S. Bordoni, 2014: Orographic effects of the Tibetan Plateau on the east asian summer monsoon: An energetic perspective. *J. Climate*, **27 (8)**, 3052–3072.

Chen, S.-C., and K. E. Trenberth, 1988: Orographically forced planetary waves in the Northern Hemisphere winter: Steady state model with wave-coupled lower boundary formulation. *J. Atmos. Sci.*, **45 (4)**, 657–681.

Chou, C., and J. D. Neelin, 2004: Mechanisms of global warming impacts on regional tropical precipitation. *J. Climate*, **17 (13)**, 2688–2701.

Chou, C., J. D. Neelin, C.-A. Chen, and J.-Y. Tu, 2009: Evaluating the "rich-get-richer" mechanism in tropical precipitation change under global warming. *J. Climate*, **22 (8)**, 1982–2005.

Chou, C., T.-C. Wu, and P.-H. Tan, 2013: Changes in gross moist stability in the tropics under global warming. *Climate dynamics*, **41 (9-10)**, 2481–2496.

Collins, M., and Coauthors, 2013: *Long-term Climate Change: Projections, Commitments and Irreversibility*, book section 12, 10291136. Cambridge University Press, Cambridge, United Kingdom and New York, NY, USA, doi:10.1017/CBO9781107415324.024, URL `www.climatechange2013.org`.

Couhert, A., T. Schneider, J. Li, D. E. Waliser, and A. M. Tompkins, 2010: The maintenance of the relative humidity of the subtropical free troposphere. *J. Climate*, **23 (2)**, 390–403.

Czaja, A., 2009: Atmospheric control on the thermohaline circulation. *J. Phys. Oceanogr.*, **39 (1)**, 234–247.

Dai, A., and K. E. Trenberth, 2002: Estimates of freshwater discharge from continents: Latitudinal and seasonal variations. *J. Hydrometeor.*, **3 (6)**, 660–687.

De Boer, A., J. Toggweiler, and D. Sigman, 2008: Atlantic dominance of the meridional overturning circulation. *J. Phys. Oceanogr.*, **38 (2)**, 435–450.

Dee, D., and Coauthors, 2011: The ERA-Interim reanalysis: Configuration and performance of the data assimilation system. *Quart. J. Roy. Meteor. Soc.*, **137 (656)**, 553–597.

Delcroix, T., C. Hénin, V. Porte, and P. Arkin, 1996: Precipitation and sea-surface salinity in the tropical Pacific Ocean. *Deep Sea Res. Part I*, **43 (7)**, 1123–1141.

Deser, C., A. S. Phillips, M. A. Alexander, and B. V. Smoliak, 2014: Projecting North American climate over the next 50 years: Uncertainty due to internal variability. *J. Climate*, **27 (6)**, 2271–2296.

Egger, J., 1976: The linear response of a hemispheric two-level primitive equation model to forcing by topography. *Monthly Weather Review*, **104 (4)**, 351–364.

Eisenman, I., C. M. Bitz, and E. Tziperman, 2009: Rain driven by receding ice sheets as a cause of past climate change. *Paleoceanography*, **24 (4)**.

Emanuel, K., 2007: Quasi-equilibrium dynamics of the tropical atmosphere. *The Global Circulation of the Atmosphere*, Princeton University Press, 186–218.

Emanuel, K. A., J. David Neelin, and C. S. Bretherton, 1994: On large-scale circulations in convecting atmospheres. *Q. J. R. Meteorol. Soc.*, **120 (519)**, 1111–1143.

Emile-Geay, J., M. A. Cane, N. Naik, R. Seager, A. C. Clement, and A. van Geen, 2003: Warren revisited: Atmospheric freshwater fluxes and "Why is no deep water formed in the North Pacific". *J. Geophys. Res.: Oceans (1978–2012)*, **108 (C6)**.

Fekete, B. M., C. J. Vörösmarty, and R. B. Lammers, 2001: Scaling gridded river networks for macroscale hydrology: Development, analysis, and control of error. *Water Resour. Res.*, **37 (7)**, 1955–1967.

Ferreira, D., J. Marshall, and J.-M. Campin, 2010: Localization of deep water formation: Role of atmospheric moisture transport and geometrical constraints on ocean circulation. *J. Climate*, **23 (6)**, 1456–1476.

Francis, J. A., and S. J. Vavrus, 2012: Evidence linking Arctic amplification to extreme weather in mid-latitudes. *Geophysical Research Letters*, **39 (6)**.

Frierson, D. M., 2007: The dynamics of idealized convection schemes and their effect on the zonally averaged tropical circulation. *J. Atmos. Sci.*, **64 (6)**, 1959–1976.

Frierson, D. M., I. M. Held, and P. Zurita-Gotor, 2006: A gray-radiation aquaplanet moist GCM. Part I: Static stability and eddy scale. *J. Atmos. Sci.*, **63 (10)**, 2548–2566.

Fyfe, J. C., 2003: Extratropical southern hemisphere cyclones: Harbingers of climate change? *J. Climate*, **16 (17)**, 2802–2805.

Gill, A. E., 1980: Some simple solutions for heat-induced tropical circulation. *Quart. J. Roy. Meteor. Soc.*, **106 (449)**, 447–462.

Greve, P., B. Orlowsky, B. Mueller, J. Sheffield, M. Reichstein, and S. I. Seneviratne, 2014: Global assessment of trends in wetting and drying over land. *Nature geoscience*, **7 (10)**, 716–721.

Held, I. M., 1983: Stationary and quasi-stationary eddies in the extratropical troposphere: Theory. *Large-scale dynamical processes in the atmosphere*, 127–168.

Held, I. M., and A. Y. Hou, 1980: Nonlinear axially symmetric circulations in a nearly inviscid atmosphere. *J. Atmos. Sci.*, **37 (3)**, 515–533.

Held, I. M., and B. J. Soden, 2000: Water vapor feedback and global warming. *Annu. Rev. Energy Environ.*, **25**, 441–475.

Held, I. M., and B. J. Soden, 2006: Robust responses of the hydrological cycle to global warming. *J. Climate*, **19 (21)**, 5686–5699.

Held, I. M., and M. Ting, 1990: Orographic versus thermal forcing of stationary waves: The importance of the mean low-level wind. *J. Atmos. Sci.*, **47 (4)**, 495–500.

Held, I. M., M. Ting, and H. Wang, 2002: Northern winter stationary waves: Theory and modeling. *J. Climate*, **15 (16)**, 2125–2144.

Hernández-Deckers, D., and J.-S. von Storch, 2010: Energetics responses to increases in greenhouse gas concentration. *J. Climate*, **23 (14)**, 3874–3887.

Hernández-Deckers, D., and J.-S. von Storch, 2011: The energetics response to a warmer climate: Relative contributions from the transient and stationary eddies. *Earth System Dynamics*, **2**, 105–120.

Hoskins, B. J., and D. J. Karoly, 1981: The steady linear response of a spherical atmosphere to thermal and orographic forcing. *J. Atmos. Sci.*, **38 (6)**, 1179–1196.

Hu, Y., and Q. Fu, 2007: Observed poleward expansion of the Hadley circulation since 1979. *Atmos. Chem. Phys.*, **7 (19)**, 5229–5236.

Huang, P., S.-P. Xie, K. Hu, G. Huang, and R. Huang, 2013: Patterns of the seasonal response of tropical rainfall to global warming. *Nat. Geosci.*, **6 (5)**, 357–361.

Joseph, R., M. Ting, and P. J. Kushner, 2004: The global stationary wave response to climate change in a coupled GCM. *J Climate.*, **17 (3)**, 540–556.

Kang, S. M., D. M. Frierson, and I. M. Held, 2009: The tropical response to extratropical thermal forcing in an idealized GCM: The importance of radiative feedbacks and convective parameterization. *Journal of the atmospheric sciences*, **66 (9)**, 2812–2827.

Kaspi, Y., and T. Schneider, 2013: The role of stationary eddies in shaping midlatitude storm tracks. *J. Atmos. Sci.*, **70 (8)**, 2596–2613.

Kushner, P. J., I. M. Held, and T. L. Delworth, 2001: Southern hemisphere atmospheric circulation response to global warming. *J. Climate*, **14 (10)**, 2238–2249.

Lehner, B., K. Verdin, and A. Jarvis, 2008: New global hydrography derived from spaceborne elevation data. *Eos, Trans. AGU*, **89 (10)**, 93–94.

Levine, X. J., and W. R. Boos, 2016: A mechanism for the response of the zonally asymmetric subtropical hydrologic cycle to global warming. *J. Climate, submitted.*

Lorenz, E. N., 1955: Available potential energy and the maintenance of the general circulation. *Tellus*, **7 (2)**, 157–167.

Lu, J., G. A. Vecchi, and T. Reichler, 2007: Expansion of the Hadley cell under global warming. *Geophys. Res. Lett.*, **34 (6)**.

Mbengue, C., and T. Schneider, 2013: Storm track shifts under climate change: What can be learned from large-scale dry dynamics. *J. Climate*, **26 (24)**, 9923–9930.

Merlis, T. M., and T. Schneider, 2011: Changes in zonal surface temperature gradients and Walker circulations in a wide range of climates. *J. Climate*, **24**, 4757–4768.

Mitchell, J. F., C. Wilson, and W. Cunnington, 1987: On CO2 climate sensitivity and model dependence of results. *Q. J. R. Meteorol. Soc.*, **113 (475)**, 293–322.

Molnar, P., W. R. Boos, and D. S. Battisti, 2010: Orographic controls on climate and paleoclimate of Asia: Thermal and mechanical roles for the Tibetan Plateau. *Annu. Rev. Earth Planet. Sci.*, **38 (1)**, 77.

Neelin, J. D., 1988: A simple model for surface stress and low-level flow in the tropical atmosphere driven by prescribed heating. *Quart. J. Roy. Meteor. Soc.*, **114 (481)**, 747–770.

Neelin, J. D., 2007: Moist dynamics of tropical convection zones in monsoons, teleconnections, and global warming. *The Global Circulation of the Atmosphere*, T. Schneider, and A. H. Sobel, Eds., Princeton University Press, 267–301.

Neelin, J. D., and I. M. Held, 1987: Modeling tropical convergence based on the moist static energy budget. *Monthly Weather Review*, **115 (1)**, 3–12.

Neelin, J. D., and J.-Y. Yu, 1994: Modes of tropical variability under convective adjustment and the Madden-Julian oscillation. Part I: Analytical theory. *J. Atmos. Sci.*, **51 (13)**, 1876–1894.

Neelin, J. D., and N. Zeng, 2000: A quasi-equilibrium tropical circulation model-formulation. *J. Atmos. Sci.*, **57 (11)**, 1741–1766.

Newman, M., G. N. Kiladis, K. M. Weickmann, F. M. Ralph, and P. D. Sardeshmukh, 2012: Relative contributions of synoptic and low-frequency eddies to time-mean atmospheric moisture transport, including the role of atmospheric rivers. *J. Climate*, **25 (21)**, 7341–7361.

Nigam, S., I. M. Held, and S. W. Lyons, 1986: Linear simulation of the stationary eddies in a general circulation model. Part I: The no-mountain model. *J. Atmos. Sci.*, **43 (23)**, 2944–2961.

Nigam, S., I. M. Held, and S. W. Lyons, 1988: Linear simulation of the stationary eddies in a GCM. Part II: The "mountain" model. *J. Atmos. Sci.*, **45 (9)**, 1433–1452.

Nilsson, J., P. L. Langen, D. Ferreira, and J. Marshall, 2013: Ocean basin geometry and the salinification of the Atlantic Ocean. *J. Climate*, **26 (16)**, 6163–6184.

O'Gorman, P. A., and T. Schneider, 2008a: Energy of midlatitude transient eddies in idealized simulations of changed climates. *J. Climate*, **21 (22)**, 5797–5806.

O'Gorman, P. A., and T. Schneider, 2008b: The hydrological cycle over a wide range of climates simulated with an idealized GCM. *J. Climate*, **21 (15)**, 3815–3832.

Peixoto, J. P., 1970: Pole to pole divergence of water vapor. *Tellus*, **22 (1)**, 17–25.

Peixoto, J. P., and A. H. Oort, 1983: The atmospheric branch of the hydrological cycle and climate. *Variations in the global water budget*, Springer, 5–65.

Peixoto, J. P., and A. H. Oort, 1992: *Physics of Climate*. American Institute of Physics, 520 pp.

Peltier, W., 2004: Global glacial isostasy and the surface of the ice-age earth: the ICE-5G (VM2) model and GRACE. *Annu. Rev. Earth Planet. Sci.*, **32**, 111–149.

Philander, S. G., 1990: *El Niño, La Niña, and the Southern Oscillation*, Vol. 46. Academic press.

Plumb, R. A., 1985: On the three-dimensional propagation of stationary waves. *J. Atmos. Sci.*, **42 (3)**, 217–229.

Reid, J. L., 1979: On the contribution of the Mediterranean Sea outflow to the Norwegian-Greenland Sea. *Deep Sea Res. Part I*, **26 (11)**, 1199–1223.

Reid Jr, J. L., 1961: On the temperature, salinity, and density differences between the Atlantic and Pacific oceans in the upper kilometre. *Deep Sea Res. (1953)*, **7 (4)**, 265–275.

Rienecker, M. M., and Coauthors, 2011: MERRA: NASA's modern-era retrospective analysis for research and applications. *J. Climate*, **24 (14)**, 3624–3648.

Rodwell, M., and B. Hoskins, 2001: Subtropical anticyclones and summer monsoons. *J. Climate*, **14 (15)**, 3192–3211.

Rodwell, M. J., and B. J. Hoskins, 1996: Monsoons and the dynamics of deserts. *Quart. J. Roy. Meteor. Soc.*, **122 (534)**, 1385–1404.

Roe, G. H., 2005: Orographic precipitation. *Annu. Rev. Earth Planet. Sci.*, **33**, 645–671.

Sardeshmukh, P. D., and B. J. Hoskins, 1988: The generation of global rotational flow by steady idealized tropical divergence. *J. Atmos. Sci.*, **45 (7)**, 1228–1251.

Schneider, T., 2006: The general circulation of the atmosphere. *Annu. Rev. Earth Planet. Sci.*, **34**, 655–688.

Schneider, T., P. A. O'Gorman, and X. J. Levine, 2010: Water vapor and the dynamics of climate changes. *Rev. Geophys.*, **48 (3)**.

Seager, R., Y. Kushnir, C. Herweijer, N. Naik, and J. Velez, 2005: Modeling of tropical forcing of persistent droughts and pluvials over western North America: 1856-2000. *J. Climate*, **18 (19)**, 4065–4088.

Seager, R., H. Liu, N. Henderson, I. Simpson, C. Kelley, T. Shaw, Y. Kushnir, and M. Ting, 2014:

Causes of increasing aridification of the Mediterranean region in response to rising greenhouse gases. *J. Climate*, **27 (12)**, 4655–4676.

Seager, R., N. Naik, and G. A. Vecchi, 2010: Thermodynamic and dynamic mechanisms for large-scale changes in the hydrological cycle in response to global warming. *J. Climate*, **23 (17)**, 4651–4668.

Seager, R., and Coauthors, 2007: Model projections of an imminent transition to a more arid climate in southwestern North America. *Science*, **316 (5828)**, 1181–1184.

Shaw, T. A., 2014: On the role of planetary-scale waves in the abrupt seasonal transition of the northern hemisphere general circulation. *J. Atmos. Sci.*, **71 (5)**, 1724–1746.

Shi, X., and D. R. Durran, 2014: The response of orographic precipitation over idealized midlatitude mountains due to global increases in CO2. *J. Climate*, **27 (11)**, 3938–3956.

Simpson, I. R., R. Seager, M. Ting, and T. A. Shaw, 2015: Causes of change in northern hemisphere winter meridional winds and regional hydroclimate. *Nature Climate Change.*

Simpson, I. R., T. A. Shaw, and R. Seager, 2014: A diagnosis of the seasonally and longitudinally varying midlatitude circulation response to global warming. *J. Atmos. Sci.*, **71 (7)**, 2489–2515.

Singh, M. S., and P. A. O'Gorman, 2012: Upward shift of the atmospheric general circulation under global warming: Theory and simulations. *J. Climate*, **25 (23)**, 8259–8276.

Sobel, A. H., and S. J. Camargo, 2011: Projected future seasonal changes in tropical summer climate. *J. Climate*, **24 (2)**, 473–487.

Sobel, A. H., J. Nilsson, and L. M. Polvani, 2001: The weak temperature gradient approximation and balanced tropical moisture waves. *J. Atmos. Sci.*, **58 (23)**, 3650–3665.

Starr, V. P., and J. P. Peixoto, 1958: On the global balance of water vapor and the hydrology of deserts. *Tellus A*, **10 (2)**.

Stephenson, D. B., and I. M. Held, 1993: GCM response of northern winter stationary waves and storm tracks to increasing amounts of carbon dioxide. *J. Climate*, **6 (10)**, 1859–1870.

Takahashi, K., and D. S. Battisti, 2007: Processes controlling the mean tropical Pacific precipitation pattern. Part II: The SPCZ and the southeast Pacific dry zone. *J. Climate*, **20 (23)**, 5696–5706.

Ting, M., 1994: Maintenance of northern summer stationary waves in a GCM. *J. Atmos. Sci.*, **51 (22)**, 3286–3308.

Ting, M., and L. Yu, 1998: Steady response to tropical heating in wavy linear and nonlinear baroclinic models. *J. Atmos. Sci.*, **55 (24)**, 3565–3582.

Trenberth, K. E., J. T. Fasullo, and J. Mackaro, 2011: Atmospheric moisture transports from ocean to land and global energy flows in reanalyses. *J. Climate*, **24 (18)**, 4907–4924.

Trenberth, K. E., L. Smith, T. Qian, A. Dai, and J. Fasullo, 2007: Estimates of the global water budget and its annual cycle using observational and model data. *J. Hydrometeor.*, **8 (4)**, 758–769.

Trenberth, K. E., D. P. Stepaniak, and J. M. Caron, 2002: Accuracy of atmospheric energy budgets from analyses. *J. Climate*, **15 (23)**, 3343–3360.

Valdes, P. J., and B. J. Hoskins, 1989: Linear stationary wave simulations of the time-mean climatological flow. *J. Atmos. Sci.*, **46 (16)**, 2509–2527.

Vallis, G. K., 2006: *Atmospheric and Oceanic Fluid Dynamics*. Cambridge University Press, Cambridge, U.K., 745 pp.

Vecchi, G. A., and B. J. Soden, 2007: Global warming and the weakening of the tropical circulation. *J. Climate*, **20 (17)**, 4316–4340.

Vecchi, G. A., B. J. Soden, A. T. Wittenberg, I. M. Held, A. Leetmaa, and M. J. Harrison, 2006: Weakening of tropical pacific atmospheric circulation due to anthropogenic forcing. *Nature*, **441 (7089)**, 73–76.

Voigt, A., and T. A. Shaw, 2015: Circulation response to warming shaped by radiative changes of clouds and water vapour. *Nat. Geosci.*

Vörösmarty, C., B. Fekete, M. Meybeck, and R. Lammers, 2000: Geomorphometric attributes of the global system of rivers at 30-minute spatial resolution. *J. Hydrol.*, **237 (1)**, 17–39.

Walker, C. C., and T. Schneider, 2006: Eddy influences on hadley circulations: Simulations with an idealized GCM. *J. Atmos Sci.*, **63 (12)**, 3333–3350.

Walker, J. M., S. Bordoni, and T. Schneider, 2015: Interannual variability in the large-scale dynamics of the South Asian summer monsoon. *J. Climate*, **28 (9)**, 3731–3750.

Warren, B. A., 1983: Why is no deep water formed in the North Pacific? *J. Mar. Res.*, **41 (2)**, 327–347.

Weaver, A., C. Bitz, A. Fanning, and M. Holland, 1999: Thermohaline circulation: High-latitude phenomena and the difference between the Pacific and Atlantic. *Annu. Rev. Earth Planet. Sci.*, **27 (1)**, 231–285.

Webster, P. J., 1981: Mechanisms determining the atmospheric response to sea surface temperature anomalies. *J. Atmos. Sci.*, **38 (3)**, 554–571.

Webster, P. J., V. O. Magana, T. Palmer, J. Shukla, R. Tomas, M. U. Yanai, and T. Yasunari, 1998: Monsoons: Processes, predictability, and the prospects for prediction. *J. Geophys. Res.: Oceans (1978–2012)*, **103 (C7)**, 14 451–14 510.

Wills, R. C., and T. Schneider, 2015: Stationary eddies and the zonal asymmetry of net precipitation and ocean freshwater forcing. *J. Climate*, **28**, 5115–5133.

Wills, R. C., and T. Schneider, 2016: How stationary eddies shape changes in the hydrological cycle: Zonally asymmetric experiments in an idealized GCM. *J. Climate, submitted.*

Wu, Y., M. Ting, R. Seager, H.-P. Huang, and M. A. Cane, 2011: Changes in storm tracks and energy transports in a warmer climate simulated by the GFDL CM2.1 model. *Climate dynamics*, **37 (1-2)**, 53–72.

Xie, S.-P., C. Deser, G. A. Vecchi, J. Ma, H. Teng, and A. T. Wittenberg, 2010: Global warming pattern formation: Sea surface temperature and rainfall. *J. Climate*, **23 (4)**, 966–986.

Yin, J. H., 2005: A consistent poleward shift of the storm tracks in simulations of 21st century climate. *Geophys. Res. Lett.*, **32 (18)**.

Yu, J.-Y., and J. D. Neelin, 1997: Analytic approximations for moist convectively adjusted regions. *J. Atmos. Sci.*, **54 (8)**, 1054–1063.

Zaucker, F., T. F. Stocker, and W. S. Broecker, 1994: Atmospheric freshwater fluxes and their effect on the global thermohaline circulation. *J. Geophys. Res.*, **99 (C6)**, 12 443–12 457.

Zweng, M. M., and Coauthors, 2013: World Ocean Atlas 2013, Volume 2: Salinity. *NOAA Atlas NESDIS*, **74**, 39 pp.